An Investigation into the Effects of Viscoelasticity on Cavitation Bubble Dynamics with Applications to Biomedicine

Michael Jason Walters
School of Mathematics
Cardiff University

A thesis submitted for the degree of
Doctor of Philosophy

9th April 2015

Summary

In this thesis, the dynamics of microbubbles in viscoelastic fluids are investigated numerically. By neglecting the bulk viscosity of the fluid, the viscoelastic effects can be introduced through a boundary condition at the bubble surface thus alleviating the need to calculate stresses within the fluid.

Assuming the surrounding fluid is incompressible and irrotational, the Rayleigh-Plesset equation is solved to give the motion of a spherically symmetric bubble. For a freely oscillating spherical bubble, the fluid viscosity is shown to dampen oscillations for both a linear Jeffreys and an Oldroyd-B fluid. This model is also modified to consider a spherical encapsulated microbubble (EMB). The fluid rheology affects an EMB in a similar manner to a cavitation bubble, albeit on a smaller scale.

To model a cavity near a rigid wall, a new, non-singular formulation of the boundary element method is presented. The non-singular formulation is shown to be significantly more stable than the standard formulation. It is found that the fluid rheology often inhibits the formation of a liquid jet but that the dynamics are governed by a competition between viscous, elastic and inertial forces as well as surface tension. Interesting behaviour such as cusping is observed in some cases.

The non-singular boundary element method is also extended to model the bubble transitioning to a toroidal form. This is achieved using the vortex ring method. If jet impact does occur, the bubble shape is thinner in the centre for a bubble in a viscoelastic fluid. Also, in the toroidal phase, the fluid elasticity can cause a rebound away from the wall.

The boundary element method is also used to model both a cavitation bubble and an EMB forced by an ultrasound field. This field is introduced through the pressure term at the bubble surface and typically causes explosive growth and collapse of the cavity. A number of different models for the pressure field are tested, relating to common biomedical applications such as shock wave lithotripsy and sonoporation. Compared to the freely oscillating bubble near a rigid wall, a more explosive collapse is seen with higher velocities and pressures produced. Even with a powerful pulse, a bubble in a viscoelastic fluid is seen to resist forming a liquid jet and becoming toroidal.

Declaration

This work has not been submitted in substance for any other degree or award at this or any other university or place of learning, nor is being submitted concurrently in candidature for any degree or other award.

Signed Date

STATEMENT 1

This thesis is being submitted in partial fulfillment of the requirements for the degree of PhD.

Signed Date

STATEMENT 2

This thesis is the result of my own independent work/investigation, except where otherwise stated. Other sources are acknowledged by explicit references. The views expressed are my own.

Signed Date

STATEMENT 3

I hereby give consent for my thesis, if accepted, to be available for photocopying and for inter-library loan, and for the title and summary to be made available to outside organisations.

Signed Date

Acknowledgments

I would like to sincerely thank my supervisor, Professor Tim Phillips, for providing constant help and guidance throughout my studies. Despite your many other commitments, I have always felt able to come to you for help and advice and it has been a pleasure working with you.

Thank you also to Professors Rhodri Williams and Russell Davies for examining this thesis and for the helpful comments and discussions.

To Tom, Liz, Jon, Angelico, Leanne, Penny, Julie, Izabella and Brad, thank you for the many tea breaks, intellectual discussions and trips to the shop which made the experience all the more enjoyable.

I would also like to thank Dr. Steve Lind for the use of his code as the starting point of my work and the help of of Dr. Qianxi Wang for his help with the non-singular formulation of the boundary element method.

I gratefully acknowledge the studentship funding I received from Cardiff School of Mathematics.

Finally, I would like to thank my family, friends and Jen for the constant moral support, I couldn't have done it without you.

Contents

Chapter 1

Introduction

This thesis is primarily focused on the development of the boundary element method for modelling bubbles in complex fluids. Understanding and controlling the dynamics of bubbles is vital not just because of their ubiquitous nature, but also due to their potential for intensifying physical or chemical processes in an efficient manner. Gas-filled bubbles exist in a number of natural processes such as fermentation, sedimentation and boiling as well as within many aspects of industry such as fluidized beds and nucleate boiling in reactors. Of particular interest is the formation of 'cavitation' bubbles, which are now discussed in detail.

1.1 Cavitation

Reducing the pressure of a liquid below the saturated vapour pressure (while keeping the temperature roughly constant) causes the liquid to be unstable and rupture with vapour pockets appearing throughout the liquid. This process is known as *cavitation*; the microscopic cavities which form then expand due to pressure differences and form macroscopic bubbles which are termed cavitation bubbles. Cavitation bubbles can form behind and damage rotating objects in fluids such as screw propellers on naval vessels due to the mechanical action of the rotating structures. It was this problem, in fact, which motivated Lord Rayleigh to produce the first numerical study of the collapse of a cavitation bubble [88]. In many applications, this rupturing of the fluid is undesirable due to the mechanical erosion which can be inflicted on solid structures.

The inception of cavitation bubbles can be carried out deliberately; usually by the

focus of a laser pulse (optic cavitation) or the application of an acoustic field (acoustic cavitation). A cavity contains either vapour, gas or a combination of both. A significant difference exists between these different internal quantities

- *Vapour filled*: When the fluid ruptures due to low pressures, vapour will condense into the bubble. A vapour filled bubble will collapse once it reaches a region of higher pressure.
- *Gas filled*: A gas filled bubble will also collapse in high pressure but as it collapses the gas is compressed leading to high pressures within the bubble. This high pressure will then cause rebound and bubble oscillations.

Regardless of the internal quantities, cavitation can be seen as a focusing of energy within the fluid and can have profound effects on nearby structures. The magnitude of these effects is dependent on the proximity of the cavity to the structure of interest. The formation of a cavity, known as *nucleation*, is a complex process which is difficult to predict and so is not explicitly modelled here.

1.1.1 Nucleation

In this thesis, the dynamics of an existing cavitation bubble are studied. The formation of the bubble, an example of nucleation, is not modelled but a brief description is provided here. Nucleation is typically divided into two types; homogeneous and heterogeneous nucleation. For homogeneous nucleation an applied pressure of at least 130MPa ruptures a fluid with microscopic voids forming and growing to become macroscopic bubbles. Heterogeneous nucleation occurs at the boundary between a liquid and solid state and is often more common in applications since the nucleation barrier is lower [91]. Cavitation nuclei are often existing bubbles containing contaminant gas which can be located either on a surface or in the bulk of the fluid, the latter termed 'free stream nuclei'. These free stream nuclei appear to be the predominant cause of cavitation in some cases [23] although controlling or even predicting the composition or character of these is extremely difficult. More detailed descriptions of nucleation can be found in the books of Brennen [23] and Brujan [27].

In the majority of real-world applications it is clear that multiple cavities will exist, often as a *bubble cloud*. The dynamics of each cavity is affected by its (near) environment, including the other nearby bubbles. Modelling the bubble cloud is thus an extremely complex problem and, although this has been studied by numerous authors (see for

example [82]), this approach is not followed here. Instead we follow a vast amount of previous work and limit our investigations to a single bubble. The relative tractability of this problem leads to a greater understanding of cavitation dynamics as a whole and is more useful in studying the effects of properties such as the fluid rheology and the influence of a rigid boundary.

1.1.2 Cavitation Damage

Despite their small size (usually of the order 1μm), cavitation bubbles can exhibit extreme physics with immense pressure and temperatures occuring during collapse (albeit over very small timescales). Their tendency to focus and concentrate energy, forces and stresses as well as emitting shockwaves means that they have a great potential for causing damage to nearby surfaces and structures. When a bubble is situated close to a surface, the asymmetry of the fluid flow can cause a jet to form as the bubble collapses, with the direction of the jet dependent on the parameters of the surface. This jet can either impact the surface directly or create a shockwave as it impacts the far side of the bubble due to a 'splashing effect'. The exact mechanisms of cavitation damage, though, are complex and difficult to observe since growth and collapse occur very rapidly and with microscopic dimensions. Some studies such as that of Chen and Israelachvili [31] show that damage to a nearby surface can actually be more likely to occur during the formation of cavities during which there are high local strains. It is clear, however, that gaining a greater understanding of cavitation damage is crucial to many engineering and biomedical applications.

1.2 Biomedical Applications

The application of acoustic cavitation has been shown to produce a range of biological effects such as the production of cavities in the ventricular wall, lung haemorrhage and the treatment of hypoplastic left heart syndrome [26]. The latter is a congenital heart disease, the treatment of which involves the creation of a flow channel between the atria of the heart. It has been shown that high-intensity ultrasound is a candidate for this treatment and that transient (inertial) cavitation is the primary mechanism of the erosion process. In this thesis, however, we restrict attention to the role of cavitation in shock-wave lithotripsy, ultrasound contrast imaging and sonoporation, which are now

described.

1.2.1 Shock-Wave Lithrotripsy

One of the prevalent applications in which cavitation bubbles play a role is a non-invasive treatment of kidney stones known as extracorporeal shock wave lithotripsy (ESWL). In ESWL, ultrasound shock waves are applied to disintegrate the renal calculi. Lithrotripters consist of a shock wave generator and systems for identifying and positioning the stone. To succesfully disintegrate ths stone, the patient must be carefully positioned to place the stone in the shock wave focus [30]. A number of different devices exist to produce the shock waves including

- Electrohydraulic lithotripters: in which electrodes generate shock waves which are focused using a reflector,
- Piezoelectric lithotripters: which contain an array of spherically aligned piezoelectric elements,
- Electromagnetic lithotripters: which focues acoustic pulses using a paraboloid reflector/lens.

The underlying physics of this problem, though, is complex and thus the exact mechanism of stone fragmentation is still debated. It has been shown, however, that cavitation has a beneficial effect on the treatment; in particular it is the combination of stress waves and cavitation which lead to mechanical stresses and the succesful disintegration of the kidney stones [32]. Initial fragmentation is caused by cracks forming due to the direct impact of the applied shock waves. Once cracks have formed, however, mechanisms such as tear and shear forces, spallation, dynamic squeezing and cavitation all contribute to damage the surfaces of the stones [86] and increase the effectiveness of the treatment.

Typical strengths for the shock wave used in ESWL are $9 - 114$MPa positive pressures followed by $2.8 - 9.9$MPa negative pressures [34]. These negative pressures are lower than the tensile strength of water and thus will only cause heterogeneous nucleation to occur. The cavitation bubbles generated will either form at the stone interface or from microscopic pockets of gas which are present, which will then expand and collapse rapidly. This can produce a liquid jet directed towards the boundary as well as emission of shock waves (typically at minimum volume [106]) which are both potentially

damaging to the stone surface. A significant amount of work has been carried out to investigate the effects of cavitation. Zhu et al. [119] mimicked the set up of ESWL using plaster-of-Paris 'stones' and found that, while the shock waves produced by the lithotripter initially breaks up the stone, cavitation weakens the structure of the stone significantly and thus increases the effectiveness of the shock waves. The effect of a cavitation bubble on the surface also depends on the dynamic response of the stone to the pressure field as well as the size of the bubble; for very small bubbles the liquid jet is seen to have a negligible effect on damage [60].

The interaction between an ultrasound shock wave and a cavitation bubble is investigated in Chapter 5 to approximately model the conditions of ESWL.

1.2.2 Ultrasound Contrast Agents and Encapsulated Microbubbles

Ultrasound imaging, also known as sonography, is the application of ultrasound to an area of the body, such as the abdomen or chest, in order to produce an image of an internal organ or structure. A transducer placed against the skin transmits acoustic pulses and receives them as they reflect off internal structures. Applications include visualisation of the cardiac chambers, enhancing tumour detection and imaging of small blood vessels such as the microvasculature [26].

In 'conventional' harmonic imaging, a fundamental frequency is transmitted and am image formed from the second harmonic component of the echoes. This is effective, but requires a narrow bandwidth since the bandwidth of the fundamental frequency cannot overlap with that of the second harmonic [3].

The efficacy of sonography is vastly improved by the introduction of encapsulated microbubbles (EMBs). These are typically filled with air or a high-molecular-weight low-solubility gas and encapsulated in either a stiff albumin shell or a more flexible lipid shell. These EMBs are termed ultrasound contrast agents due to their enhancing effect on the echoes produced from the ultrasound. The bubbles are typically $1 - 10\mu$m [111] and so are small enough to pass through capillaries when suspended in blood and so can reach almost any desired area. The interaction of an ultrasound beam with a microbubble causes the bubble to contract and expand since the internal gas is much more compressible than the surrounding tissue; this occurs most readily for a particular frequency known as the resonance frequency. This frequency depends on the size

of the bubble and shell parameters but for a typical EMB with size of the order 1μm the resonance frequency lies within the range typically used for ultrasound imaging $(2-10\text{MHz})$ [35]. Due to this the EMBs return significantly stronger echoes (than tissue reflectors of a similar size such as red blood cells) when interacting with a pressure pulse and it is this response that lies behind their efficacy as contrast agents.

For medium strength ultrasound fields, EMBs can produce strong echoes which make them the predominant choice for contrast agents. A strong enough pressure field, however, can lead to fragmentation of the bubble [35] causing it to dissolve into the surrounding fluid. Although this is not advantageous in sonography it is the main concept behind a type of gene and drug delivery called sonoporation. The threshold at which fragmentation occurs depends on initial size of the bubble, shell thickness and the shell and gas properties although the exact details are outside the scope of this thesis.

1.2.3 Sonoporation

The application of (powerful enough) ultrasound and the ensuing cavitation are well known to have the potential to cause cell membrane damage [73] which, if severe enough, can cause cell break down and disintegration. It is reasonable to describe a cell membrane as a 'semi-flexible' boundary rather than a rigid wall and thus to model this situation accurately some kind of elastic response to the fluid is required. This elastic membrane modelling, however, is left for future development.

This is an adverse effect in most circumstances but is usually accompanied by some sublethal membrane damage in which transient pores open and allow uptake of large molecules into the cell before resealing and cell survival. The use of ultrasound to achieve this increased cell permeability is termed *sonoporation*. Cavitation has been identified as the probable mechanism behind the cell permeability and the effectiveness has been shown [4] to be further enhanced using cavitation nuclei such as EMBs. The exact mechanism by which cavitation causes cell permeability and damage is not completely understood although it is widely proposed [26] that jetting is responsible; as the jet impacts the boundary it spreads out along the substrate causing a strong gradient in the parallel velocity component and a resulting shear stress.

The dynamics of an encapsulated microbubble are studied for the spherical case in Chapter 2 and for a nonspherical EMB near a rigid wall in Chapter 6.

1.3 Scope and Direction

Following many previous studies, a single bubble is considered to allow a comprehensive study of the dynamics. The effects of viscoelasticity, stand-off distance from a solid boundary, surface tension effects and the influence of a pressure pulse/field are investigated for a range of cases which pertain to certain biomedical applications. The interaction between bubbles, while important, is not considered so as to focus on the effects of these parameters. An investigation of spherical bubbles is undertaken to provide verification for the nonspherical models as well as giving a primary analysis of viscoelastic effects and acoustic forcing on dynamics.

The boundary element method is chosen to model nonspherical bubbles due to its simplicity and computational speed. It also has a remarkable agreement with more complex methods and experiments, despite a number of simplifying assumptions. Furthermore, the bubble surface is modelled as a true discontinuity in pressure/density which is highly desirable since viscous effects have been shown [5] to be particular important in thin boundary layers around the surfaces. Other more complex models which may provide a more realistic description of the physics involved often must approximate this discontinuity.

A modification to the spherical and BEM models allows the consideration of encapsulated microbubbles (EMBs) which, as discussed previously, are important in many biomedical applications where cavitation is utilised. This, along with the effect of an acoustic field, give an initial foray into modelling cavitation bubbles in applications such as shock wave lithotripsy and sonoporation.

1.4 Organisation

In Chapter 2, a spherically symmetric cavitation bubble in an infinite, incompressible fluid is considered. The Rayleigh-Plesset equation is derived for a general viscoelastic fluid and a range of viscoelastic models are derived and discussed. Attention is focused on the Linear Jeffrey's and (nonlinear) Oldroyd-B models for which results are presented to highlight the rheological effects on bubble dynamics. The Rayleigh-Plesset is also modified to model the encapsulated microbubbles present in applications such as sonoporation. Using a 'thin-shell' approximation, this is constructed for a spherically symmetric EMB exposed to an ultrasound field.

Chapter 3 uses the Boundary Element Method (BEM) to consider a bubble situated near a rigid wall. The effects of viscoelasticity have been extensively studied for this case by Lind & Phillips [67]. The aim of this chapter is to provide a more accurate BEM code to compare to these previous results. This is achieved through the use of quintic splines to discretise the bubble surface and a nonsingular form of the integral equation for the velocity potential. Furthermore, in [67] a vapour filled bubble with constant internal pressure was considered whereas here a gas-filled oscillating bubble is modelled and it will be seen that this can lead to significantly different dynamics.

The presence of the rigid wall often causes a jet to form during collapse which can eventually impact the far side of the bubble. The non-singular BEM code is extended in Chapter 4 to model the transition to a toroidal bubble geometry (if jet impact occurs) by smoothing the impact point and seeding a vortex ring inside the bubble, accounting for the circulation now present in the fluid. The influence of rheological effects on jet velocity, bubble volume and pressures at the rigid wall are investigated.

In Chapters 5 and 6, the interaction of a shock wave with a cavitation bubble and an EMB are modelled, respectively, using the boundary element method. The effects of the shock wave are introduced through the pressure in the Bernoulli equation for the velocity potential. These results are an initial step towards modelling the biomedical applications mentioned above where the bubble size and shock parameters can be fitted to known values for each application. Often in these applications the bubble dynamics can happen on a time scale smaller than the time between ultrasound pulses. Therefore, the interaction of a bubble and a single pulse is usually modelled.

Finally, the conclusions of this study are presented and further work discussed in Chapter 7.

Chapter 2

Incompressible Spherical Dynamics for Freely Oscillating and Forced Bubbles

2.1 Introduction

When cavities exist near surfaces or other structures it is known that the resulting dynamics tend to be asymmetric [18]. This is due to the fluid moving slower between the bubble and the wall as a result of higher pressures in this region. In fact, even in a large, roughly symmetric expanse of fluid the effects of surface tension can destabilise any initial spherical symmetry as the cavity evolves in time. If surface tension, gravity, buoyancy and deviations in the pressure field are neglected, however, bubbles can theoretically exhibit spherically symmetric oscillations. While this behaviour may not be realistic in many real world applications it is nevertheless a useful indicator of the effects of fluid parameters on bubble dynamics as well as being a useful reference for more realistic, complex studies.

In this chapter, the evolution of a spherical bubble in a viscoelastic fluids is investigated. A range of viscous and viscoelastic models are discussed and particular comparisons made between the linear Jeffreys model and the (nonlinear) Oldroyd-B model. Following this, the dynamics of spherical encapsulated microbubbles are studied using a thin shell approximation and a modified Rayleigh-Plesset equation.

2.2 Discussion of Assumptions

To fully describe the motion of a bubble in a surrounding fluid requires an explicit description of the bubble contents throughout the bubble, modelling of the entire fluid domain using the equations of motion (along with any kinematic relations and constitutive equations) as well as modelling the heat and mass transfer through the bubble surface. To do this would clearly be extremely complicated as well as computationally difficult and expensive. Thus in the majority of previous work a number of assumptions have been made in order to make the problem more tractable. Throughout this thesis the following assumptions are made

1. No heat or mass transfer takes place through the bubble/fluid interface and the temperature is constant throughout the fluid and in time,
2. The bubble consists of some vapour and gas which is homogeneous inside the bubble.

The process of mass transfer between the bubble and the surrounding fluid is complicated and thus difficult to model. It is neglected in this work for the sake of simplicity although since the process of collapse occurs so quickly it can be argued that there is insufficient time for significant mass transfer to occur.

In theory, accurately modelling the behaviour of the bubble contents would require the solution of mass, momentum and energy equations for the contents along with some appropriate boundary conditions. Calvisi et al. [28] used a van der Waals equation of state and derived a time evolution equation for the pressure inside the bubble taking into account heat and mass transfer across the interface and the chemistry of the bubble contents. Here, however, a more elementary description is employed following many previous studies (see, for example, Best and Kucera [11]) wherein the bubble contents are some mixture of liquid vapour and a non-condensible gas. It is assumed that the vapour evaporates as the bubble expands and condensation occurs at the bubble surface while the bubble shrinks thus keeping the vapour pressure p_v roughly constant in time. This is only valid when the speed of the bubble wall is small compared to the speed of sound [64] and although high velocities are obtained during collapse up to approximately 200m/s, the error is assumed to be negligible as this occurs over very small time scales (typically a few microseconds). Furthermore, as in [64], the vapour and gas are assumed to be sufficiently diluted such that Dalton's Law applies and they do not influence each other. Under these assumptions and for a bubble with partial

pressure p_{g0} at some reference size R_0 and temperature T_B the internal bubble pressure can be written as [23]

$$p_i(t) = p_v(T_B) + p_{g0}\left(\frac{T_B}{T_\infty}\right)\left(\frac{R_0}{R(t)}\right)^{3\kappa}, \tag{2.1}$$

where $p_v(T_b)$ is the vapour pressure and κ is the ratio of the specific heats for the gas which is assumed to be constant. It is assumed that the gas is ideal and that there is negligible heat exchange between the bubble and the fluid; consequently the compression and expansion of the gas are modelled as adiabatic. Eq. (2.1) simplifies further, in fact, since the temperature of the bubble is assumed constant: $T_B = T_\infty$. The expression that will hereby be used for the bubble pressure is then

$$p_i(t) = p_v + p_{g0}\left(\frac{R_0}{R(t)}\right)^{3\kappa}. \tag{2.2}$$

For air (which is predominantly a diatomic gas) the ratio of specific heats is $\kappa = 1.4$. This value will be used for all subsequent computations unless otherwise stated. The value of the vapour pressure p_v is often small and will be neglected in this study. Finally, since the bubble contents are homogeneous their effects can be applied approximately through a boundary condition at the bubble surface rather than described throughout the bubble.

In addition, the effects of gravity are neglected since small cavitation bubbles are being considered and since high velocities occur during collapse. It is noted, however, that the effects of gravity can easily be included as an extra term in the momentum equation (2.4). Under all these assumptions the equation of motion for a spherically symmetric bubble in an infinite, incompressible fluid is now derived.

2.3 Derivation of the Rayleigh-Plesset Equation

The consideration of three kinds of quantity are required when discussing the mechanics of a fluid: stresses, strains and displacements. These quantities are connected by three types of equations:

- Equations of motion,
- Kinematic relations,

- Constitutive equations.

The equations of motion relate the stresses, kinematic relations express strains in terms of displacements and the constitutive equations relate the relationship between stresses and strains and describe the influence of the specific material begin considered.

The equations of motion for any fluid motion are conservation of mass, momentum and energy; expressed in the form

$$\frac{\mathrm{D}\rho}{\mathrm{D}t} + \rho(\nabla \cdot \mathbf{u}) = 0, \tag{2.3}$$

$$\rho\frac{\mathrm{D}\mathbf{u}}{\mathrm{D}t} = [\nabla \cdot \boldsymbol{\pi}], \tag{2.4}$$

$$\rho\frac{\mathrm{D}\hat{U}}{\mathrm{D}t} = -(\nabla \cdot \mathbf{q}) - (\boldsymbol{\pi} : \nabla\mathbf{u}), \tag{2.5}$$

where ρ is the fluid density, $\mathbf{u}$ is the velocity field, $\boldsymbol{\pi}$ is the Cauchy stress tensor, $\mathbf{q}$ is the heat flux, $\hat{U}$ is the internal energy per unit mass and gravity has been neglected. We restrict ourselves to isothermal conditions and thus neglect the conservation of energy equation. The stress $\boldsymbol{\pi}$ is due to the molecular motions and interactions within the fluid and is often decomposed into an isotropic part related to the pressure and a remaining anisotropic part; the components being

$$\pi_{ij} = -p\delta_{ij} + \tau_{ij}, \tag{2.6}$$

where $p = -\frac{1}{3}\pi_{ii}$ is the (static) fluid pressure and $\boldsymbol{\tau}$ is the deviatoric or extra stress tensor due entirely to the motion of the fluid. Substituting this expression for $\boldsymbol{\pi}$ into the conservation of momentum Eq. (2.4) results in what is usually known as the Navier-Stokes equation of motion

$$\rho\frac{\mathrm{D}\mathbf{u}}{\mathrm{D}t} = -\nabla p + \nabla \cdot \boldsymbol{\tau}. \tag{2.7}$$

Since a spherical bubble is being considered it is now useful to express Eq. (2.7) in terms of spherical polar coordinates. Due to the assumed spherical symmetry of the bubble, the only non-trivial equation is in the radial direction

$$\frac{\partial u}{\partial t} + u\frac{\partial u_r}{\partial r} = -\frac{1}{\rho}\left[\frac{\partial p}{\partial r} + \frac{\partial \tau_{rr}}{\partial r} + 2\frac{\tau_{rr} - \tau_{\theta\theta}}{r}\right], \tag{2.8}$$

where u is the radial component of $\mathbf{u}$ and use has been made of the fact that $\tau_{\theta\theta} = \tau_{\phi\phi}$ for a spherical bubble. Now, due to the assumed incompressibility of the fluid, conservation

of mass implies

$$\frac{\mathrm{D}\rho}{\mathrm{D}t} + \rho(\nabla \cdot \mathbf{u}) = 0 \;\Rightarrow \nabla \cdot \mathbf{u} = 0. \tag{2.9}$$

Expressing this in spherical coordinates then leads to the following relation

$$\frac{\partial u}{\partial r} = -2\frac{u}{r}, \tag{2.10}$$

with the solution

$$u(r,t) = \frac{F(t)}{r^2}, \tag{2.11}$$

for some function $F(t)$. Using the assumption of zero mass transfer over the bubble interface, the velocity of the fluid on the bubble wall should be equal to that of the boundary: $u(R,t) = \dot{R}$. Using this, the velocity u is found to be

$$u(r,t) = \frac{R^2(t)\dot{R}(t)}{r^2}. \tag{2.12}$$

Substituting this into Eq. (2.8) and integrating with respect to r from the bubble wall to infinity results in

$$\frac{2R\dot{R}^2 + R^2\ddot{R}}{R} - \frac{R^4\dot{R}^2}{2R^4} = \frac{1}{\rho}(p_B - p_\infty) + \frac{1}{\rho}\left[\tau_{rr}|_R - 2\int_R^\infty \frac{\tau_{rr} - \tau_{\theta\theta}}{r}dr\right], \tag{2.13}$$

where p_B is the pressure on the fluid side of the bubble wall and it has been assumed that $p \to p_\infty$, $\tau_{rr} \to 0$ and $\tau_{\theta\theta} \to 0$ as $r \to \infty$. Balancing the normal stresses over the bubble surface (in the absence of heat/mass transfer) gives an expression for the pressure p_B at the fluid side of the interface

$$p_B = p_i - \frac{2\sigma}{R} - \tau_{rr}|_R, \tag{2.14}$$

where σ is the (static) surface tension of the bubble wall and p_i is the pressure on the inside of the bubble interface given by Eq. (2.2). Note that Eq. (2.14) also assumes the bubble interface is 'clean', i.e. no contaminating particles are present. Finally, substituting this pressure into Eq. (2.13) gives the general Rayleigh-Plesset equation

$$R\ddot{R} + \frac{3}{2}\dot{R}^2 = \frac{1}{\rho}\left[p_i - \frac{2\sigma}{R} - p_\infty - 2\int_R^\infty \left(\frac{\tau_{rr} - \tau_{\theta\theta}}{r}\right)dr\right]. \tag{2.15}$$

This was first derived by Rayleigh [88] for an empty cavity. Note, though, that an empty cavity will collapse to nothing leading unbounded pressures occuring. This is

obviously impossible; in reality the bubble contents will become compressed and will cause rebound to the high pressures generated as the bubble shrinks.

Eq. (2.15) is a nonlinear ordinary differential equation for the bubble radius R which, when coupled to constitutive equations for the stresses, can be solved using standard numerical techniques. Fig. 2.1 shows the (non-dimensionalised) solution of the Rayleigh-Plesset equation for a bubble filled with an adiabatic gas in an inviscid, incompressible fluid.

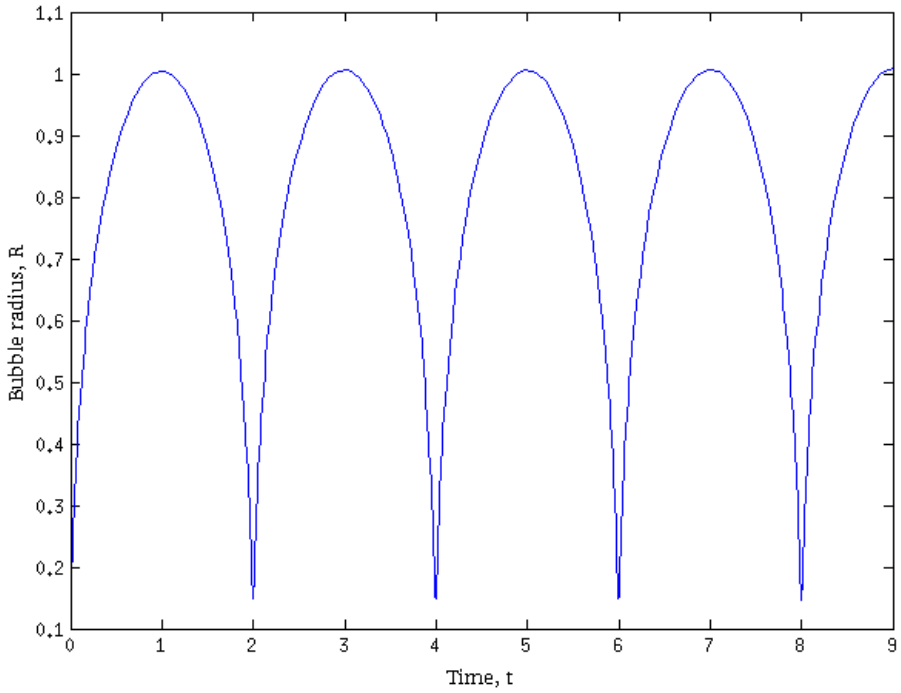

Figure 2.1: Example solution of the Rayleigh-Plesset equation for a gas filled bubble in an inviscid fluid.

The bubble is assumed to be at some radius R_0^* and have a zero initial velocity. This initial radius is chosen so that the maximum non-dimensionalised radius is one for the inviscid case. The bubble initially expands due to a high pressure inside the bubble, 'pushing' the fluid outwards. This expansion rate then declines until the bubble reaches its maximum volume. At this point the pressure outside the fluid is higher than that inside and the bubble begins to collapse. At $t \approx 2$ it reaches its minimum radius which is equal to the initial radius R_0^*. Since there are no mechanisms for energy loss, the conditions at each minimum are identical to the initial conditions and the bubble undergoes periodic oscillations.

2.4 Purely Viscous Fluids

A brief discussion of purely viscous fluids is now presented as a prelude to a more thorough examination of viscoelastic fluids (which is the focus of this work). The simplest, and perhaps most commonly used, purely viscous model is the Newtonian fluid.

2.4.1 Newtonian Fluids

Fluids with a linear relation between the extra stress tensor $\boldsymbol{\tau}$ and the rate of strain tensor $\mathbf{D}$ are known as *Newtonian* fluids. For such fluids the Cauchy stress tensor $\boldsymbol{\pi}$ has the following form

$$\boldsymbol{\pi} = -p\mathbf{I} + \boldsymbol{\tau} = -p\mathbf{I} + 2\eta\mathbf{D}, \tag{2.16}$$

where η is the viscosity and $\mathbf{D}$ is the rate of strain of tensor, written in terms of velocity gradients as

$$\mathbf{D} = \frac{1}{2}\Big(\nabla\mathbf{u} + (\nabla\mathbf{u})^T\Big). \tag{2.17}$$

For an incompressible, Newtonian fluid the extra stress tensor $\boldsymbol{\tau}$ is traceless [27] and we have

$$\tau_{rr} + \tau_{\theta\theta} + \tau_{\phi\phi} = \tau_{rr} + 2\tau_{\theta\theta} = 0 \;\Rightarrow\; \tau_{rr} - \tau_{\theta\theta} = \frac{3}{2}\tau_{rr}, \tag{2.18}$$

since the bubble is spherically symmetric and $\tau_{\theta\theta} = \tau_{\phi\phi}$. The Rayleigh-Plesset equation (2.15) then becomes

$$R\ddot{R} + \frac{3}{2}\dot{R}^2 = \frac{1}{\rho}\left[p_i - \frac{2\sigma}{R} - p_\infty - 3\int_R^\infty \frac{\tau_{rr}}{r}dr\right]. \tag{2.19}$$

For an incompressible fluid the velocity is given by $u = R^2\dot{R}/r^2$ (irrespective of the fluid rheology) and the radial stress component for a Newtonian fluid is

$$\tau_{rr} = 2\eta\frac{\partial u}{\partial r} = -4\eta\frac{R^2\dot{R}}{r^3}. \tag{2.20}$$

Substituting this into Eq. (2.19) gives the Rayleigh-Plesset equation for a Newtonian fluid

$$R\ddot{R} + \frac{3}{2}\dot{R}^2 = \frac{1}{\rho}\left[p_i - \frac{2\sigma}{R} - p_\infty - 4\eta\frac{\dot{R}}{R}\right] \tag{2.21}$$

Describing the stress tensor by Newton's law of viscosity (2.16) has been a useful approximation (for a large range of strain rates) for many fluids which are roughly incompressible and structurally simple. There are, however, many fluids that cannot be accurately described using (2.16) such as blood (due to the red blood cells) and polymeric liquids [12]. In order to describe these non-Newtonian fluids a range of constitutive equations have been proposed to describe the stress $\boldsymbol{\pi}$; these range from purely viscous *generalized Newtonian* fluids to complex, nonlinear viscoelastic expressions.

2.4.2 Non-Newtonian Purely Viscous Fluids

Assuming that the stress tensor $\boldsymbol{\pi}$ is a function of the fluid density ρ as well as the velocity gradient the most general form for the stress tensor that satisfies invariance in this case is [89]

$$\boldsymbol{\pi} = \alpha\mathbf{I} + \phi_1\mathbf{D} + \phi_2\mathbf{D}^2, \tag{2.22}$$

where α is a Lagrangian multiplier and ϕ_1,ϕ_2 depend on ρ as well as the three principal invariants of the rate of strain tensor $\mathbf{D}$.

Fluids satisfying (2.22) are sometimes known as *Reiner-Rivlin* fluids. Due to thermodynamic considerations and the behaviour of real fluids [89], however, attention is usually restricted to a subset of these known as *generalized Newtonian* fluids for which the stress tensor satisfies

$$\boldsymbol{\pi} = -p\mathbf{I} + \boldsymbol{\tau} = -p\mathbf{I} + 2\eta(S)\mathbf{D}, \tag{2.23}$$

where $S = -4\mathrm{II}_{\mathbf{D}}$ and p is the mechanical pressure. Note that this is just Eq. (2.22) with ϕ_2 assumed to be zero and ϕ_1 only dependent on the second invariant of $\mathbf{D}$. This can also be viewed as a generalisation of Eq. (2.16) with the viscosity η replaced by a non-constant, effective viscosity $\eta(S)$. A vast range of models exist for specific forms of the viscosity $\eta(S)$; a few of which are now presented.

Generalized Newtonian Fluids

One of the simplest generalized Newtonian fluids is the Power Law (or Oswald-de-Waele) model for which the effective viscosity is described, in a spherically symmetric setting, by

$$\eta(S) = KS^{(n-1)/2} = K\dot{\gamma}^{n-1}, \tag{2.24}$$

where u is the component of the velocity in the radial direction and $\dot{\gamma} = \frac{\partial u}{\partial r}$ is the shear rate. For $n < 1$ and $n > 1$ it describes a shear-thinning and shear-thickening fluid, respectively, with $n = 1$ pertaining to the case of a Newtonian fluid. For a shear-thinning (thickening) fluid the fluid viscosity decreases (increases) with increasing shear rate. The Power Law is limited, though, since the effective viscosity decreases indefinitely with increasing shear rate as well as being non-zero at a zero shear rate. Other more complex models exist which solve some or all of these problems such as the Carreau model and Cross model for which the effective viscosities are given by (2.25) and (2.26), respectively

$$\eta(S) = \eta_\infty + \frac{\eta_0 - \eta_\infty}{[1 + \lambda_c^2 \dot{\gamma}^2]^{(1-n)/2}}, \tag{2.25}$$

$$\eta(S) = \frac{\eta_0}{1 + (\lambda_c \dot{\gamma})^{1-n}}, \tag{2.26}$$

where λ_c is a time constant, n, N are dimensionless exponents. The Cross model behaves as a Newtonian fluid at low shear rates and a Power-Law fluid at high shear rates. The Bingham plastic model is used to describe fluids that display a yield stress below which they do not flow at all, common examples of which are toothpaste or mayonnaise. In terms of the extra stress $\boldsymbol{\tau}$

$$|\frac{1}{2}(\boldsymbol{\tau} : \boldsymbol{\tau})| < \tau_0 \Rightarrow \mathbf{D} = 0, \tag{2.27}$$

$$|\frac{1}{2}(\boldsymbol{\tau} : \boldsymbol{\tau})| \geq \tau_0 \Rightarrow \boldsymbol{\tau} = 2\left(\eta + \frac{\tau_0}{(\mathbf{D} : \mathbf{D})}\right)\mathbf{D}. \tag{2.28}$$

The oscillations of a bubble in a Power Law fluid have been studied numerically by Street et al. [95] as well as Yang and Yeh [114] who found that collapse velocities increased with decreasing n. Bubble dynamics have also been investigated for many other purely viscous models; an extensive list of which can be found in [27]. Typically though, attention has been restricted to Newtonian fluids when considering a cavity in a purely viscous fluid.

2.5 Viscoelastic Fluids

For certain fluids (such as polymers and many biological materials) the stress is dependent on the strain rate as well as strain. Such fluids are known as viscoelastic and can

exhibit a range of interesting behaviour in response to deformation.

2.5.1 Previous Studies of Bubbles In Viscoelastic Fluids

One of the first studies to focus on the effects of viscoelasticity on bubble growth was a theoretical analysis by Street [94]. A spherically symmetric bubble inside a large sphere of fluid was considered with an Oldroyd 3-constant model chosen to describe the fluid and the gas inside the bubble assumed to be constant. Due to the intractability of finding an exact solution to the governing equations a simple solution of the form $\alpha = \dot{R}(t)/R(t)$ was sought for some constant α. The main conclusion of the study was a high initial growth rate for a bubble in a viscoelastic fluid relative to a Newtonian fluid of the same shear viscosity.

Following this, a revolutionary paper by Fogler and Goddard [42] numerically modelled a spherical bubble in a Linear Maxwell model. The Linear Maxwell model and the Rayleigh-Plesset equation were combined to form an integro-differential equation for the bubble radius. Their results indicated that the elasticity of the fluid can cause either collapse or oscillations about some radius depending on the ratio of p_∞ to the elastic modulus of the fluid. However, since the bubble was modelled as an empty void the physical relevance of the results is questionable and problems with errors in the numerical integration were encountered after a few bubble oscillations. This work was also extended to a vapour-filled bubble with a constant vapour pressure and forced by an acoustic wave [43]. Similar studies by Tanasawa and Yang [98] and Ting [99] used an Oldroyd 3-constant model for a gas and vapour filled bubble, respectively, although numerical difficulties similar to those in [43] were encountered.

More recently, Allen and Roy in two papers [1,2] examined the oscillations of an acoustically forced, spherical bubble in a Linear Maxwell and Upper Convective Maxwell (UCM) model, respectively. The Linear Maxwell case can be expressed as a set of ordinary differential equations; details of which are given in the following section. Due to the extra terms present in the upper convective derivative, however, this is not as straightforward for the UCM case and leads to an integro-differential equation for the bubble radius. This led Allen and Roy to solve the stresses over a grid of nodes in order to calculate the integral term in Eq. (2.15). Due to this complication the authors encountered numerical difficulties when integrating the equations in time necessitating the use of temporal transformation methods as well as a high order time stepping method.

Another difficulty encountered was the choice of the grid of nodes which must be both sufficiently fine near the bubble interface (where the stresses have a high gradient) and extend far enough to approximate the zero-stress boundary condition at infinity. These difficulties were overcome to produce a numerical method that was more stable than those used in previous works. However, this was achieved at the expense of significantly increased computational time and storage.

In this chapter an alternative, more efficient method is derived based on the methods of Shulman and Levitskii [92] who considered a form of the 4-constant Oldroyd model with an interpolated time derivative. For certain parameter values, one of which corresponds to the Oldroyd-B model, they demonstrated that the system of equations to be solved can be reduced to a system of ordinary differential equations which can be solved using standard numerical methods. This method has been used by Gubaidullin et al. [48] to investigate shock waves in non-Newtonian bubbly liquids as well as by Jiménez-Fernández and Crespo [55] for cases pertaining to ultrasonic biomedical applications.

2.5.2 Linear Viscoelastic models

The General Linear Viscoelastic Model

The theory of linear viscoelasticity is based on the Boltzmann Superposition Principle that the effects of sequential changes in strain are additive and that instantaneous stresses at a point in time depend on the deformation history (principle of fading memory). For a general linear viscoelastic model, Pipkin [84] considered the stress response to a step history for an arbitrary number of steps. Passing to the limit of arbitrarily small time steps the following forms can be formally derived

$$\boldsymbol{\tau} = \int_{-\infty}^{t} G(t-t')\mathbf{D}(t')dt', \tag{2.29}$$

$$\boldsymbol{\tau} = \int_{-\infty}^{t} M(t-t')\boldsymbol{\gamma}(t,t')dt', \tag{2.30}$$

where $G(t-t')$ is the relaxation modulus, $M(t-t')$ is the memory function, $\mathbf{D} = \dot{\boldsymbol{\gamma}}$ is the rate of strain tensor and the following relations hold

$$M(t-t') = \frac{\partial G(t-t')}{\partial t'}, \quad \gamma(t,t') = \int_{t}^{t'} \dot{\gamma}(t'')dt''. \tag{2.31}$$

Note that Eqs. (2.29) and (2.30) are only equivalent if the rate of strain tensor $\mathbf{D} = \dot{\boldsymbol{\gamma}}$ is finite at time $t = -\infty$ [13].

A number of linear viscoelastic models exist that imitate forms of the time dependence of G using combinations of linear springs and dashpots. The spring is an ideal element modelled by Hooke's Law (purely elastic) while the dashpot is an ideal viscous element representing a Newtonian fluid. Each spring is assigned a stiffness and each dashpot assigned a frictional resistance (analagous to a contribution to the viscosity). These elements can be combined in series or in parallel to produce more complex models, some common examples of which are

- Linear Maxwell: A spring and dashpot connected in series,
- Kelvin-Voigt: A spring and dashpot connected in parallel,
- Standard Linear Solid: A spring and Linear Maxwell model connected in parallel.

In theory this process of combining springs and dashpots can be increased indefinitely, for example taking the Linear Maxwell model and letting the number of elements tend to infinity results in the General Maxwell model with a continuous spectrum of relaxation times (see Eq. (2.34). By taking a sufficient number of elements, any relaxation modulus form can be represented by the sum over the contributions from each element. Since a particular fluid is not being considered here, however, it is acceptable to choose a constitutive equation with a single relaxation time to analyse the effects of fluid rheology on bubble dynamics.

The Jeffreys Model

Another commonly used linear viscoelastic model is the Jeffreys model, first proposed by Sir Harold Jeffreys ([54] p.265). The model is a combination of a dashpot and a Kelvin-Voigt unit in series [93] as shown in Fig. 2.2. It can be expressed as the following partial differential equation

$$\boldsymbol{\tau} + \frac{\mu_1 + \mu_2}{G}\frac{\partial \boldsymbol{\tau}}{\partial t} = \mu_1\left(\mathbf{D} + \frac{\mu_2}{G}\frac{\partial \mathbf{D}}{\partial t}\right), \tag{2.32}$$

where G is the shear modulus and μ_1, μ_2 are the first and second coefficients of viscosity, respectively. More commonly this is written as

$$\boldsymbol{\tau} + \lambda_1 \frac{\partial \boldsymbol{\tau}}{\partial t} = \eta_0 \left(\mathbf{D} + \lambda_2 \frac{\partial \mathbf{D}}{\partial t} \right), \tag{2.33}$$

where η_0 is the total viscosity and λ_1, λ_2 are the relaxation and retardation times, respectively with

$$\lambda_1 = \frac{\mu_1 + \mu_2}{G}, \quad \lambda_2 = \frac{\mu_2}{G}, \quad \eta_0 = \mu_1. \tag{2.34}$$

The relaxation time λ_1 is a measure of the time required for the stress to relax to some limiting value whereas λ_2 is a measure of the time required for the spring to return to its equilibrium length while retarded by the dashpot.

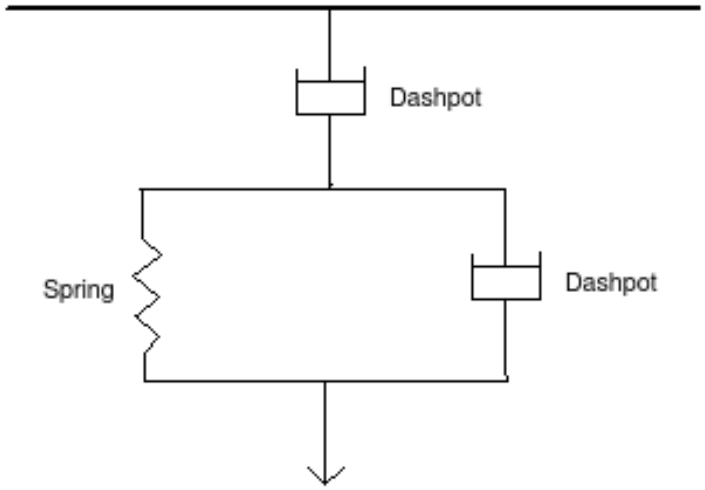

Figure 2.2: A diagrammatic representation of the Jeffreys model.

The model can also be recast in the integral forms of Eqs. (2.29) and (2.30) with a relaxation modulus and memory function [13] given by

$$G(s) = \frac{\eta_0}{\lambda_1} \left(1 - \frac{\lambda_2}{\lambda_1} \right) e^{-\frac{s}{\lambda_1}} + 2 \frac{\eta_0 \lambda_2}{\lambda_1} \delta(s), \tag{2.35}$$

$$M(s) = \frac{\eta_0}{\lambda_1^2} \left(1 - \frac{\lambda_2}{\lambda_1} \right) e^{-\frac{s}{\lambda_1}} - 2 \frac{\eta_0 \lambda_2}{\lambda_1} \dot{\delta}(s), \tag{2.36}$$

where δ is the Dirac delta function and $s = t - t'$.

If the retardation time λ_2 is set to zero the Jeffreys model reduces to the linear Maxwell

model; the simplest model that describes both viscosity and elasticity

$$\boldsymbol{\tau} + \lambda_1 \frac{\partial}{\partial t}\boldsymbol{\tau} = \eta_0 \mathbf{D}. \tag{2.37}$$

If the relaxation time λ_1 is also set to zero (or for steady-state motions) this simplifies to the stress for a Newtonian fluid: see Eq. (2.16).

To find the motion of a spherically symmetric bubble in a Jeffreys fluid the Jeffreys model must be coupled to the Rayleigh Plesset Eq. (2.15). To do this the method of Allen and Roy [1] is used in which the problem is cast as a system of nonlinear, ordinary differential equations. Similar to a Newtonian fluid, the stress tensor is traceless for an incompressible, linear viscoelastic fluid [25] so that only the radial stress τ_{rr} is required and the Rayleigh-Plesset Eq. (2.15) becomes

$$R\ddot{R} + \frac{3}{2}\dot{R}^2 = \frac{1}{\rho}\left[p_i - \frac{2\sigma}{R} - p_\infty - 3\int_R^\infty \frac{\tau_{rr}}{r}dr\right]. \tag{2.38}$$

The Jeffreys model for the radial stress is expressed in the form

$$\tau_{rr} + \lambda_1 \frac{\partial \tau_{rr}}{\partial t} = -2\eta_0\left(\frac{\partial u}{\partial r} + \lambda_2 \frac{\partial}{\partial t}\frac{\partial u}{\partial r}\right). \tag{2.39}$$

Since the velocity is $u = \dot{R}R^2/r^2$ this becomes

$$\tau_{rr} + \lambda_1 \frac{\partial \tau_{rr}}{\partial t} = 4\frac{\eta_0}{r^3}\left[\dot{R}R^2 + \lambda_2(2R\dot{R}^2 + R^2\ddot{R})\right]. \tag{2.40}$$

Dividing Eq. (2.40) by r and integrating from R to ∞ gives

$$\int_R^\infty \frac{\tau_{rr}(r,t)}{r}dr + \lambda\int_R^\infty \frac{\partial}{\partial t}\left(\frac{\tau_{rr}(r,t)}{r}\right)dr = 4\eta_0\left[\int_R^\infty \frac{R^2\dot{R}}{r^4}dr + \lambda_2\int_R^\infty \frac{2R\dot{R}^2 + R^2\ddot{R}}{r^4}dr\right]. \tag{2.41}$$

Using the Leibnitz integral rule to simplify the second term and evaluating the integrals on the right-hand side of Eq. (2.41) results in

$$S + \lambda\left(\frac{dS}{dt} + \frac{\dot{R}}{R}\tau_{rr}(R)\right) = \frac{4\eta_0}{3}\left[\frac{\dot{R}}{R} + \lambda_2\left(\frac{2\dot{R}^2 + R\ddot{R}}{R^2}\right)\right], \tag{2.42}$$

where S is the integral term required in the Rayleigh-Plesset equation

$$S(R,t) = \int_R^\infty \frac{\tau_{rr}(r,t)}{r} dr. \tag{2.43}$$

To find the stress at the bubble surface, $\tau_{rr}(R)$, Eq. (2.39) is evaluated at $r = R(t)$ giving

$$\tau_{rr}(R) + \lambda \frac{\partial}{\partial t}\tau_{rr}(R) = 4\eta_0 \left[\frac{\dot{R}}{R} + \lambda_2 \left(\frac{2\dot{R}^2 + R\ddot{R}}{R^2} \right) \right]. \tag{2.44}$$

Eqs. (2.38,2.42,2.44) complete the system of ordinary differential equations which will be solved for the bubble radius and stresses by integrating them simultaneously in time. Results for a bubble situated in a linear Jeffreys fluid are shown later in this chapter.

The linear relations described in this section are strictly only valid for fluid motions involving infinitely small displacement gradients. Also, they cannot describe shear-rate dependence of viscosity, normal-stress phenomena (nonlinear) or small-strain phenomena if there are large displacement gradients due to superposed rigid rotations [13]. In order to obtain a description of fluids undergoing larger deformations, nonlinear models must be considered.

2.5.3 Nonlinear Differential Constitutive Equations

The linear differential models in the previous section can be used to generate 'quasilinear corotational models' by replacing the partial time derivatives with a more complex derivative. While this allows the introduction of nonlinearities in order to describe flows with large strains and large rates-of-strain, this must be done in such a way that the constitutive relation remains objective (no dependence on local rate of rotation).

General Forms

The majority of rheological models can be expressed as the following set of differential equations [65]

$$\begin{aligned}\boldsymbol{\tau} &= \sum_{\alpha,\beta} \boldsymbol{\tau}^{(\alpha\beta)},\\ \frac{\mathrm{D}\boldsymbol{\tau}^{(\alpha\beta)}}{\mathrm{D}t} + K_\alpha \boldsymbol{\tau}^{(\alpha\beta)} + \mathbf{B}_\beta^T \cdot \boldsymbol{\tau}^{(\alpha\beta)} + \boldsymbol{\tau}^{(\alpha\beta)} \cdot \mathbf{B}_\beta &= p_\alpha(\mathbf{B}_\beta^T + \mathbf{B}_\beta),\\ \frac{dp_\alpha}{dt} + K_\alpha p_\alpha &= -\phi_\alpha,\end{aligned} \tag{2.45}$$

where the scalar parameters K_α, ϕ_α and the tensor $\mathbf{B}_\beta$ are expressed in terms of the tensors $\mathbf{D}$ and $\boldsymbol{\tau}^{(\alpha\beta)}$. The form of the expressions for these parameters depend on the particular model chosen. One such example is the generalized Maxwell model which includes the most general time derivative of the stress tensor

$$\begin{aligned}\boldsymbol{\tau} &= \sum_{\alpha} \boldsymbol{\tau}^{(\alpha)},\\ \boldsymbol{\tau}^{(\alpha)} + \lambda_\alpha \mathbf{F}_{abc} \boldsymbol{\tau}^{(\alpha)} &= 2\eta_\alpha \mathbf{D},\\ \mathbf{F}_{abc}\boldsymbol{\tau} = \frac{\mathrm{D}\boldsymbol{\tau}}{\mathrm{D}t} + a(\boldsymbol{\tau}\cdot\mathbf{D} + &\mathbf{D}\cdot\boldsymbol{\tau}) + b\mathbf{I}tr(\boldsymbol{\tau}\cdot\mathbf{D}) + c\mathbf{D}tr(\boldsymbol{\tau}).\end{aligned} \tag{2.46}$$

Convected Jeffreys Model

Taking the Jeffreys model (2.33) and replacing the partial time derivative with a convected time derivative produces the convected Jeffreys model or Oldroyd-B model, first proposed by Oldroyd [80]

$$\boldsymbol{\tau} + \lambda_1 \overset{\nabla}{\boldsymbol{\tau}} = \eta\left(\mathbf{D} + \lambda_2 \overset{\nabla}{\mathbf{D}}\right), \tag{2.47}$$

where $\overset{\nabla}{\boldsymbol{\tau}}$ is the convected time derivative; defined by

$$\overset{\nabla}{\boldsymbol{\tau}} = \frac{\mathrm{D}\boldsymbol{\tau}}{\mathrm{D}t} - \left((\nabla\mathbf{u})^T \cdot \boldsymbol{\tau} + \boldsymbol{\tau}\cdot(\nabla\mathbf{u})\right) \tag{2.48}$$

In a similar manner to the linear model, if $\lambda_2 = 0$ then the Oldroyd-B model reduces to the Upper Convected Maxwell (UCM) model (Eq. (2.51)). The stress is often split into a (purely viscous) solvent part and a polymeric part which describes the viscoelastic

properties. In this case the Oldroyd-B can be reformulated as

$$\boldsymbol{\tau} = \boldsymbol{\tau}^s + \boldsymbol{\tau}^p, \tag{2.49}$$

$$\boldsymbol{\tau}^s = \eta_s \dot{\boldsymbol{\gamma}}, \tag{2.50}$$

$$\boldsymbol{\tau}^p + \lambda_1 \overset{\nabla}{\boldsymbol{\tau}}_p = \eta_p \dot{\boldsymbol{\gamma}}, \tag{2.51}$$

where η_s and η_p are the solvent and polymeric viscosities, respectively, and can be written in terms of the relaxation and retardation times as

$$\eta_s = \frac{\lambda_2}{\lambda_1}\eta, \quad \eta_p = \left(1 - \frac{\lambda_2}{\lambda_1}\right)\eta. \tag{2.52}$$

Substituting the above expressions for the solvent and polymeric stress into the Rayleigh-Plesset equation results in

$$R\ddot{R} + \frac{3}{2}\dot{R}^2 = \frac{1}{\rho}\left[p_i - \frac{2\sigma}{R} - p_\infty + 4\eta_s\frac{\dot{R}}{R} - S_p(t)\right], \tag{2.53}$$

where the term $-4\eta_s\dot{R}/R$ arises from the integral of the solvent stress and

$$S_p(t) = 2\int_R^\infty \frac{\tau^p_{rr}(r,t) - \tau^p_{\theta\theta}(r,t)}{r}dr, \tag{2.54}$$

is the corresponding integral for the polymeric stress. Equations for the relevant components of the polymeric stress can be written from Eq. (2.47) as

$$\tau^p_{rr} + \lambda_1\left(\frac{\partial\tau^p_{rr}}{\partial t} + \frac{R^2\dot{R}}{r^2}\frac{\partial\tau^p_{rr}}{\partial r} + \frac{4R^2\dot{R}}{r^3}\tau^p_{rr}\right) = 4\eta_0\frac{R^2\dot{R}}{r^3}, \tag{2.55}$$

$$\tau^p_{\theta\theta} + \lambda_1\left(\frac{\partial\tau^p_{\theta\theta}}{\partial t} + \frac{R^2\dot{R}}{r^2}\frac{\partial\tau^p_{\theta\theta}}{\partial r} - \frac{2R^2\dot{R}}{r^3}\tau^p_{\theta\theta}\right) = -2\eta_0\frac{R^2\dot{R}}{r^3}, \tag{2.56}$$

By solving these equations and substituting the solutions for τ^p_{rr} and $\tau^p_{\theta\theta}$ into Eq. (2.54) we obtain the following expression for $S_p(t)$ (details of which are found in Appendix A)

$$S_p(t) = \frac{2\eta_p}{\lambda_1 R^4(t)}\int_0^t \mathrm{e}^{\frac{\xi-t}{\lambda_1}}\left(R^3(\xi) + R^3(t)\right)\dot{R}(\xi)d\xi. \tag{2.57}$$

This integral can be determined from a system of first-order differential equations [92]

since the integrand can be represented in the form $\sum_{k=1}^{K} \varphi_k(t)\psi_k(\xi)$ with $K = 2$ and

$$\varphi_1(t) = \mathrm{e}^{-t/\lambda_1}, \quad \psi_1(\xi) = \mathrm{e}^{\,\xi/\lambda_1} R^3(\xi)\dot{R}(\xi), \tag{2.58}$$

$$\varphi_2(t) = R^3(t)\mathrm{e}^{-t/\lambda_1}, \quad \psi_2(\xi) = \mathrm{e}^{\,\xi/\lambda_1} \dot{R}(\xi). \tag{2.59}$$

Using this separability the integral is split as follows

$$S_p(t) = S^{(1)}(t) + S^{(2)}(t), \tag{2.60}$$

$$= A(t) \int_0^t \psi_1(\xi)\varphi_1(t)d\xi + A(t) \int_0^t \psi_2(\xi)\varphi_2(t)d\xi, \tag{2.61}$$

with $A(t) = 2\eta_p/(\lambda_1 R^4)$. Differentiating $S^{(1)}$ results in

$$\begin{aligned} \dot{S}^{(1)} &= \dot{A}(t) \int_0^t \psi_1(\xi)\varphi_1(t)d\xi + A(t)\left[\int_0^t \psi_1(\xi) \frac{\mathrm{d}\varphi_1(t)}{\mathrm{d}t} d\xi + \psi_1(t)\varphi_1(t) \right] \\ &= \left(-\frac{1}{\lambda_1} - 4\frac{\dot{R}}{R} \right) S^{(1)} + 2\frac{\eta_p}{\lambda_1}\frac{\dot{R}}{R}, \end{aligned} \tag{2.62}$$

Similarly, $S^{(2)}$ satisfies the following differential equation

$$\dot{S}^{(2)} + \left(\frac{1}{\lambda_1} + \frac{\dot{R}}{R} \right) S^{(2)} = 2\frac{\eta_p}{\lambda_1}\frac{\dot{R}}{R} \tag{2.63}$$

Eqs. (2.63), (2.62) and (2.53) form the system which can be integrated in time to give the motion of a spherically symmetric bubble in an infinite, incompressible Oldroyd-B fluid. The manipulation of the governing equations for the stresses τ_{rr}^p and $\tau_{\theta\theta}^p$ has allowed the integral term $S_p(t)$ to be determined from two ordinary differential equations. This has a massive computational advantage over the method of Allen and Roy [2] in which the constitutive Eqs. (2.55,2.56) are solved over a grid of nodes (approximately 4000-5000 for their calculations).

The Oldroyd-B model can be written in integral form as

$$\boldsymbol{\tau}(t) = \int_{-\infty}^{t} M(t - t') \Big(\mathbf{B}(t, t') - \mathbf{I} \Big) dt', \tag{2.64}$$

where $\mathbf{B}$ is the *Finger strain tensor* [13] and with the memory function

$$M(s) = \frac{\eta_0}{\lambda_1^2} \left[\left(1 - \frac{\lambda_2}{\lambda_1} \right) e^{-(s)/\lambda_1} + 2\lambda_1\lambda_2\dot{\delta}(s) \right]. \tag{2.65}$$

Other Nonlinear Models

The Oldroyd-B model (2.47) contains quadratic terms in the velocity gradient although, as noted by Oldroyd [81], not in any systematic manner. Thus the Oldroyd 8-constant model was suggested which contains all possible quadratic terms involving products of $\boldsymbol{\tau}$ with $\mathbf{D}$ and of $\mathbf{D}$ with itself

$$\begin{aligned}\boldsymbol{\tau}+\lambda_1\overset{\nabla}{\boldsymbol{\tau}}+\frac{1}{2}\lambda_3[\mathbf{D}\cdot\boldsymbol{\tau}+\boldsymbol{\tau}\cdot\mathbf{D}]+\frac{1}{2}\lambda_5(\mathrm{tr}\boldsymbol{\tau})\mathbf{D}+\frac{1}{2}\lambda_6(\boldsymbol{\tau}:\mathbf{D})\mathbf{I}\\ =-\eta_0\left[\mathbf{D}+\lambda_2\frac{\mathrm{d}\mathbf{D}}{\mathrm{d}t}+\lambda_4(\mathbf{D}\cdot\mathbf{D})+\frac{1}{2}\lambda_7(\mathbf{D}:\mathbf{D})\mathbf{I}\right].\end{aligned} \tag{2.66}$$

A variety of other, more complex, constitutive equations have also been developed to describe viscoelastic fluids. The Giesekus model [45] and Phan-Thien-Tanner (PTT) model [83] are similar to the Oldroyd-B model but with nonlinear terms in $\boldsymbol{\tau}$. The constitutive equation for the polymeric stress for each is given by Eqs. (2.67) and (2.68), respectively,

$$\boldsymbol{\tau}_p+\lambda_1\boldsymbol{\tau}_{p_{(1)}}-\alpha\frac{\lambda_1}{\eta_p}(\boldsymbol{\tau}_p\cdot\boldsymbol{\tau}_p)=2\eta_p\mathbf{D} \tag{2.67}$$

$$\boldsymbol{\tau}_p+\lambda_1\boldsymbol{\tau}_{p_{(1)}}+\left[\exp\left(\frac{\lambda_1}{\eta_p}tr(\boldsymbol{\tau}_p)\right)-1\right]\boldsymbol{\tau}_p=2\eta_p\mathbf{D} \tag{2.68}$$

The Giesekus model is often preferred to the Oldroyd 8-constant since it is derived from physical arguments; it is a simple dumbbell model with an anisotropic drag force which is a function of the stress tensor. It also produces very realistic material properties, especially considering how simple the model is.

Molecular-Kinetic Theories

All the viscoelastic models presented above are general in that the parameters have no dependence on the specific structure of the fluid being considered. For a polymer the polymer structure and kinematic properties can be determined using a molecular-kinetic theory such as Kirkwood-Riseman-Zimm (KRZ) or Kargin-Slonimski-Rouse (KSR) theory. In KSR theory a macromolecule is modelled as a bead-spring chain with the beads as the centers of interaction with a solvent and the springs modelling elastic linkage between the beads [65]. In fact, much more complex models exist taking into account for example internal viscosity of the subchains and many other factors. However, these

detailed descriptions of fluid structure are beyond the scope of this work. For the majority of the thesis the Oldroyd-B model is employed to model fluid rheology since it can describe a range of viscoelastic behaviour but is simple enough to easily incorporate into numerical simulations.

2.6 Numerical Comparisons

Some numerical comparisons are now provided for both freely oscillating bubbles and bubbles forced by an acoustic pulse. The Linear Jeffrey's and Oldroyd-B models are considered to highlight the different dynamics that results when considering either linear or nonlinear rheological models.

2.6.1 Energy Balance

The accuracy of the numerical solution can be monitored using an energy check: the kinetic and potential energy of the system should be balanced by the work done (if there is any acoustic forcing) and the resulting dissipation of the system. By multiplying the Rayleigh-Plesset Eq. (2.15) by $4\pi\rho\dot{R}R^2$ it can be written in the form

$$\begin{aligned}\frac{\mathrm{d}}{\mathrm{d}t}\left[2\pi\rho\dot{R}^2R^3\right] + \frac{4\pi}{3}\frac{\mathrm{d}}{\mathrm{d}t}\left[R^3\left(p_0 + \frac{p_{g0}}{\kappa-1}\left(\frac{R_0}{R}\right)^{3\kappa} + \frac{3\sigma}{R}\right)\right] \\ = -4\pi p_0 a\sin(\omega t)\dot{R}R^2 - 8\pi\dot{R}R^2\int_R^\infty\left(\frac{\tau_{rr}-\tau_{\theta\theta}}{r}\right)dr + E_0. \qquad (2.69)\end{aligned}$$

where E_0 is the initial energy and the pressure term has been expressed in terms of a constant part p_0 and an oscillatory part $p_A\sin(\omega t)$. For a constant pressure term the sine term in the above expression will vanish. It is helpful to integrate (2.69) with respect to time to give

$$\begin{aligned}2\pi\rho\dot{R}^2R^3 + \frac{4\pi}{3}R^3\left(p_0 + \frac{p_{g0}}{\kappa-1}\left(\frac{R_0}{R}\right)^{3\kappa} + \frac{3\sigma}{R}\right) \\ = -4\pi p_0 a\int_0^t\sin(\omega t)\dot{R}R^2dt - 8\pi\int_0^t\left[\dot{R}R^2\int_R^\infty\left(\frac{\tau_{rr}-\tau_{\theta\theta}}{r}\right)dr\right]dt + E_0. \qquad (2.70)\end{aligned}$$

The left hand side of Eq. (2.70) is the bubble energy while the right hand side is the work done by the acoustic forcing and viscous dissipation. Comparing the two will give

a measure of numerical accuracy and stability.

2.6.2 Freely Oscillating Bubbles

For a freely oscillating bubble the pressure term at infinity is constant

$$p_\infty = p_0 = P_{ref}. \tag{2.71}$$

In this case the following non-dimensionalisation will be employed

$$R = R_m R^*, \quad t = \frac{R_m}{U} t^*, \quad \tau_{ij} = \frac{\eta}{R_m} U \tau_{ij}^*, \tag{2.72}$$

where R_m is the maximum bubble radius attained by a single gas bubble in an inviscid, infinite fluid, $U = \sqrt{P_{ref}/\rho}$ and $P_{ref} = 101\text{kPa}$ is atmospheric pressure. The value of R_0 will be chosen in such a way as to make the non-dimensionalised maximum radius of the bubble in an inviscid fluid equal to one.

Non-Dimensionalised Jeffreys Model

Substituting these into the Jeffreys model gives the following system of equations (where the asterisks have been dropped for clarity)

$$\frac{\mathrm{d}R}{\mathrm{d}t} = \dot{R}, \tag{2.73}$$

$$\frac{\mathrm{d}\dot{R}}{\mathrm{d}t} = \frac{1}{R}\left\{ -\frac{3}{2}\dot{R}^2 + \bar{p}_g \left(\frac{\bar{R}_0}{R}\right)^{3\kappa} - \frac{We}{R} - 1 - \frac{3}{Re} S \right\}, \tag{2.74}$$

$$\frac{\mathrm{d}S}{\mathrm{d}t} = \frac{1}{De}\left\{ -S - De\frac{\dot{R}}{R}\tau_{rr}(R) + \frac{4}{3}\left[\frac{\dot{R}}{R} + \lambda De\left(\frac{2\dot{R}^2 + R\ddot{R}}{R^2}\right)\right]\right\}, \tag{2.75}$$

$$\frac{\mathrm{d}\tau_{rr}(R)}{\mathrm{d}t} = \frac{1}{De}\left\{ -\tau_{rr}(R) + 4\left[\frac{\dot{R}}{R} + \lambda De\left(\frac{2\dot{R}^2 + R\ddot{R}}{R^2}\right)\right]\right\}, \tag{2.76}$$

where $\lambda = \lambda_2/\lambda_1$, $\bar{R}_0 = R_0/R_m$ is the initial radius of a single gas bubble in an inviscid, infinite fluid and $\bar{p}_g = p_{g0}/P_{ref}$ is the relative strength of the internal bubble pressure to the (initial) pressure in the fluid. The following non-dimensional parameters have

also been defined

$$Re = \frac{P_{ref} R_m}{\eta U}, \quad We = \frac{2\sigma}{P_{ref} R_m}, \quad De = \lambda_1 \frac{U}{R_m}. \tag{2.77}$$

The Deborah (De) number is a ratio of the relaxation time of the fluid to some time scale for the bubble whereas the Weber (We) and Reynolds (Re) numbers are measures of the relative importance of inertia to surface tension and viscous effects, respectively.

Non-Dimensionalised Oldroyd-B Model

The non-dimensionalised equations for the Oldroyd-B case are

$$\frac{\mathrm{d}R}{\mathrm{d}t} = \dot{R}, \tag{2.78}$$

$$\frac{\mathrm{d}\dot{R}}{\mathrm{d}t} = \frac{1}{R}\left\{ -\frac{3}{2}\dot{R}^2 + \bar{p}_g \left(\frac{\bar{R}_0}{R}\right)^{3\kappa} - \frac{We}{R} - 1 + \frac{4\varepsilon}{Re}\frac{\dot{R}}{R} - S^{(1)} - S^{(2)} \right\} \tag{2.79}$$

$$\frac{\mathrm{d}S^{(1)}}{\mathrm{d}t} = -\left(\frac{1}{De} + 4\frac{\dot{R}}{R}\right) S^{(1)} + 2\frac{(1-\varepsilon)}{DeRe}\frac{\dot{R}}{R} \tag{2.80}$$

$$\frac{\mathrm{d}S^{(2)}}{\mathrm{d}t} = -\left(\frac{1}{De} + \frac{\dot{R}}{R}\right) S^{(2)} + 2\frac{(1-\varepsilon)}{DeRe}\frac{\dot{R}}{R}, \tag{2.81}$$

where $\varepsilon = \eta_s/\eta = \lambda_2/\lambda_1$.

Initial Conditions

The initial conditions for the (non-dimensional) variables are given by

$$R(0) = \bar{R}_0, \quad \dot{R}(0) = \tau_{rr}(0) = \tau_{\theta\theta}(0) = 0 \tag{2.82}$$

For an infinite, inviscid fluid the non-dimensionalised Rayleigh-Plesset equation is

$$R\ddot{R} + \frac{3}{2}\dot{R}^2 = \bar{p}_g \left(\frac{\bar{R}_0}{R}\right)^{3\kappa} - 1. \tag{2.83}$$

Multiplying by $2R^2\dot{R}$ and integrating

$$R^3\dot{R}^2 = \frac{2\bar{p}_g\bar{R}_0^{3\kappa}R^{3(1-\kappa)}}{3(1-\kappa)} - \frac{2}{3}R^3 + c, \tag{2.84}$$

for some constant c. Since $\dot{R}(0) = 0$ the constant c is found to be

$$c = \frac{2}{3}\bar{R}_0^3 - \frac{2\bar{p}_g\bar{R}_0^3}{3(1-\kappa)}. \tag{2.85}$$

Combining Eqs. (2.84,2.85) and the fact that $\dot{R} = 0$ when $R = R_{\max} = 1$ the following equation can be found relating $\bar{R}_0$, $\bar{p}_g$ and κ

$$\frac{\bar{p}_g}{1-\kappa}(\bar{R}_0^{3\kappa} - \bar{R}_0^3) = -1 + \bar{R}_0^3 \tag{2.86}$$

The values $\bar{p}_g = 100$, $\kappa = 1.4$ will be used in this chapter unless otherwise stated. In this case Eq. (2.86) gives the initial bubble radius $\bar{R}_0 = 0.165$.

Numerical Results

Fig. 2.3 shows the radius plotted against time for a bubble in a Newtonian fluid for a range of Reynolds number. For the inviscid case ($Re = \infty$), the bubble undergoes periodic oscillations between the initial radius $\bar{R}_0$ and the maximum radius $\bar{R}_m = 1$. For finite values of Re, the oscillations are damped and the bubble eventually reaches some equilibirum radius which is independent of Re. Consistent with previous numerical work an increase in viscosity results in fewer oscillations of lower amplitude as the bubble loses energy through viscous dissipation. For the highly viscous case $Re = 1$, the oscillations are completely suppressed and the bubble undergoes a monotonic increase to some equilibrium radius.

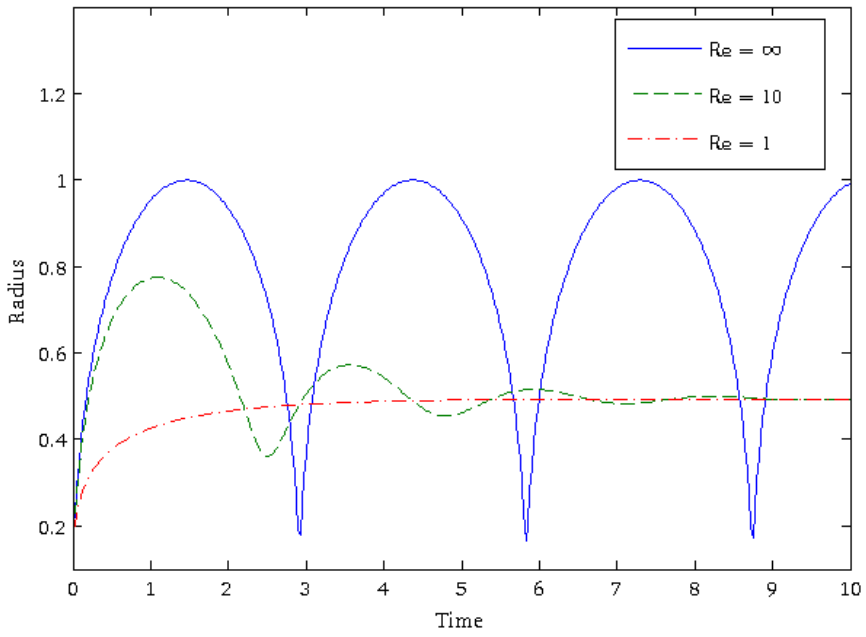

Figure 2.3: Radius vs. time plots for a bubble in a Newtonian fluid with varying viscosity.

The effect of elasticity on bubble dynamics is shown in Fig. 2.4 for the Linear Maxwell model (a) and UCM model (b) and a fixed viscosity ($Re = 10$). For the UCM, an increase in fluid elasticity results in slower oscillations with a higher amplitude and higher rebound velocities. These higher velocities are due to a build up of elastic potential as the bubble grows. As $De \to \infty$ the dynamics approach that of the inviscid case as the elastic effects negate the viscosity and the dynamics become inertia dominated. Similar dynamics are seen for the Linear Maxwell model although the oscillations do not necessarily increase with increasing De.

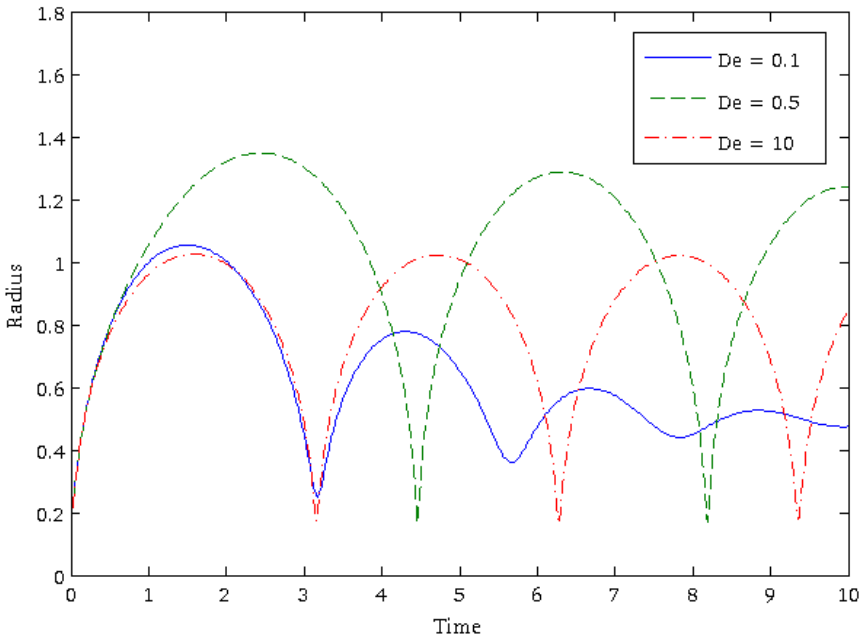

(a) Radius time curves for a linear Maxwell fluid for $Re = 10, We = 0$ and different De.

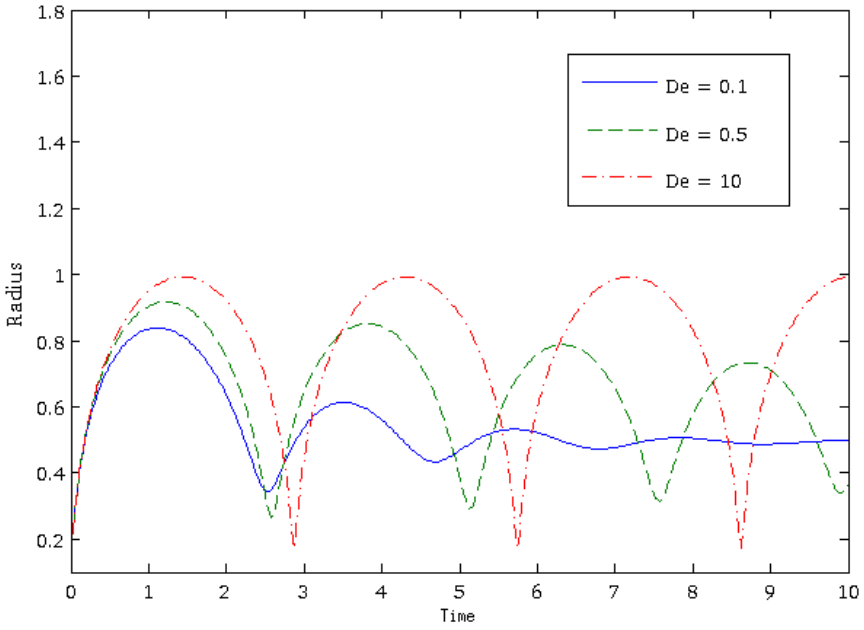

(b) Radius time curves for an UCM fluid for $Re = 10, We = 0$ and different De.

Figure 2.4: A comparison of the linear Maxwell and UCM models for $Re = 10$, $We = 0$ and different De.

The energy balance given by Eq. (2.70) allows us to monitor the solution behaviour and gives a measure of the errors involved. Fig. 2.5 gives an example of this for the Linear Maxwell and UCM models with $Re = 10, De = 0.1, We = 0$. For both models the error is small, indicating that the numerical scheme for both models is accurate. In this case there are larger error spikes for the Linear Maxwell model, in particular at $t \approx 3$ (see Fig.2.4). This is a result of hgher velocities occuring in the Linear Maxwell model, however, rather than a less accurate numerical scheme compared to the UCM.

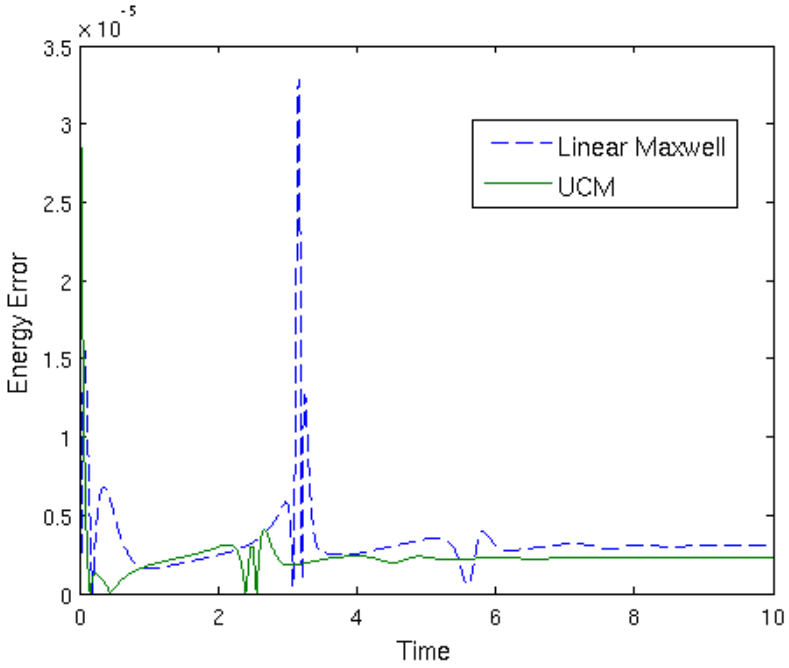

Figure 2.5: The difference between energy and the work done by viscous dissipation normalised by the initial energy E_0 for the Linear Maxwell and UCM models with: $Re = 10, De = 0.1, We = 0$ (Solid lines in Fig.2.4)

The pressure at the fluid side of the bubble wall p_B is calculated using Eq. (2.14) and is shown for the Linear Maxwell and UCM models in Fig. 2.6. For large deformations the Linear Maxwell becomes inaccurate and predicts a more explosive growth and consequent collapse of the bubble. This leads to significantly higher pressures being predicted at minimum volume as the internal gas is compressed (shown by the spikes in Fig. 2.6). Since the bubble expands to a larger maximum radius the oscillations are also shifted in time compared to the corresponding UCM fluid. Note that small negative pressures are generated as the expanding bubble 'pushes' the fluid outwards.

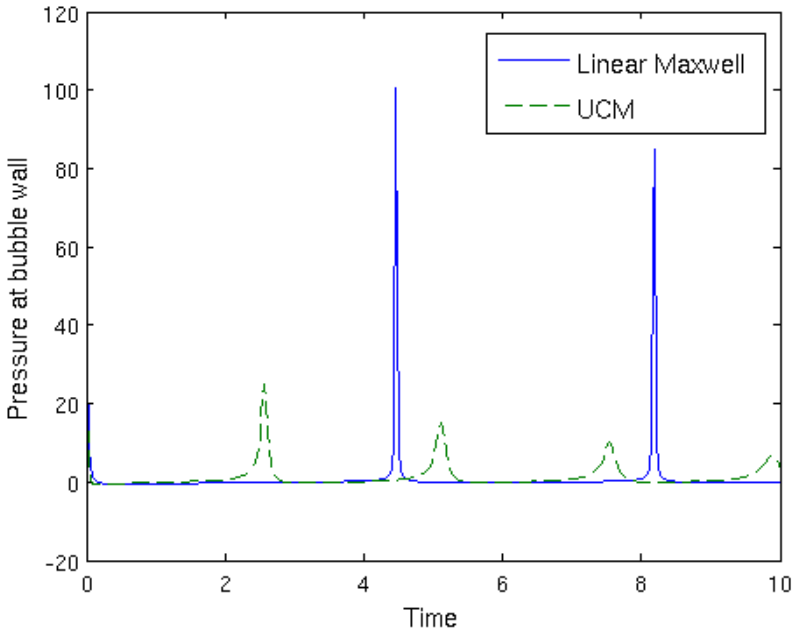

Figure 2.6: Pressure at the bubble wall (relative to p_∞) for the Linear Maxwell (LM) and Upper-Convected Maxwell (UCM) models for the case $Re = 10$ and $De = 0.5$ in Fig. 2.4.

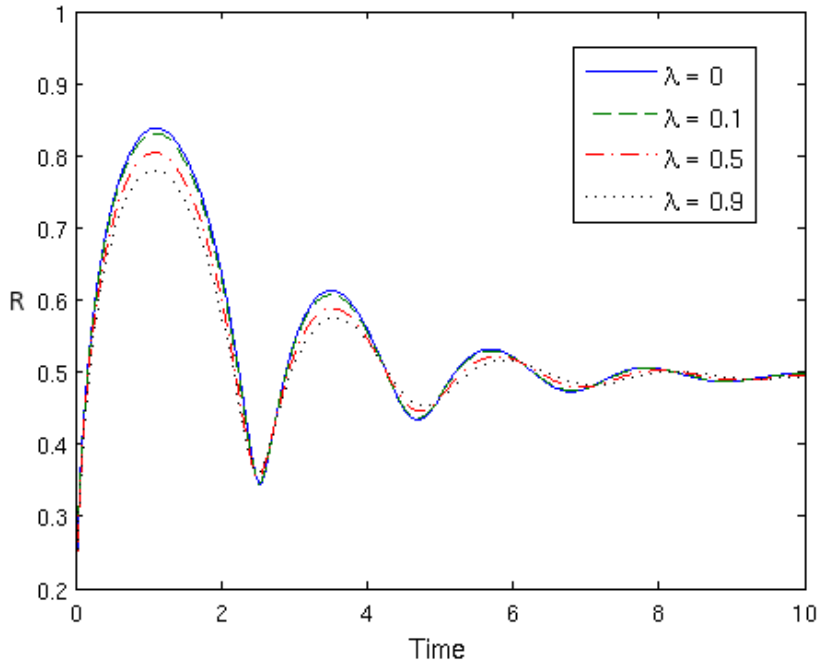

Figure 2.7: Radius vs. time plots for the Oldroyd-B model with $Re = 10, De = 0.1, We = 0$ and varying λ.

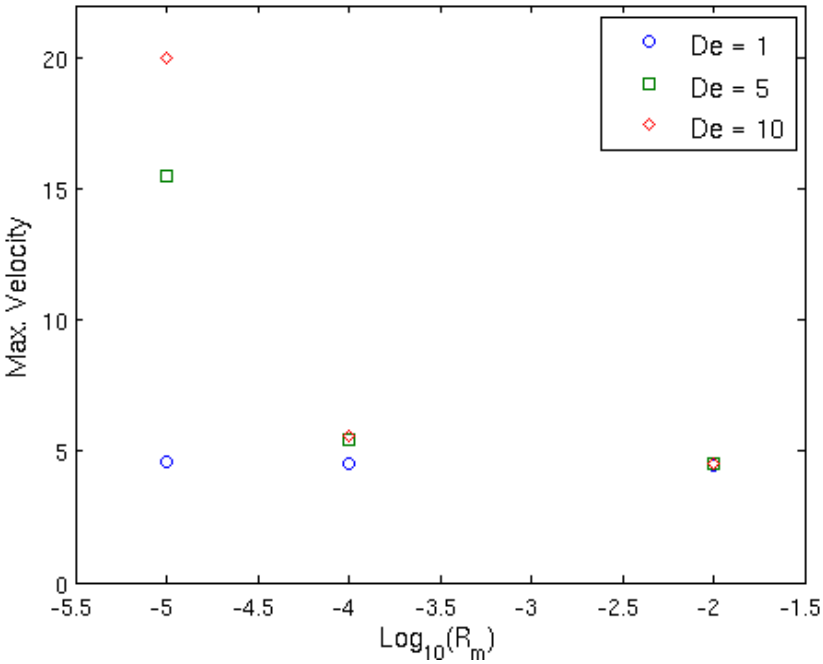

Figure 2.8: Maximum velocities for a range of bubble sizes and $De = 1, 5, 10$.

The influence of the parameter $\lambda = \lambda_2/\lambda_1 = \eta_s/\eta$ is shown in Fig. 2.7. The value of λ is expected to be small for most relevant viscoelastic fluids [1] although the question of what is a typical value is difficult to answer. Fig. 2.7 shows the case $Re = 10, De = 0.1$ for a UCM fluid and a variety of values $0 < \lambda < 1$. It is clear that, at least in this case, changing λ has little effect other than a slight damping of the oscillations. A small (but non-zero) value of $\lambda = 0.1$ will be chosen for all subsequent calculations .

Fig. 2.8 shows how the rheology of the fluid affects bubble dynamics for a range of bubble size. The pressure and density at infinity are taken as atmospheric pressure and the density of water, respectively; $p_0 = 101325\text{Pa}$, $\rho = 999\text{kg/m}^3$ and the value $\eta = 30\text{mPa·s}$ is used. For this fixed viscosity a change in Re relates to a change in the maximum radius R_m. Maximum radii of $10^{-5}, 10^{-4}, 10^{-2}$ are chosen corresponding to $Re = 3.4, 34, 3400$, respectively. It is observed that a change in the Deborah number of order ten significantly increases the maximum velocity observed for small bubbles and almost no effect on bubbles of the order 10^{-2}. These findings agree qualitatively with the experimental findings of Brujan ([27],p.77).

2.6.3 Forced Oscillations Due to an Acoustic Pulse

The forced oscillations of a bubble due to a sinusoidal pulse in both a linear Jeffreys and a UCM fluid have been studied by Allen and Roy [2]. In [2] the acoustic forcing was modelled through the pressure term at infinity as

$$p_\infty = p_0 + p_A \sin(\omega t). \tag{2.87}$$

In an effort to more accurately model a pulse in biomedical applications such as ultrasound imaging and sonoporation a Gaussian pulse [113] is chosen instead

$$p_\infty(t) = p_0 + p_{div} = p_0 + p_A \sin[2\pi f(t - t_c)]\exp[-\pi^2 h^2 f^2 (t - t_c)^2]. \tag{2.88}$$

The time dependent part p_{div} is shown in Fig. 2.9 for some typical values $f = 2\text{MHz}$ and $p_A = 200\text{kPa}$. The parameters h and t_c determine the width and centre of the pulse, respectively and have values $h = 1/3$ and $t_c = 3/f$ unless otherwise stated (it has been shown [113] that the results are not particularly dependent on these parameters).

Since the pulse has a frequency f it makes sense to use a different non-dimensionalisation

to the freely oscillating bubble, given by

$$R = R_0 R^*, \quad t = t_c t^* = \frac{1}{\omega} t^*, \quad \tau_{ij} = p_c \tau_{ij}^* = \rho \omega^2 R_0^2 \tau_{ij}^*, \tag{2.89}$$

where $\omega = 2\pi f$. This leads to slightly different definitions for the Reynolds (Re), Weber (We) and Deborah (De) numbers from the freely oscillating bubble

$$Re = \frac{\rho w R_0^2}{\eta}, \quad We = \frac{2\sigma}{p_c R_0}, \quad De = \lambda_1 w. \tag{2.90}$$

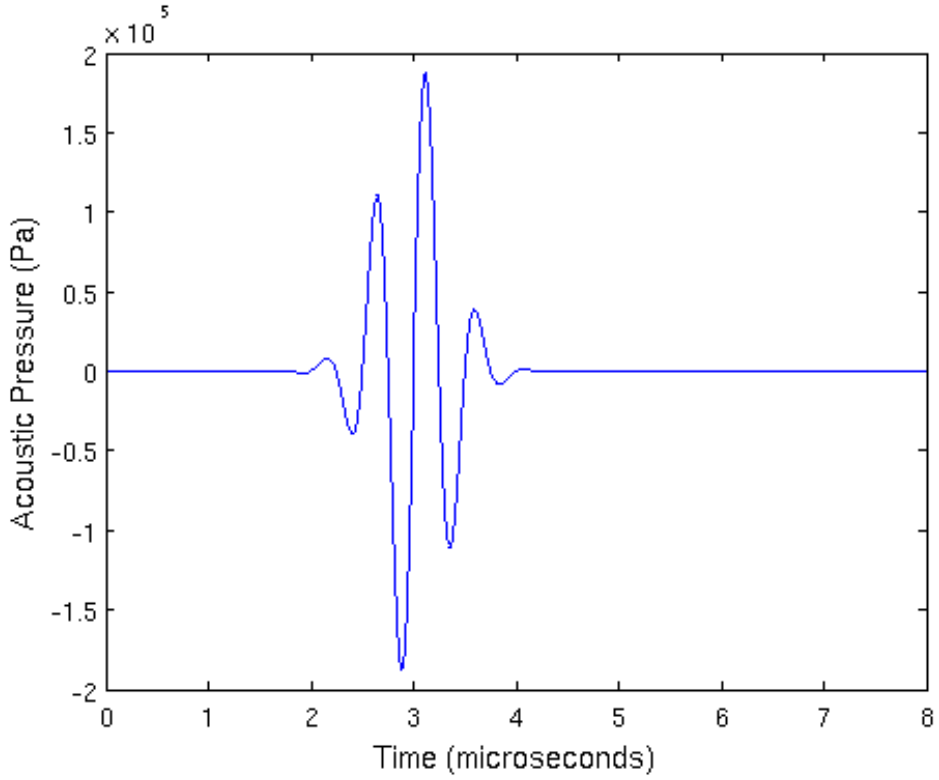

Figure 2.9: Gaussian pulse with $f = 2$MHz and $p_A = 200$kPa.

For a gas-filled cavitation bubble the resonant frequency can be found by writing $R(t) = \delta(t) + R_0$, linearising the Rayleigh-Plesset Eq. (2.15) and dropping higher order terms. It can be shown that this gives a resonant frequency of

$$f_r = \frac{1}{2\pi} \sqrt{\frac{1}{\rho R_0^2} \left[3\kappa p_{g0} - \frac{2\sigma}{R_0} \right]}. \tag{2.91}$$

Note that if surface tensions is neglected ($\sigma = 0$) then this is the Minnaert resonance of a single bubble in an infinite domain [75].

Assuming the cavitation bubble has a high internal pressure $p_{g0} = (100 \cdot P_{ref}) = 10.1$MPa, surface tension coefficient $\sigma = 0.0725$N/m and given $\rho = 998$kg/m^3, $\kappa = 1.4$ the resonant frequencies for a range of bubble sizes are shown in Table 2.1. As R_0 increases, the resonant frequency decreases although even for a relatively large bubble size of 10^{-3} the value of f_r is larger than the typical frequency used for sonoporation and ultrasound imaging of 20kHz [73]. For shock-wave lithotripsy, however, the typical frequency of pulses is $f \approx 100$kHz and it is thus possible for bubbles of the order $10^{-4} - 10^{-3}$m to be driven at their resonant frequency and thus oscillate at maximum amplitude.

Table 2.1: Resonant frequencies

R_0	0.1μm	0.5μm	1μm	5μm	10μm
f_r	322.47MHz	65.41MHz	32.76MHz	6.56MHz	3.28MHz
R_0	50μm	0.1mm	0.5mm	1mm	
f_r	656.23kHz	328.12kHz	65.62kHz	32.81kHz	

2.7 Encapsulated Microbubbles in an Acoustic Field

Thus far in this chapter the gas-fluid interface of the bubble under consideration has been assumed to be 'clean', i.e. no contaminating particles are present on the bubble surface. An encapsulated microbubble (EMB) is a gas filled bubble with a surrounding solid shell. As discussed in Chapter 1, this shell stabilises the bubble and allows it to be used in applications such as ultrasound imaging and sonoporation. Modelling this shell

as a layer of incompressible, elastic material, Church [33] derived a Rayleigh-Plesset type equation for an EMB in a Newtonian fluid

$$R_1\ddot{R}_1\left[1+\left(\frac{\rho_L}{\rho_S}-1\right)\frac{R_1}{R_2}\right]+\frac{3}{2}\dot{R}_1^2\left[1+\left(\frac{\rho_L}{\rho_S}-1\right)\left(\frac{4R_2^3-R_1^3}{3R_2^3}\right)\frac{R_1}{R_2}\right]$$
$$=\frac{1}{\rho_S}\left[p_{g0}\left(\frac{R_{10}}{R_1}\right)^{3\kappa}-\frac{2\sigma_1}{R_1}\frac{2\sigma_2}{R_2}-4\eta_L\frac{R_1^2\dot{R}_1}{R_2^3}-p_0-P_{driv}(t)-S_{1,2}\right], \tag{2.92}$$

where R_1,R_2 are the inner and outer radii of the shell, respectively, subscripts L and S refer to parameters of the fluid and shell, respectively, and

$$S_{1,2}=-3\int_{R_1}^{R_2}\frac{\tau_{rr}^{(S)}(r,t)}{r}dr, \tag{2.93}$$

where $\tau_{rr}^{(S)}$ is the viscous stress of the shell. Many of the EMBs employed in applications have very thin shells [37] with a thickness, R_2-R_1, much smaller than the radius, R_1, of the bubble i.e. $R_2-R_1<<R_1$. It is therefore worthwhile to consider a thin-shell approximation. Taking Eq. (2.92) to this limit results in

$$R\ddot{R}+\frac{3}{2}\dot{R}^2=\frac{1}{\rho_L}\left[p_{g0}\left(\frac{R_0}{R}\right)^{3\kappa}-\frac{2\sigma}{R}-p_0-P_{driv}(t)-3\int_R^\infty\frac{\tau_{rr}-\tau_{\theta\theta}}{r}dr-S_{1,2}\right]. \tag{2.94}$$

The choice of expression for $\tau_{rr}^{(S)}$ allows us to choose different rheological laws for the shell. Assuming the shell is a viscoelastic solid (as in [77], [37]) the term $S_{1,2}$ can be separated into a viscous and elastic part such as in [37] in which a Kelvin-Voigt model was used.

Another way to derive an equation for the bubble radius under the thin shell assumption is to write $R_2=R_1+\varepsilon$ for some small parameter ε and consider the Rayleigh-Plesset equation

$$R\ddot{R}+\frac{3}{2}\dot{R}^2=\frac{1}{\rho}\left[p_B-p_\infty-\tau_{rr}^{(sh)}|_R-2\int_{R_1}^{R_1+\varepsilon}\left(\frac{\tau_{rr}^{(sh)}-\tau_{\theta\theta}^{(sh)}}{r}\right)dr+\right.$$
$$\left.\tau_{rr}|_R-2\int_{R_2}^{\infty}\left(\frac{\tau_{rr}-\tau_{\theta\theta}}{r}\right)dr\right]. \tag{2.95}$$

Due to the shell, the force balance across the interfaces results in (cf. Eq. (2.14))

$$p_B=p_i-\frac{2\sigma}{R}-\tau_{rr}+\tau_{rr}^{(sh)}-\frac{2\chi}{R}\left(\frac{R_0}{R}\right)^2. \tag{2.96}$$

The term $\frac{-2\chi}{R}(\frac{R_0}{R})^2$ arises by taking into account the changing surface tension at the interface due to the varying bubble radius [47] (and assuming an instantaneous thermodynamic equilibrium during bubble oscillations). Using the polytropic law gives

$$p_i(\frac{4}{3}\pi R^3)^\kappa = \text{ const.} \tag{2.97}$$

and thus the internal bubble pressure is

$$\begin{aligned} p_i &= p_{i,eq}\left(\frac{R_0}{R}\right)^{3\kappa} \\ &= \left(p_0 + \frac{2\sigma}{R_0} + \frac{2\chi}{R_0}\right)\left(\frac{R_0}{R}\right)^{3\kappa}. \end{aligned} \tag{2.98}$$

Assuming the shell viscosity is Newtonian and that the shell thickness remains constant during bubble oscillation gives the (Newtonian) thin-shell modified Rayleigh-Plesset equation

$$\begin{aligned} R\ddot{R} + \frac{3}{2}\dot{R}^2 = \frac{1}{\rho}\Bigg[&\left(p_0 + \frac{2\sigma}{R_0} + \frac{2\chi}{R_0}\right)\left(\frac{R_0}{R}\right)^{3\kappa} - \frac{2\sigma}{R} - (p_0 + P_{driv}(t)) \\ &- \frac{2\chi}{R}\left(\frac{R_0}{R}\right)^2 - 12\eta_{(sh)}\varepsilon\frac{\dot{R}}{R(R-\varepsilon)} - 2\int_R^\infty \left(\frac{\tau_{rr} - \tau_{\theta\theta}}{r}\right)dr\Bigg], \end{aligned} \tag{2.99}$$

where χ and $\eta_{(sh)}$ are the shell elasticity and viscosity, respectively. The same non-dimensionalisation as in the previous section is used to give

$$\begin{aligned} R\ddot{R} + \frac{3}{2}\dot{R}^2 = &\left(\bar{p}_0 + We + A\right)\left(\frac{1}{R}\right)^{3\kappa} - \frac{We}{R} - \frac{A}{R^3} - \frac{12\bar{\varepsilon}}{Re_{sh}}\frac{\dot{R}}{R(R-\bar{\varepsilon})} \\ &- \bar{p}_0 - \bar{p}_A\sin(t-\bar{t}_c)\exp[-\frac{h^2}{4}(t-\bar{t}_c)^2] - 2\int_R^\infty \left(\frac{\tau_{rr} - \tau_{\theta\theta}}{r}\right)dr, \end{aligned} \tag{2.100}$$

where the asterisks have been dropped and

$$\bar{p}_0 = p_0/p_c, \quad \bar{p}_A = p_A/p_c, \quad p_c = \rho w^2 R_0^2, \quad A = \frac{2\chi}{p_c R_0}, \quad \bar{t}_c = wt_c, \quad \bar{\varepsilon} = \frac{\varepsilon}{R_0}. \tag{2.101}$$

Eq. (2.100) will now be integrated numerically to model the dynamics of a spherical EMB in a viscoelastic fluid. The following physical parameters (taken from [113]) will be used

$$\rho = 998\text{kg/m}^3, \quad p_0 = 101\text{kPa}, \quad \varepsilon = 1\text{nm}, \quad \sigma = 0.051\text{N/m}, \tag{2.102}$$

where the interfacial tension σ contains contributions from both the bubble and the shell. The other parameters will be varied to consider their effect on the bubble dynamics. Similar to Eq. (2.91) for the 'clean' bubble the resonant frequency for an EMB can be shown to be

$$f_r = \frac{1}{2\pi}\sqrt{\frac{3\kappa}{\rho R_0^2}\left(p_0 + \frac{2(\sigma+\chi)}{R_0}\right) - \frac{2\sigma+6\chi}{\rho R_0^3}} \tag{2.103}$$

For an EMB of initial radius $R_0 = 1\mu$m and using $\chi = 0.5$N/m (taken from [113]) gives a resonant frequency $f_r \approx 4.4$MHz, which is in the typical range for ultrasound contrast imaging. In fact, it is this property that results in their success as contrast agents. The resonant frequency obviously decreases with increased bubble size; for an EMB of radius 4μm the resonant frequency is $f_r \approx 0.83$MHz.

2.7.1 Dynamics at low pressure amplitudes (ultrasound contrast imaging)

The encapsulating shell is defined by ε, χ and η_{sh} which are the shell thickness, interfacial tension and viscosity, respectively. The values of these parameters are chosen following Wu et al. [113] who found them to be $\varepsilon = 1$nm, $\chi = 0.5$N/m and $\eta_{sh} = 1$Pa·s using experimentally obtained radius-time curves for the contrast agent MP1950. The majority of EMB contrast agents have been shown [102] to undergo stable, harmonic (nonlinear) oscillations for pressure amplitudes roughly $50 - 200$kPa. Higher amplitude pressure fields can lead to spontaneous acoustic emissions and fragmentation of the EMB.

In Fig. 2.10, the effect of changing the frequency f is shown for $R_0 = 1\mu$m, $P_A = 100$kPa, $Re = 6.3$ and $De = 0$ for both an EMB and a clean cavitation bubble. The 'cavitation bubble' is assumed to be clean and to have reached a stable equilibrium radius before the arrival of the pulse. The oscillations due to the pulse are observed to be smaller in amplitude for the EMB in comparison to the clean bubble due to the stabilising shell. A lower frequency pulse in this case results in larger oscillations for both types of bubble. Note that for $f = 4$MHz the dynamics of the two bubbles differ only in amplitude. For $f = 2$MHz the clean bubble is clearly more erratic with extra oscillations observed compared to the EMB. Increasing the pressure amplitude to $P_A = 200$kPa and keeping all other parameters fixed leads to similar behaviour, as

seen in Fig. 2.11. An increase in P_A, however, does result in a larger response from the bubbles. For $f = 2$Mz the clean bubbles is seen to reach a very small radius at $t \approx 3\mu$s which would lead to high pressures and potentially a shock wave being produced. The EMB on the other hand exhibits stable, nonlinear oscillations.

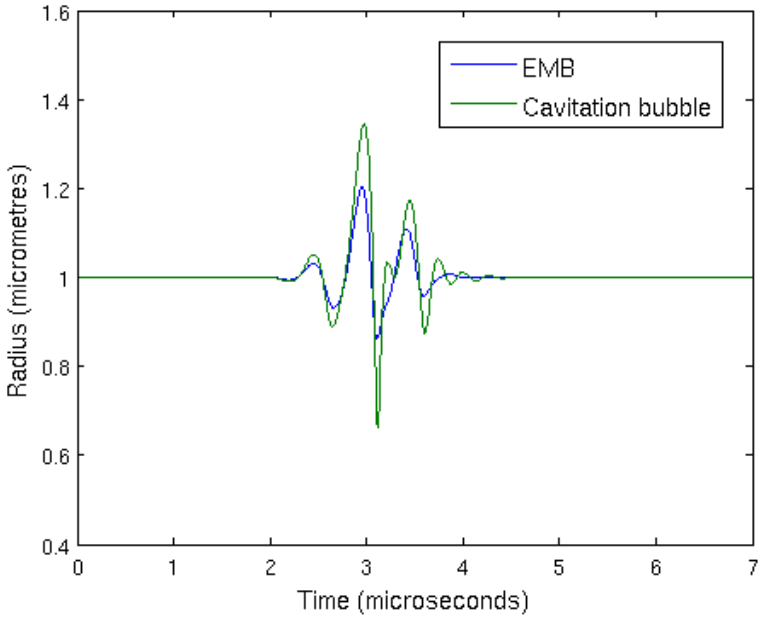

(a) $R_0 = 1\mu$m, $f = 2$MHz, $P_A = 100$kPa, $Re = 6.3$, $De = 0$.

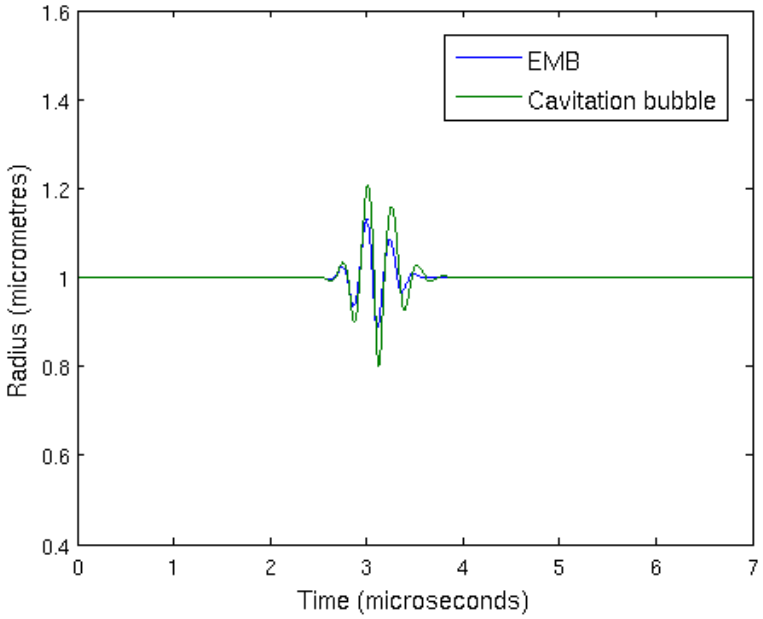

(b) $R_0 = 1\mu$m, $f = 4$MHz, $P_A = 100$kPa, $Re = 6.3$, $De = 0$.

Figure 2.10: Effect of changing the frequency of the pulse.

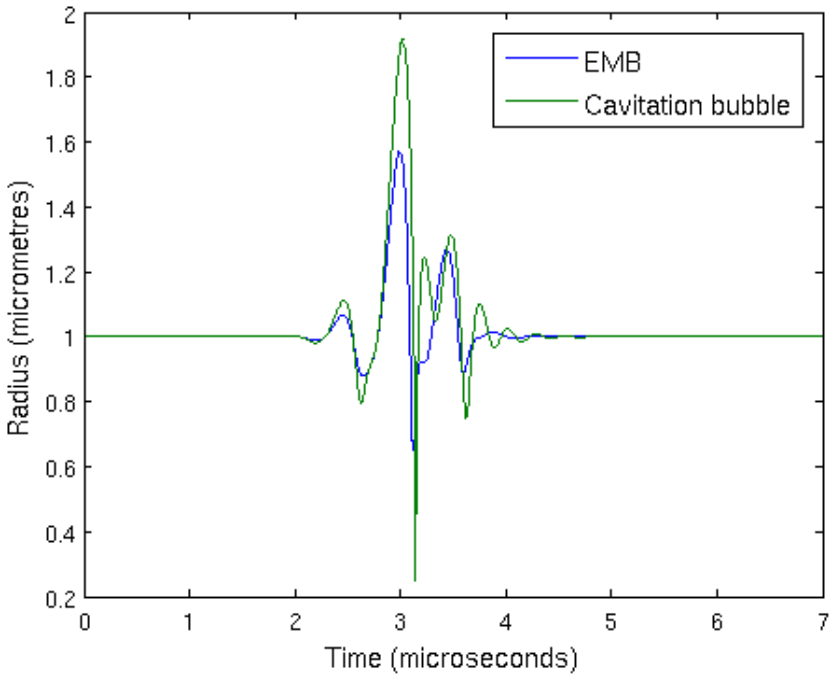

(a) $R_0 = 1\mu$m, $f = 2$MHz, $P_A = 200$kPa, $Re = 6.3$, $De = 0$.

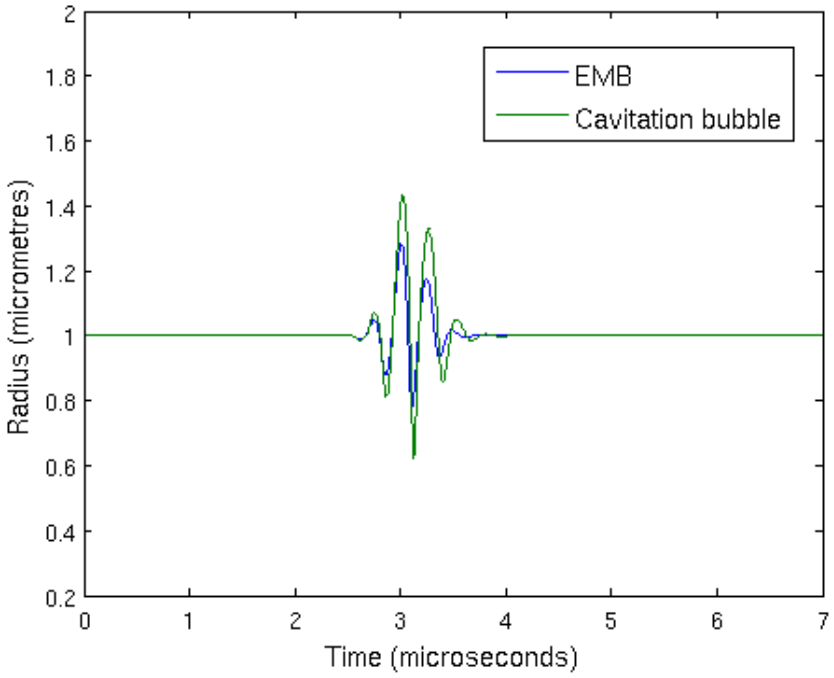

(b) $R_0 = 1\mu$m, $f = 4$MHz, $P_A = 200$kPa, $Re = 6.3$, $De = 0$.

Figure 2.11: Effect of changing the frequency of the pulse.

The effects of fluid viscosity are shown in Fig. 2.12 for an EMB with $P_A = 200\text{kPa}$, $R_0 = 1\mu\text{m}$, $f = 2\text{MHz}$, $De = 0$ and $Re = 1, 6, 15$. Similarly to the freely oscillating, clean cavitation bubble considered in Section 2.6, an increase in viscosity leads to damped oscillations in bubble radius.

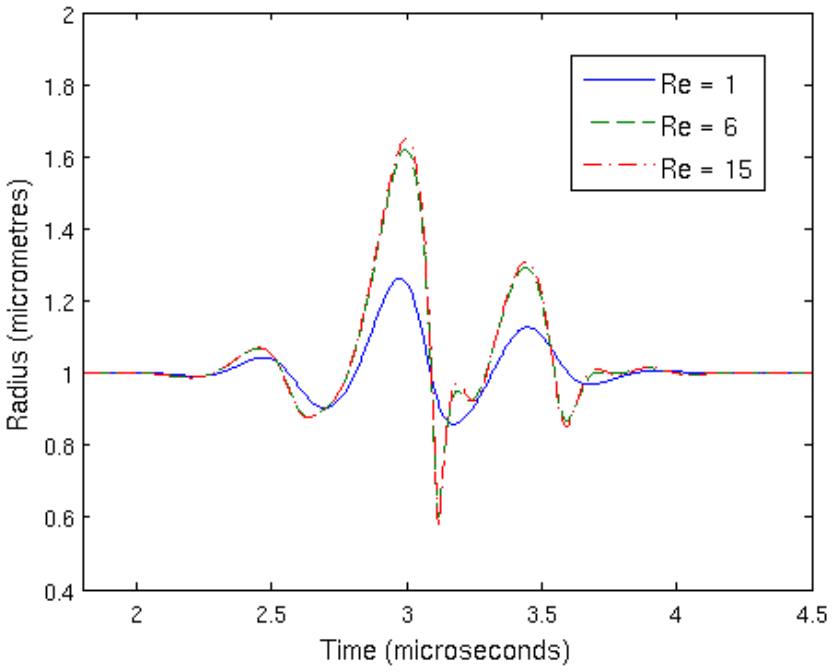

Figure 2.12: Effect of viscosity on dynamics. Parameters: $P_A = 200\text{kPa}$, $De = 0$, $R_0 = 1\mu\text{m}$ and $f = 2\text{MHz}$.

The effects of fluid elasticity are shown in Fig. 2.13 for an EMB with $P_A = 200\text{kPa}$, $R_0 = 1\mu\text{m}$, $f = 2\text{MHz}$, $Re = 6.3$ and $De = 0, 4, 15$. In comparison, changing De has little effect since the highly viscous shell dominates the dynamics. An increase in elasticity results in larger oscillations, although the difference between the cases shown is very small.

Fig. 2.14 shows the effect of changing initial radius for an EMB with parameters $P_A = 200\text{kPa}$, $f = 1\text{MHz}$, $Re = 6.3$, $De = 1$ and $R_0 = 1, 4, 10\mu\text{m}$. The non-dimensionalised radius is plotted against time to make comparisons more clear. The intensity of oscillations is seen to increase as initial bubble radius is decreased. For $R_0 = 1\mu\text{m}$ the oscillations, as well as being larger, are much more chaotic than the cases $R_0 = 4, 10\mu\text{m}$.

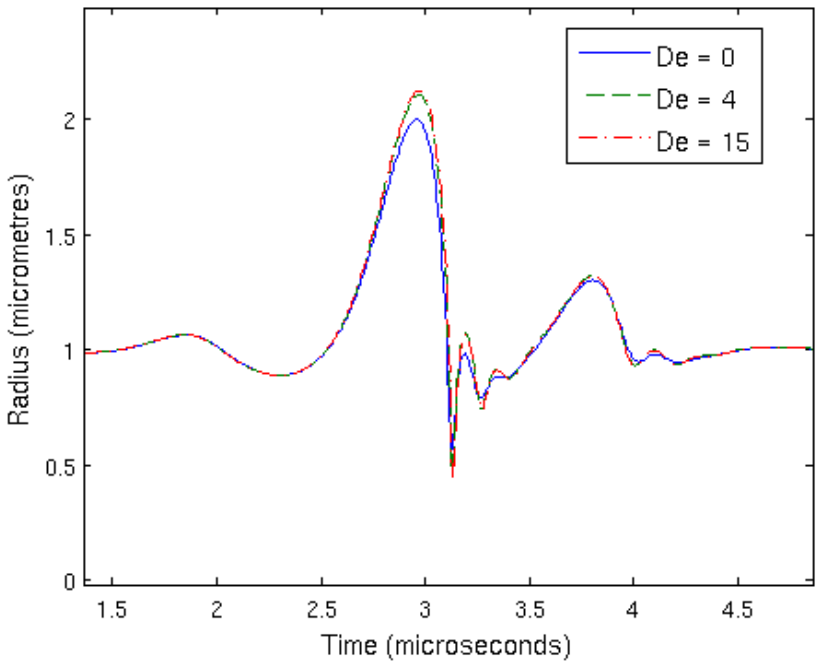

Figure 2.13: Effect of elasticity on dynamics. Parameters: $P_A = 200$kPa, $Re = 6.3$, $R_0 = 1\mu$m and $f = 1$MHz.

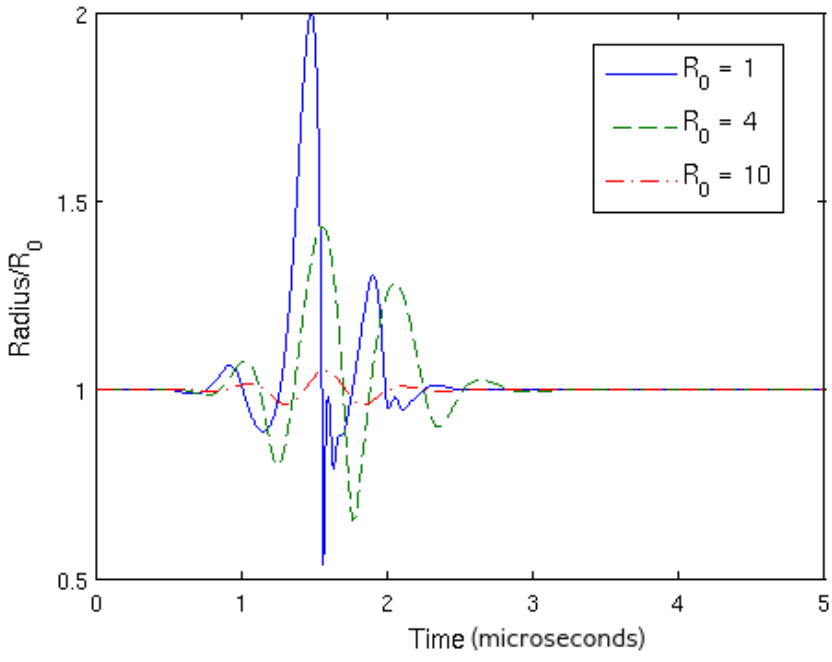

Figure 2.14: Effect of bubble size for an acoustically forced EMB with parameters: $P_A = 200$kPa, $Re = 6.3$, $De = 1$ and $f = 1$MHz.

2.7.2 Dynamics at high pressure amplitudes (sonoporation)

For higher amplitude pressure pulses it is possible to see very fast growth up to a maximum radius which is much larger than the initial radius . In practical applications this is likely to be accompanied by the emission of shock waves into the fluid and possible fragmentation or disintegration of the bubble. This behaviour is seen for a $R_0 = 4\mu$m sized bubble with $P_A = 2$MPa in Figs. 2.15 and 2.16a for frequencies $f = 0.5, 1, 2$MHz. In all these cases this large growth and collapse are seen with maximum amplitude achieved for the case $f = 0.5$MHz. At this low frequency the bubble reaches a maximum radius almost nine times that of its initial radius. The spherical model used here has no mechanism to predict fragmentation of the bubble but it is suggested that for these very large oscillations the bubble will most likely disintegrate. For higher frequencies (see Fig.2.16b and 2.16d) large amplitude but stable oscillations are seen with the bubble eventually returning to its initial radius.

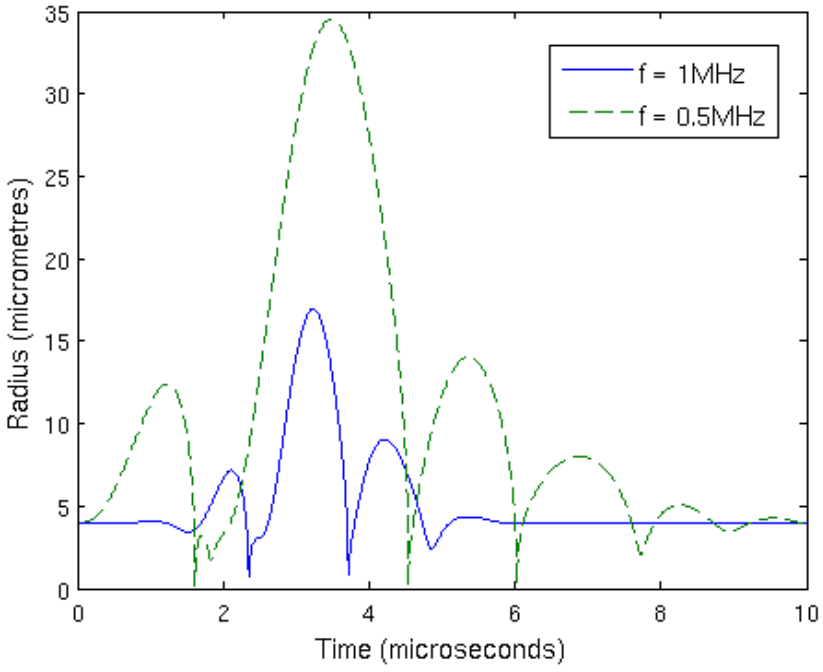

Figure 2.15: Radius vs. time curves for an EMB bubble with $R_0 = 4\mu$m, $Re = 6.3$, $P_A = 2$MPa and $f = 1$MHz (solid line), $f = 0.5$MHz (dashed line).

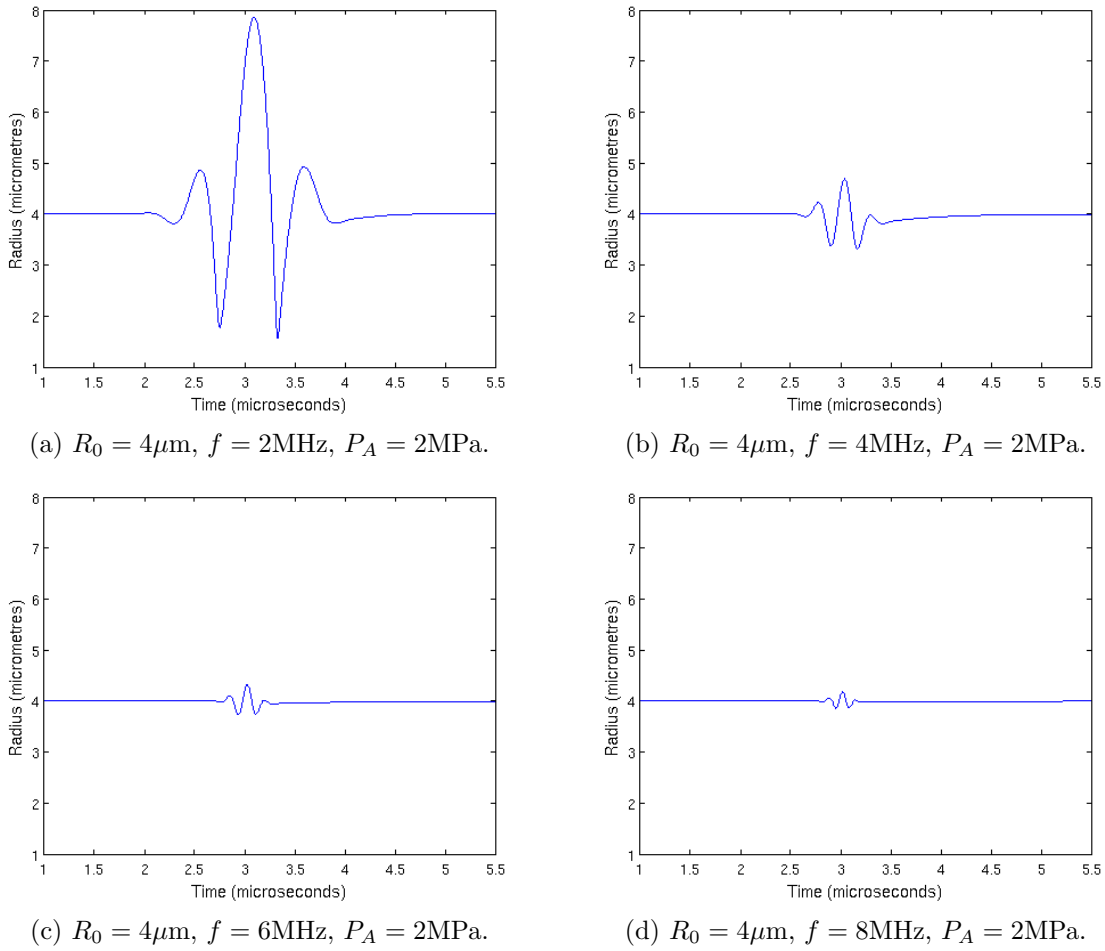

(a) $R_0 = 4\mu$m, $f = 2$MHz, $P_A = 2$MPa.

(b) $R_0 = 4\mu$m, $f = 4$MHz, $P_A = 2$MPa.

(c) $R_0 = 4\mu$m, $f = 6$MHz, $P_A = 2$MPa.

(d) $R_0 = 4\mu$m, $f = 8$MHz, $P_A = 2$MPa.

Figure 2.16: Radius vs. time curves for a 4μm EMB in a Newtonian fluid with $Re = 6.3$, $P_A = 2$MPa and varying frequencies.

For forced oscillations of spherical EMBs in a viscoelastic fluid it has been found that the fluid rheology effects are similar to those seen for a cavitation bubble, but on a smaller scale. In particular, the effect of the fluid elasticity is drastically reduced. This is a consequence of the shell being highly viscous and thus dominating the bubble dynamics. The dynamics are, however, dependent on the frequency and amplitude of the pressure pulse. For pressure amplitudes P_A between 50kPa and 200kPa we see relatively stable, nonlinear oscillations with increasing amplitudes as the frequency is lowered. At higher pressure amplitudes (roughly 2MPa) explosive growth and collapse is seen with lower frequencies again producing higher amplitudes. In reality this explosive growth and collapse is expected to result in bubble fragmentation although this mechanism is not modelled here.

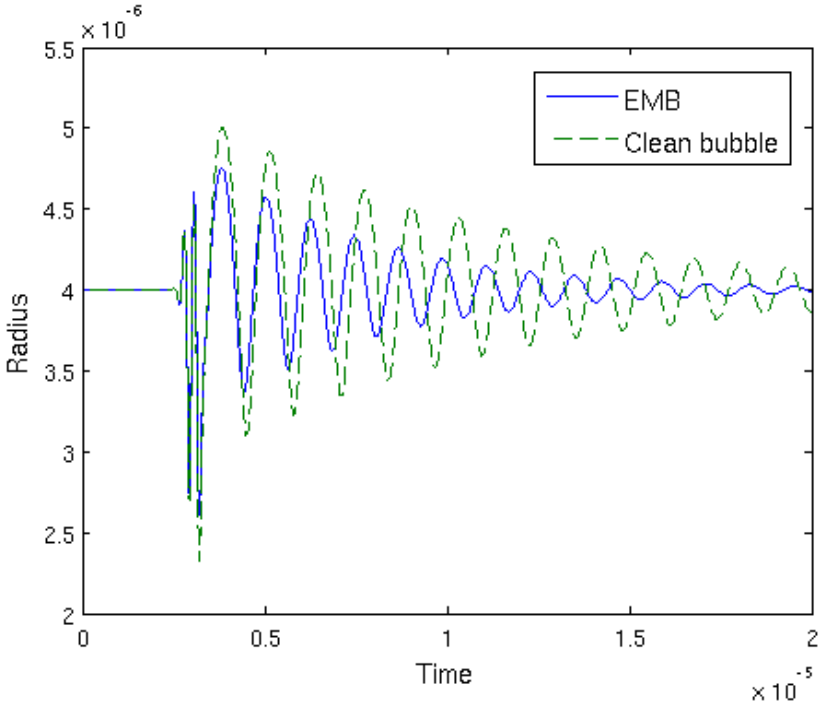

Figure 2.17: Radius vs. time curves for an EMB and a clean bubble with $R_0 = 4\mu$m, $Re = 6.3$, $f = 4$MHz, $P_A = 2$MPa and $Re = 6.3$.

Extremely high pressures are achieved at the bubble surface in all these cases as seen in Fig. 2.18 where p_B is given by

$$p_B = \left(p_0 + \frac{2\sigma}{R_0} + \frac{2\chi}{R_0}\right)\left(\frac{R_0}{R}\right)^{3\kappa} - \frac{2\sigma}{R} - \tau_{rr}|_R + \tau_{rr}^{(sh)}|_R - \frac{2\chi}{R}\left(\frac{R_0}{R}\right)^2. \tag{2.104}$$

The very high positive pressures produced are a consequence of the bubble contents becoming highly compressed as the bubble shrinks whereas the negative pressures are caused by the growth of the bubble due to the pressure pulse forcing.

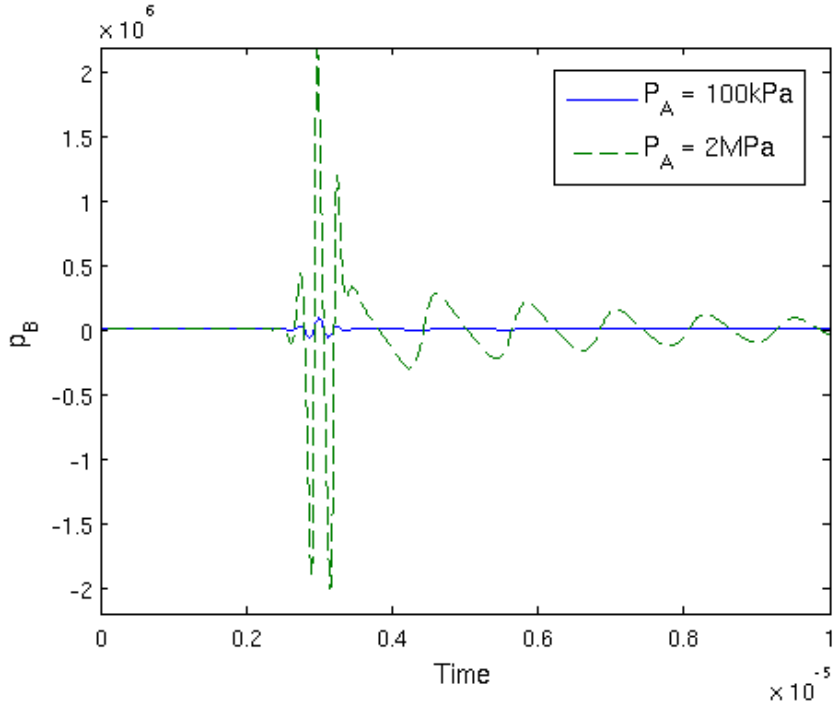

Figure 2.18: Pressure at the bubble surface for an EMB with $R_0 = 4\mu$m, $Re = 6.3$, $f = 4$MHz, $Re = 6.3$ and $P_A = 100$kPa (solid line), $P_A = 2$MPa (dashed line).

2.8 Summary and Conclusions

In this chapter the dynamics of spherically symmetric clean and encapsulated microbubbles have been investigated numerically in a range of fluids. For a clean bubble, consistent with previous studies, the viscous effects of the surrounding fluid result in dampened oscillations of the bubble radius. In both a linear Jeffreys and Oldroyd-B fluid, however, the dynamics are governed by a competition between the viscous, elastic and inertial forces. Thus for a large enough value of De the dynamics approach that of the inviscid case. An increase in fluid elasticity results in larger, slower oscillations in bubble radius with higher collapse velocities for both the Linear Jeffreys and Oldroyd-B models. The rheology of the fluid is also found to have more effect as the maximum bubble radius is decreased.

An encapsulated microbubble with shell parameters typical for an ultrasound contrast agent has been studied under the forcing of a Gaussian pulse. This approximately describes the effect of the interaction between an applied pressure field and an EMB which occurs during sonoporation and ultrasound contrast imaging. Due to the stabilising ef-

fect of the (highly viscous) shell the fluid rheology is found to affect the dynamics of an EMB much less than a similar sized, clean cavitation bubble. Pressure amplitudes in the range $50 - 200$kPa are found to produce stable, nonlinear oscillations and, for the range of frequencies typical to contrast imaging, amplitudes are foudn to increase with decreasing frequency of the pressure field. Applying higher pressure field amplitudes of the order 1GPa result in explosive growth and collapse of the EMB which in reality would ultimately lead to rupture of the shell and disintegration of the bubble.

The results provided in the chapter provide an initial indicator of the effect of fluid rheology on cavitation bubbles and encapsulated microbubbles. In reality, however, the assumption that the bubble will remain spherical is not valid for the majority of applications we are interested in. Any other bubbles or structures in the vicinity will cause asymmetries in the fluid flow which will ultimately disturb the bubble from spherically symmetric oscillations. Furthermore, it is expected that fragmentation of the bubble will occur if it is forced at a high enough amplitude which the spherical model cannot predict. To model this non-spherical behaviour a different numerical method is required. The dynamics of a non-spherical EMB are modelled in Chapter 6 using the boundary element method which is now introduced.

Chapter 3

Modelling Bubbles in an Incompressible Fluid Using the Boundary Element Method

3.1 Introduction

In this chapter, a single cavitation bubble in a semi-infinite fluid near a rigid wall is modelled using the boundary element method (BEM). To begin with an overview of previous studies on single bubble dynamics is presented with a focus on numerical modelling. A detailed description of the numerical method follows in which a new non-singular formulation of the boundary element method is presented. In this formulation the singularities in the integrals are removed at the onset rather than treated numerically, as is common practice in the standard formulation of the BEM. Finally, some results are presented detailing the effects of viscoelasticity, initial stand-off distance and surface tension on the bubble dynamics.

3.2 Previous Studies on Single Bubble Dynamics

In 1917, Rayleigh [88] developed the spherically symmetric solution for a collapsing cavitation bubble in an infinite fluid. Early theoretical work modelling a bubble near a rigid wall was based on perturbations from this solution, such as Rattray [87] and Yeh

and Yang [115] and later, Chahine and Bovis [29] who included surface tension on the bubble surface. They used matched asymptotic expansions in powers of ϵ; defined by

$$\epsilon = \frac{R_m}{h}, \tag{3.1}$$

where R_m and h are the maximum radius and distance from the centre of the bubble to the wall, respectively. This then leads to a system of differential equations that can be solved numerically. These studies, however, are only valid for small values of ϵ and thus are misleading for the cases of interest here where the bubble is near the wall ($\epsilon \approx 1$). A different theoretical study was undertaken by Naude [78] who solved the Laplace equation for the velocity potential using Legendre polynomials and extended the theory to larger perturbations.

The development of high-speed cameras has allowed accurate photographs of bubble shape, the most notable early experimental study being that of Benjamin and Ellis [8]. Their experiments involved a Perspex sheet with cavities grown from nuclei situated at various small distances from it. The main phenomena captured by their experiments was the formation of a liquid jet in the direction of the rigid wall and the subsequent transition to a toroidal form. Benjamin and Ellis also seem to have been the first to realise the importance of the Kelvin Impulse in cavitation bubble dynamics. The Kelvin Impulse is the apparent inertia of the cavitation bubble and can be used to determine the direction of the bubble centroid and liquid jet [14].

Another notable study was that of Lauterborn and Bolle [63] who measured jet velocities up to 120m/s for a bubble near a solid plate and observed a small counterjet away from the boundary due to the bubble being driven towards the wall during collapse.

Early numerical methods included the Marker and Cell method, used by Mitchell et al. [76], allowing them to consider later stages of collapse than possible with the perturbation techniques mentioned previously. The first fully numerical paper for describing the complete collapse of a cavitation bubble near a rigid wall was by Plesset and Chapman [85]. A finite difference method was used, based on cylindrical coordinates with the velocity potential determined from boundary conditions at the surfaces and at infinity. Their model predicted the jet formation found by previous experimental studies; in particular, demonstrating a remarkable agreement with the experiments of Lauterborn and Bolle [63].

3.2.1 Boundary Element Method

The first use of the Boundary Element Method to model a cavitation bubble was that of Guerri, Lucca and Prosperetti [49]. This was developed in the work of Blake, Taib and Doherty [18, 19] where a single, axisymmetric, vapour filled cavitation bubble near a rigid boundary and free surface were considered, respectively. The authors neglected surface tension as well as viscous forces, the latter being justified by the high velocities as well as the small boundary layers present confining the viscous forces to the immediate proximity of the stress-free bubble surface. Thus the fluid was assumed to be inviscid as well as incompressible and the flow irrotational. Buoyancy forces, however, were included to allow them to independently vary the ambient pressure field around the bubble and investigate its influence on the growth and collapse of the bubble. Simulations were carried out for various initial stand-off distances from the nearby surface as well as varying buoyancy forces showing that the rigid wall always attracts the cavitation bubble due to the Bjerknes effect. This effect can be either overcome or aided by these buoyancy effects. Their simulations also showed the expected formation of a liquid jet and were able to continue their simulations until this jet impacted the opposite side of the bubble wall, in agreement with experimental observations, with the authors postulating that the final collapsed state of the bubble would be two toroidal bubbles of opposite circulation. Other conclusions to result from this study were the importance of the initial location of the bubble, the growth phase and the relative strength of buoyancy forces on the following collapse phase.

Since the publication of these initial papers, there have been a plethora of further studies using the BEM to model cavitation bubbles. The reason for the success of the method is the computational speed and the remarkable agreements with experiments even though many features of the problem are neglected (such as the viscous and compressible effects of the fluid). This accuracy has often been attributed to the fact that the bubble collapse is inertia dominated. An early development of the theory was the inclusion of non-condensible bubble contents to model explosion bubbles by Best and Kucera [11]. These contents were modelled using an adiabatic gas law; the bubble pressure p_i being given by

$$p_i = p_{vapour} + p_{g0}\left(\frac{V_0}{V}\right)^{\lambda}, \tag{3.2}$$

where p_{g0} is the (partial) gas pressure. Furthermore, the surface was discretised using cubic splines (rather than the isoparametric approximation used by Blake et al. [18])

following the work of Dommermuth and Yue [38]. This discretisation allows a very accurate representation of the bubble surface and has been utilised in many subsequent works, such as that of Lind and Phillips [67].

Bubbles Near Other Boundaries

Another development of the Boundary Element Method for bubbles has been the inclusion of other types of nearby surfaces and their effect on the dynamics of the bubble. Most common, perhaps, has been that of a free surface; with some of the first studies being undertaken by Dommermuth and Yue [38] and Blake et al. [19]. The results in these papers showed the formation of a free surface jet as well as a liquid jet penetrating the bubble with the direction of fluid motion and fluid jet again being determined by the magnitude of buoyancy forces, with good agreement with the results of Blake and Gibson [16]. Another difference found between the case of a rigid wall and a free surface is the importance of the growth phase of the bubble in the latter case, due to the resulting distortion of the free surface.

A cavitation bubble near an elastic membrane has also been modelled in detail by Klaseboer and Khoo [57] and later by Turangun et al. [101]. In their model the bubble is situated in a fluid, separated from another fluid by an elastic membrane. Boundary conditions on the membrane are used to find the normal velocities and pressure differences thereon and the boundary integral equation is then solved to find the velocity at the bubble surface and interface. The foremost dynamics predicted (which are not present for a bubble near a non-elastic wall), were the formation of a mushroom-shaped bubble and the splitting of the bubble into two smaller parts. These phenomena are caused by the elasticity of the second fluid pushing the bubble back when it is near maximum volume causing a perturbation that propagates over the bubble surface. This has a significance in biomedicine since a cell wall can be modelled as an elastic membrane. The interaction between a microbubble and a cell wall is particulary relevant to sonoporation which is discussed in Chapter 1.

Viscous and Viscoelastic Fluids

So far all the numerical works mentioned have assumed that the fluid surrounding the bubble can be modelled as being inviscid. As discussed in detail by Batchelor [5], for inertia dominated phenomena such as bubble collapse and jet formation, shear viscous

effects are only important in thin boundary layers near surfaces and thus the bulk viscosity of the fluid can often be neglected. Also, the bubble surface is shear stress-free and generates little vorticity resulting in a flow within the boundary layer which is approximately irrotational [5]. Therefore, the viscous or viscoelastic effects of the surrounding fluid can be introduced through the normal stress boundary condition at the bubble surface as a good approximation.

An example of this are the two papers by Boulton-Stone [21, 22] which focused on a gas bubble bursting at a free surface and considered a boundary layer at high Reynolds numbers. This boundary layer was modelled as a perturbation on the irrotational velocity field and the inclusion of a tangential surface stress condition. Similarly Rush and Nadim [90] included the effects of a viscous Newtonian fluid on a freely oscillating drop by modifying the normal stress balance boundary condition at the bubble surface. A similar treatment of viscoelastic effects was undertaken by Lind and Phillips [68] for a vapour filled spherical bubble in a fluid modelled using the Material Maxwell model.

3.2.2 Experimental Work

As already mentioned, one of the early experimental studies on cavitation dynamics was performed by Benjamin and Ellis [8] who, amongst other things, observed the formation of liquid jets first postulated by Kornfeld and Suvorov [61]. Since then significant developments have been made in experiments allowing more stable conditions and more numerous and clear measurements. An example of this is the advent of 'single-bubble cavitation' where a single, acoustically driven bubble is isolated and studied under specific and well-defined experimental conditions. Many recent experimental studies have also focused on conditions specific to applications such as shock wave lithotripsy or sonoporation.

There have also been many recent studies investigating sonoluminescence; the emission of short bursts of light resulting from the extreme temperatures and pressures achieved during bubble compression. For example Flannigan and Suslick [40] studied Xenon and Argon bubbles in sulphuric acid and found temperatures as high as 15000 Kelvin were produced over very short time scales during bubble collapse. Gaitan et al. [44] produced experimental radius-time curves for single bubbles pulsating at large amplitudes and observed the light emission originating at the centre of the bubble.

Although there has been a significant improvement in the experimental observations of

cavitation bubbles in recent years, there are still measurements such as radial velocity, temperature and pressure values at minimum radii which have not been achieved due to the small distances and time scales involved. Consequently, detailed comparisons between numerical calculations and experimental observations are not very common, although some measures such as jet velocities and pressures are possible as well as qualitative descriptions of bubble shape.

3.2.3 Other Numerical Methods

It is noted that other numerical methods such as finite elements, finite volumes and spectral methods have also been used to model the growth and collapse of bubbles. For example, a spectral method was used by Lind and Phillips [66] employing the full compressible equations of motion in two dimensions. These equations are solved on a fixed Eulerian grid with the two phases modelled using a marker particle method. They found good qualitative agreement between this spectral method and previous BEM studies on the effects of viscoelasticity on bubble dynamics. Similar behaviour was found in both schemes, including increased amplitude oscillations with increasing Deborah and Weber numbers and jet prevention. Arguably the spectral method contains a more complete description of the physics of the problem but it is computationally much more expensive. The BEM is computationally fast and requires little memory since it is only the boundary that needs to be discretised rather than the whole domain. Furthermore, the bubble surface is a true discontinuity in pressure/density in the BEM model while not being well-defined in the spectral method.

Although the boundary element method makes a large number of assumptions (some of which may not seem to be completely justified) the method produces results in good qualitative agreement with more complicated models and experimental findings. Due to this and its computational efficiency it remains the predominant method used to simulate small numbers of bubbles in a variety of situations.

3.3 Method Description

The boundary element method is now described in detail and applied to an initially spherical, gas-filled bubble in a viscoelastic fluid. A non-singular formulation of the boundary integral equation with a quintic spline discretisation of the surface is derived.

A number of assumptions are made in the numerical method employed in this chapter; the motivation behind these and their validity are now discussed.

3.3.1 Assumptions

1. The bubble remains axisymmetric for all time. The bubble is initially spherical and it is assumed that the bubble remains axisymmetric for all time, effectively reducing the dimensions of the problem by one (see Fig. 3.1). Inherent in this is the assumption that the bubble is stable to distortions from this symmetry and, although not always the case, this is generally found to be true for small cavitation bubbles [23]. Furthermore, the axisymmetric case can be seen as providing the instance of maximum jet speeds and pressures and thus is an indicator of maximum potential damage to nearby surfaces.

2. The fluid is assumed to be incompressible. As will be described in detail later, a boundary integral formulation of the Laplace equation is used to find the velocity at the bubble surface. In order to formulate a velocity potential, ϕ, which solves the Laplace equation, it is necessary to assume incompressibility. The primary condition needed in order for this approximation to be valid can be shown to be [5]

$$\frac{U^2}{c^2} << 1, \tag{3.3}$$

   where c is the speed of sound in the liquid and U is the magnitude of variations of the fluid velocity with respect to both position and time. The ratio $\frac{U}{c}$ is known as the Mach-number and is reasonable to assume incompressibility if $\frac{U^2}{c^2} < 0.2$. As noted by Brujan [25] in the late stages of collapse when a jet forms the bubble wall velocities can approach the speed of sound meaning that the condition (3.3) does not hold and liquid compressibility can no longer be ignored. These high velocities also give rise to very large pressures in the fluid. Nevertheless, to begin with we impose incompressibility in order to describe the standard BEM for bubbles. A modification to the BEM to allow the effects of weak compressibility is summarised in Chapter 7.

3. The effects of fluid rheology are non-negligible only in thin boundary layers near the bubble surface and thus can be approximately modelled through a boundary condition at the bubble interface. It is known [5] that, for most cases, viscous effects are only important in thin boundary layers and so can be considered in

this way and we follow previous work such as [6,67] and extend this consideration to viscoelasticity. This is confirmed later in the chapter by comparing the BEM results for a spherical bubble with the direct solutions computed in Chapter 2.

3.3.2 Governing Equations and Boundary Conditions

This chapter focuses on a single, initially spherical bubble situated at an initial stand-off distance h above a rigid wall, as represented schematically by Fig. 3.1. Due to the assumption of axisymmetry the dimension of the problem is effectively reduced from three to two. Since the bubble surface is symmetric about the z-axis it is also convenient to model only one half of the surface.

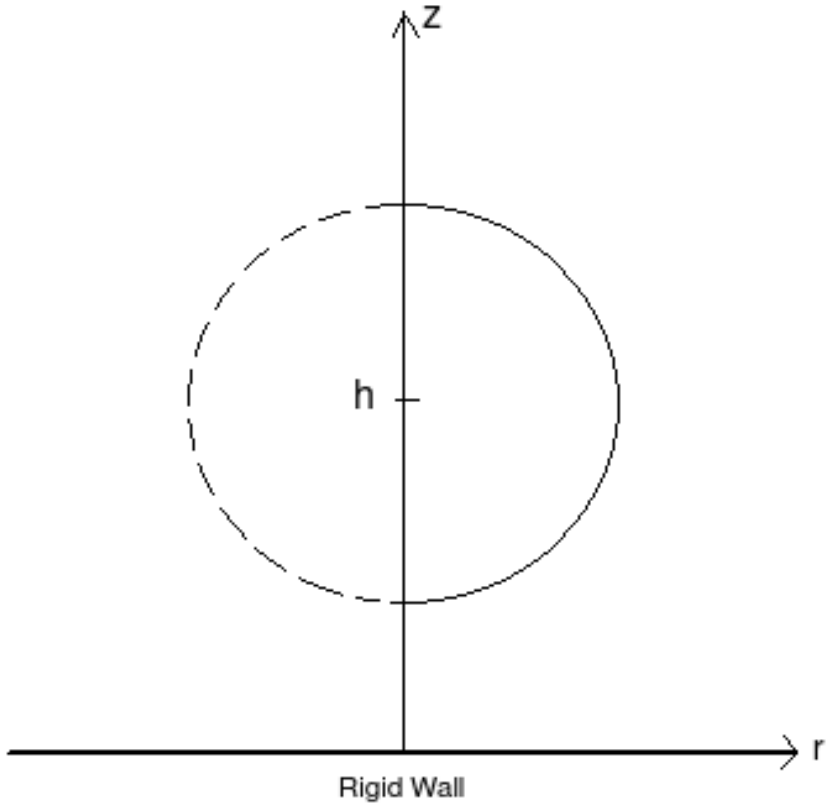

Figure 3.1: A single bubble at a distance h from a rigid wall.

The three basic independent dynamic laws for the fluid (and thus the bubble) are the continuity equation, the momentum equation and the internal energy equation, [116].

The continuity and momentum equations are given by Eqs. (3.4) and (3.5), respectively

$$\frac{\mathrm{D}\rho}{\mathrm{D}t} + \rho\nabla\cdot\mathbf{u} = 0, \tag{3.4}$$

$$\rho\frac{\mathrm{D}\mathbf{u}}{\mathrm{D}t} = \rho\mathbf{f} + \nabla\cdot\boldsymbol{\pi}, \tag{3.5}$$

where ρ is the fluid density, $\mathbf{u}$ is the fluid velocity field, $\mathbf{f}$ contains the body forces and $\boldsymbol{\pi}$ is the stress tensor. The internal energy equation is ignored since there is no heat or mass transfer through the boundary and the temperature is assumed to be constant. The stress tensor (for an incompressible fluid) can be regarded as the sum of an isotropic part and a remaining anisotropic part with the components given by

$$\pi_{ij} = -p\delta_{ij} + \tau_{ij}, \tag{3.6}$$

where τ_{ij} denotes the components of the deviatoric or extra stress tensor $\boldsymbol{\tau}$. So in the absence of body forces the momentum equation becomes

$$\rho\frac{\mathrm{D}\mathbf{u}}{\mathrm{D}t} = -\nabla p + \nabla\cdot\boldsymbol{\tau}, \tag{3.7}$$

(as mentioned in Chapter 2 gravity is neglected for the moment since we are considering small cavitation bubbles). Since the fluid is assumed to be incompressible the fluid density ρ is constant and the continuity equation reduces to the constraint

$$\nabla\cdot\mathbf{u} = 0. \tag{3.8}$$

The assumption of irrotationality results in the curl of the velocity vanishing, thus implying the existence of a velocity potential $\nabla\phi = \mathbf{u}$. Substituting this into Eq. (3.8) it can be seen that this potential satisfies Laplace's equation in the fluid domain

$$\nabla^2\phi = 0, \tag{3.9}$$

while the momentum Eq. (3.5) becomes

$$\rho\left(\frac{\partial}{\partial t}(\nabla\phi) + \nabla\phi\cdot\nabla(\nabla\phi)\right) = -\nabla p + \nabla\cdot\boldsymbol{\tau} \tag{3.10}$$

or, since the operators commute

$$\nabla\left(\rho\frac{\partial\phi}{\partial t}+\frac{\rho}{2}|\nabla\phi|^2+p\right)=\nabla\cdot\boldsymbol{\tau}. \tag{3.11}$$

Eq. (3.11) can be integrated to give an irrotational equation of motion provided that

$$\nabla\cdot\boldsymbol{\tau}=\nabla\varphi\Longleftrightarrow\nabla\times(\nabla\cdot\boldsymbol{\tau})=0, \tag{3.12}$$

is satisfied for some scalar function φ. In general, $\nabla\times(\nabla\cdot\boldsymbol{\tau})$ is non-zero and will produce a 'torque' generating vorticity and thus most constitutive equations are not compatible with the assumption that $\nabla\times\mathbf{u}=0$ (see [56]). In this case, however, due to the fact that the viscoelastic effects are only introduced through the boundary conditions, it has been assumed that the bulk viscosity is negligible and thus

$$\nabla\cdot\boldsymbol{\tau}=0\Rightarrow\nabla\times\nabla\cdot\boldsymbol{\tau}=0. \tag{3.13}$$

Eq. (3.12) is then satisfied for any constant φ and Eq. (3.11) is integrated to give

$$\rho\frac{\partial\phi}{\partial t}+\frac{\rho}{2}|\nabla\phi|^2+p-\varphi=C(t), \tag{3.14}$$

for some function $C(t)$. In fact, $C(t)$ can be found by noting that ϕ,$\varphi\to0$ as $t\to\infty$ giving $C(t)=p_\infty$; the (undisturbed) pressure at infinity. Then, evaluating (3.14) at the bubble surface

$$\begin{aligned}p_B&=-\rho\frac{\partial\phi}{\partial t}-\frac{\rho}{2}|\nabla\phi|^2+p_\infty\\&=-\rho\left(\frac{\partial\phi}{\partial t}+|\nabla\phi|^2\right)+\frac{\rho}{2}|\nabla\phi|^2+p_\infty\\&=-\rho\frac{\mathrm{D}\phi}{\mathrm{D}t}+\frac{\rho}{2}|\nabla\phi|^2+p_\infty\end{aligned} \tag{3.15}$$

where p_B is the pressure on the liquid side of the bubble surface, φ has been taken to be zero and $\mathrm{D}/\mathrm{D}t$ is the material derivative. Since it has been assumed there is no mass transfer through the bubble surface, balancing the normal forces across the surface gives

$$\begin{aligned}\pi_{nn}(\text{liquid})=-p_B+\tau_{nn}&=\pi_{nn}(\text{gas})+\sigma C,\\&=-p_i+\sigma C\end{aligned} \tag{3.16}$$

where σ is the (static) surface tension, C is the curvature and p_i is the internal bubble pressure. Note that Eq. (3.16) also assumes the bubble interface is 'clean' (no surfactants present) and only the normal component is required since the bubble interface is a stress-free free surface. Finally, combining (3.15) and (3.16) to eliminate p_B then gives the following equation which will be used to update the velocity potential ϕ

$$\rho \frac{\mathrm{D}\phi}{\mathrm{D}t} = \frac{\rho}{2}|\nabla\phi|^2 - \tau_{nn} + \sigma C + p_\infty - p_i. \tag{3.17}$$

The bubble surface must also be updated in time. Since the bubble surface is stress-free, fluid particles which begin on the surface will remain there and thus the surface can be updated in a Lagrangian manner

$$\frac{\mathrm{D}\mathbf{x}}{\mathrm{D}t} = \nabla\phi, \tag{3.18}$$

where $\mathbf{x}$ is a point on the surface. The bubble contents are modelled as in Eq. (2.2) (with $p_v = 0$) using

$$p_i(t) = p_0 \left(\frac{R_0}{R} \right)^{3\kappa}. \tag{3.19}$$

Eqs. (3.17) - (3.19) comprise the set of equations which are integrated in time to update the system. To do this, however, the velocities $\nabla\phi$ must be calculated and a constitutive equation chosen for τ_{nn}.

3.3.3 Boundary Integral Equation

In order to integrate Eqs. (3.17,3.18) and advance them in time, the variables $\nabla\phi$ and τ_{nn} are required. To find $\nabla\phi$, use is made of the fact that the potential satisfies Laplace's Eq. (3.9). Using Green's third identity, ϕ can be defined in terms of a boundary integral equation

$$c(\mathbf{p})\phi(\mathbf{p}) = \int_{\partial\Omega} \left(\frac{\partial\phi}{\partial n}(\mathbf{q}) G(\mathbf{p},\mathbf{q}) - \phi(\mathbf{q}) \frac{\partial G}{\partial n}(\mathbf{p},\mathbf{q}) \right) dS, \tag{3.20}$$

where $c(\mathbf{p})$ is given by

$$c(\mathbf{p}) = \begin{cases} 2\pi & \text{if } \mathbf{p} \in \partial\Omega \\ 4\pi & \text{if } \mathbf{p} \in \Omega \backslash \partial\Omega, \end{cases}$$

and Ω, $\partial\Omega$ are the fluid domain and its boundary, respectively. The constant $c(\mathbf{p})$ arises from the integral over a small region surrounding the singularity of the Green's function

G; for a point on the boundary $\partial\Omega$ this region is a semicircle rather than a circle giving the value 2π rather than 4π. Here $\mathbf{p}$ and $\mathbf{q}$ are points in the fluid and on the boundary, respectively and can be written in cylindrical polar coordinates as

$$\mathbf{p} = (r_0, 0, z_0), \quad \mathbf{q} = (r, \theta, z). \tag{3.21}$$

Note that the second component of $\mathbf{p}$ can be taken to be zero without loss of generality due to the axisymmetry of the problem. In cartesian coordinates these become

$$\mathbf{p} = (r_0, 0, z_0), \quad \mathbf{q} = (r\cos\theta, r\sin\theta, z). \tag{3.22}$$

In an infinite fluid the Green's function is the fundamental solution to Laplace's equation [97] which is (in three dimensions)

$$G_1(\mathbf{p}, \mathbf{q}) = \frac{1}{\mid \mathbf{p} - \mathbf{q} \mid}. \tag{3.23}$$

In the case of a bubble situated near a rigid wall the domain of integration $\partial\Omega$ includes the wall. In order to simplify the integral to be only over the bubble surface a modified Green's function is used, given by

$$G(\mathbf{p}, \mathbf{q}) = G_1(\mathbf{p}, \mathbf{q}) + G_2(\mathbf{p}, \mathbf{q}) = \frac{1}{\mid \mathbf{p} - \mathbf{q} \mid} + \frac{1}{\mid \mathbf{p}' - \mathbf{q} \mid}, \tag{3.24}$$

where $\mathbf{p}' = (r_0, 0, -z_0)$ is the image point of $\mathbf{p}$ (reflected in the rigid wall). It can be seen by differentiating Eq. (3.20) that this modified Green's function results in ϕ satisfying the no penetration condition

$$\frac{\partial \phi}{\partial z} = 0 \quad \text{at} \quad z = 0, \tag{3.25}$$

and alleviates the need to integrate over the rigid wall. Substituting the cartesian forms of $\mathbf{p}$ and $\mathbf{q}$ into G_1 results in

$$\begin{aligned} G_1(\mathbf{p}, \mathbf{q}) &= \frac{1}{[(r_0 - r\cos\theta)^2 + r^2\sin^2\theta + (z_0 - z)^2]^{1/2}} \\ &= \frac{1}{[(r + r_0)^2 + (z - z_0)^2 - 4rr_0\cos^2(\frac{\theta}{2})]^{1/2}}, \end{aligned} \tag{3.26}$$

with a normal derivative

$$\begin{aligned}\frac{\partial G_1}{\partial n} &= \nabla G_1 \cdot \mathbf{n} \\ &= \frac{-(r - r_0\cos\theta)n_r - (z - z_0)n_z}{[(r + r_0)^2 + (z - z_0)^2 - 4rr_0\cos^2(\frac{\theta}{2})]^{3/2}},\end{aligned} \tag{3.27}$$

where the normal vector is $\mathbf{n} = (n_r, 0, n_z)$. Similar expressions exist for the second term G_2 with z_0 replaced by $-z_0$.

In the standard BEM formulation the normal velocities are found using the following steps

1. The bubble surface is split into N segments with $N + 1$ nodes, resulting in a discretised form of Eq. (3.20)
2. The integrals over each segment are approximated using numerical quadrature.
3. If an integral over a segment contains the collocation point then a weak logarithmic singularity occurs. Since the solution is well-behaved on the boundary this is a result of the mathematical formulation and must be dealt with. Typically this is done by splitting a necessary integral into a singular and non-singular part; the latter is then calculated using a log-Gaussian quadrature rule (see, for example, [97]).
4. The resulting matrix system is then solved for the unknown velocities.

In this chapter the method of Klaseboer et al. [96] is applied to formulate a non-singular version of the boundary integral equation in which the singularities are removed analytically at the onset without generating any additional unknowns.

3.3.4 Non-Singular Formulation

Following Klaseboer et al. [96], in order to remove the singularities from the boundary integral equation the following variables are defined for $i = 1, \ldots, N + 1$

$$\psi_i(\mathbf{p}) = \phi(\mathbf{p}_i) + \left(\frac{\partial\phi}{\partial n}\right)_i f_i(\mathbf{p}), \tag{3.28}$$

where the functions f_i are constructed to satisfy the following conditions

$$\nabla^2 f_i(\mathbf{p}) = 0, \quad f_i(\mathbf{p}_i) = 0, \quad \frac{\partial f_i}{\partial n}(\mathbf{p}_i) = 1. \tag{3.29}$$

Here the points $\mathbf{p}_i$ are the nodes on the bubble surface which has been discretised as shown in Fig. 3.2.

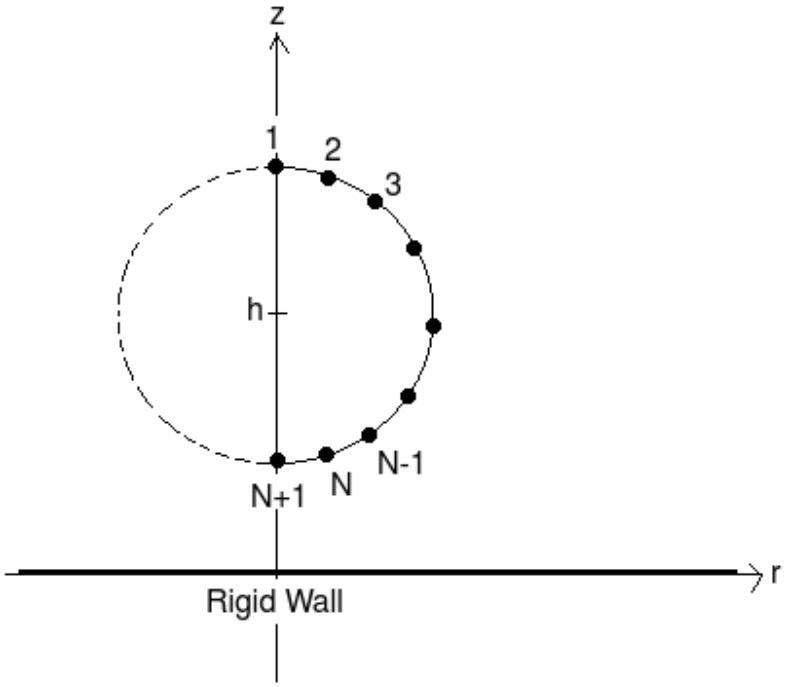

Figure 3.2: Discretisation of the bubble surface.

The variables ψ_i are constructed to satisfy Laplace's equation and consequently can also be written in terms of a boundary integral equation

$$c(\mathbf{p}_i)\psi_i(\mathbf{p_i}) + \int_S \psi_i(\mathbf{q})\frac{\partial G}{\partial n}(\mathbf{p}_i, \mathbf{q})dS = \int_S \frac{\partial \psi_i}{\partial n}(\mathbf{q})G(\mathbf{p}_i, \mathbf{q})dS. \tag{3.30}$$

Subtracting Eq. (3.30) from (3.20) gives the following, modified integral equation

$$\begin{aligned}\int_S \left[\phi(\mathbf{q}) - \phi(\mathbf{p}_i) - \left(\frac{\partial \phi}{\partial n}\right)_i f_i(\mathbf{q})\right]\frac{\partial G}{\partial n}(\mathbf{p}_i, \mathbf{q})dS \\ = \int_S \left[\frac{\partial \phi}{\partial n}(\mathbf{q}) - \left(\frac{\partial \phi}{\partial n}\right)_i \frac{\partial f_i}{\partial n}(\mathbf{q})\right] G(\mathbf{p}_i, \mathbf{q})\end{aligned} \tag{3.31}$$

where $(\frac{\partial \phi}{\partial n})_i$ is the velocity at node i. Moving the unknowns to the right-hand side

results in

$$\int_S \left[\phi(\mathbf{q}) - \phi(\mathbf{p}_i)\right] \frac{\partial G}{\partial n}(\mathbf{p}_i, \mathbf{q}) dS = \int_S \frac{\partial \phi}{\partial n}(\mathbf{q}) G(\mathbf{p}_i, \mathbf{q}) + \left(\frac{\partial \phi}{\partial n}\right)_i \int_S \left(f_i(\mathbf{q}) \frac{\partial G}{\partial n}(\mathbf{p}_i, \mathbf{q}) - \frac{\partial f_i}{\partial n}(\mathbf{q}) G(\mathbf{p}_i, \mathbf{q}) \right) dS. \tag{3.32}$$

Choosing the functions f_i

In general, any functions f_i can be used provided they satisfy the conditions given in Eq. (3.29). In an infinite domain, with no wall present, if we assume they are of the form $A + (B \times G)$ (where G is the fundamental solution of Laplace's equation) then the conditions (3.29) lead to [96]

$$f_i(\mathbf{p}) = \frac{|\mathbf{p}_i - \mathbf{p}_D|^2}{\mathbf{n}_i \cdot (\mathbf{p}_i - \mathbf{p}_D)} \left(1 - \frac{|\mathbf{p}_i - \mathbf{p}_D|^2}{|\mathbf{p} - \mathbf{p}_D|^2}\right). \tag{3.33}$$

The constant vector $\mathbf{p}_D$ can be any point located outside the domain provided that $\mathbf{n}_i \cdot (\mathbf{p}_i - \mathbf{p}_D) \neq 0$. In order to ensure ψ_i are axisymmetric functions, the point $\mathbf{p}_D$ is chosen to be located on the z-axis; $\mathbf{p}_D = (0, 0, z_D)$. This ensures that f_i is constant in θ and can be taken out of the azimuthal integral over the bubble surface.

For the case of a bubble near a rigid wall the following condition must also be satisfied to ensure no integration over the wall is necessary

$$\frac{\partial f_i}{\partial z} = 0 \text{ at } z = 0. \tag{3.34}$$

This, along with the conditions given in Eq. (3.29), leads to the following form for f_i (details of which are given in Appendix C)

$$f_i(\mathbf{p}) = \frac{-\rho_i^3 \bar{\rho}_i^3}{\bar{\rho}_i^3 \sigma_i + \rho_i^3 \bar{\sigma}_i} \left[\left(\frac{1}{\rho} - \frac{1}{\rho_i}\right) + \left(\frac{1}{\bar{\rho}} - \frac{1}{\bar{\rho}_i}\right) \right], \tag{3.35}$$

where

$$\rho \equiv \sqrt{r^2 + (z - z_D)^2}, \;\; \bar{\rho} \equiv \sqrt{r^2 + (z + z_D)^2} \;\; \sigma \equiv r n_r + (z - z_D) n_z, \;\; \bar{\sigma} \equiv r n_r + (z + z_D) n_z, \tag{3.36}$$

and the suffix i indicates evaluation at $(r, 0, z) = (r_i, 0, z_i)$.

It was found during simulations that care must be taken with the choice of z_D; since for

certain values of z_D the term $\bar{\rho}_i^3\sigma_i + \rho_i^3\bar{\sigma}_i$ in f_i can be very small leading to numerical problems. During jet formation one side of the bubble accelerates towards the other causing nodes 1 and $N+1$ (which are on the axis) to be very close together. This severely restricts the possible choices of z_D and it was found that instabilities did occur during bubble collapse. A solution to this problem was found by considering the point $\mathbf{p}_D = (0, 0, z_D)$ to be *inside* the domain (in the fluid). This of course results in the functions f_i (and thus ψ_i) possessing a singularity at the point $\mathbf{p}_D$. This can be removed in a similar manner in which the singularity in G is removed in Eq. (3.20). In this case both $\mathbf{p}_D$ and $\mathbf{p}_i$ are surrounded by very small spheres of radius ϵ and from Green's second identity

$$\int_{\Omega-\Omega_\epsilon-\Omega_\epsilon^D} \left(\psi_i \nabla^2 G - G\nabla^2\psi_i\right) dA = \int_{\Gamma-\Gamma_\epsilon-\Gamma_\epsilon^D} \left(\psi_i \frac{\partial G}{\partial n} - G\frac{\partial \psi_i}{\partial n}\right) d\Gamma, \tag{3.37}$$

where $\Omega_\epsilon, \Omega_\epsilon^D$ are the spheres surrounding $\mathbf{p}_i$ and $\mathbf{p}_D$, respectively and $\Gamma_\epsilon, \Gamma_\epsilon^D$ the corresponding boundaries of these spheres. Since G and ψ satisfy Laplace's equation everywhere except at $\mathbf{p}_i$ and $\mathbf{p}_D$, respectively, the left hand side of Eq. (3.37) is clearly zero. The integration over Γ_ϵ yields the term $c(\mathbf{p}_i)\phi(\mathbf{p}_i)$ and

$$\int_{\Gamma_\epsilon^D} \left(\psi_i \frac{\partial G}{\partial n} - G\frac{\partial \psi_i}{\partial n}\right) d\Gamma =$$
$$\lim_{\epsilon\to 0} \int_{\varphi=0}^{\pi}\int_{\theta=0}^{2\pi} \left\{ \left[\phi_i + \left(\frac{\partial\phi}{\partial n}\right)_i f_i\right] \frac{\partial G}{\partial n}(\mathbf{p}_i, \mathbf{p}) - \left(\frac{\partial\phi}{\partial n}\right)_i \frac{\partial f_i}{\partial n} G(\mathbf{p}_i, \mathbf{p}) \right\} \epsilon^2 \sin(\varphi) d\theta d\varphi. \tag{3.38}$$

Around the point $\mathbf{p}_D$ the singular parts of f_i and $\partial f_i/\partial n$ behave as B/ϵ and $-B/\epsilon^2$, respectively (where B is given in Appendix C). Thus the singular term in f_i as well as all non-singular terms vanish as $\epsilon \to 0$ and we are left with

$$\int_{\Gamma_\epsilon^D} \left(\psi_i \frac{\partial G}{\partial n} - G\frac{\partial \psi_i}{\partial n}\right) d\Gamma = 4\pi \frac{\rho_i^3\bar{\rho}_i^3}{\bar{\rho}_i^3\sigma_i + \rho_i^3\bar{\sigma}_i} G(\mathbf{p}_i, \mathbf{p}_D) \left(\frac{\partial\phi}{\partial n}\right)_i, \tag{3.39}$$

with, finally, the new integral equation for ψ_i for the case of $\mathbf{p}_D$ in the domain

$$c(\mathbf{p}_i)\psi_i(\mathbf{p_i}) + \int_S \psi_i(\mathbf{q}) \frac{\partial G}{\partial n}(\mathbf{p}_i, \mathbf{q}) dS = \int_S \frac{\partial \psi_i}{\partial n}(\mathbf{q}) G(\mathbf{p}_i, \mathbf{q}) dS$$
$$-4\pi \frac{\rho_i^3\bar{\rho}_i^3}{\bar{\rho}_i^3\sigma_i + \rho_i^3\bar{\sigma}_i} G(\mathbf{p}_i, \mathbf{p}_D) \left(\frac{\partial\phi}{\partial n}\right)_i. \tag{3.40}$$

Note that in general a different point $\mathbf{p}_D(i)$ can be chosen for each node if required to avoid any numerical difficulties.

Discretised Equations

Using the discretisation of the bubble surface, the integral over the surface is approximated as a sum of integrals over each segment. Eq. (3.32) is then

$$\sum_{j=1}^{N}\int_{s_j}^{s_{j+1}}\Big(\phi(s)-\phi(\mathbf{p}_i)\Big)\beta_i(s)ds+S_\infty^{(1)}=\sum_{j=1}^{N}\int_{s_j}^{s_{j+1}}\frac{\partial\phi}{\partial n}(s)\alpha_i(s)ds$$
$$+\left(\frac{\partial\phi}{\partial n}\right)_i\Big[\sum_{j=1}^{N}\int_{s_j}^{s_{j+1}}f_i(s)\beta_i(s)ds-\sum_{j=1}^{N}\int_{s_j}^{s_{j+1}}\frac{\partial f_i}{\partial n}(s)\alpha_i(s)ds+S_\infty^{(2)}\Big],$$
$$-4\pi\frac{\rho_i^3\bar{\rho}_i^3}{\bar{\rho}_i^3\sigma_i+\rho_i^3\bar{\sigma}_i}G(\mathbf{p}_i,\mathbf{p}_D)\left(\frac{\partial\phi}{\partial n}\right)_i \tag{3.41}$$

where the final term is only present if $\mathbf{p}_D$ is in the domain and $S_\infty^{(1)}, S_\infty^{(2)}$ are the non-zero integrals over the 'surface at infinity'

$$S_\infty^{(1)}=-\phi(\mathbf{p}_i)\int_{S_\infty}\frac{\partial G}{\partial n}(\mathbf{p}_i,\mathbf{q})dS,\quad S_\infty^{(2)}=\frac{\rho_i^2\bar{\rho}_i^3+\rho_i^3\bar{\rho}_i^2}{\bar{\rho}_i^3\sigma_i+\rho_i^3\bar{\sigma}_i}\int_{S_\infty}\frac{\partial G}{\partial n}(\mathbf{p}_i,\mathbf{q})dS \tag{3.42}$$

As $\mathbf{q}\to\infty$ we have $G\to 1/r$ and $\partial G/\partial n\to -1/(r^2)$. It follows then that

$$\int_{S_\infty}\frac{\partial G}{\partial n}(\mathbf{p}_i,\mathbf{q})dS=\lim_{r\to\infty}\int_0^\pi\int_0^{2\pi}\left(\frac{-1}{r^2}\right)r^2\sin\varphi\mathrm{d}\theta\mathrm{d}\varphi$$
$$=-2\pi\int_0^\pi\sin(\varphi)\mathrm{d}\varphi=-4\pi. \tag{3.43}$$

Note that when the rigid wall is present there will be a contribution from both G_1 and G_2. However, since the fluid domain is now semi-infinite the surface at infinity becomes half a sphere and thus the extra terms $S_\infty^{(1)}$ and $S_\infty^{(2)}$ remain the same as for the infinite fluid. The terms $\alpha_i(s)$ and $\beta_i(s)$ are the azimuthal integrals

$$\alpha_i(s)=\int_0^{2\pi}G_1(\mathbf{p}_i,s)r(s)d\theta,\quad \beta_i(s)=\int_0^{2\pi}\frac{\partial G_1}{\partial n}(\mathbf{p}_i,s)r(s)d\theta, \tag{3.44}$$

Following the calculations of Taib [97], the following expressions are used to evaluate these integrals

$$Ia=\int_0^{2\pi}\frac{d\theta}{(1-k^2\cos^2\frac{\theta}{2})^{3/2}}=\frac{4E(k)}{1-k}, \tag{3.45}$$

$$Ib=\int_0^{2\pi}\frac{\cos\theta\ d\theta}{(1-k^2\cos^2\frac{\theta}{2})^{3/2}}=\left(\frac{8}{k}-4\right)\frac{E(k)}{1-k}-\frac{8}{k}K(k), \tag{3.46}$$

where $K(k)$ and $E(k)$ are the complete elliptic integrals of the first and second kind, respectively. Expressions for $\alpha_i(s)$ and $\beta_i(s)$ can then be found

$$\alpha_i = \int_0^{2\pi} G_1(\mathbf{p}_i, s) r(s) d\theta = \frac{4r(s)K(k)}{M}, \tag{3.47}$$

$$\begin{aligned}\beta_i = \int_0^{2\pi} \frac{\partial G_1}{\partial n}(\mathbf{p}_i, s) r(s) d\theta &= -\frac{r(s)}{M^3}\left\{ r\frac{dz}{ds}Ia - r_i\frac{dz}{ds}Ib - \frac{dr}{ds}(z - z_i)Ia \right\}, \\ &= -\frac{4r(s)}{M^3}\left(\left[\frac{dz}{ds}(r + r_i - \frac{2r_i}{k}) - \frac{dr}{ds}(z - z_i) \right] \frac{E(k)}{1-k} + \frac{2r_i}{k}\frac{dz}{ds}K(k) \right),\end{aligned} \tag{3.48}$$

where the following quantities have been defined

$$M = \sqrt{(r(s) + r_i)^2 + (z(s) - z_i)^2}, \quad k(s) = \frac{4r(s)r_i}{M^2}. \tag{3.49}$$

Using results from [51], the complete elliptic integrals can be approximated by,

$$K(k) \approx P(x) - Q(x)\ln(x), \tag{3.50}$$

$$E(k) \approx R(x) - S(x)\ln(x), \tag{3.51}$$

where $x = 1 - k^2(s)$ and P, Q, R and S are tabulated polynomials.

If we assume the velocities vary approximately linearly over each segment Eq. (3.41) becomes

$$\begin{aligned}\sum_{j=1}^{N} E_{ij} + 4\pi\phi_i = \sum_{j=1}^{N} \left(B_{ij}\frac{\partial\phi}{\partial n}(s_j) + C_{ij}\frac{\partial\phi}{\partial n}(s_{j+1}) \right) + \\ \left(\frac{\partial\phi}{\partial n}\right)_i \left[\sum_{j=1}^{N}(A_{ij} - D_{ij}) - 4\pi\frac{\rho_i^2\bar{\rho}_i^3 + \rho_i^3\bar{\rho}_i^2}{\bar{\rho}_i^3\sigma_i + \rho_i^3\bar{\sigma}_i} - 4\pi\frac{\rho_i^3\bar{\rho}_i^3}{\bar{\rho}_i^3\sigma_i + \rho_i^3\bar{\sigma}_i}G(\mathbf{p}_i, \mathbf{p}_D) \right]\end{aligned} \tag{3.52}$$

where

$$A_{ij} = \int_{s_j}^{s_{j+1}} f_i(s)\beta_i(s)ds, \tag{3.53}$$

$$B_{ij} = \int_{s_j}^{s_{j+1}} \left(\frac{s_{j+1}-s}{s_{j+1}-s_j}\right)\alpha_i(s)ds, \tag{3.54}$$

$$C_{ij} = \int_{s_j}^{s_{j+1}} \left(\frac{s-s_j}{s_{j+1}-s_j}\right)\alpha_i(s)ds, \tag{3.55}$$

$$D_{ij} = \int_{s_j}^{s_{j+1}} \frac{\partial f_i}{\partial n}(s)\alpha_i(s)ds, \tag{3.56}$$

$$E_{ij} = \int_{s_j}^{s_{j+1}} \Big(\phi(s)-\phi_i\Big)\beta_i(s)ds. \tag{3.57}$$

Eq. (3.52) for $i = 1, \ldots, N+1$ is a system of $N+1$ equations which can be solved for the velocities $\partial\phi/\partial n$ at the nodes on the bubble surface. The system can be written in matrix form as

$$\mathbf{h} = \mathbf{G}\mathbf{v}, \tag{3.58}$$

where $\mathbf{v}$ is the vector of velocities. It can be seen from Eqs. (3.53) - (3.57) and (3.59) that the singularities present in the original BEM are now suppressed by the terms $(\phi(s)-\phi_i)$, f_i and $\partial f_i/\partial n$. Consequently, a simple Gaussian quadrature can be used over the whole bubble surface. On the diagonal of matrix G the term G_{ii} $(i \neq 1, N+1)$ is

$$\begin{aligned} G_{ii} &= \sum_{j=1}^{N}\Big(A_{ij}-D_{ij}\Big) + B_{ii} + C_{i,i-1} - 8\pi\frac{\rho_i^2\bar{\rho}_i^3+\rho_i^3\bar{\rho}_i^2}{\bar{\rho}_i^3\sigma_i+\rho_i^3\bar{\sigma}_i} \\ &= \sum_{j=1}^{N} A_{ij} - \sum_{j\neq i,i-1} D_{ij} + \int_{s_i}^{s_{i+1}}\left(\frac{s_{i+1}-s}{s_{i+1}-s_i} - \frac{\partial f_i}{\partial n}(s)\right)\alpha_i(s)ds \\ &+ \int_{s_{i-1}}^{s_i}\left(\frac{s-s_{i-1}}{s_i-s_{i-1}} - \frac{\partial f_i}{\partial n}(s)\right)\alpha_i(s)ds - 8\pi\frac{\rho_i^2\bar{\rho}_i^3+\rho_i^3\bar{\rho}_i^2}{\bar{\rho}_i^3\sigma_i+\rho_i^3\bar{\sigma}_i}. \end{aligned} \tag{3.59}$$

The singularities of $\alpha_i(s_i)$ are suppressed in the above integrals since the terms in brackets tend to zero as we approach s_i. The non-singular nature of the integrals has been proven in [58] using linear functions for f_i.

Cubic and Quintic Splines

The functions ϕ and $\frac{\partial \phi}{\partial n}$ are known at the nodes on the bubble surface but, in addition to this, the values of these functions at intermediate points between the nodes must be found in order to approximate the integrals in (3.53) - (3.57). Previous works such as [62] have used linear elements and assumed ϕ and its normal derivative were linear on each segment. In order to more accurately represent the surface variables we follow the work of Lind and Phillips [67] and use splines. Spline interpolation is desirable since it provides similar results to higher order polynomial interpolation without the problem of Runge's phenomenon. In [67], cubic splines were used so that in each segment (s_i, s_{i+1}) the variables are represented by a third order polynomial

$$q_i(s) = a_i(s - s_i)^3 + b_i(s - s_i)^2 + c_i(s - s_i) + d_i, \tag{3.60}$$

for some set of constants (a_i, b_i, c_i, d_i), $i = 1, \ldots, N$. In order to increase the accuracy of the discretisation and decrease any errors which may arise, quintic splines are now considered. Using these, the variables are represented in each segment (s_i, s_{i+1}) by a fifth order polynomial

$$q_i(s) = \bar{a}_i(s - s_i)^5 + \bar{b}_i(s - s_i)^4 + \bar{c}_i(s - s_i)^3 + \bar{d}_i(s - s_i)^2 + \bar{e}_i(s - s_i) + \bar{f}_i, \tag{3.61}$$

for some set of constants $(\bar{a}_i, \bar{b}_i, \bar{c}_i, \bar{d}_i, \bar{e}_i, \bar{f}_i)$, for $i = 1, \ldots, N$, the details of which are given later in this chapter.

3.3.5 Calculating the Extra Stress Tensor

For a Newtonian fluid the extra stress tensor is given by

$$\boldsymbol{\tau} = \mu\dot{\gamma} = \mu\bigg((\nabla \mathbf{u}) + (\nabla \mathbf{u})^T\bigg) = 2\mu(\nabla \mathbf{u}), \tag{3.62}$$

since the assumption of irrotationality implies the velocity gradient is symmetric [5]. The required normal component τ_{nn} is then

$$\tau_{nn} = 2\mu\frac{\partial^2 \phi}{\partial n^2}. \tag{3.63}$$

A summary of some common viscoelastic models is given in Chapter 2. In this chapter

the Oldroyd-B model is chosen since it is complicated enough to model a range of rheological behaviour while still being relatively simple to implement. For the Oldroyd-B model the polymeric stress $\boldsymbol{\tau}$ can be written as

$$\boldsymbol{\tau} = \boldsymbol{\tau}^s + \boldsymbol{\tau}^p, \tag{3.64}$$

$$\boldsymbol{\tau}^s = 2\eta_s \nabla \mathbf{u}, \tag{3.65}$$

$$\boldsymbol{\tau}^p + \lambda_1 \overset{\nabla}{\boldsymbol{\tau}^p} = 2\eta_p \nabla \mathbf{u}, \tag{3.66}$$

where η_s,η_p and λ_1 are the solvent viscosity, polymeric viscosity and relaxation time of the fluid, respectively and the velocity $\mathbf{u}$ will be written in terms of the potential ϕ.

3.3.6 Updating the System in Time

The following equations have been derived to update the bubble surface as well as the velocity potential thereon

$$\frac{\mathrm{D}\mathbf{x}}{\mathrm{D}t} = \nabla\phi, \tag{3.67}$$

$$\rho\frac{\mathrm{D}\phi}{\mathrm{D}t} = \frac{\rho}{2}|\nabla\phi|^2 - \tau_{nn} + \sigma C + p_\infty - p_0\left(\frac{V_0}{V}\right)^\kappa, \tag{3.68}$$

where $\nabla\phi$ is found from Laplace's equation, as described in section 3.3.4. For a Newtonian fluid the expression (3.63) is substituted directly into (3.68). For an Oldroyd-B fluid the set of governing equations become

$$\frac{\mathrm{D}\mathbf{x}}{\mathrm{D}t} = \nabla\phi, \tag{3.69}$$

$$\rho\frac{\mathrm{D}\phi}{\mathrm{D}t} = \frac{\rho}{2}|\nabla\phi|^2 - 2\eta_s\frac{\partial^2\phi}{\partial n^2} - \tau^p_{nn} + \sigma C + p_\infty - p_0\left(\frac{V_0}{V}\right)^\kappa, \tag{3.70}$$

$$\lambda_1\frac{\mathrm{D}\tau^p_{nn}}{\mathrm{D}t} = -\tau^p_{nn} - 2\lambda_1\tau^p_{nn}\frac{\partial^2\phi}{\partial n^2} - 2\eta_p\frac{\partial^2\phi}{\partial n^2} \tag{3.71}$$

In this case an extra equation for the stress (3.71) must be solved simultaneously with the equations for the position and potential of each node.

Non-Dimensionalisation

The non-dimensionalisation of the problem is performed in a similar manner to Chapter 2

$$r^* = \frac{r}{R_m}, \quad z^* = \frac{z}{R_m} \tag{3.72}$$

$$t^* = \frac{U}{R_m}t = \frac{t}{R_m}\left(\frac{P_{ref}}{\rho}\right)^{1/2} \tag{3.73}$$

$$\phi^* = \frac{\phi}{UR_m} = \frac{\phi}{R_m}\left(\frac{\rho}{P_{ref}}\right)^{1/2} \tag{3.74}$$

where R_m is the maximum bubble radius attained by a single gas bubble in an inviscid infinite fluid and $U = (P_{ref}/\rho)^{1/2}$ is used as a characteristic velocity. The pressure term $p_\infty = P_{ref} = 100$kPa is atmospheric pressure. The relevant non-dimensionalised equations for the Newtonian and Oldroyd-B cases are presented in Table 3.1.

Table 3.1: Non-dimensionalised equations

Newtonian Fluid
$\frac{\mathrm{D}\mathbf{x}^*}{\mathrm{D}t^*} = \nabla\phi^*$ $\frac{\mathrm{D}\phi^*}{\mathrm{D}t^*} = 1 + \frac{1}{2} \mid \nabla\phi^* \mid^2 - \frac{2}{Re}\frac{\partial^2\phi^*}{\partial n^{*2}} + \frac{C}{We} - \varepsilon\left(\frac{\bar{V}_0}{V}\right)^{3\kappa}$
Oldroyd-B Fluid
$\frac{\mathrm{D}\mathbf{x}^*}{\mathrm{D}t^*} = \nabla\phi^*,$ $\frac{\mathrm{D}\phi^*}{\mathrm{D}t^*} = 1 + \frac{1}{2} \mid \nabla\phi^* \mid^2 - \frac{2E}{Re}\frac{\partial^2\phi^*}{\partial n^{*2}} - \tau_{nn}^{p^*} + \frac{C}{We} - \varepsilon\left(\frac{\bar{V}_0}{V}\right)^{3\kappa}$ $\frac{\mathrm{D}\tau_{nn}^{p^*}}{\mathrm{D}t} = \frac{1}{De}\left[- \tau_{nn}^{p^*} - 2\left(De\tau_{nn}^{p^*} + \frac{(1-E)}{Re}\right)\frac{\partial^2\phi^*}{\partial n^{*2}}\right]$

Here, $E = \eta_s/\eta$ and De, Re and We are the Deborah, Reynolds and Weber numbers, respectively, defined by

$$De = \frac{\lambda_1}{R_m}\left(\frac{P_{ref}}{\rho}\right)^{1/2}, \quad Re = \frac{R_m((P_{ref})\rho)^{1/2}}{\eta}, \quad We = \frac{\rho U^2 R_m}{\sigma} = \frac{R_m P_{ref}}{\sigma}. \tag{3.75}$$

Note that for $E = 0$ the Oldroyd-B equations reduce to those valid for an Upper-Convected Maxwell fluid. To update the system in time the relevant set of equations are integrated using a fourth-order Runge-Kutta time stepping scheme. The time step used (following [18]) is chosen to be

$$\triangle t = \frac{\triangle t_{\max}}{\max(\mathrm{D}\phi^*/\mathrm{D}t)}, \tag{3.76}$$

where the value of $\triangle t_{\max}$ is taken to be 10^{-3}, unless otherwise stated. The reason for this choice of time step is to deal with the rapidly changing velocity that can occur during bubble collapse; for large velocities the time step will become small in order to capture the high speed dynamics of the bubble.

Redistribution and Smoothing of Nodes

As the bubble surface evolves in time saw-tooth instabilities can occur due to the numerical modelling of the surface. To reduce this unphysical behaviour a smoothing scheme is applied as is standard procedure in Lagrangian methods. The method of Lundgren and Mansour is chosen [69] which computes the smoothed function $\bar{f}$ using the following five-point formula

$$\frac{\partial f}{\partial t} = -\lambda \frac{\partial^4 f}{\partial s^4}, \tag{3.77}$$

$$\bar{f}_i = f_i - \lambda\Big(f_{i-2} - 4f_{i-1} + 6f_i - 4f_{i+1} + f_{i+2}\Big), \tag{3.78}$$

for the variables $f = \varphi, \tau_{nn}, r$ and z. Note that although ϕ is discontinuous at nodes $1/N + 1$ the variables $f = \varphi, \tau_{nn}, r$ and z are all continuous in space and thus the smoothing can be applied near the discontinuity using the nodes either side.

This smoothing is applied periodically, unless otherwise stated every 20 time steps, and in addition to this the nodes are redistributed using the splines every time step to be evenly spaced with respect to arclength. This prevents 'bunching up' of nodes and the

resulting numerical instabilities.

3.3.7 Derivation of Quintic Splines

The constants $\bar{a}_i, \ldots, \bar{f}_i$ from Eq. (3.61) are found by enforcing continuity of the spline function as well as continuity of its derivatives at each node $\mathbf{p}_i$, thus ensuring the bubble surface is smooth. For quintic splines the continuity conditions are, for $i = 1, ..., N-1$

- $q_i(s_{i+1}) = q_{i+1}(s_{i+1})$
- $q_i^{(1)}(s_{i+1}) = q_{i+1}^{(1)}(s_{i+1})$,
- $q_i^{(2)}(s_{i+1}) = q_{i+1}^{(2)}(s_{i+1})$,
- $q_i^{(3)}(s_{i+1}) = q_{i+1}^{(3)}(s_{i+1})$,
- $q_i^{(4)}(s_{i+1}) = q_{i+1}^{(4)}(s_{i+1})$,

In terms of the constants $\bar{a}_i, \ldots, \bar{f}_i$ these continuity conditions can be written as

$$\bar{f}_i + \bar{e}_i h_i + \bar{d}_i h_i^2 + \bar{c}_i h_i^3 + \bar{b}_i h_i^4 + \bar{a}_i h_i^5 = \bar{f}_{i+1}, \tag{3.79}$$

$$\bar{e}_i + 2\bar{d}_i h_i + 3\bar{c}_i h_i^2 + 4\bar{b}_i h_i^3 + 5\bar{a}_i h_i^4 = \bar{e}_{i+1}, \tag{3.80}$$

$$2\bar{d}_i + 6\bar{c}_i h_i + 12\bar{b}_i h_i^2 + 20\bar{a}_i h_i^3 = 2\bar{d}_{i+1}, \tag{3.81}$$

$$6\bar{c}_i + 24\bar{b}_i h_i + 60\bar{a}_i h_i^2 = 6\bar{c}_{i+1}, \tag{3.82}$$

$$24\bar{b}_i + 120\bar{a}_i h_i = 24\bar{b}_{i+1}, \tag{3.83}$$

where $h_i = s_{i+1} - s_i$ for $i = 1, \ldots, N$.

The system of Eqs. (3.79 - 3.83) is now transformed into two systems of equations for the unknowns $\bar{b}_i$ and $\bar{d}_i$. Substituting Eq. (3.83) into Eq. (3.81) to eliminate $\bar{a}_i$ gives

$$3\bar{c}_i = \frac{1}{h_i}\Big(\bar{d}_{i+1} - \bar{d}_i\Big) - 2h_i\Big(\bar{b}_{i+1} + 2\bar{b}_i\Big). \tag{3.84}$$

Combining this with Eq. (3.82) to eliminate $\bar{c}_i$ yields

$$2h_{i+1}\bar{b}_{i+2} + 4\Big(h_{i+1} + h_i\Big)\bar{b}_{i+1} + 2h_i\bar{b}_i = \frac{1}{h_{i+1}}\bar{d}_{i+2} - \left(\frac{1}{h_{i+1}} + \frac{1}{h_i}\right)\bar{d}_{i+1} + \frac{1}{h_i}\bar{d}_i. \tag{3.85}$$

The other system of equations is found by substituting Eq. (3.84) into (3.79) to find $\bar{e}_i$ and substituting this into (3.80) gives

$$\frac{-7h_{i+1}^3}{15}\bar{b}_{i+2} - \frac{8}{15}\Big(h_{i+1}^3 + h_i^3\Big)\bar{b}_{i+1} - \frac{7h_i^3}{15}\bar{b}_i + \frac{h_{i+1}}{3}\bar{d}_{i+2} + \frac{2}{3}\Big(h_{i+1} + h_i\Big)\bar{d}_{i+1} + \frac{h_i}{3}\bar{d}_i$$

$$= \frac{1}{h_{i+1}}\Big(\bar{f}_{i+2} - \bar{f}_{i+1}\Big) - \frac{1}{h_i}\Big(\bar{f}_{i+1} - \bar{f}_i\Big). \tag{3.86}$$

The above equations are valid for $i = 1, \ldots, N-1$. To close the system, boundary conditions are required at the end points.

Natural and Clamped Boundary Conditions

Different boundary conditions are required for different variables defined on the bubble surface depending on whether they are even or odd about the axis of symmetry. For natural splines the even derivatives are zero at the end points which in the case of quintic splines is

$$q_1^{(2)}(s_1) = q_N^{(2)}(s_{N+1}) = 0, \tag{3.87}$$

$$q_1^{(4)}(s_1) = q_N^{(4)}(s_{N+1}) = 0. \tag{3.88}$$

In terms of the constants to be found these become

$$\bar{d}_1 = \bar{d}_{N+1} = 0, \tag{3.89}$$

$$\bar{b}_1 = \bar{b}_{N+1} = 0, \tag{3.90}$$

respectively.

On the other hand for clamped quintic splines the conditions are

$$q_1^{(1)}(s_1) = q_N^{(1)}(s_{N+1}) = 0, \tag{3.91}$$

$$q_1^{(3)}(s_1) = q_N^{(3)}(s_{N+1}) = 0, \tag{3.92}$$

which, after some manipulation of Eqs. (3.79-3.83) can be written as

$$2h_1\Big(\bar{b}_2 + 2\bar{b}_1\Big) = \frac{1}{h_1}\Big(\bar{d}_2 - \bar{d}_1\Big), \tag{3.93}$$

$$2h_N\left(2\bar{b}_{N+1}+\bar{b}_N\right)=-\frac{1}{h_N}\left(\bar{d}_{N+1}-\bar{d}_N\right), \tag{3.94}$$

$$-\frac{h_1^3}{15}\left(7\bar{b}_2+8\bar{b}_1\right)+\frac{h_1}{3}\left(\bar{d}_2+2\bar{d}_1\right)=\frac{1}{h_1}\left(\bar{f}_2-\bar{f}_1\right), \tag{3.95}$$

$$-\frac{h_N^3}{15}\left(8\bar{b}_{N+1}+7\bar{b}_N\right)+\frac{h_N}{3}\left(2\bar{d}_{N+1}+\bar{d}_N\right)=\frac{1}{h_N}\left(\bar{f}_{N+1}-\bar{f}_N\right). \tag{3.96}$$

Eqs. (3.85) and (3.86) along with either the natural or clamped boundary conditions derived can be written as two matrix systems

$$A\bar{\mathbf{b}}=B\bar{\mathbf{d}}, \tag{3.97}$$

$$C\bar{\mathbf{b}}+D\bar{\mathbf{d}}=\bar{\mathbf{f}}, \tag{3.98}$$

where A, B, C and D are tridiagonal matrices and $\bar{\mathbf{b}}, \bar{\mathbf{d}}$ are vectors containing the constants $\bar{b}_i$ and $\bar{d}_i$ (for $i = 1, \ldots, N+1$).

To solve this system, Eq. (3.97) is rearranged and a matrix E defined as

$$\bar{\mathbf{b}}=A^{-1}B\bar{\mathbf{d}}=E\bar{\mathbf{d}}. \tag{3.99}$$

To find the matrix E the system $AE = B$ is solved using a tridiagonal solver. Substituting this into Eq. (3.98) gives

$$\left(CE+D\right)\bar{\mathbf{d}}=\bar{\mathbf{f}}, \tag{3.100}$$

which is solved for the vector $\bar{\mathbf{d}}$ using Gaussian elimination. Finally $\bar{\mathbf{b}} = E\bar{\mathbf{d}}$ is calculated and the other constants of (3.61) found from equations (3.79-3.83). The quintic spline is then fully determined along the bubble surface. The radial coordinate of the bubble nodes is found using the natural splines while the z-coordinate and the variables ϕ and τ_{nn} require the clamped splines.

The use of cubic splines to discretise the bubble surface has been undertaken in previous works such as [66, 67]. In particular, the full derivation of the constants $a_i, \ldots, d_i$ can be found in [66]. The process is similar to that for the quintic splines although the system to be solved is simpler due to the lower order of the polynomials involved and only requires the solution of one system of equations.

3.4 Validation

In the following section the non-singular BEM code with quintic splines presented in this chapter is compared with the cubic (singular) formulation of Lind and Phillips [66]. This cubic BEM code is validated in [66] for inviscid and viscous Newtonian fluids using comparisons with the direct solution of the Rayleigh-Plesset equation and for a void with $R_0 = 1$, $\phi_0 = 1$ to test the Laplace solver.

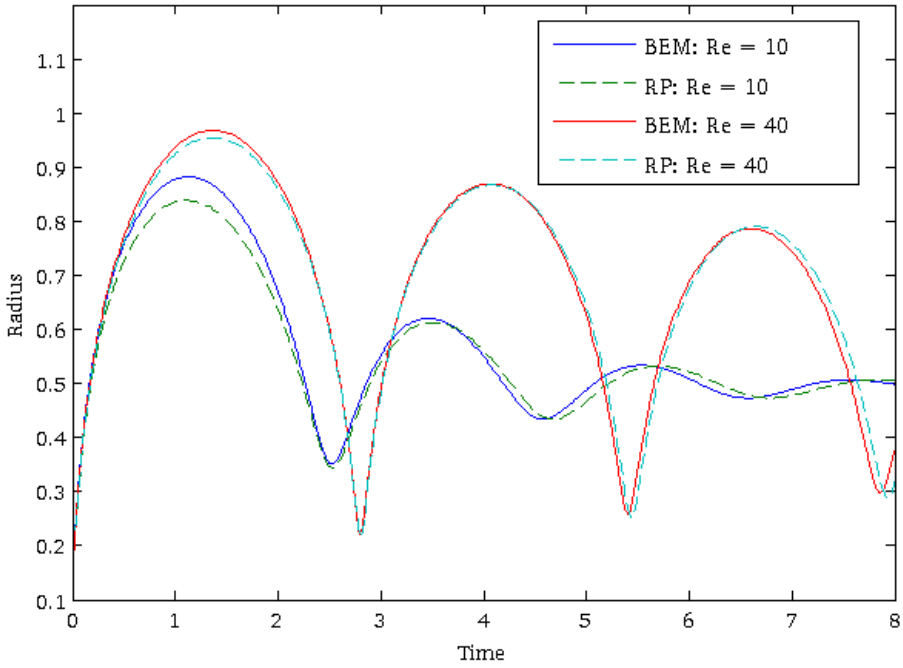

Figure 3.3: Comparisons of the quintic BEM with the direct solution of the Rayleigh-Plesset equation for an Oldroyd-B fluid with $We = 0$, $De = 0.1$ and $Re = 10$, $Re = 40$.

Fig. 3.3 shows a comparison of the quintic BEM with the direct solution of the Rayleigh-Plesset equation for a spherical bubble in an infinite UCM fluid. For both $Re = 10$ and $Re = 40$, qualitative agreement is found between the BEM model and the spherical model. The BEM model predicts slightly larger oscillations, however, and higher velocities due to the neglection of bulk viscosity.

3.5 Numerical Comparisons

Numerical comparisons are now made between the cubic, singular formulation and the new quintic, non-singular formulation presented in this chapter. The non-condensible bubble contents (3.19) cause an oscillation in the bubble which, in an infinite, inviscid fluid, causes the circumference of the (2D) bubble at its maximum size to be roughly seven times larger than that at its minimum. There are thus potential numerical problems since the bubble must be adequately resolved at large bubble volumes but the nodes must not be too close together for small bubble volumes since this causes instabilities. Through a number of different tests the aim is to make a comparison between the cubic standard BEM and the new quintic non-singular BEM. As in Chapter 2, the initial radius is found to be $R_0 = 0.165$ for the case $\varepsilon = 100$.

For the standard (singular) BEM the quintic spline and cubic spline discretisations have been compared. For a spherical oscillating bubble the maximum deviation of the nodes from the average and the error in total energy give measures of instabilities at small volume and errors at large volumes, respectively. As seen in Fig. 3.4 the quintic discretisation reduces both types of error, although the improvement is relatively small. For nonspherical collapse however (such as the toroidal bubble presented in Chapter 4) it can be argued that a greater distortion of the bubble will increase the importance of having the most accurate and stable description of the surface.

The remainder of the results in this chapter will compare the standard cubic BEM to the new method incorporating both quintic splines and the non-singular discretisation of Laplace's equation described in section 3.3.4.

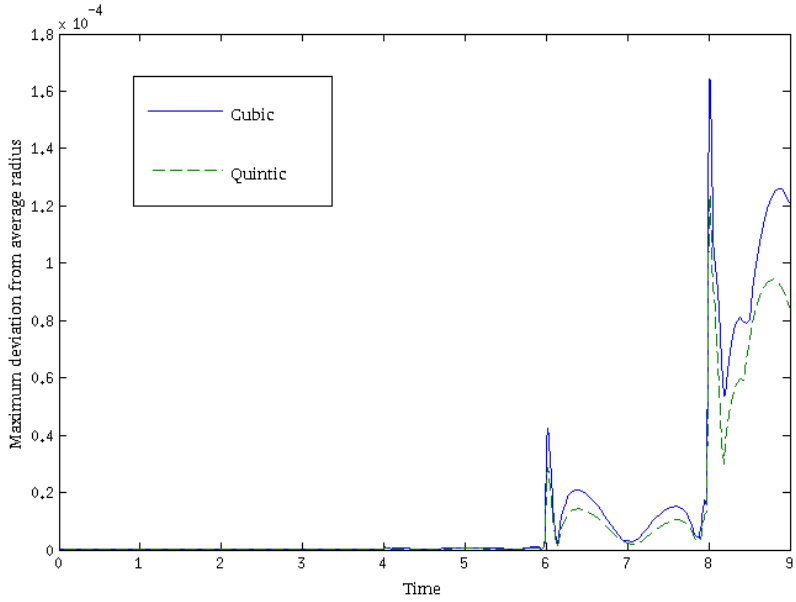

(a) Maximum deviation from average radius with smoothing every 20 time steps.

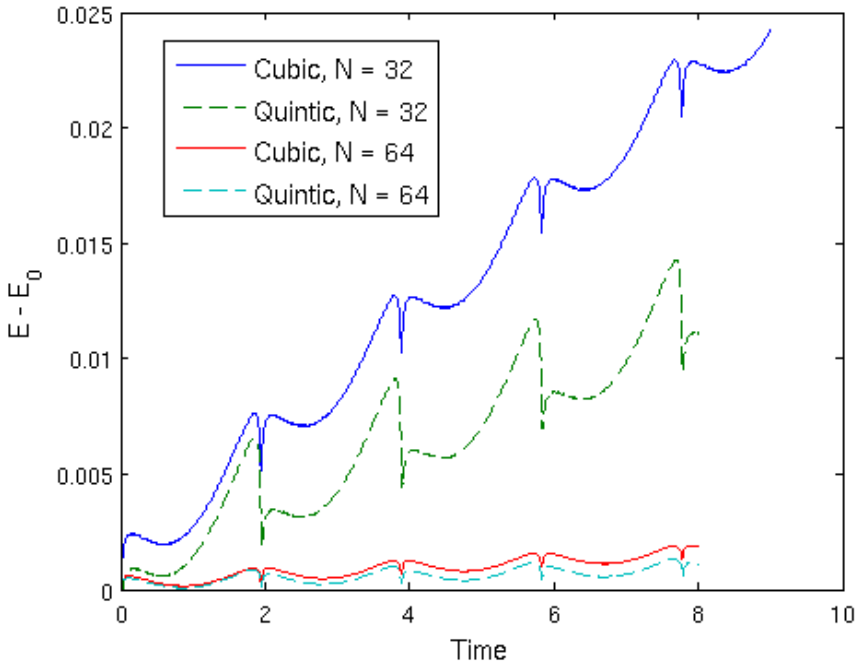

(b) Error in total energy over time for $N = 32$ and $N = 64$.

Figure 3.4: Measures of errors for the standard BEM with cubic and quintic spline discretisations for a bubble in an infinite, inviscid fluid.

Instabilities

For an initially spherical bubble in an infinite fluid (neglecting surface tension) the surface should remain spherical and thus any deviation from this arises purely from numerical errors. Thus the following quantity gives an estimate of the numerical errors

$$\max\left(r_{dev}(i)\right) = \max\left(|\mathbf{d}_i| - \sum_{i=1}^{N+1} \frac{|\mathbf{d}_i|}{N+1}\right), \tag{3.101}$$

where $|\mathbf{d}_i| = \sqrt{r_i^2 + z_i^2}$ and the bubble is centred at the origin. This is the difference between the radius at a node and the average radius of the bubble. In Fig. 3.5 this deviation is plotted against time for both the cubic standard BEM and the quintic non-singular BEM with no smoothing applied. It can be seen that the error is considerably lower for the non-singular BEM; in fact the cubic BEM code fails at roughly time = 4 (end of second oscillation) as growing instabilities cause unnaturally high velocities. The new non-singular method allows the compuations to run until the end of the fourth oscillation before it succumbs to similar problems.

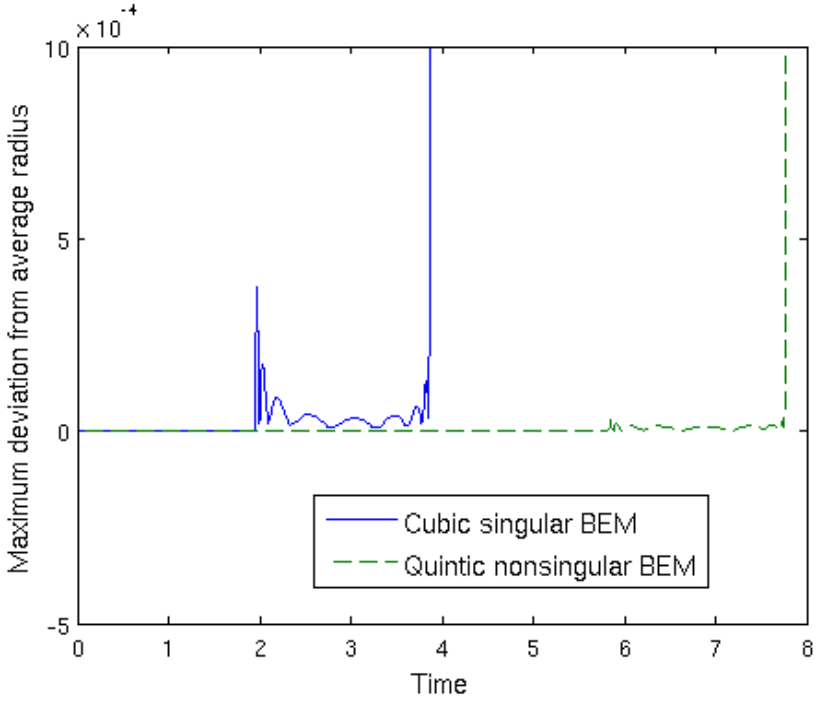

Figure 3.5: Max. deviation from average radius with no smoothing and $N = 32$.

For both cases, spikes can be seen at roughly $t = 2, 4, 6, 8$ corresponding to the bubble at minimum volume; at these instances in time the nodes are very close together and

errors arise from the influence on the observation node of the singular kernel centred at the nearby node. This is also shown in Fig. 3.6 in which the bubble surfaces close to jet impact are shown for the case $h = 1.2$, $N = 32$ and no smoothing. The singular BEM crashed due to the instabilities manifesting and causing spurious velocities whereas the non-singular formulation remains smooth and well behaved. Note that the jet will continue to form if the non-singular model is allowed to continue but has been stopped to make comparisons with the standard formulation model. Considering Figs. 3.5 and 3.6 it is clear that the non-singular BEM is clearly less succeptible to these instabilities. This agrees with the conclusions of Klaseboer et al. [96] who considered two nearly touching spheres and found numerical errors in the region where the spheres nearly touch using the standard BEM, but not for the non-singular formulation.

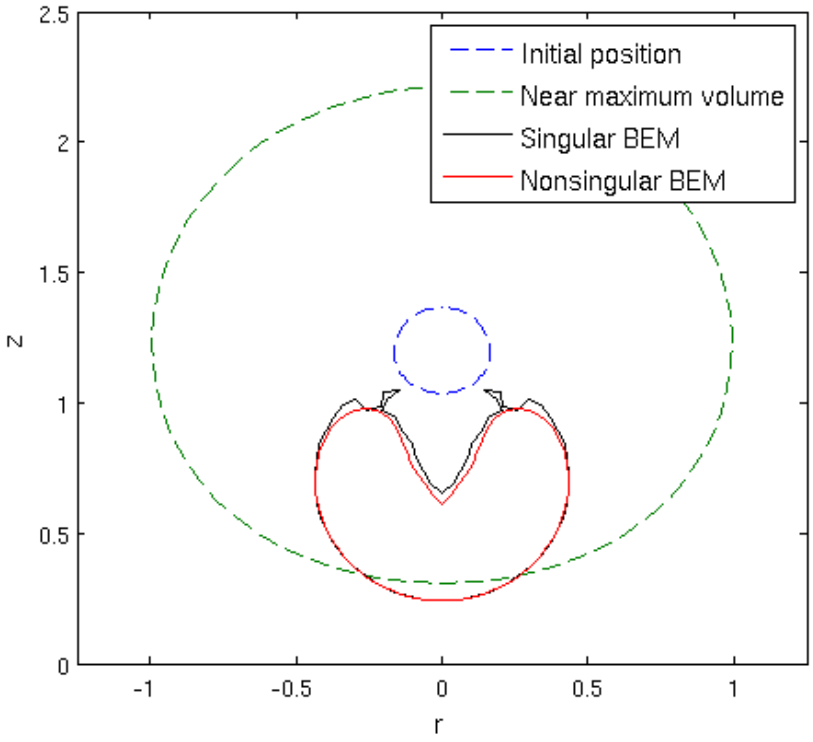

Figure 3.6: Plots of the bubble surface as a jet forms for the case $h = 1.2$ and an inviscid fluid with no smoothing applied. The solid black line shows saw-tooth instabilities occuring for the singular BEM but not for the non-singular formulation.

Energy error for a bubble near a rigid wall

For a singly connected (3D) bubble in an inviscid fluid (and neglecting buoyancy) the energy of the fluid domain is given up to a constant by [117]

$$\frac{1}{2}\int_{S_B}\phi\frac{\partial\phi}{\partial n}dS + V + \frac{\varepsilon V}{\lambda-1}\left(\frac{V_0}{V}\right)^{\lambda}, \tag{3.102}$$

where S_B is the surface of the bubble and $V = V(t)$ is the volume of the bubble. This energy should remain constant throughout the simulation since any energy loss mechanisms such as viscous dissipation are neglected, thus any change in the total energy indicates numerical error. The first term is the kinetic energy and the second and third terms are the potential energy due to the size of the bubble and its contents, respectively. Due to the axisymmetry of the bubble, the kinetic energy term becomes

$$\frac{1}{2}\int_{S_B}\phi\frac{\partial\phi}{\partial n}dS = \pi\int_{S}\phi\frac{\partial\phi}{\partial n}dS = \pi\sum_{i=1}^{N}\int_{s_i}^{s_{i+1}}\phi(s)\frac{\partial\phi}{\partial n}(s)r(s)ds, \tag{3.103}$$

where S is the two dimensional bubble surface (in the plane $(r,0,z)$), N is the number of nodes and $\phi(s)$, $\frac{\partial\phi}{\partial n}(s)$ and $r(s)$ are represented using the splines.

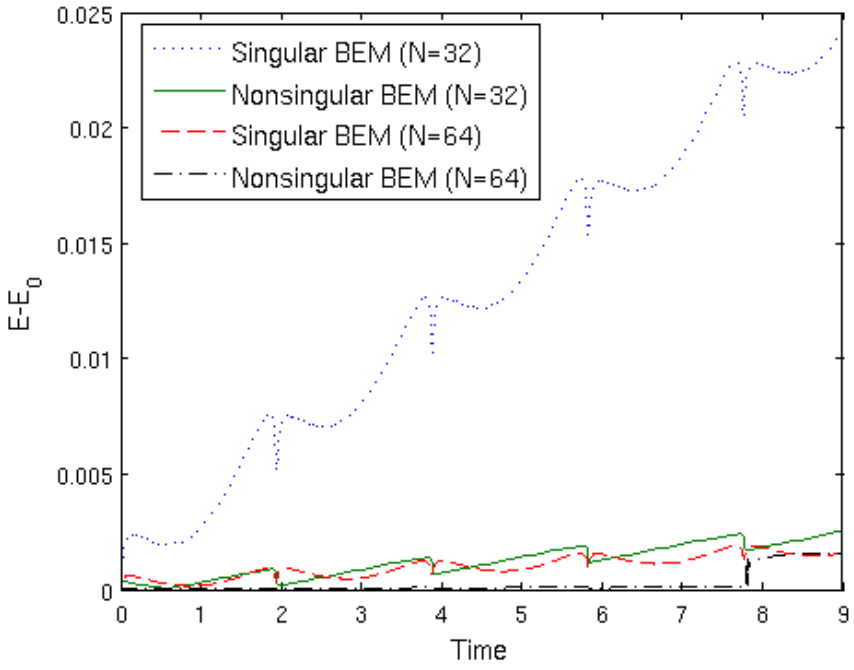

Figure 3.7: Error in total energy over time for $N = 32$ and $N = 64$.

For the cases $N = 32$ and $N = 64$ the deviation from the initial energy is plotted against time in Figure 3.7. Both cases show an increase in error during the growth phase of the bubble due to the changing position of the nodes as the arclength of the bubble surface increases. For both cases, however, the non-singular BEM clearly accumulates much less error over time with the case $N = 32$ producing errors similar to the case $N = 64$ for the standard BEM.

Computational Time

For the inviscid case and initial stand-off distance $h = 1.5$ the computation times are shown in Table 3.2 for the two BEM codes being considered. It can be seen that the quintic non-singular BEM takes roughly twice as long as the corresponding cubic case, mostly due to the extra matrix system that must be solved to find the spline coefficients. However, since using the boundary element method considerably reduces computational time compared to other numerical methods the times are still relatively small and it is argued that the increased accuracy and stability of the new method is preferred. Considering Fig. 3.7 it can also be seen that the energy error for the non-singular quintic BEM with 32 nodes is comparable to the error for the cubic BEM with 64 nodes, the new BEM code can then be considered to be faster for a given accuracy and stability.

Nodes	Cubic standard BEM	Quintic non-singular BEM
16	16.17s	37.61s
32	55.55s	108.32s
64	222.41s	385.87s

Table 3.2: Computation times from initial bubble to jet impact for the cubic standard BEM and quintic non-singular BEM.

3.6 Effects of fluid rheology, surface tension and initial position on bubble dynamics

The non-singular BEM described in this chapter is now used to simulate a gas filled bubble in an Oldroyd-B fluid near a rigid wall. For a vapour filled (constant pressure) bubble the effects of viscoelasticity have been investigated extensively by Lind and Phillips [66]. Here some results on the effects of viscoelasticity, initial stand-off distance and surface tension on an oscillating, gas-filled bubble are presented.

3.6.1 Effects of initial stand-off distance

For the inviscid case (with no surface tension) the effect of the initial stand-off distance is shown in Fig. 3.8. The pressure at the rigid wall can be seen as an indicator of potential damage caused by the cavitation bubble. In Fig. 3.8a the pressure at the centre point of the wall is plotted against time for a range of initial stand-off distances h. At $t = 0$ the initial bubble has a high internal pressure which is communicated to the wall by the incompressible fluid. The pressure then drops for the majority of the bubble growth and collapse until the final stages where the shrinking bubble volume and large jet velocities correspond to very high pressures at the wall. This second maximum in the wall pressure is found not to necessarily grow with decreasing h. Similar results were found by Wang et al. [110], who concluded than an optimal stand-off distance exists for damage to the rigid wall. The higher velocities and pressures, however, could be due to jet impact occuring at closer to minimum bubble volume for $h = 2$. Note that the final jet velocities in Fig. 3.8b correspond to dimensional values of roughly $75 - 160$m/s which are high enough to damage even metal surfaces.

The simulations are stopped when the distance between nodes 1 and $N + 1$ falls below 0.01. At this point the surface must be smoothed at the impact point and transitioned to a toroidal form; this extension of the boundary element method is considered in Chapter 4. Just prior to jet impact the pressure along the wall is plotted as a function of r in Fig. 3.9. The peak pressure occurs at the centre point (origin) due to the assumed axisymmetry of the bubble with the pressure tending to zero in either direction due to the assumed axisymmetry of the bubble.

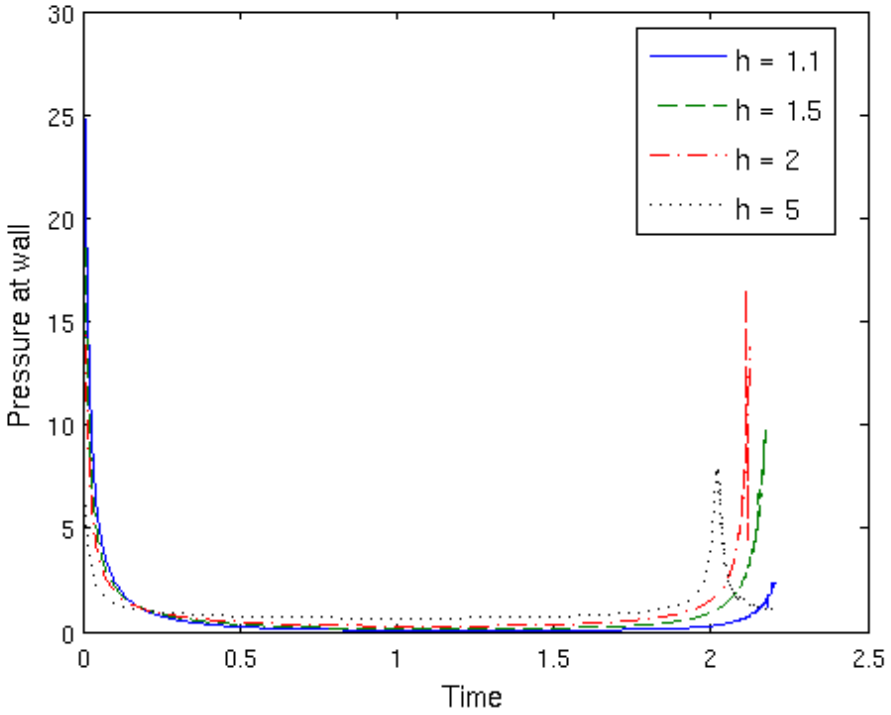

(a) Pressure at the midpoint of the wall (given as a multiple of P_{ref}) for the inviscid case and different initial stand-off distances h.

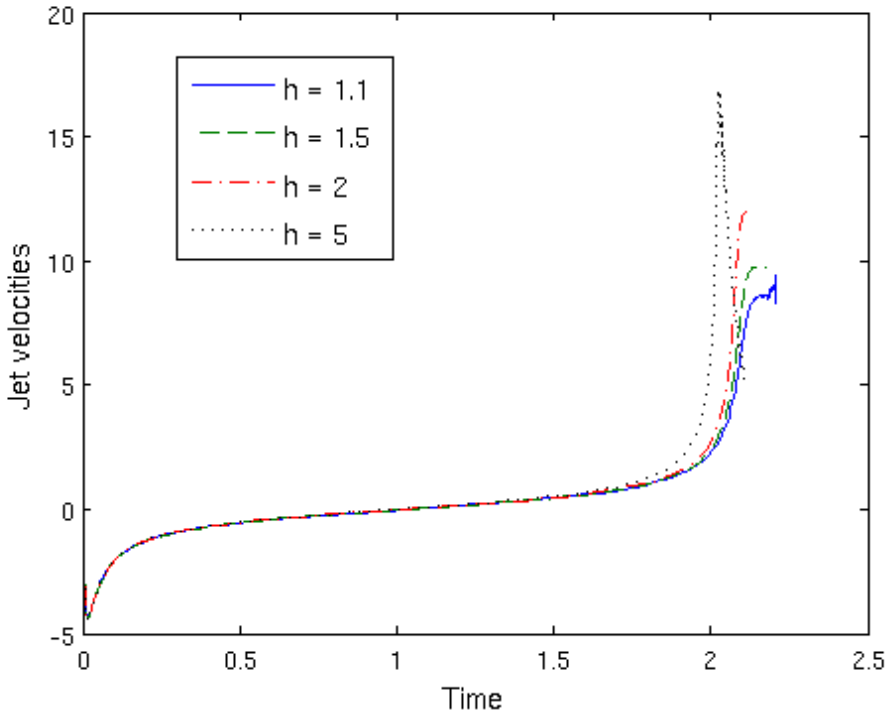

(b) Jet velocities for the inviscid case and different initial stand-off distances h.

Figure 3.8: Effect of initial stand-off distance for an inviscid fluid.

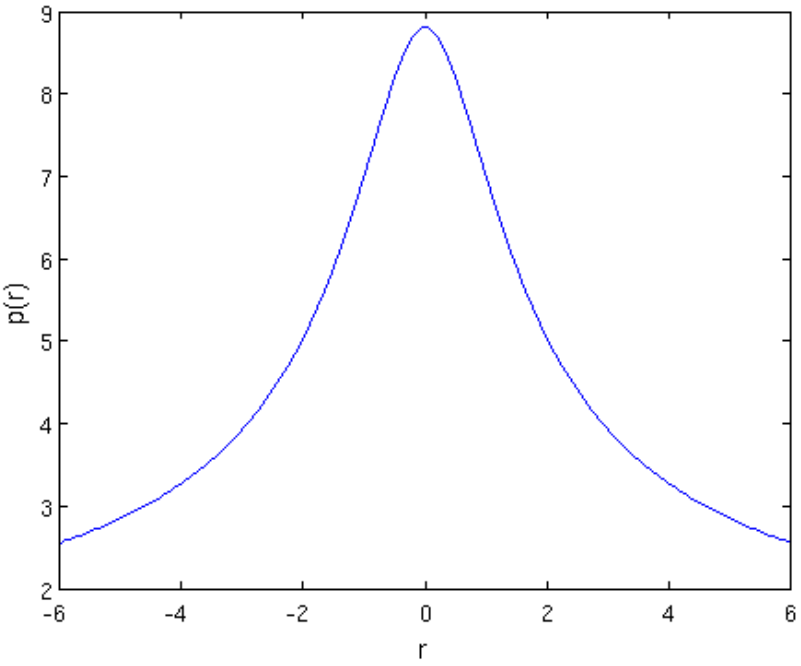

Figure 3.9: Pressure along the rigid wall at jet impact for the inviscid case and stand-off distance $h = 2$.

The effect of the rigid boundary will clearly decrease with increased initial stand-off distance and thus the bubble should remain roughly spherical if initiated far enough away from the wall. The maximum deviation from a spherical bubble can be measured using a modified form of Eq. (3.101)

$$\max\left(r_{dev}(i)\right) = \max\left(|\mathbf{d}_i| - \sum_{i=1}^{N+1} \frac{|\mathbf{d}_i|}{N+1}\right), \tag{3.104}$$

where $|\mathbf{d}_i| = \sqrt{r_i^2 + (z_i - h)^2}$. This deviation can be seen in Fig. 3.10 for an inviscid fluid and a range of initial stand-off distances. As expected, the deviation increases with decreasing h and the bubble is essentially unaffected by the wall at a distance of about $25 \times R_{max}$.

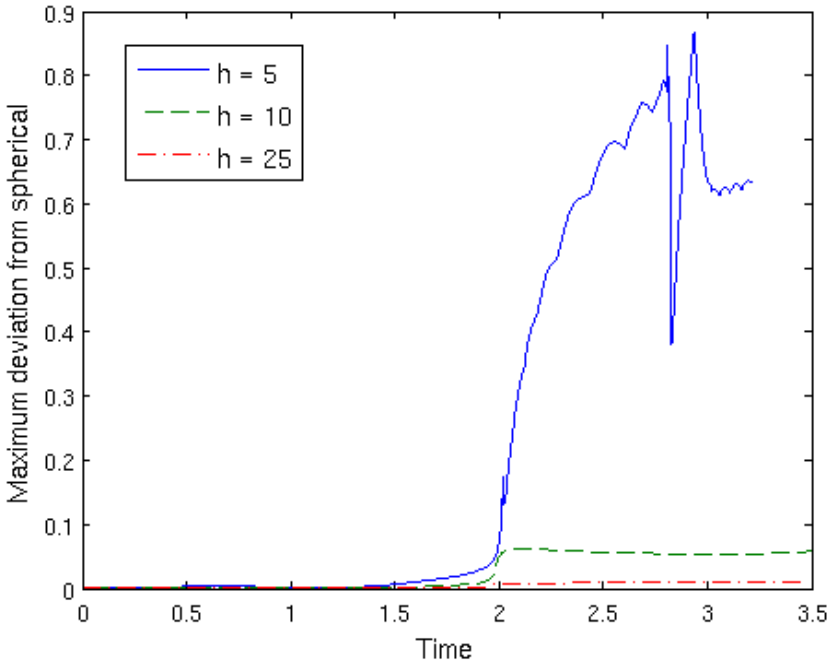

Figure 3.10: Maximum deviation from a spherical bubble for a bubble in an inviscid fluid and initial stand-off distances $h = 5, 10, 25$.

In Fig. 3.11 the effect of initial stand-off distance is shown for a bubble in an Oldroyd-B fluid with $Re = 5$, $De = 2$. In contrast to the inviscid case, starting the bubble closer to the wall leads to higher pressure occuring at the midpoint of the wall whereas the jet velocities are relatively unaffected. The pressures at the rigid wall are actually larger for $Re = 5$, $De = 2$ than in the inviscid case, despite the fact that a significant liquid jet does not occur. When near minimum volume, the presence of the small bubble with high internal pressure (as well as the liquid jet) contributes to the large pressures at the rigid wall. Note, though, that the inviscid computations only run up to jet impact which can occur before the bubble reaches its minimum volume and thus larger pressures could well be reached in the toroidal phase (modelled in Chapter 4). Even though the jet velocities are relatively low (roughly 20m/s), very high pressures are still produced (up to 3MPa) and thus damage to nearby structures is still possible for this case.

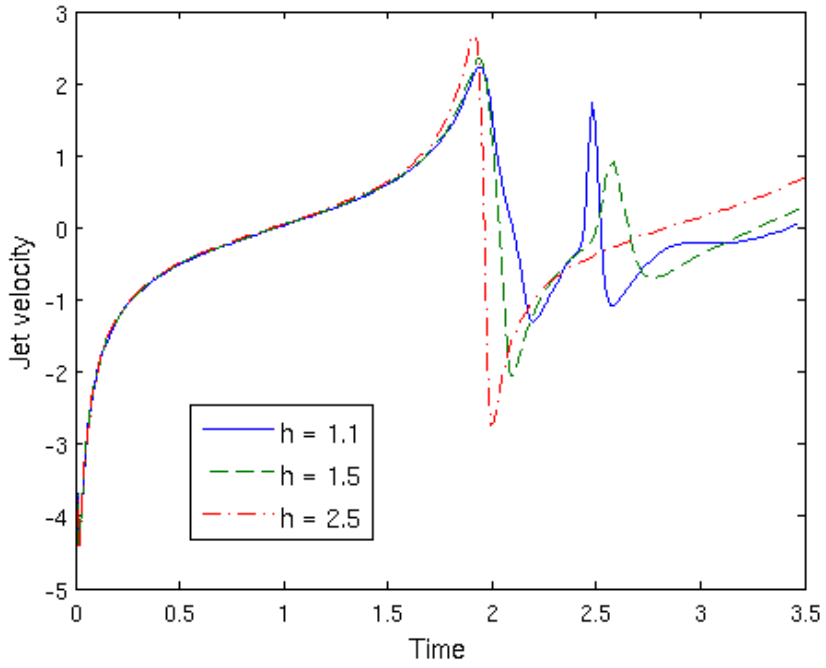

(a) Jet velocities vs. time for $Re = 5$, $De = 2$ and a range of h.

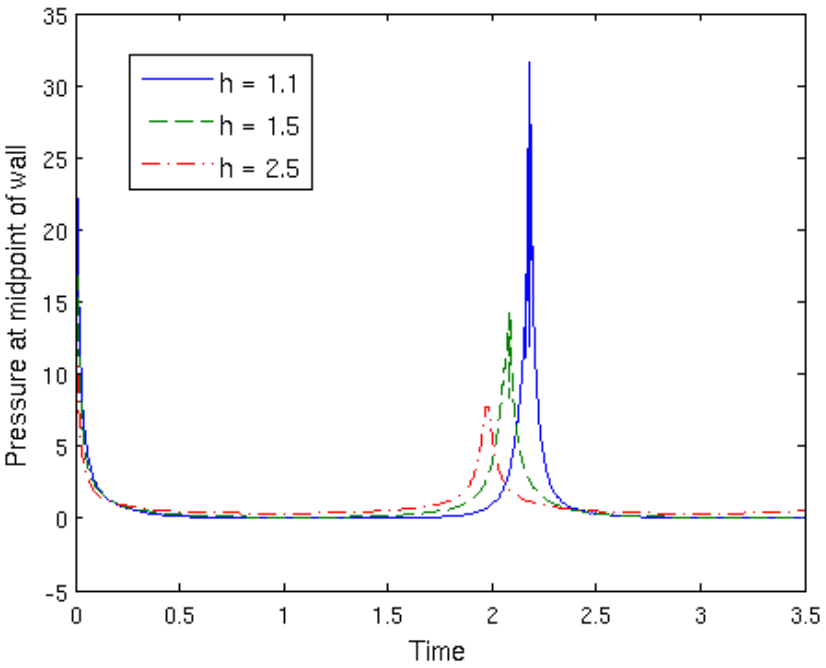

(b) Pressure at the rigid wall vs. time for $Re = 5$, $De = 2$ and a range of h.

Figure 3.11: Effect of inital stand-off distance for a bubble in an Oldroyd-B fluid with $Re = 5$, $De = 2$.

3.6.2 Effects of fluid rheology

For a fixed initial stand-off distance $h = 1.5$ the effects of altering the viscosity are shown in Fig. 3.12. As was seen for the spherical bubble in Chapter 2 an increase in viscosity results in higher frequency, lower amplitude oscillations. As in the inviscid case the peak pressures at the wall conincide with bubble minimum volume where the bubble pressure and wall velocities are largest even though the viscosity inhibits jet formation.

Fig. 3.13 shows the pressure at the wall (a) and the bubble volume (b) for $h = 1.5$, $Re = 1$ and a range of Deborah numbers (changing fluid elasticity). An increase in Deborah number corresponds to increased amplitude oscillations and higher pressures occurring at the bubble wall. For the case $De = 10$, jet impact occurs and the simulation is terminated. The pressures produced at the rigid boundary are also similar to those produced in the inviscid case with the same stand-off distance. For a large Deborah number (high elasticity) the dynamics approach that of the inviscid case as the elasticity overcomes the debilitating effect of viscosity. The high pressures in Fig.3.13a are a consequence of the internal gas of the bubble becoming highly compressed as it collapses.

In Fig. 3.15 the bubble centroid position is shown in time for a bubble in an Oldroyd-B fluid for the same parameters as Fig. 3.13. It is well known that the Bjerknes effect for a cavitation bubble is directed towards a rigid wall [18] causing the bubble to migrate towards the boundary. In a fluid with higher elasticity the bubble translates towards the wall faster since it undergoes larger oscillations with higher velocities. However, for the case $Re = De = 1$ the position of the bubble centroid remains relatively constant, showing that the fluid viscosity can negate the Bjerknes effect from the wall.

In general, it has been shown that fluid viscoelasticity suppresses jet formation and the bubble will remain singly connected. This agrees with studies of bubbles in fluids with polymer additives such as Williams et al. [112] and Barrow et al. [71]. In these studies it was concluded that the polymer additive resists elongational flow and thus liquid jets are shortened or entirely suppressed. The dynamics of this model, however, are governed by the competition between inertial, shear viscosity, elastic and surface tension effects and it will be seen that large jets can form even for a bubble in a viscoelastic fluid; in particular when the elasticity or surface tension effects are large enough to negate the fluid viscosity.

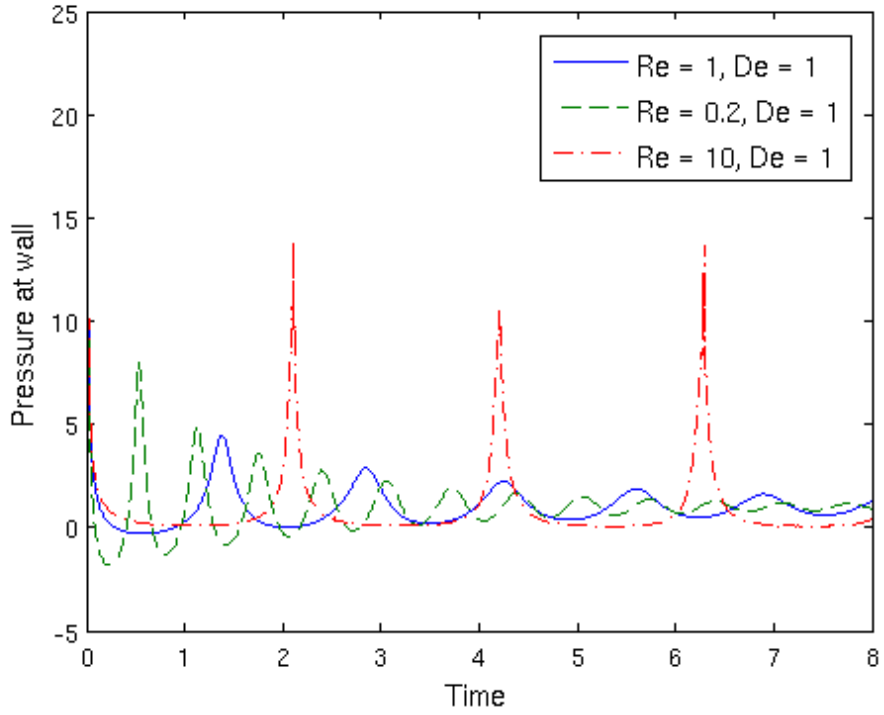

(a) Pressure at the midpoint of the wall for $h = 1.5$, $De = 1$ and a range of Reynolds numbers.

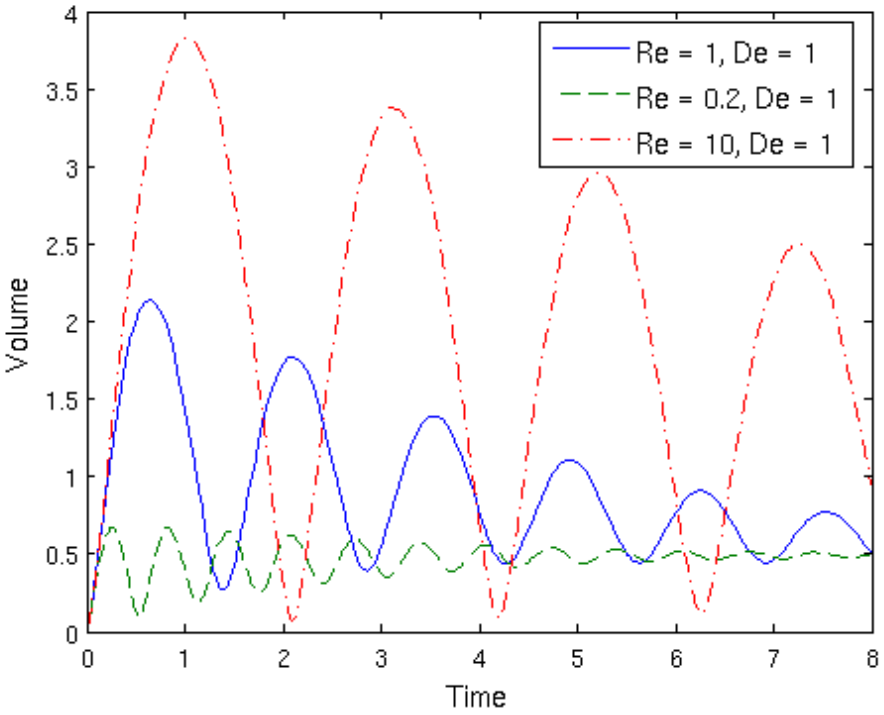

(b) Bubble volume for $h = 1.5$, $De = 1$ and a range of Reynolds numbers.

Figure 3.12: Effect of varying viscosity for a given stand-off distance $h = 1.5$.

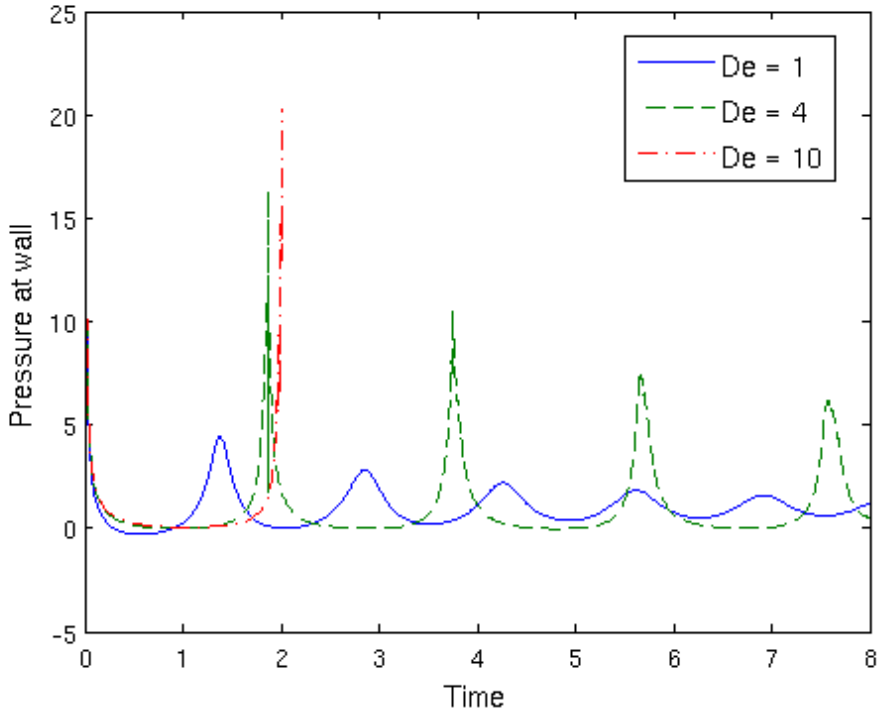

(a) Pressure at the midpoint of the wall for $h = 1.5$, $Re = 1$ and a range of Deborah numbers.

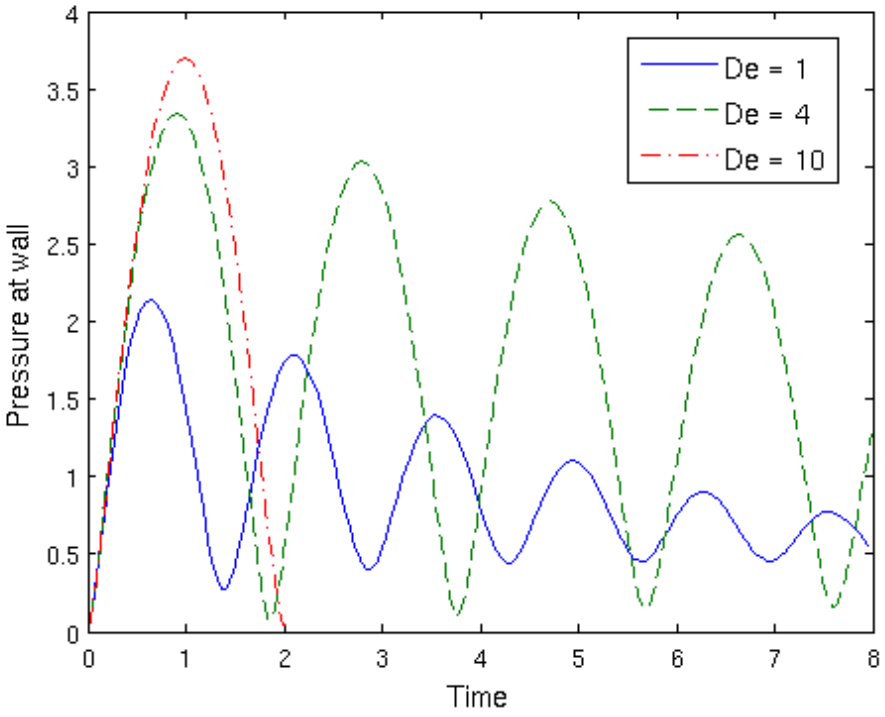

(b) Bubble volume for $h = 1.5$, $Re = 1$ and a range of Deborah numbers.

Figure 3.13: Effect of varying elasticity for a given stand-off distance $h = 1.5$.

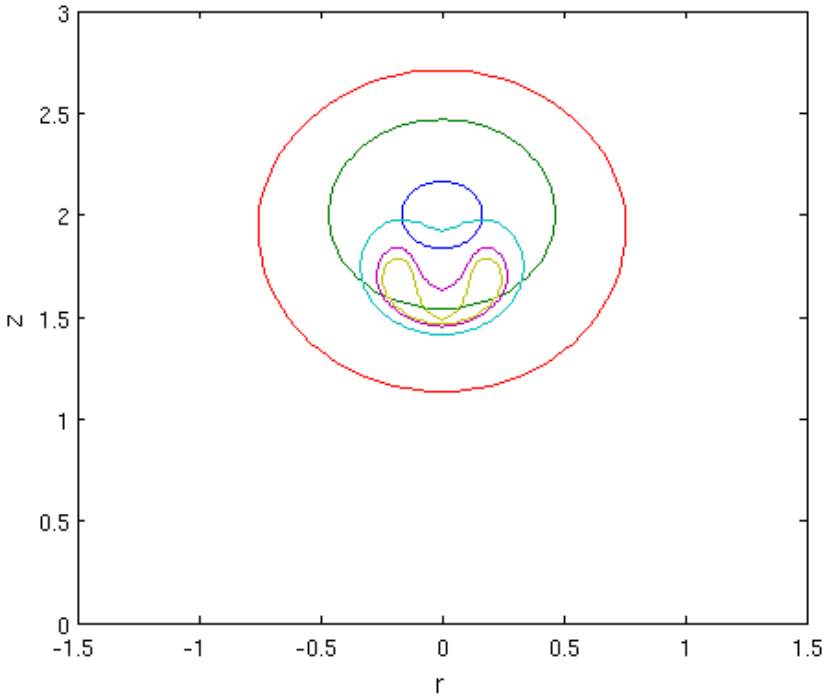

(a) $Re = \infty$, $De = 0$, $h = 2$.

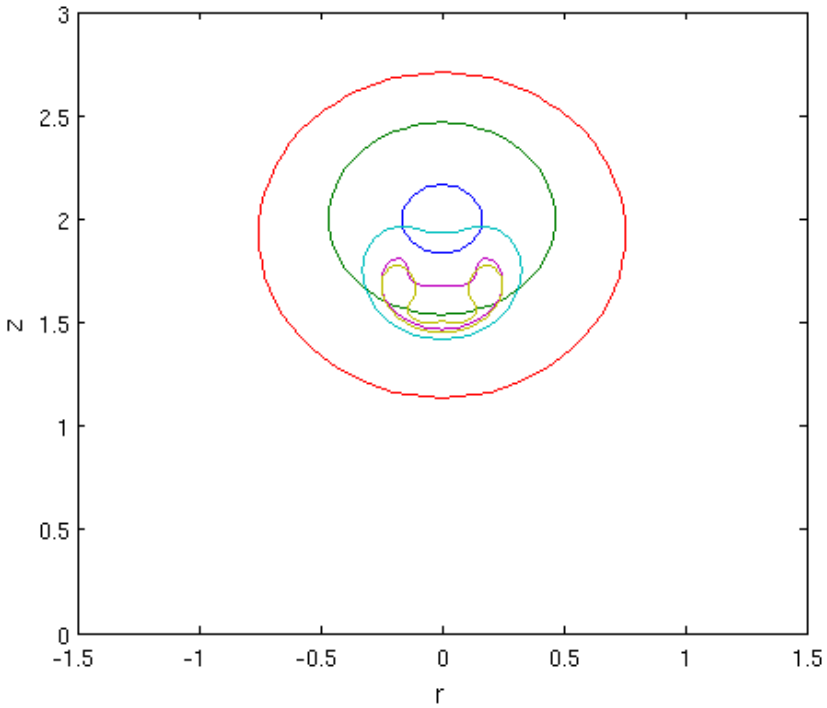

(b) $Re = 10$, $De = 10$, $h = 2$.

Figure 3.14: Bubble surfaces for an inviscid fluid (a) and an Oldroyd-B fluid with $Re = De = 10$. The initial stand-off distance is $h = 2$.

For the parameters $Re = De = 10$, $1/We = 0.0718$ and $h = 2$ jet impact does occur, in fact. The bubble surfaces for this case and for the inviscid case are shown in Fig. 3.14. For both cases the bubble growth is very similar; both remain roughly spherical and grow to a similar size of $R_{eq} \approx 1$. In the late stages of collapse, however, different behaviour is observed for the viscoelastic case. The high velocities observed in the centre of the bubble give rise to higher stresses in this region. This causes the centre of the bubble to flatten (yellow line, Fig. 3.14b). The rest of the bubble surface (away from the jet) looks very similar to the inviscid case since the stresses are negligible in this region.

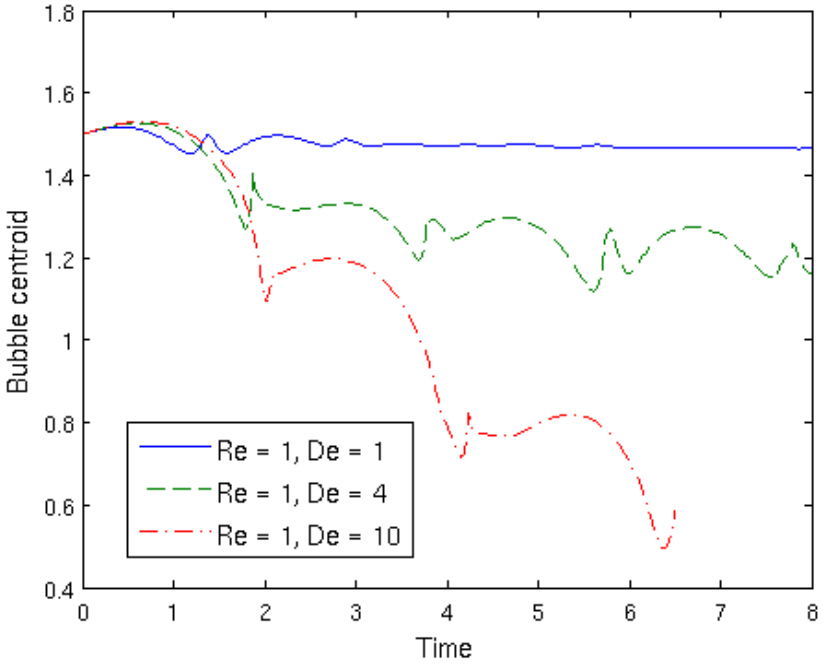

Figure 3.15: Bubble centroid position for $h = 1.5$, $Re = 1$ and a range of Deborah numbers.

3.6.3 Effects of surface tension

Cavitation bubbles are typically of the order of 1μm and consequently the effects of surface tension cannot be ignored. In a paper by Zhang and Zhang [118], a buoyant cavity growing and collapsing in an inviscid fluid near a rigid wall was investigated. They found that in the late stages of collapse when the Kelvin Impulse was not small, surface tension had little effect on the dynamics. However, just before the collapse stage when the Kelvin Impulse was small, the effects of the surface tension included changing the direction of the liquid jet and preventing the bubble from rebounding before jet impact.

The surface tension appears as the term $\frac{C}{We}$ in the non-dimensionalised Bernoulli equation used to update the potential ϕ. The curvature C is calculated using the standard equation for a parameterised curve $(r(s), z(s))$

$$C = -\left(\frac{dr}{ds}\frac{d^2z}{ds^2} - \frac{dz}{ds}\frac{d^2r}{ds^2}\right)\left(\left(\frac{dr}{ds}\right)^2 + \left(\frac{dr}{ds}\right)^2\right)^{-3/2}, \tag{3.105}$$

where the tangential derivatives are approximated using the spline discretisation.

The Weber number is defined as $We = R_m P_{ref}/\sigma$ with $P_{ref} = 101$MPa and surface tension coefficient $\sigma = 0.0725$N/m. Using these values, maximum radii of $R_{max} = 1, 6, 10\mu$m correspond to $1/We = 0.718, 0.119, 0.0718$, respectively. For these cases (with no wall present) radius-time curves are shown in Fig. 3.16. Since the surface tension is assumed to be constant, an initial spherical bubble in an infinite fluid remains spherical even when surface tension is considered. An increase in $1/We$ though, which corresponds to a decrease in R_{max}, results in lower amplitude and higher frequency oscillations.

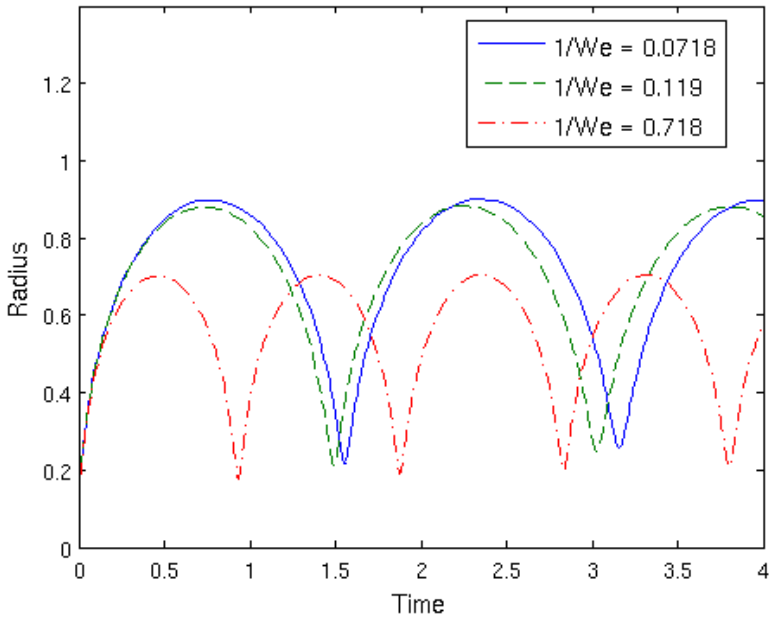

Figure 3.16: Effect of surface tension: Radius vs time curves for a range of Weber numbers.

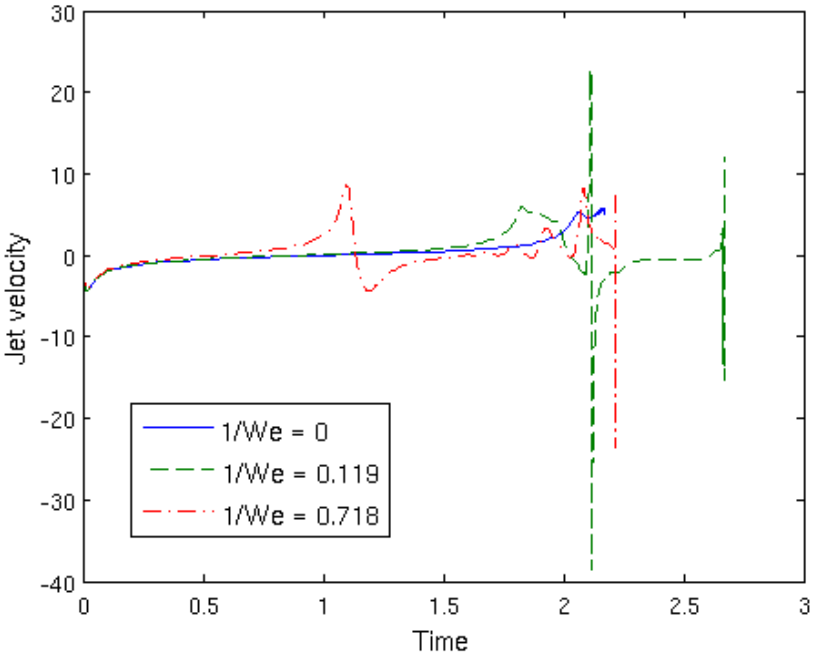

Figure 3.17: Jet velocities for the case $Re = 10$, $De = 5$, $h = 1.5$ and $1/We = 0, 0.119, 0.718$.

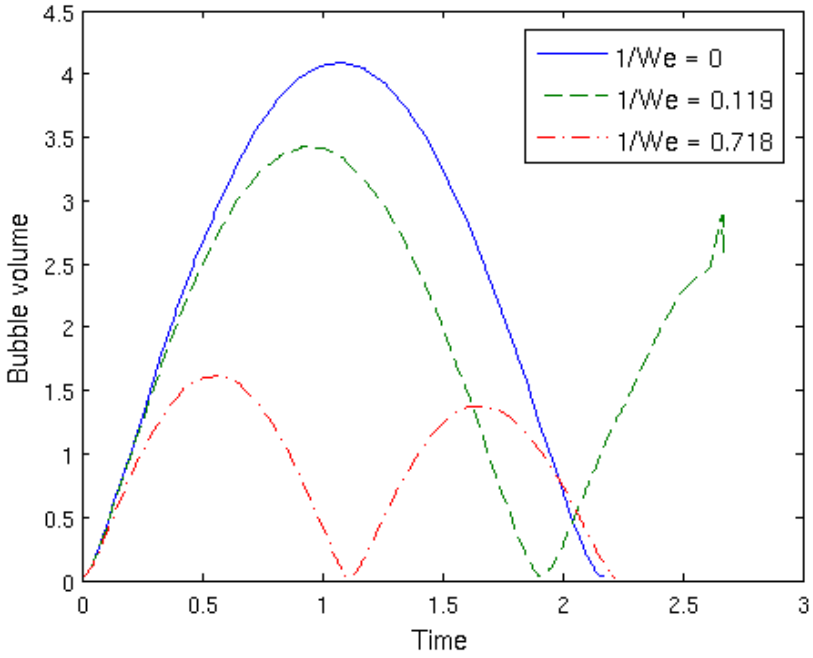

Figure 3.18: Bubble volumes for the same cases as Fig. 3.17.

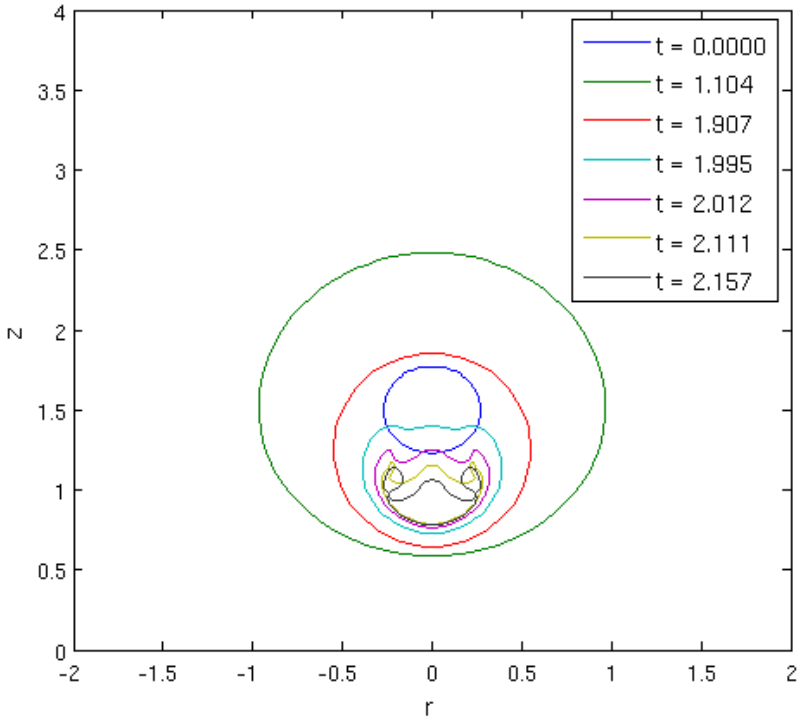

Figure 3.19: Bubble surfaces for $Re = 10$, $De = 5$, $h = 1.5$ and $1/We = 0$ (no surface tension).

Considering the same parameters as Fig. 3.16 but including a rigid wall at $z = 0$ the jet velocities are shown in Fig. 3.17. As for the infinite fluid the surface tension effects cause higher frequency oscillations. The jet velocities (velocities of the bubble wall at axis) are more erratic when surface tension is included since the top and bottom of the bubble are oscillating out of phase. Bubble surfaces are shown for $1/We = 0$ (no surface tension),$1/We = 0.119$ and $1/We = 0.718$ in Figs. 3.19, 3.20 and 3.21, respectively. For $1/We = 0$, two points of the bubble surface become very close together as it collapses as seen in Fig.3.19 (black line). It is hypothesised that at this point a small portion of the bubble will separate from the rest. This behaviour is due to the elastic effects causing portions of the increasingly asymmetric bubble surface to rebound as the jet forms. The simulation ends at this point due to points on the bubble surface becoming too close but it is hypothesised that at this point the bubble will split into multiple bubbles, though this is not modelled here.

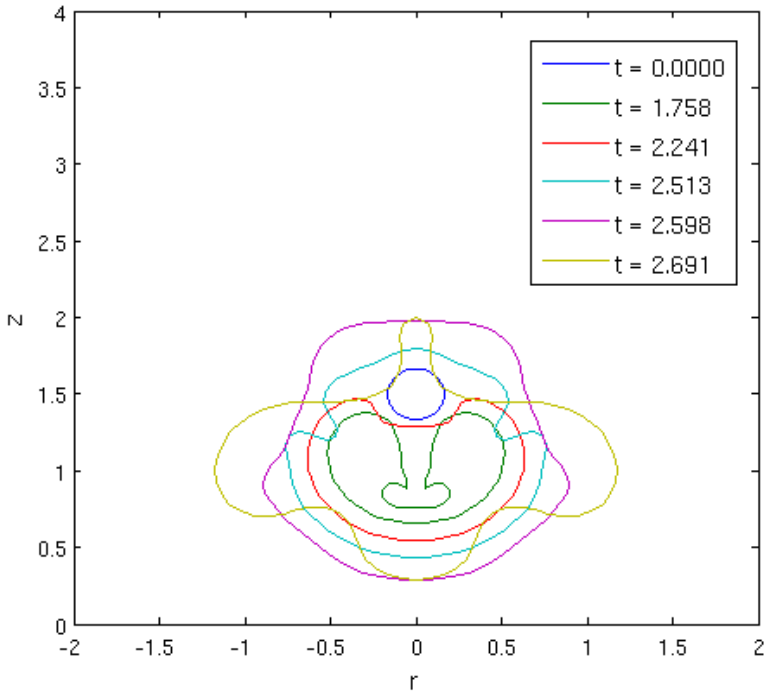

Figure 3.20: Bubble surfaces for $Re = 10$, $De = 5$, $h = 1.5$ and $1/We = 0.119$.

When surface tension is also considered (Figs. 3.20 and 3.21) the bubble surface deforms even more, particularly near the end of collapse which gives rise to the sharp jumps in jet velocity seen in Fig. 3.17. When surface tension is included, the bubble growth is no longer spherical and the surface becomes very deformed. A jet still forms during

collapse but even more of the bubble volume is 'squeezed' outwards. Note that the sharp portions of the surface in Fig. 3.20 are due to the plotting and not the discretisation of the surface (which is smooth). Increasing the surface tension further to $1/We = 0.718$ (Fig. 3.21) leads to faster oscillations with a significantly reduced maximum volume. A liquid jet also does not form, unlike the cases $1/We = 0, 0.119$.

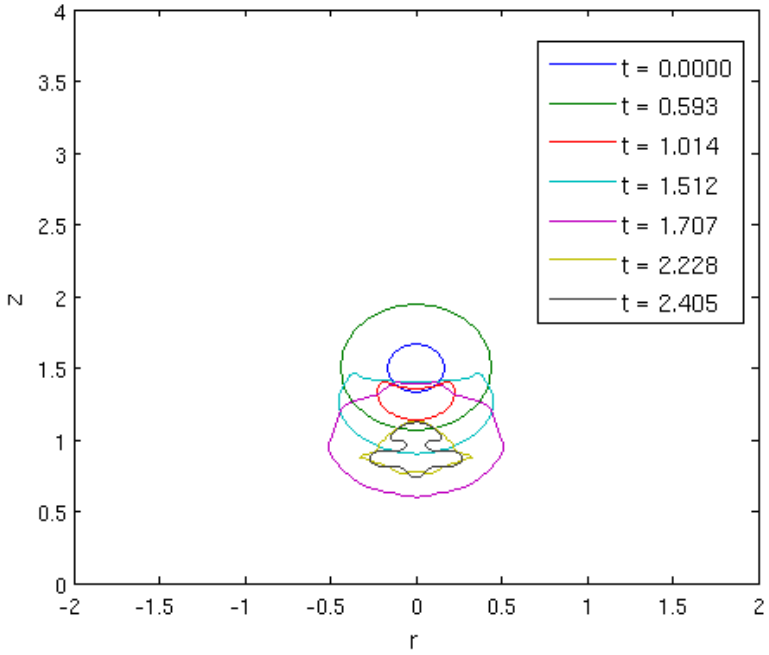

Figure 3.21: Bubble surfaces for $Re = 10$, $De = 5$, $h = 1.5$ and $1/We = 0.718$.

3.7 Conclusions

A non-singular formulation of the boundary element method based on that of Klaseboer et al. [96] is presented for a single cavitation bubble near a rigid wall. This new method is found to be significantly more stable to saw-tooth instabilities than the standard formulation and produces less error over time. The model is validated by comparisons to the spherical dynamics presented in Chapter 2 and the good agreement for an Oldroyd-B fluid indicates the validity of the assumption that bulk viscosity effects are of little importance.

Numerical results for a range of parameter values have been shown to convey the importance of the fluid rheology, the initial conditions and surface tension effects. In

particular it was found that viscosity tends to inhibit the formation of liquid jets, agreeing with previous studies (e.g. [67]), but that jets may still form in a viscoelastic fluid if the fluid elasticity or surface tension effects are large enough to overcome the fluid viscosity. For cases where this occurs, the fluid rheology results in a much flatter bubble centre due to a build up of extra stress in this region. The remainder of the bubble surface looks very similar to the inviscid case since the stress is much lower in these regions. The inclusion of surface tension into the model results in lower amplitude oscillations and more erratic jet velocities as different parts of the bubble oscillate out of phase. The large deformations observed can also prevent a jet occuring.

The numerical model provided in this chapter must terminate when a jet forms and the two sides of the bubble become too close together. At this point the bubble must be transformed to a vortex ring bubble for the computations to proceed, the details of which are given in Chapter 4.

It is important to note that an essential assumption in this model is the neglection of bulk viscosity to allow viscoelastic effects to be included approximately at the bubble surface boundary condition. This assumption is argued to be reasonable for the fluids encountered in biomedical applications, which is the focus behind this work. For complex fluids such as highly concentrated polymer solutions this assumption will not be reasonable and bulk viscosity effects will affect the bubble dynamics.

Chapter 4

Modelling Toroidal Bubbles in an Incompressible Fluid Using the Vortex Ring Method

4.1 Introduction

In this chapter, the non-singular boundary element method described in Chapter 3 is extended to model toroidal bubbles. Initially a small, spherical cavitation bubble is located at a distance h from a rigid boundary. The presence of a nearby rigid boundary gives rise to an asymmetry in the pressure field which can cause one side of the bubble to collapse more rapidly resulting in the formation of a liquid jet. This jet can eventually impact on the far side of the bubble (see Fig. 4.1).

It was postulated by Benjamin and Ellis [8] that when jet impact occurs the bubble transitions to a doubly-connected toroidal shape. In order to explain the reasoning behind this it is helpful at this point to define the Kelvin impulse; $\mathbf{I}$ [15]

$$\mathbf{I} = \rho \int_S \phi \mathbf{n} dS, \tag{4.1}$$

where ρ is the density, S is the bubble surface and $\mathbf{n}$ is the outward normal to the bubble surface (into the bubble). The Kelvin impulse corresponds to the apparent inertia of the bubble and its sign can be used as an indicator of the direction of the bubble movement [14]. Benjamin and Ellis considered a bubble collapsing to nothing

(zero volume) and argued that the liquid remaining singly connected as this occurs would cause the Kelvin impulse to vanish (not allowed in the absence of an external force). Thus, in order to preserve the Kelvin impulse, the bubble must become toroidal resulting in a vortex system possessing the original Kelvin impulse as well as a newly imparted circulation Γ in the fluid.

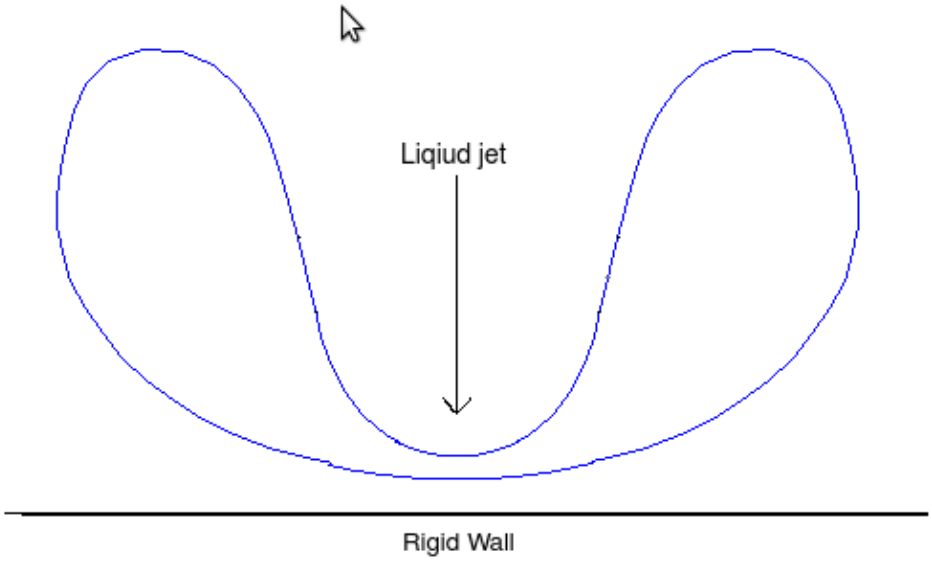

Figure 4.1: Jet formation during bubble collapse.

This transition to a ring bubble has also been seen in experiments such as those by Ellis [39] or Walters and Davidson [103] in which pulses of air released through a tube in the bottom of a water- filled tank create toroidal bubbles.

4.1.1 Previous Work

Best [9] was the first to model the transition between a singularly connected bubble into a toroidal form using the *domain cut* method. An artifical impact surface T is introduced connecting the two sides of the bubble over which the potential is discontinuous with the jump equal to the circulation Γ. The boundary integral equation becomes an integral over the cut as well as the bubble surface. Knowledge of the position of the cut is required; Best propagated the cut along its normal using a finite difference approximation for the velocity. This technique, however, meant that the cut often becomes distorted during the evolution of the bubble and sometimes 'wraps around' the bubble ending the computation. A better method to handle the cut, developed by Best [10]

and used in [17], is known as dynamic cut relocation. This is based on the realisation that the cut is an artificial surface and thus its geometry is arbitrary. Instead of following the cut surface it can simply be redefined every time step as a straight line for simplicity. A problem still occurs, however, at the point at which the cut meets the bubble surface. At this point the normal is not well defined and the velocities must be approximated using an average of the nodes either side.

In this chapter, an alternative to the domain cut method is described in which a vortex ring is placed inside the bubble. This approach was originally used by Lundgren and Mansour [70] for rising vortex ring bubbles although they were unable to model the transition between a singularly connected bubble and the vortex ring bubble. The boundary element method from Chapter 3 is extended in order to model the transition to a toroidal bubble and the subsequent bubble motion. The method is similar to that of Wang et al. [110], although the quintic splines and nonsingular formulation developed in Chapter 3 provide a more accurate, stable surface discretisation. The aim of this chapter is to investigate how the fluid rheology affects the transition to a toroidal form and how the bubble develops should this transition take place.

4.2 Numerical Method

A singly connected (initially spherical) bubble is modelled using the standard boundary element method described in Chapter 3. Jet formation depends on the proximity of the rigid wall as well as the fluid rheology and bubble surface tension. If a jet does form, though, it will eventually impact on the far side of the bubble at which point the simulation will crash. Just before this happens we will model a change to a toroidal geometry. This is achieved by a local smoothing of the bubble surface around the impact site, details of which are given later in the chapter. The doubly connected toroidal bubble also imparts a circulation to the flow around the gaseous tube of the toroidal bubble which is accounted for by the introduction of a vortex ring placed inside the bubble, as in Fig. 4.2.

This vortex ring has a strength Γ equal to the circulation in the flow, which is obtained by integrating the velocity around some closed curve that thread the torus. Taking the bubble surface as this curve gives the circulation as the difference between the potentials

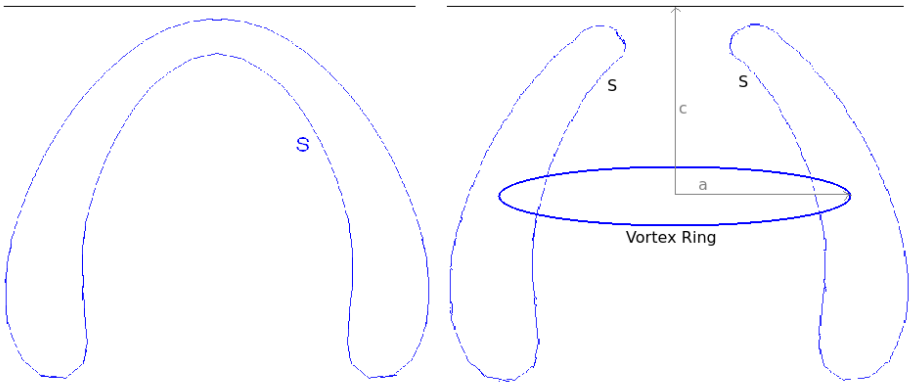

Figure 4.2: Introduction of the vortex ring.

ϕ at nodes 1 and $N+1$

$$\Gamma = \oint_C \nabla\phi \cdot d\mathbf{l} = \phi(N+1) - \phi(1). \tag{4.2}$$

It was shown by Best [9] that for an incompressible potential flow, this circulation Γ is constant in time.

The exact location of the vortex ring is unimportant provided it lies completely within the bubble. If the vortex ring is too close to a node on the bubble surface, however, numerical instabilities will occur. In order to minimise these instabilites, the vortex ring is placed as far from the bubble surface as possible.

4.2.1 Placing the Vortex Ring

To heuristically calculate the internal point furthest from the bubble surface a grid of Cartesian nodes is calculated in a box containing the bubble (see Fig. 4.3). The horizontal and vertical distances between the nodes are h_r and h_z, respectively where

$$h_r = \frac{r_{\max} - r_{\min}}{N_v}, \quad h_z = \frac{z_{\max} - z_{\min}}{N_v}. \tag{4.3}$$

Since the point does not need to be calculated with much precision the value of the integer N_v does not need to be large and, unless otherwise stated, $N_v = 20$ is used for all calculations.

Clearly some of the nodes will not be inside the bubble and so must be neglected as candidates. If the surface is approximated as straight lines between the bubble nodes

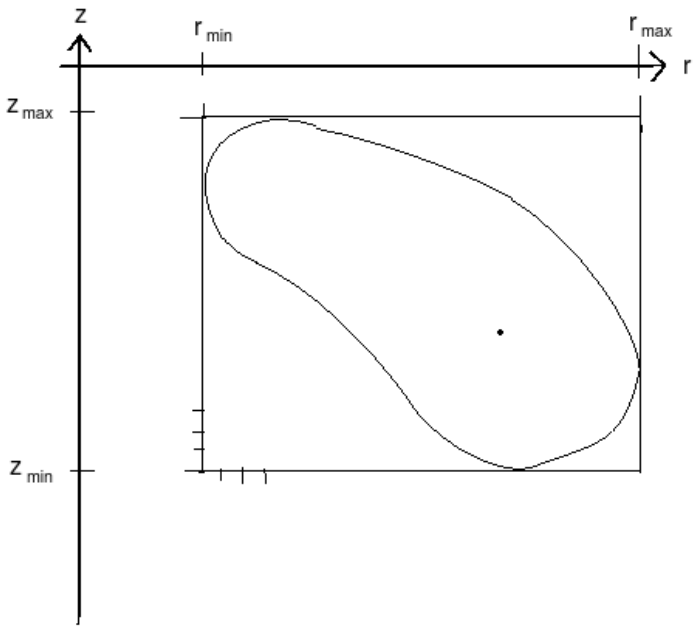

Figure 4.3: Calculating the internal point furthest from the bubble surface.

this is a 'Point in Polygon' problem and a Ray Casting Algorithm can be used for this purpose. Once these nodes have been neglected the minimum distance to a bubble node is calculated for the remaining Cartesian nodes. The height c and radius a of the vortex ring are then defined as the z- and r-coordinates of the furthest point from the nodes

$$a = r_p, \quad c = z_p. \tag{4.4}$$

The potential of the bubble is then decomposed into the vortex-ring potential φ^{vr} and a single-valued remnant potential φ

$$\phi(r, z, t) = \varphi^{vr}(r, z) + \varphi(r, z, t). \tag{4.5}$$

This vortex potential φ^{vr} is a multivalued function, a single branch of which is selected by introducing an imaginary surface stretching over the ring. The potential φ^{vr} is discontinuous and jumps by an amount Γ over this surface which in this model is taken to coincide with the impact surface (i.e. nodes $1/N+1$), although this is not necessary.

4.2.2 Overview of the numerical procedure

Once jet impact occurs the numerical procedure is as follows:

1. The vortex potential, φ^{vr}, is calculated using the Biot-Savart Law.
2. The remnant potential is found from Eq. (4.5).
3. The bubble is smoothed around the impact site to create the toroidal geometry and the nodes redistributed.
4. The vortex potential is then recalculated on the new node distribution.
5. The bubble surface and remnant potential are updated using kinematic and dynamic boundary conditions.
6. If the evolving bubble surface becomes too close to the vortex-ring the ring is relocated.
7. The vortex and remnant potentials are recalculated for this new vortex ring location.
8. Steps 5-8 are repeated.

4.2.3 Calculating the Vortex Ring Field

In the numerical simulations 'jet impact' is taken to be when node 1, moving with the liquid jet, comes within a certain distance of node $N + 1$ (see Fig. 4.4). Unless otherwise stated, for all calculations in this chapter this distance is taken to be 0.01. This ensures the two sides of the bubble are close enough to approximate jet impact but not too close to cause numerical instabilities.

In reality the process of the jet impact represents a physical singularity in time and space which is smeared over time and space by material compressibility and viscosity [117]. For simplicity, however, these effects are not modelled here and the numerical smoothing that takes place due to the discretisation does not represent a physical event and is actually an error. This error is kept sufficiently small though, through the use of a fine mesh and small time steps. Before the smoothing takes place the remnant potential φ is required; this can be calculated from Eq. (4.5) following the calculation of the vortex potential φ^{vr}; the details of which are now given.

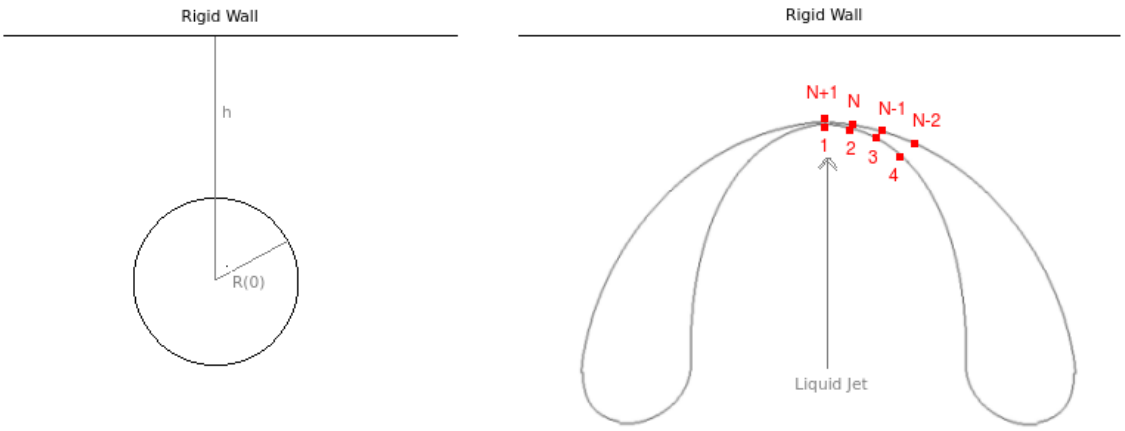

Figure 4.4: Evolution of bubble up until jet impact.

By the Biot-Savart law the velocity field of a vortex ring of radius a, strength Γ, centered at the origin is given by [110]

$$\mathbf{v}_0^{vr}(r,z) = \frac{\Gamma}{4\pi}\oint_C \frac{d\mathbf{l}\times(\mathbf{p}-\mathbf{q})}{|\mathbf{p}-\mathbf{q}|^3}, \tag{4.6}$$

where $\mathbf{p} = (r,0,z)$, $\mathbf{q} = (a\cos\theta, a\sin\theta, 0)$ and $d\mathbf{l} = ad\theta(-\sin\theta,\cos\theta,0)$ is the tangent to the vortex ring. Substituting these into Eq. (4.6) gives

$$\mathbf{v}_0^{vr}(r,z) = \frac{\Gamma a}{4\pi}\int_0^{2\pi} \frac{(\mathbf{i}z\cos\theta + \mathbf{j}z\sin\theta + \mathbf{k}(a-r\cos\theta)d\theta}{(r^2+z^2+a^2-2ar\cos\theta))^{\frac{3}{2}}}. \tag{4.7}$$

Due to the symmetry of $\cos\theta$ about $\theta=\pi$ and the corresponding asymmetry of $\sin\theta$ the above equation simplifies to

$$\mathbf{v}_0^{vr}(r,z) = \frac{\Gamma a}{2\pi d^3}\int_0^{\pi} \frac{\mathbf{i}z\cos\theta + \mathbf{k}(a-r\cos\theta)}{(1-k\cos\theta)^{\frac{3}{2}}}d\theta, \tag{4.8}$$

where the following variables have been defined

$$k(r,z) = \frac{2ar}{d^2}, \quad d = (r^2+z^2+a^2)^{\frac{1}{2}}. \tag{4.9}$$

Then, defining the integrals I_1 and I_2 as

$$I_1(r,z) = \int_0^{\pi} \frac{\cos\theta}{(1-k\cos\theta)^{\frac{3}{2}}} d\theta, \tag{4.10}$$

$$I_2(r,z) = \int_0^{\pi} \frac{1}{(1-k\cos\theta)^{\frac{3}{2}}} d\theta, \tag{4.11}$$

allows Eq. (4.8) to be written as

$$\mathbf{v}_0^{vr}(r,z) = \frac{\Gamma a}{2\pi d^3}\Big\{[zI_1(r,z)]\mathbf{i} + [aI_2(r,z) - rI_1(r,z)]\mathbf{k}\Big\}. \tag{4.12}$$

In this application, the vortex ring will never be centred at the origin (since this is located on the rigid wall). To find the velocity field of a ring centred at $z = c$ the method of images is used

$$\begin{aligned}\mathbf{v}^{vr}(r,z) &= \mathbf{v}_0^{vr}(r,z+c) - \mathbf{v}_0^{vr}(r,z-c) \\ &= u^{vr}(r,z)\mathbf{i} + w^{vr}(r,z)\mathbf{k},\end{aligned} \tag{4.13}$$

where the components of $\mathbf{v}^{vr}$ are

$$u^{vr}(r,z) = \frac{\Gamma a}{2\pi}\Big\{\frac{z+c}{d(r,z+c)^3} I_1(r,z+c) - \frac{z-c}{d(r,z-c)^3} I_1(r,z-c)\Big\}, \tag{4.14}$$

$$w^{vr}(r,z) = \frac{\Gamma a}{2\pi}\Big\{\frac{aI_2(r,z+c) - rI_1(r,z+c)}{d(r,z+c)^3} - \frac{aI_2(r,z-c) - rI_1(r,z-c)}{d(r,z-c)^3}\Big\}. \tag{4.15}$$

4.2.4 Calculating the Vortex and Remnant Potentials

The vortex potential φ^{vr} at a node can be calculated by integrating the vortex velocity $\mathbf{v}^{vr}$ from minus infinity to the point $\mathbf{x}(i) = (r(i), z(i))$ being considered

$$\varphi^{vr}(r_j, z_j) = \varphi^{vr}(r_1, z_1) + \int_{s_1}^{s_j} \mathbf{v}^{vr}(r,z) \cdot \mathbf{dl}, \tag{4.16}$$

where $\varphi^{vr}(r_1, z_1)$ is the potential at node 1, given by

$$\varphi^{vr}(r_1, z_1) = \int_{-\infty}^{z_1} w^{vr}(0,z)dz + \int_0^{r_1} u^{vr}(r, z_1)dr. \tag{4.17}$$

An alternative, more efficient, method is to use solid angles to explicitly calculate the vortex potential. Eq. (4.6) for the vortex velocity can be rewritten as [74]

$$\mathbf{v}_0^{vr}(r,z) = \frac{\Gamma}{4\pi}\oint_{(C)} d\mathbf{l} \times \nabla\left(\frac{1}{r}\right), \tag{4.18}$$

where $\mathbf{r} = \mathbf{p} - \mathbf{q}$ and $r = |\mathbf{r}|$. Using Stokes' Theorem this becomes

$$\mathbf{v}_0^{vr}(r,z) = \frac{\Gamma}{4\pi}\int_{(S)} \Big(\mathbf{n} \times \nabla\Big) \times \left[\nabla\left(\frac{1}{r}\right)\right] dS, \tag{4.19}$$

where S is any surface with C for a boundary. Using an identity for the triple vector product

$$\Big(\mathbf{n} \times \nabla\Big) \times \nabla\left(\frac{1}{r}\right) = \nabla\left[\mathbf{n}\nabla\left(\frac{1}{r}\right)\right] - \mathbf{n}\left[\nabla^2\left(\frac{1}{r}\right)\right] = \nabla\left[\mathbf{n}\nabla\left(\frac{1}{r}\right)\right], \tag{4.20}$$

(since $1/r$ is a spherical harmonic) and using $\mathbf{n}\nabla = \frac{\partial}{\partial n}$ then gives

$$\mathbf{v}_0^{vr}(r,z) = \frac{\Gamma}{4\pi}\int_{(S)} \nabla\left[\frac{\partial}{\partial n}\left(\frac{1}{r}\right)\right] dS = -\nabla\left[\frac{\Gamma}{4\pi}\int_{(S)} \frac{\partial}{\partial n}\left(\frac{1}{r}\right) dS\right], \tag{4.21}$$

which immediately results in the following expression for the vortex potential

$$\varphi^{vr}(r,z) = \frac{\Gamma}{4\pi}\int_{(S)} \frac{\partial}{\partial n}\left(\frac{1}{r}\right) dS. \tag{4.22}$$

Now, $\frac{\partial}{\partial n}(1/r) = \cos(\alpha)/r^2$ where α is the angle between dn and the line r. Since $dS\cos(\alpha)$ is the projection of the area dS on the plane perpendicular to r then $dS\cos(\alpha)/r^2$ is the elementary solid angle subtended at $\mathbf{p}$ by dS. It then follows that

$$\varphi^{vr}(\mathbf{x}(i)) = \frac{\Gamma\Theta(\mathbf{x}(i))}{4\pi}, \tag{4.23}$$

where $\Theta(\mathbf{x}(i))$ is the solid angle subtend at the point $\mathbf{x}(i)$ by the surface of discontinuity which extends over the vortex ring. For simplicity this surface of discontinuity is simply taken as the flat plane bounded by the ring.

It can be seen that the problem reduces to finding the solid angle of a cone; the formula for which is

$$\Theta(\mathbf{x}(i)) = 2\pi\left[1 - \cos\left(\frac{\theta(\mathbf{x}(i))}{2}\right)\right], \tag{4.24}$$

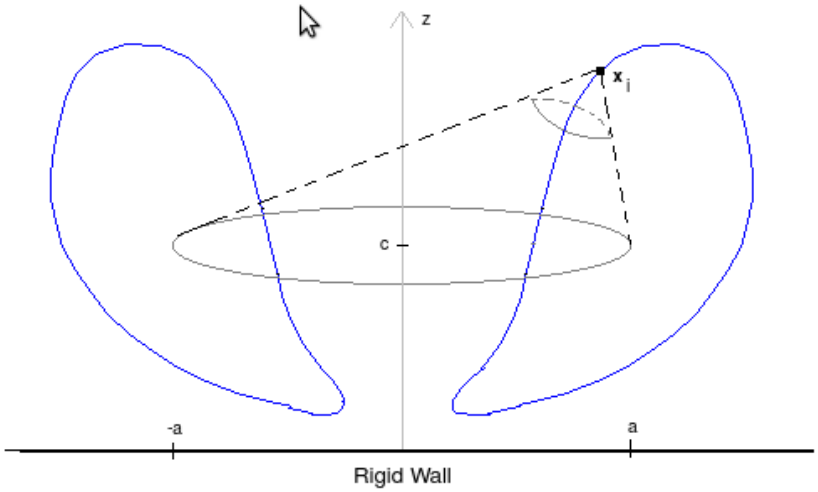

Figure 4.5: Diagram of the bubble and vortex ring and the solid angle subtended at a point.

where $\theta(\mathbf{x}(i))$ is the apex angle of the cone. The term $\cos\theta(\mathbf{x}(i))$ can be found using the dot product of the two vectors described by the dashed lines in Fig. 4.5. The solid angle jumps by 4π over the surface of discontinuity S_c and thus from Eq. (4.23) it can be seen that the vortex potential jumps by an amount equal to Γ. The vortex potential φ^{vr} thus completely accounts for the circulation in the fluid and the remnant potential is smooth everywhere.

The vortex potential has now been found at each node of the bubble surface and the fluid potential is known from the final time step before the transition to toroidal geometry. The remnant potential can then be defined as; for $i = 1, \ldots, N+1$

$$\varphi(r_i, z_i) = \phi(r_i, z_i) - \varphi^{vr}(r_i, z_i). \tag{4.25}$$

This remnant potential is smooth since the discontinuity has been 'removed' by the vortex potential. The remnant potential is now known at the nodes at the instant of jet impact. The bubble is smoothed in order to make the transition from a singly-connected bubble to a doubly-connected toroidal bubble.

4.2.5 Transition to Toroidal Geometry: Smoothing at Impact Point

Following the paper by Wang et. al [110], the impact of the liquid jet is assumed to take place at a single point. Energy is conserved using this model with all the effects of the impact completely transformed into the circulation in the fluid. Since the fluid is incompressible the disturbances are transmitted throughout the fluid at an infinite speed establishing the flow field in the toroidal geometry instantly.

To model this numerically, nodes 1 and $N+1$ are removed and replaced by a single node located at the mean positions of nodes $1, 2, N$ and $N+1$ (see Fig. 4.6). The remnant potential (and all other variables) at this new node is then taken as the mean value of its value at these nodes i.e.

$$\varphi_{\text{new}}(1) = \varphi_{\text{new}}(N+1) = \frac{\varphi(1) + \varphi(2) + \varphi(N) + \varphi(N+1)}{4} \tag{4.26}$$

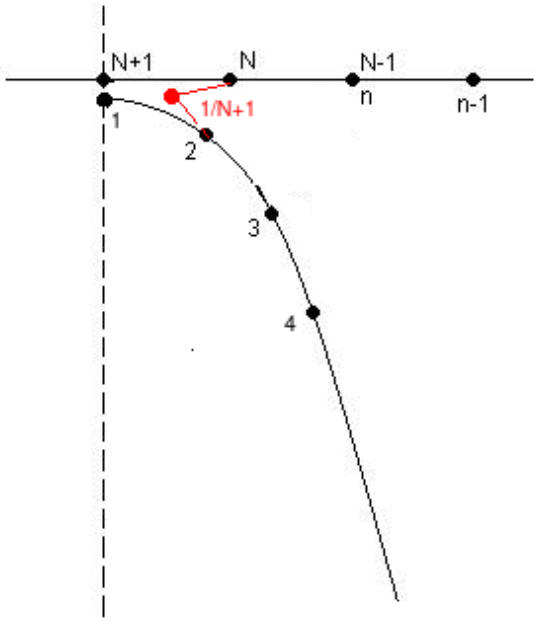

Figure 4.6: Smoothing of nodes at the impact site.

The nodes are then smoothed and redistributed to ensure that they are equally spaced in a similar manner to that used in Chapter 3, to prevent instabilities. Although the distances shown in Fig. 4.6 are exaggerated, a small amount of bubble volume is lost during this smoothing. The number of nodes N must be chosen to be large enough

so that this loss in volume (and hence in potential energy) is not too large. Typically, $N = 44$ is used.

4.2.6 Updating the Remnant Potential

As in Chapter 3, the surface and surface variables must now be updated to proceed in time. Substituting the decomposed potential (4.5) into the original bubble evolution conditions (Table 3.1) gives the following evolution conditions for the toroidal bubble

$$\frac{d\mathbf{x}}{dt} = \nabla\varphi + \mathbf{v}^{vr}, \tag{4.27}$$

$$\frac{d\varphi}{dt} = 1 - \mathbf{v}^{vr}\cdot(\nabla\varphi + \mathbf{v}^{vr}) + \frac{1}{2}|\nabla\varphi + \mathbf{v}^{vr}|^2 - \frac{2E}{Re}\frac{\partial^2\phi}{\partial n^2} - \tau^p_{nn} - \sigma C - \varepsilon\left(\frac{V_0}{V}\right)^{\gamma}, \tag{4.28}$$

$$\frac{d\tau^p_{nn}}{dt} = \frac{1}{De}\left[-\tau^p_{nn} - 2\left(De\tau^p_{nn} - \frac{2(1-E)}{Re}\right)\frac{\partial^2\phi}{\partial n^2}\right]. \tag{4.29}$$

In order to integrate these equations, the velocities $\nabla\varphi$ at the nodes are required.

Solving the Integral Equation for the Remnant Potential

Since the vortex potential can be written in terms of a potential φ^{vr} it can be seen from Eqs. (4.13-4.15) that φ^{vr} satisfies the Laplace equation in the fluid domain and decays at infinity. The remnant potential, therefore, also satisfies the Laplace equation in the fluid domain and decays at infinity and consequently its normal derivative can be found from a modified form of the integral equation (3.52).

The nonsingular formulation described in Chapter 3 is again used but for the toroidal bubble the point $\mathbf{p}_d = (0, 0, z_d)$ is always in the fluid. The extra term dealing with the singularity described by Eqs. (3.38) - (3.40) must then be included at all times. Also, nodes 1 and $N+1$ now coincide and setting $\mathbf{p}_1 = \mathbf{p}_{N+1}$, $\phi_1 = \phi_{N+1}$ results in a system of N equations (rather than $N+1$ equations for the singly connected bubble). The system is solved using a Thomas algorithm for periodic systems.

Once this system of equations has been solved for $\frac{\partial\varphi}{\partial n}$, the tangential derivative $\frac{\partial\varphi}{\partial s}$ is found using the splines, as in Chapter 3. The remnant potential is now fully determined on the bubble surface and Eqs. (4.27-4.29) can be solved to update the system in a similar manner to that described in Chapter 3.

Since the bubble surface is now closed, periodic boundary conditions are required for the quintic splines (given in Appendix B).

4.2.7 Finding the Normal Derivative of the Potential

Although the fluid potential is not being updated in the manner described in Chapter 3, the normal derivative of the potential is still required in calculating jet velocities, energy terms for the toroidal bubble and for the extra stress for an Oldroyd-B fluid. The potential ϕ can be found from (4.5) at each time step but the normal velocity cannot be found by solving the integral equation since it is multivalued at the node $1/N + 1$. Instead, use is made of (4.5) to find the normal velocity in terms of known quantities

$$\phi = \varphi^{vr} + \varphi \Rightarrow \frac{\partial \phi}{\partial n} = \frac{\partial \varphi}{\partial n} + \frac{\partial \varphi^{vr}}{\partial n}, \tag{4.30}$$

then, using the chain rule gives

$$\frac{\partial \varphi^{vr}}{\partial n} = \frac{\partial \varphi^{vr}}{\partial r}\frac{\partial r}{\partial n} + \frac{\partial \varphi^{vr}}{\partial z}\frac{\partial z}{\partial n}. \tag{4.31}$$

Combining these yields the following expression for the normal velocity

$$\frac{\partial \phi}{\partial n} = \frac{\partial \varphi}{\partial n} + u^{vr} n_r + w^{vr} n_z, \tag{4.32}$$

where $n_r = \frac{\partial r}{\partial n} = \frac{dz}{ds}$, $n_z = \frac{\partial z}{\partial n} = -\frac{dr}{ds}$ are calculated using the splines. In a similar manner the tangential derivative for ϕ is found from

$$\frac{\partial \phi}{\partial s} = \frac{\partial \varphi}{\partial s} + u^{vr} s_r + w^{vr} s_z, \tag{4.33}$$

with $s_r = \frac{\partial r}{\partial s}$, $s_z = \frac{\partial z}{\partial s}$.

4.2.8 Smoothing and Redistribution of Nodes

As for the singly-connected bubble, a smoothing scheme is periodically applied to prevent saw-tooth instabilities occuring. Due to the closed bubble surface, however, the scheme must be altered slightly from Chapter 3. For $f = r, z, \varphi$ it is as follows:

$$\bar{f}_i = f_i - \lambda(f_{i-2} - 4f_N + 6f_i - 4f_{i+1} + f_{i+2}), \tag{4.34}$$

for $i = 3, N-1$. Although the potential ϕ is discontinuous over nodes $1/N+1$, the variables r, z and φ are continuous and so the nodes either side are used for the smoothing near the discontinuity point:

$$\begin{aligned}
\bar{f}_1 &= f_1 - \lambda(f_{N-1} - 4f_N + 6f_1 - 4f_2 + f_3), \\
\bar{f}_2 &= f_2 - \lambda(f_N - 4f_1 + 6f_2 - 4f_3 + f_4), \\
\bar{f}_N &= f_N - \lambda(f_{N-2} - 4f_{N-1} + 6f_N - 4f_{N+1} + f_2), \\
\bar{f}_{N+1} &= \bar{f}_1.
\end{aligned} \tag{4.35}$$

The vortex potential φ^{vr} is also smoothed; however, since it suffers a jump of Γ over nodes $1/N+1$ this value is added or subtracted when smoothing the nodes around the discontinuity

$$\begin{aligned}
\bar{f}_1 &= f_1 - \lambda(\ (f_{N-1} - \Gamma) - 4(f_N - \Gamma) + 6f_1 - 4f_2 + f_3), \\
\bar{f}_2 &= f_2 - \lambda(\ (f_N - \Gamma) - 4f_1 + 6f_2 - 4f_3 + f_4), \\
\bar{f}_N &= f_N - \lambda(f_{N-2} - 4f_{N-1} + 6f_N - 4f_{N+1} + (f_2 + \Gamma)\ ), \\
\bar{f}_{N+1} &= \bar{f}_1.
\end{aligned} \tag{4.36}$$

4.2.9 Relocating the Vortex Ring

Note that in Eqs. (4.9) and (4.11), if the parameter k is equal to one there will be a singularity at the end points of the integrals (where $\cos\theta = 1$). Due to the image method described in Eq. (4.13), k appears in the calculations as

$$k = \frac{2ar}{r^2 + (z-c)^2 + a^2} = \frac{2ar}{(r-a)^2 + 2ar + (z-c)^2} \leq 1. \tag{4.37}$$

So if $r \sim a$ and $z \sim c$ then $k \sim 1$. That is, if the vortex ring is too close to a node it will cause an instability. To prevent this the radius and height of the ring are recalculated if the minimum distance to the nodes falls below 3 times that of an element length of the bubble surface. When this happens the vortex-ring potential (and remnant potential) must be recalculated and then updated as described above.

4.2.10 Reconnection of Bubble

As the toroidal bubble re-expands the two sides of the bubble tend to move towards each other as the eye of the torus shrinks. If the bubble comes within 10^{-2} of the vertical axis it is assumed that the bubble 'reconnects' into a singly connected form. In order to carry out this transition the opposite procedure to jet impact is carried out (see Fig. 4.7)

- The node closest to the axis (node k in the diagram) is identified,
- The new nodes 1 and $N+1$ are placed on the axis midway between node k and its immediate neighbours,
- The nodes are renumbered (red numbers in Fig. 4.7).

The bubble is now singly connected again and can be updated in the manner described in Chapter 3.

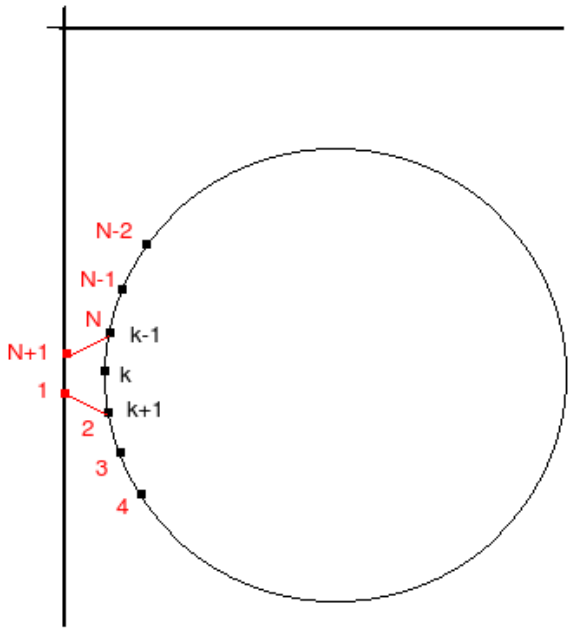

Figure 4.7: Reconnection process for the toroidal bubble. Only one side is shown since the bubble is reflected in the vertical axis.

4.2.11 Bubble Energy

The non-dimensional total energy of the fluid domain and the bubble content (for a fully three-dimensional bubble) is given up to a constant by

$$\frac{1}{2}\int_{S_{3D}} \phi \frac{\partial \phi}{\partial n} dS + \frac{1}{2}\Gamma Q + V(1-\delta^2 z_c) + \frac{\epsilon V}{\lambda - 1}\left(\frac{V_0}{V}\right)^{\lambda}, \tag{4.38}$$

where S_{3D} is the surface of the 3D bubble [117]. The four terms in this expression are labelled E_1 to E_4, respectively. The terms E_1 and E_2 are the kinetic energy of the fluid domain, E_2 being the energy associated with the circulation around the toroidal bubble (zero for singly-connected bubble) and Q being the volumetric flow rate through the eye of the torus. E_3 is the potential energy associated with the size and position of the bubble where z_c is the z-coordinate of the bubble centroid. (Note that δ is a buoyancy term which is neglected in this work). Finally, E_4 is the potential energy associated with the bubble contents.

Since the bubble is assumed to be axisymmetric the first term becomes

$$E_1 = \pi \int_{\partial\Omega} \phi \frac{\partial \phi}{\partial n} dS = \pi \sum_{i=1}^{n} \int_{s_i}^{s_{i+1}} \phi(s) \frac{\partial \phi}{\partial n}(s) r(s) ds, \tag{4.39}$$

using the spline discretisation of the surface. These segment integrations can then be calculated using a 6-point Gaussian quadrature scheme.

Volumetric Flow Rate Through Torus

The volumetric flow rate can be defined by

$$Q = \int\int_A \mathbf{v} \cdot \mathbf{A} dA, \tag{4.40}$$

where A is the area of the torus and

$$\mathbf{A} = A\mathbf{n} = \pi r_{min}^2 \mathbf{e}_z. \tag{4.41}$$

Then, using the axisymmetry of the bubble

$$Q = \pi r_{min}^2 \int_0^{2\pi} \int_0^{r_{min}} \frac{\partial \phi}{\partial z} r \; dr d\theta = 2\pi^2 r_{min}^2 \int_0^{r_{min}} \frac{\partial \phi}{\partial z} r \; dr. \tag{4.42}$$

The boundary integral equation for φ is used to calculate values of φ along the line of integration as well as above and below it. A finite difference approximation of $\frac{\partial \varphi}{\partial z}$ at some point (r_i, z_i) is then

$$\frac{\partial \varphi}{\partial z}(r_i, z_i) = \frac{\varphi(r_i, z_i + dh) - \varphi(r_i, z_i - dh)}{2dh}, \tag{4.43}$$

for some small distance dh (usually taken to be 10^{-2}). An approximate value of $\frac{\partial \phi}{\partial z}$ can then be obtained as

$$\frac{\partial \phi}{\partial z}(r_i, z_i) = \frac{\partial \varphi}{\partial z}(r_i, z_i) + w^{vr}(r_i, z_i). \tag{4.44}$$

The integral in Eq. (4.42) is then approximated using Gaussian quadrature.

4.2.12 Bubble Volume and Jet Velocity

The bubble surface is parameterised by a curve $(r(t), z(t))$ so using the parametric form of the volume of a solid of revolution the bubble volume is

$$V = \int_{\partial\Omega} \pi r^2 \frac{dz}{dt} dt. \tag{4.45}$$

This integral is evaluated using Gaussian quadrature with the variables r and z represented using the periodic splines discussed earlier in this chapter.

For the pre-toroidal bubble, the jet velocity can simply by calculated as the normal derivative of the potential at the first node (see Chapter 3). For the toroidal bubble this is not possible since the jet now flows through the eye of the torus. In this case, a procedure similar to that described above for the volumetric flow rate is followed. The potential ϕ is calculated for two points on the axis, defined as

$$U = (0, z_1 + \delta), \quad L = (0, z_1 - \delta). \tag{4.46}$$

The jet velocity is then approximated by

$$\text{jet velocity} \approx \frac{\phi(U) - \phi(L) + \Gamma}{2\delta}. \tag{4.47}$$

4.2.13 Pressure Field

As in Chapter 3, the pressure at a point $\mathbf{x}$ in the domain can be found using the Bernoulli equation which, when non-dimensionalised, gives

$$p(\mathbf{x}) = \frac{\partial \phi}{\partial t} - \frac{1}{2}|\nabla \phi|^2 + 1. \tag{4.48}$$

For the toroidal bubble ϕ cannot be calculated directly from the integral equation since it is discontinuous. However, the remnant potential can be calculated at any point in the fluid using the integral equation and the vortex potential by Eq. (4.23). The potential $\phi(\mathbf{x})$ at some point $\mathbf{x}$ in the fluid is $\phi(\mathbf{x}) = \varphi(\mathbf{x}) + \varphi^{vr}(\mathbf{x})$. At the midpoint of the rigid wall (the origin) the pressure is given by

$$p(0,0) = \frac{\partial \varphi(0,0)}{\partial t} + 1, \tag{4.49}$$

since the vortex velocities are zero at the origin (see Eqs. (4.14),(4.15)).

4.3 Results

4.3.1 Validations

In Fig. 4.8, the normal velocites $\frac{\partial \phi}{\partial n}$ are plotted against bubble surface arclength for the singly-connected bubble just before jet impact and for the corresponding toroidal bubble once the impact surface has been smoothed and the vortex ring placed inside the bubble. At the instant of jet impact node 1 is moving rapidly towards the opposite side of the bubble (node $N+1$) which has a much lower velocity. Once the impact point is smoothed the velocity of the 'new' node $1/N+1$ takes a value roughly that of the average of the velocities of the previous nodes labelled 1 and $N+1$. The normal velocities at the remaining nodes (which have not been moved) show a good agreement with their values before the transition.

For an inviscid fluid the total energy given by Eq. (4.38) should remain constant throughout the computations due to the assumption of incompressibility. The impact of the liquid jet is a violent event though and this, along with the change in topology of the fluid domain, results in strong instabilities in the toroidal bubble surface. Although these instabilities are suppressed by the smoother described in Section 4.2.8, they are

not completely removed.

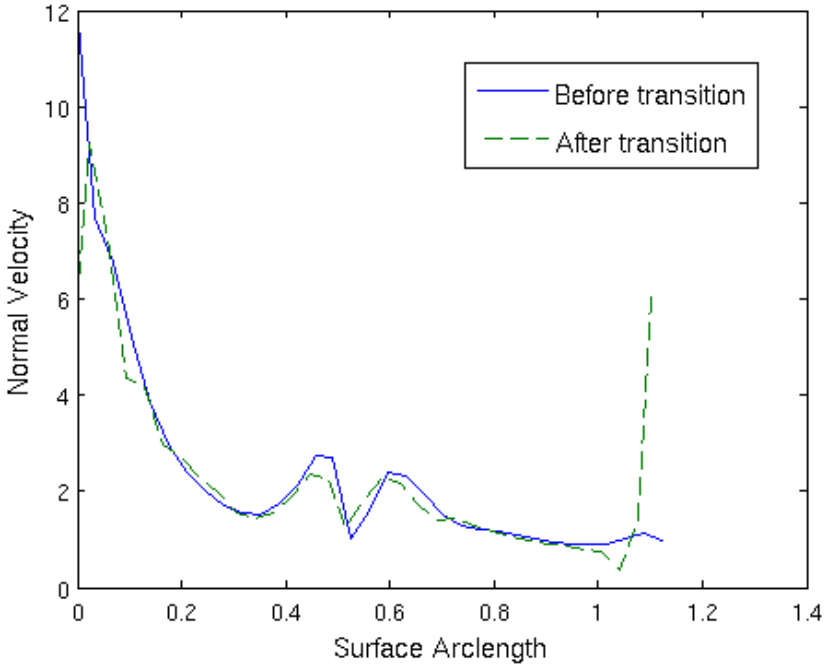

(a) $N = 32$.

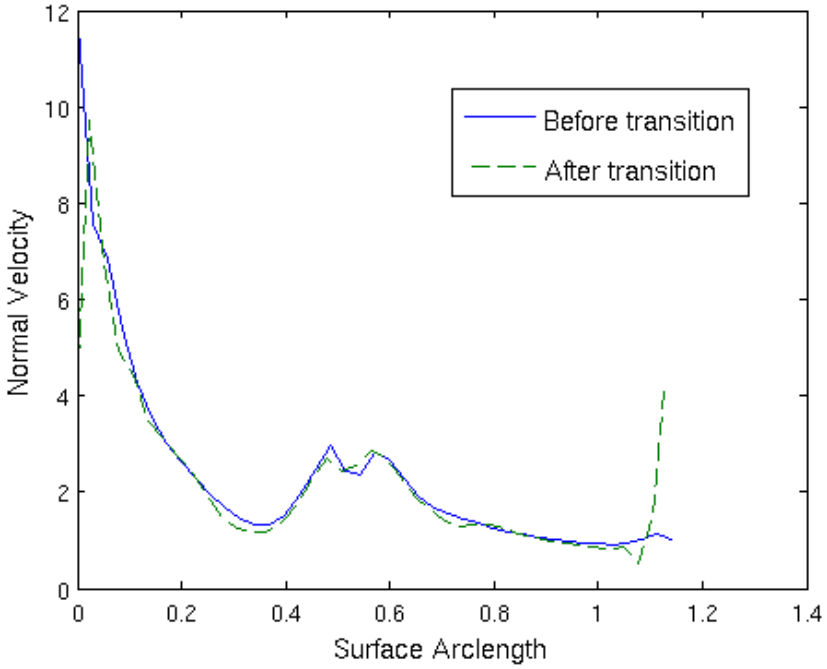

(b) $N = 40$.

Figure 4.8: Comparing the normal velocities before and after the transition from a singly-connected bubble to a toroidal bubble for 32 and 40 nodes.

4.3.2 Inviscid Fluid

For a bubble in an inviscid fluid and neglecting surface tension, the bubble surface at snapshots in time are shown in Figs. 4.9, 4.10 for the case $h = 2$. Fig. 4.9a shows the initial growth and collapse phase from an initial size $R_0^* = 0.165$ (Dark blue line). Despite the presence of the rigid wall the initial growth is approximately spherical. As the bubble collapses, though, the fluid (and thus the bubble surface) nearer the wall moves slower due to the higher pressure in that region. This ultimately leads to the formation of a liquid jet in the later stages (yellow line) and subsequent jet impact at roughly $t = 2.12$.

Shortly after the transition to a toroidal form the bubble reexpands due to the bubble contents. This is shown in Fig. 4.9b where the plots run from $t = 2.12$ (innermost) to $t = 2.256$ (outermost). Following the procedure outlined in Section 4.2.10, once a node reaches within 0.01 of the z-axis the bubble is reconnected, as seen in Fig. 4.10a. The second singly-connected phase is very short in this case with a jet forming almost immediately; this is thought to be due to the reconnection process, which occurs at the top of the bubble and the connected regions accelerating downwards. Throughout the oscillations the bubble is travelling towards the rigid wall at $z = 0$ due to Bjerknes forces. Once the bubble reaches its second toroidal phase and re-expands it is very close to the boundary (see Fig. 4.10b). At this point the circulation of the flow means that there is fluid moving down through the torus and impacting on the rigid boundary. It will then move radially outwards back into the bulk of the fluid. This will cause shear stress to the boundary which is known to be a cause of cavitation damage.

The effect of initial stand-off distance for a bubble in an inviscid fluid is shown in Figs. 4.11, 4.12 and 4.13. In Chapter 3, it was found that the jet velocities and pressures up until jet impact for $h = 2$ exceeded those for the case $h = 1.5$. However, this is a result of jet impact occuring closer to bubble minimum volume for $h = 2$ than for $h = 1.5$. When computations are able to proceed into the toroidal phase, we see higher jet velocities and pressures occuring as the initial stand-off distance is decreased. The jet velocity for the toroidal bubble is the vertical speed of the fluid moving through the eye of the torus and is calculated using Eq. (4.47).

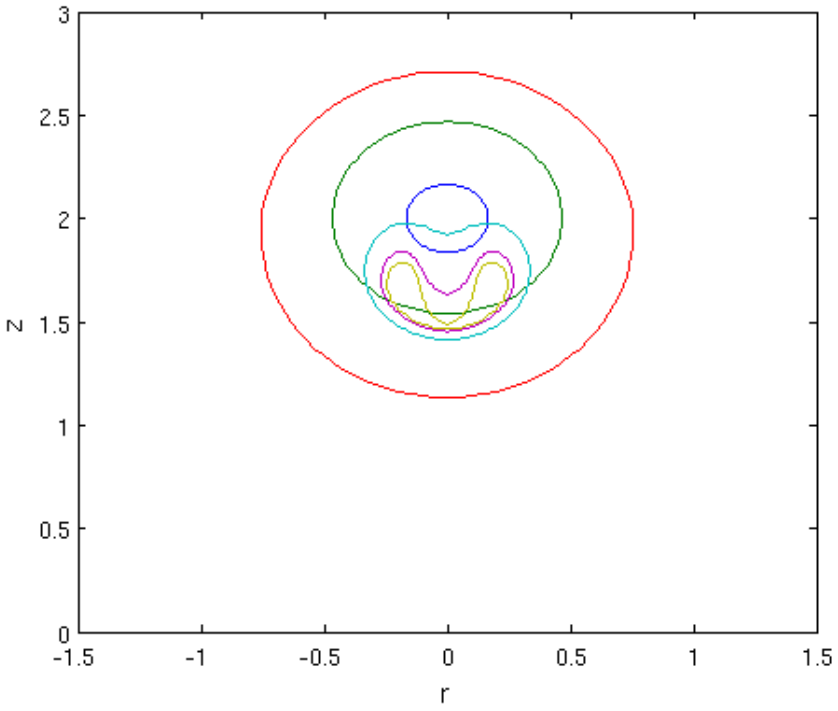

(a) Initial growth and collapse (until jet impact).

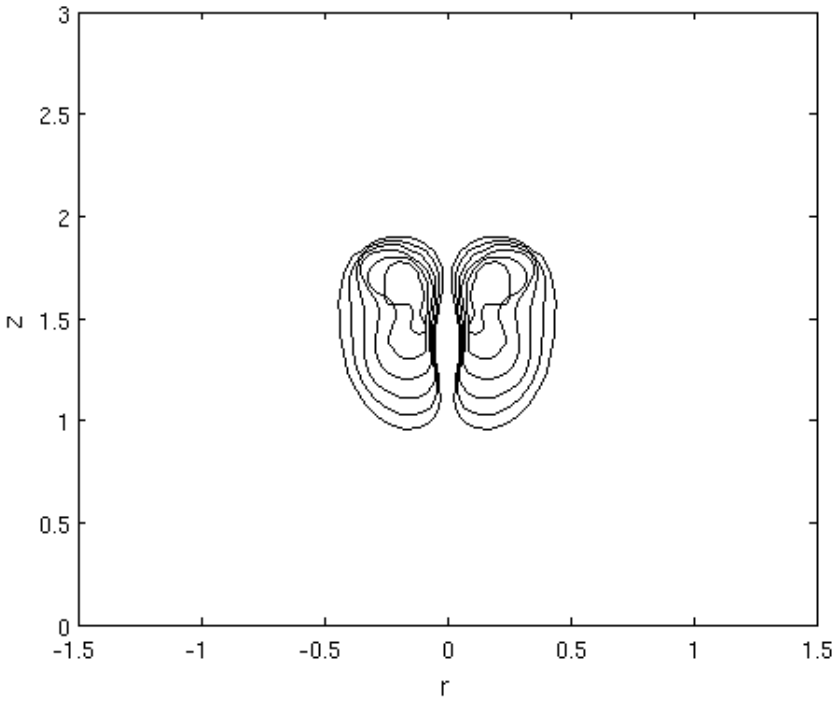

(b) Reexpansion of bubble after transition to a toroidal form.

Figure 4.9: Bubble surfaces for the initial singly connected phase (a) and first toroidal phase (b) for the inviscid case with $h = 2$.

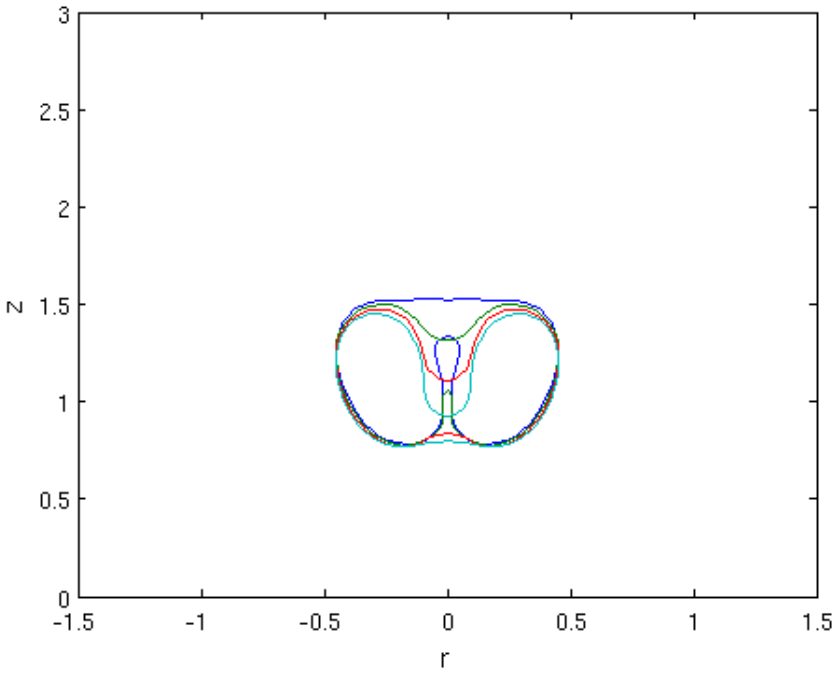

(a) Second singly connected phase once reconnection of the bubble has occured.

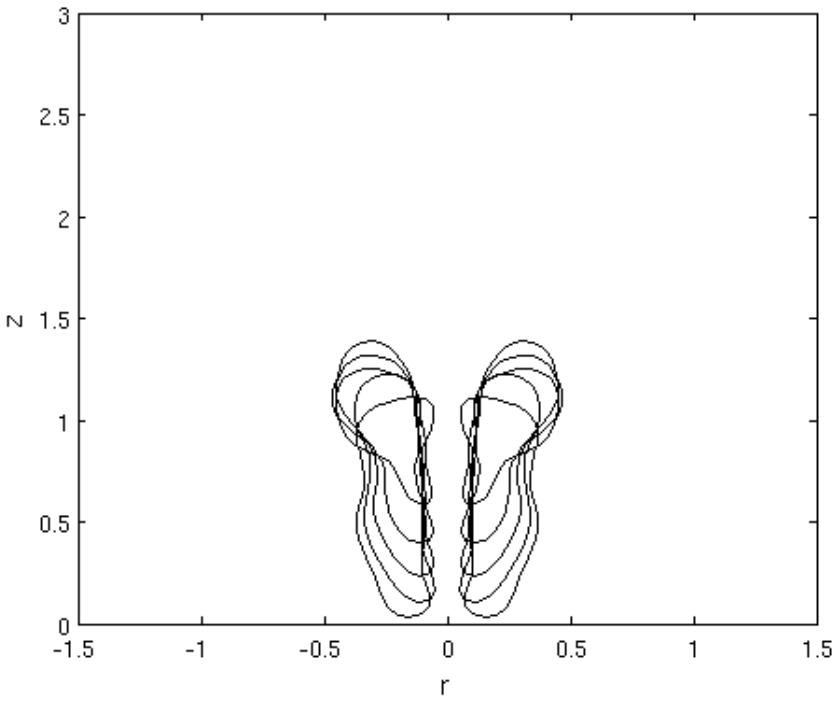

(b) Second toroidal phase.

Figure 4.10: Bubble surfaces for the second singly connected phase (a) and the second toroidal phase (b) for the inviscid case with $h = 2$.

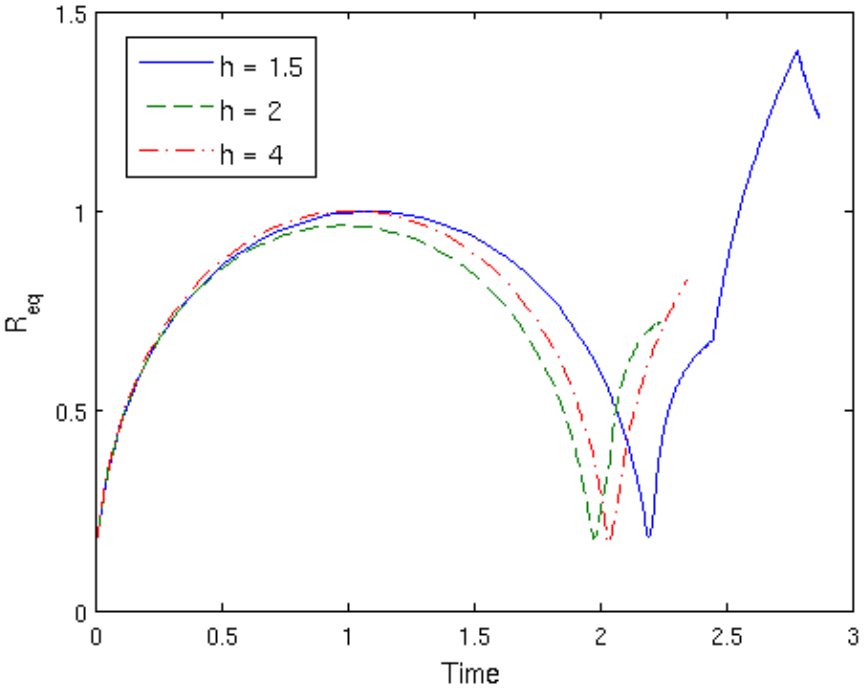

Figure 4.11: Equivalent radius R_{eq} for a bubble in an inviscid fluid with $h = 1.5, 2, 4$.

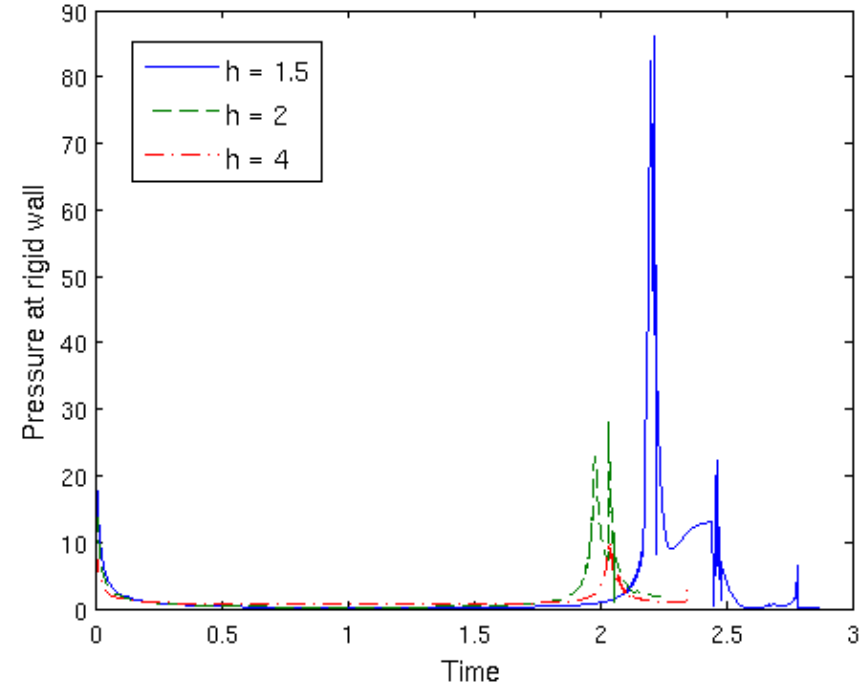

Figure 4.12: Pressure at the rigid wall for a bubble in an inviscid fluid with $h = 1.5, 2, 4$.

Instabilities are observed after jet impact, particularly in the jet velocity. This is due to the violence of the jet impact and the difficulty in modelling a change of geometry. After jet impact, the toroidal bubble surface is highly corrugated which leads to spurious velocities and thus instabilities. Over time, however, these instabilities disappear as the bubble grows and the surface becomes smoother.

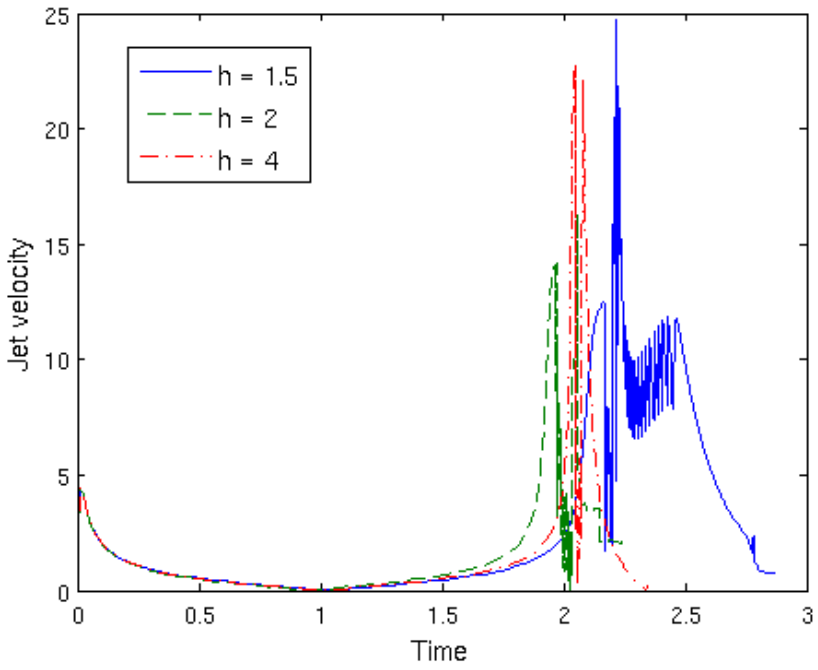

Figure 4.13: Jet velocities vs. time for a bubble in an inviscid fluid with $h = 1.5, 2, 4$.

4.3.3 Effects of Viscoelasticity

It is known that the viscosity of the surrounding fluid tends to inhibit a cavitation bubble forming a jet and thus transitioning to a toroidal form. It was seen in Chapter 3, however, that jets can form for a bubble in a viscoelastic fluid due to elastic, surface tension or inertial effects overcoming the influence of the fluid viscosity. Furthermore, as will be seen in Chapter 5, the application of a pressure field can often lead to liquid jets forming.

Bubble surfaces for the case $Re = De = 10$ and $h = 2$ are shown in Figs. 4.14 - 4.16. Fig. 4.14 shows the first singly-connected phase with the formation of the liquid jet. As discussed in Chapter 3, the viscoelasticity in this case only has an effect near the end of collapse. The centre of the bubble is thinner than in the inviscid case with two 'lobes' forming either side. The bubble is still shrinking as jet impact occurs in this case. The rest of the collapse phase is shown in Fig. 4.15 in toroidal form. Due to the very thin centre of the bubble and fluid elasticity the eye of the torus rapidly grows with the centre of the bubble pulled outwards. The bubble then expands due to its contents , as shown in Fig. 4.16.

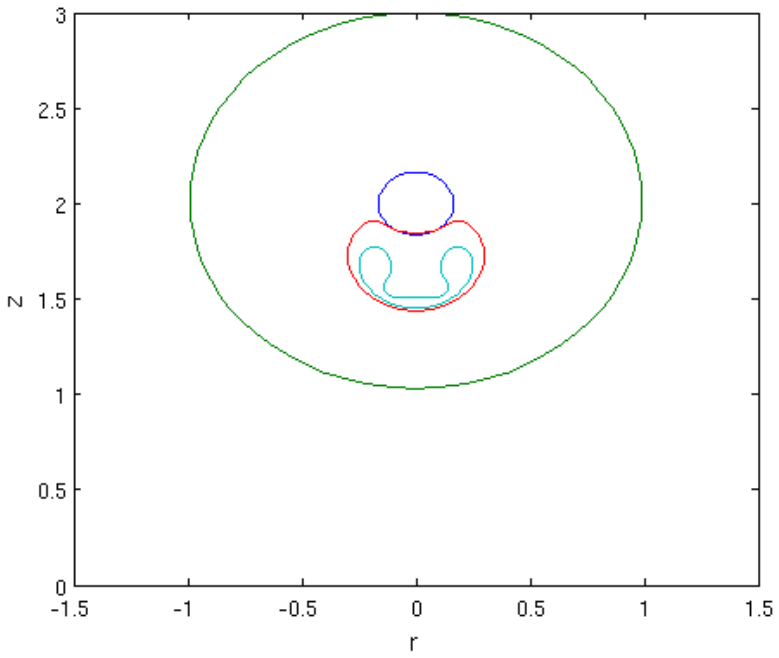

Figure 4.14: First singly-connected phase for parameters $h = 2$, $Re = De = 10$. Initial (dark blue) and final (light blue) times are $t = 0$ and $t \approx 2.101$, respectively.

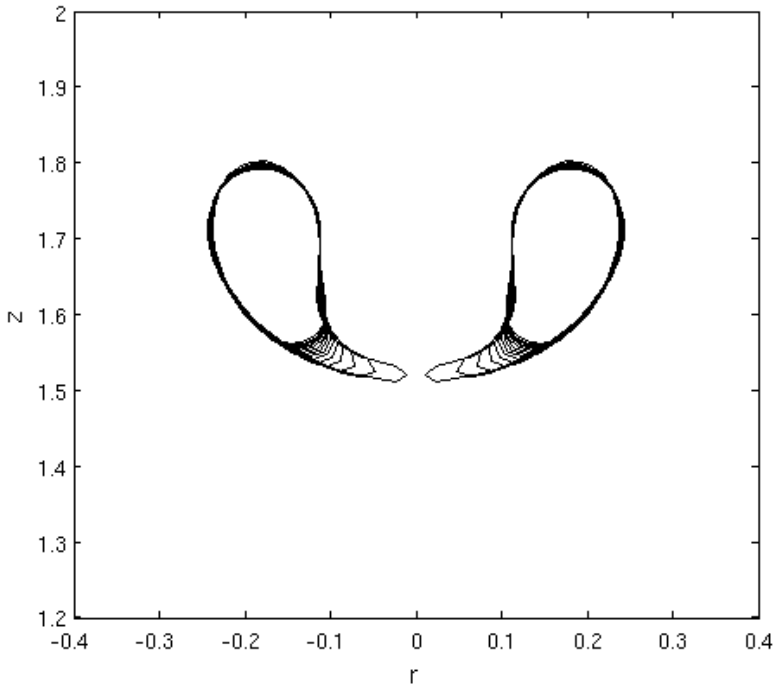

Figure 4.15: Collapse phase in toroidal form for parameters $h = 2$, $Re = De = 10$. Initial (outer) and final (inner) times are $t \approx 2.101$ and $t \approx 2.148$, respectively.

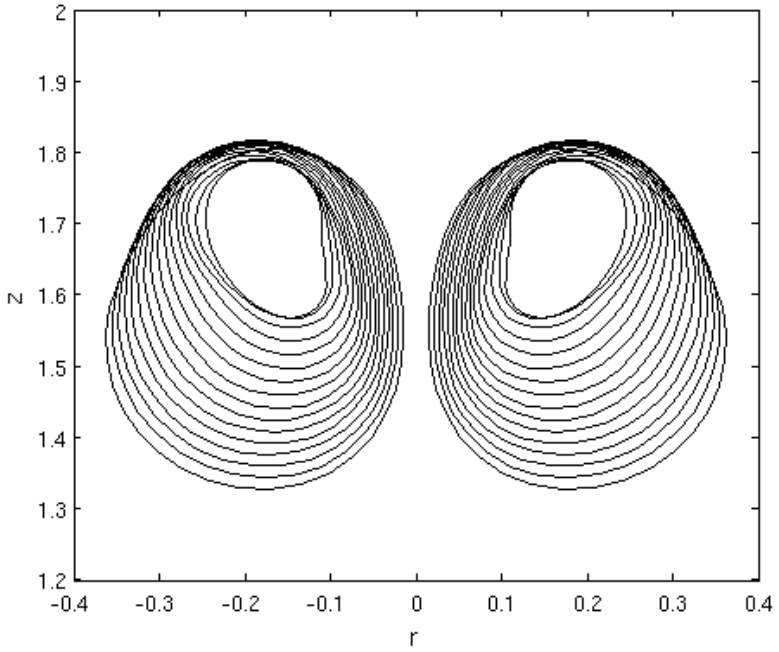

Figure 4.16: Growth phase in toroidal form for parameters $h = 2$, $Re = De = 10$. Initial (inner) and final (outer) times are $t \approx 2.148$ and $t \approx 2.415$, respectively.

Figs. 4.17 and 4.18 show bubble size, bubble position, jet velocities and pressures (at the rigid wall) for two viscoelastic cases with $h = 2$, $De = 10$ and $Re = 10, 20$. For both cases, a liquid jet forms and the bubbles become toroidal. Due to the lower viscosity, the case $Re = 20$ shows a more rapid collapse with more movement towards the bubble wall. Higher jet velocities are also observed although both cases produce lower jet velocities than the corresponding inviscid case, as expected (see Fig. 4.13). This is echoed in the pressure at the rigid wall; the maximums obtained are approximately nineteen and sixteen for the cases $Re = 20$ and $Re = 10$, respectively. Note that these values are non-dimensionalised and correspond to 1.919MPa and 1.616MPa, respectively. Large negative pressures are also produced up to roughly -1.2MPa; these could result in the inception of other cavitation bubbles and potentially more damage to the rigid wall.

The bubble centroid is also seen to move away from the wall slightly in the toroidal phase due to the fluid elasticity causing the bubble to rebound and the eye of the torus to grow as the bubble continues to collapse (as in Fig. 4.15). For $Re = 20$, $De = 10$ the bubble centroid is seen in Fig. 4.17a to move away from the wall a second time with negative jet velocities observed. This occurs during the reconnected phase, in which the bubble is singly connected again (Fig. 4.19). At this point the fluid rheology is actually overcoming the Bjerknes effect of the wall. This is another example of the interesting competition between forces which makes the dynamics of gas-filled bubbles difficult to predict.

The effect of initial stand-off distance for a bubble in an Oldroyd-B fluid with $Re = De = 10$ is shown in Figs. 4.20 and 4.21 for $h = 1.5, 2, 2.5$. In contrast to the inviscid case, the distance of the bubble centroid from the rigid wall does not decrease monotonically for a bubble in a viscoelastic fluid. As the bubble re-expands due to the bubble contents, the elasticity of the fluid causes the bubble to rebound away from the wall slightly in all cases. Similar to the inviscid case, however, the pressures produced at the rigid wall increase with decreasing h. For $h = 2.5$, the bubble rebounds just before jet impact and does not become toroidal since the Bjerknes effect of the wall is no longer powerful enough to overcome the viscous effects of the fluid.

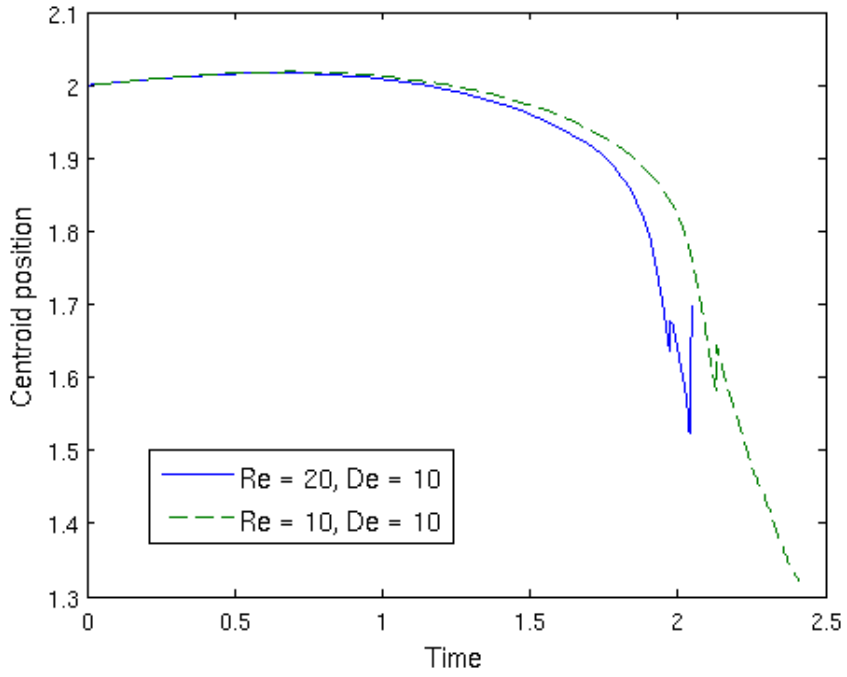

(a) Centroid position vs. time.

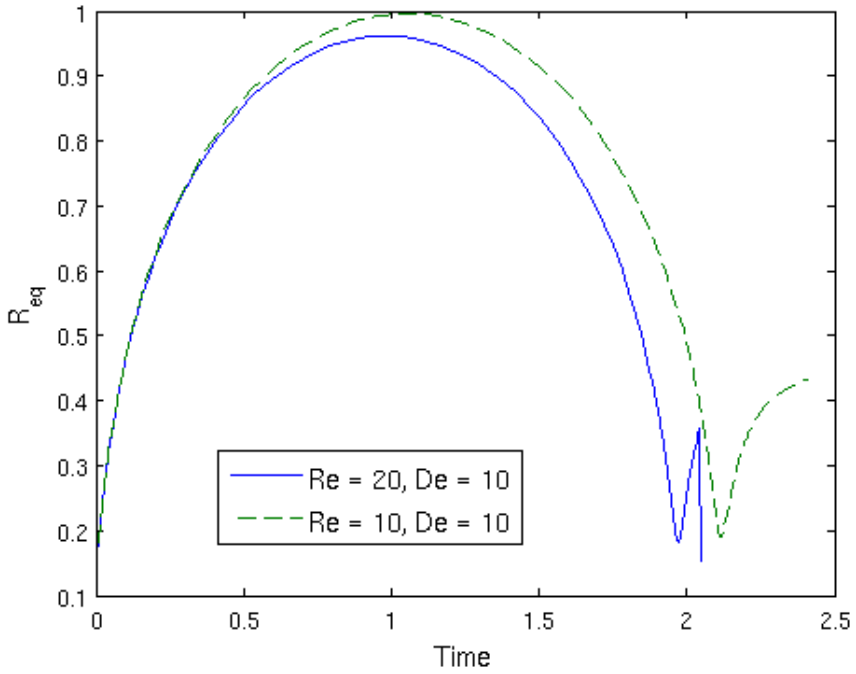

(b) Equivalent radius vs. time.

Figure 4.17: Effect of changing viscosity on bubble position and size for a bubble situated in an Oldroyd-B fluid with parameters $h = 2$, $1/We = 0.0718$, $De = 10$ and $Re = 10, 20$.

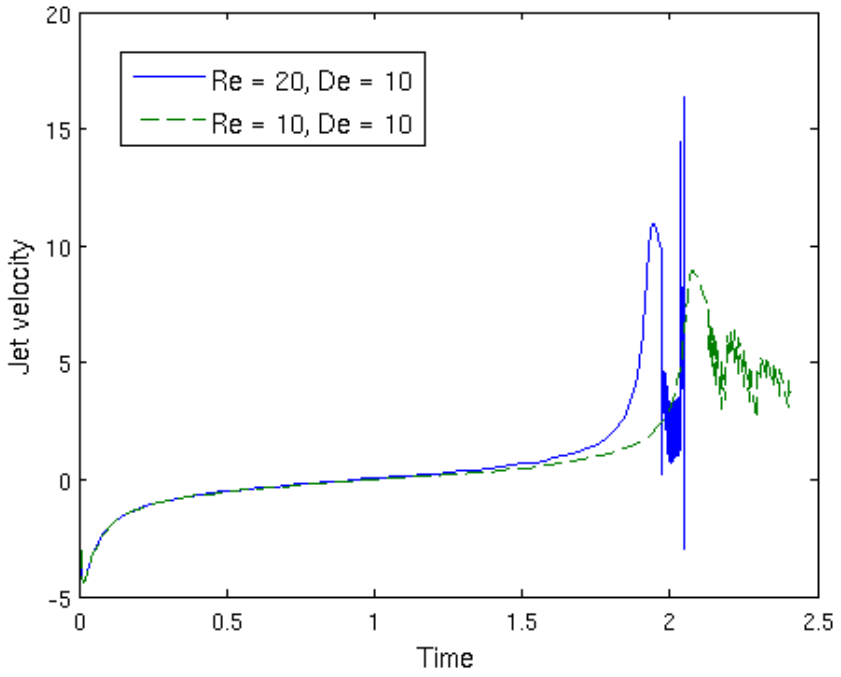

(a) Jet velocity vs. time.

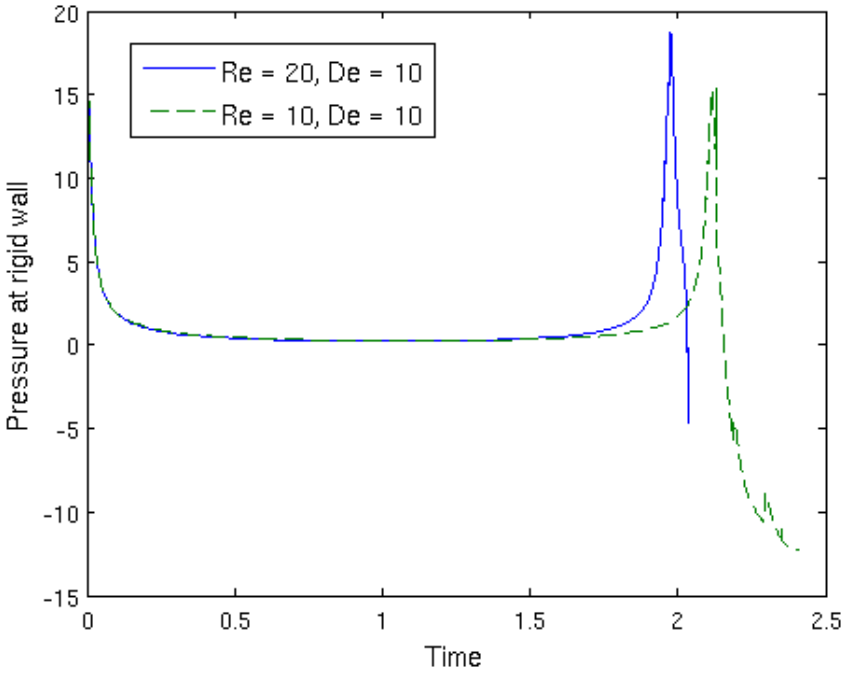

(b) Pressure at the centre of the rigid wall vs. time.

Figure 4.18: Effect of changing viscosity on jet velocities and wall pressures for a bubble situated in an Oldroyd-B fluid with parameters $h = 2$, $1/We = 0.0718$, $De = 10$ and $Re = 10, 20$.

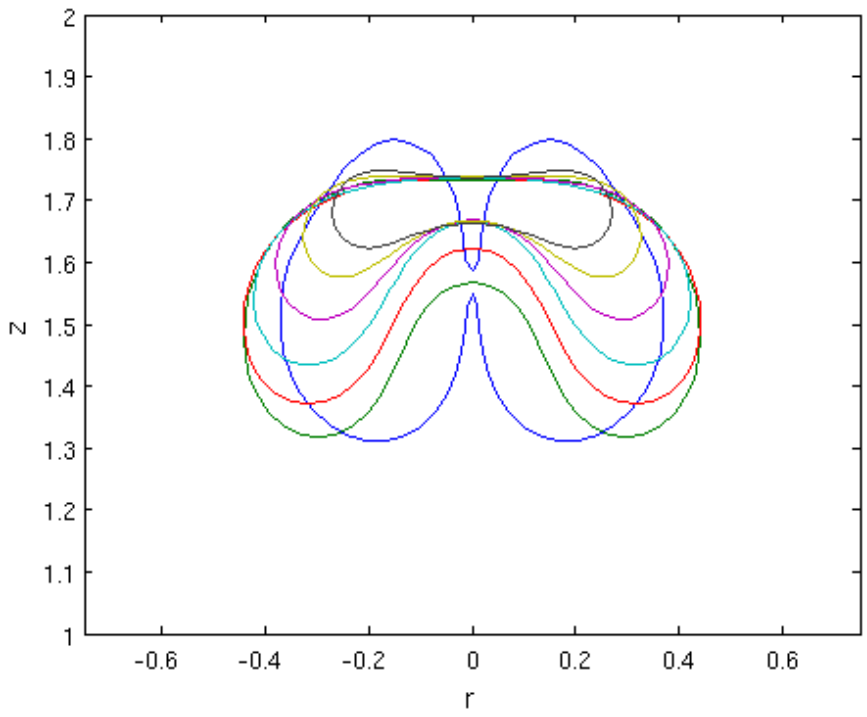

Figure 4.19: Second singly-connected phase (once the bubble is reconnected) for parameters $h = 2$, $Re = 20$ and $De = 10$. Initial (dark blue solid line) and final (black solid line) times are $t \approx 2.041$ and $t \approx 2.069$, respectively.

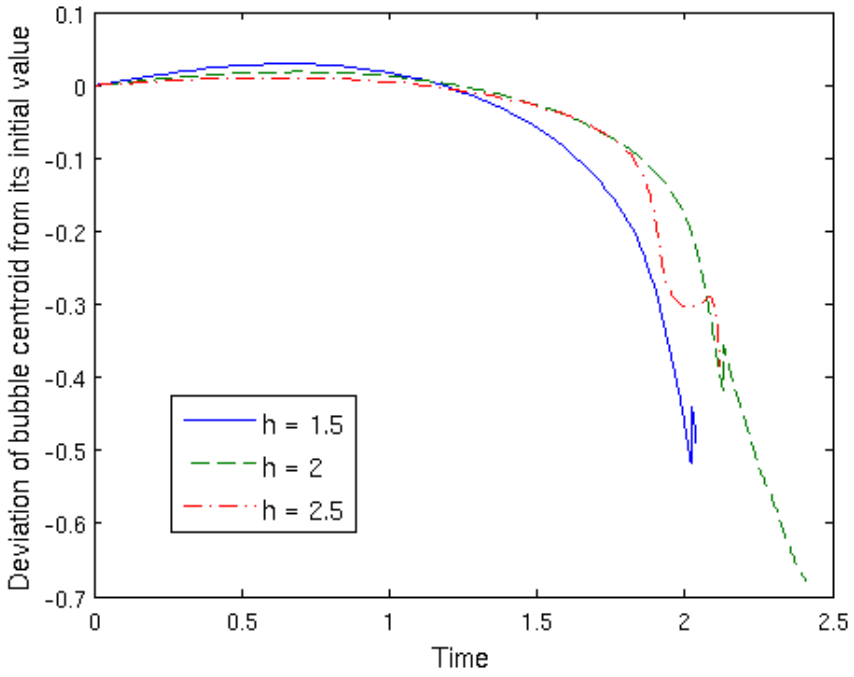

Figure 4.20: Deviation of the bubble centroid from its initial position for $Re = De = 10$ and a range of initial stand-off distances.

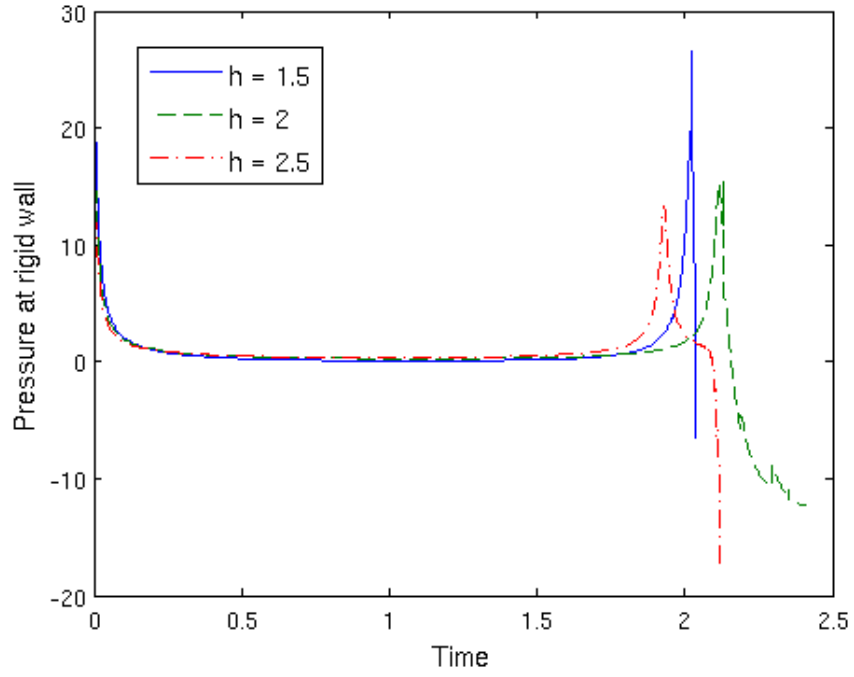

Figure 4.21: Pressure at the rigid wall for $Re = De = 10$ and a range of initial stand-off distances.

4.4 Conclusions

In this chapter, the boundary element method of Chapter 3 has been extended to model toroidal bubbles in a viscoelastic fluid. The potential is discontinuous for the toroidal bubble and the fluid possesses a circulation due to the doubly-connected domain. These problems are accounted for using the vortex ring method, in which a vortex ring is placed within the bubble and the potential due to this ring subtracted from the actual fluid potential.

In Chapter 3 it was observed that a bubble in a viscoelastic fluid is less likely to form a liquid jet and become toroidal. It is not impossible, however, and the dynamics seem to be mostly determined by the relationship between the parameters Re and De, as well as the initial stand-off distance h. If a bubble in a viscoelastic fluid does become toroidal it is observed that the bubble shape at jet impact has a thinner centre due to a build up of stress in this region. This results in the bubble rebounding in its toroidal form and potentially moving away from the rigid wall. Due to this, negative pressures occur at the rigid wall which is a feature not observed for a bubble in an inviscid fluid. It is possible that these negative pressures could cause cavitation to occur at the wall which has implications to the damage which is caused. A decrease in viscosity also leads to higher velocities and pressures produced, similarly to the singly-connected bubble considered in Chapter 3.

It is also found that the pressures produced at the wall from the bubble oscillations increase as the initial stand-off distance is decreased for a bubble in both an inviscid fluid and an Oldroyd-B fluid. This suggests that cavitation bubbles closer to a rigid surface will cause more damage. If the bubble is close enough, the bubble will attach to the boundary as it grows and the liquid jet will strike the wall directly.

Chapter 5

Modelling Cavitation Bubbles in an Ultrasound Field

5.1 Introduction

Cavitation occurs in many different forms in a wide variety of applications. A particularly prevalent example is that of *acoustic cavitation* in which the application of an ultrasound field results in rupturing of the fluid and the formation of cavities. Common examples of the use of acoustic cavitation are extracorporeal shock wave lithotripsy (ESWL) and sonoporation. Detailed discussions of these applications are provided in Chapter 1.

Due to the high velocities and very short length and time scales involved, experiments that seek to investigate interactions between cavitation bubbles and a pressure field are difficult to perform. Recently, however, experimental findings have improved due to advances in technology such as 'single-bubble cavitation' and high-speed photography. This has allowed a single bubble to be acoustically forced and measurements such as jet velocities obtained. Numerical investigations provide an alternative technique with which insight into the dynamics can be gained.

In this chapter, the boundary element method developed in Chapter 3 and 4 is extended to model the interaction between a pressure pulse and a single, gas filled bubble. To begin with, a simple step function model of the pressure pulse is presented, following the work of Klaseboer et al. [59]. A more realistic description of a typical pulse is then presented to more accurately simulate the conditions present in shock wave lithotripsy.

5.2 Review of BEM Model

A single bubble in an Oldroyd-B fluid is now considered, both in an infinite fluid and near a rigid wall. The BEM modelling of this situation is described in Chapters 3 and 4 for a freely oscillating bubble. At each node $\mathbf{x}_i = (r_i, z_i)$ for $i = 1, \ldots, N+1$ on the discretised bubble surface the equations for the position, potential and stress at these points are (see Equations (3.69) - (3.71))

$$\frac{\mathrm{D}\mathbf{x}_i}{\mathrm{D}t} = \nabla\phi(\mathbf{x}_i), \tag{5.1}$$

$$\begin{aligned}\rho\frac{\mathrm{D}\phi(\mathbf{x}_i)}{\mathrm{D}t} &= p_\infty(\mathbf{x}_i) - p_0\left(\frac{V_0}{V}\right)^\kappa + \frac{\rho}{2}|\nabla\phi(\mathbf{x}_i)|^2 \\ &\quad - 2\eta_s\frac{\partial^2\phi(\mathbf{x}_i)}{\partial n^2} - T^p_{nn}(\mathbf{x}_i) + \sigma\kappa(\mathbf{x}_i)\end{aligned} \tag{5.2}$$

$$\lambda_1\frac{\mathrm{D}T^p_{nn}(\mathbf{x}_i)}{\mathrm{D}t} = -T^p_{nn}(\mathbf{x}_i) + 2\left(\lambda_1 T^p_{nn} + \eta_p\right)\frac{\partial^2\phi(\mathbf{x}_i)}{\partial n^2}, \tag{5.3}$$

where all parameters are defined as in Chapters 3 and 4. For the freely oscillating bubble, the pressure term is constant, given by $p_\infty(\mathbf{x}_i) = P_{ref} = 1 \times 10^5$Pa for all nodes. In this chapter, the effects of a pressure pulse interacting with the bubble are introduced by modifying the Bernoulli equation (5.2) through the term p_∞.

5.3 Step Function Pressure Pulse

A simple first approximation for the pressure pulse is to replace the constant term p_∞ in the Bernoulli equation (5.2) by a step function in time. This approach was introduced by Klaseboer et al. [59] for a bubble in an inviscid fluid. The pressure term at each node $\mathbf{x}_i = (r(i), z(i))$ is written as

$$p_\infty(\mathbf{x}_i) = \begin{cases} P_{ref}: & z(i) > z_0(1) + z^{(p)} - tU_s + W_s \\ P_s: & z_0(1) + z^{(p)} - tU_s < z(i) < z_0(1) + z^{(p)} - tU_s + W_s \\ P_{ref}: & z(i) < z_0(1) + z^{(p)} - tU_s, \end{cases}$$

where $z_0(1)$ is the initial position of node 1, W_s, U_s are the width and velocity of the pressure pulse, respectively and P_s is the strength of the pulse. The initial configuration of the bubble and pressure pulse are displayed schematically in Figure 5.1. The variable $z^{(p)}$ is the initial distance of the pulse from the bubble; this can be varied so that the

pulse hits at different stages in the bubble's oscillation cycle.

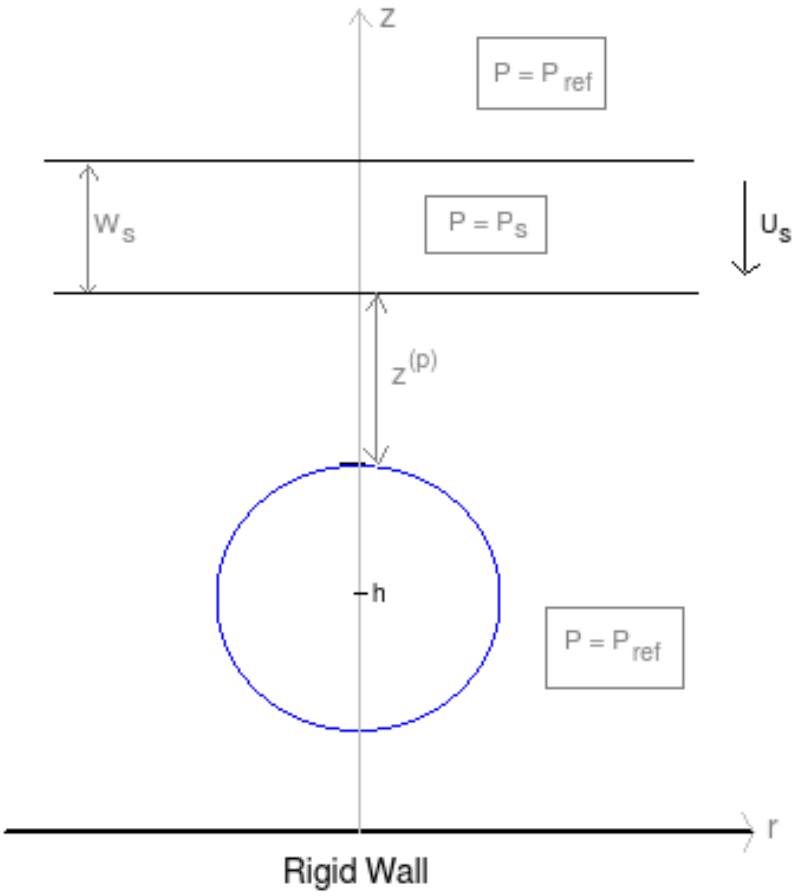

Figure 5.1: Initial configuration of the bubble and pressure pulse.

For the inviscid case, Klaseboer [59] compared jet velocities and bubble centroid positions with Free-Lagrange Method (FLM) and Arbitrary Lagrangian-Eulerian (ALE) simulations by Jamaluddin [53] and Ding and Gracewski [36], respectively. Although the BEM simulations of Klaseboer et al. do not take into account compressibility of the fluid or wave propagation in the bubble they found good qualitative agreement with the more complex models presented in [53] and [36] for jet velocities, bubble centroid position and velocity vectors. It can be argued, therefore, that the boundary element method can be used successfully to approximately model the interaction between a bubble and a pressure pulse despite its simplicity. It also suggests that the dynamics of the bubble before jet impact are dominated by inertia rather than compressibility effects.

Pressure pulse velocity

For a shock wave, the pressure P_s and shock velocity U_s are not independent [59]. Given a shock strength P_s, the shock velocity can be calculated from the Equations (5.4) - (5.6)

$$\rho^* = \left(\frac{P_s}{B} + 1\right)^{1/n} \rho_{Rd}, \tag{5.4}$$

$$u^* = u_u + \sqrt{\left(\frac{\rho^* - \rho_u}{\rho^* \rho_u}\right)(P_s - P_u)}, \tag{5.5}$$

$$U_s = a_k + A_k u^*. \tag{5.6}$$

Equation a) is a rearrangement of the Tait equation of state which is assumed to apply. This is reasonable as the Tait equation only produces non-negligible errors when the liquid pressure exceeds 10GPa [50], which is higher than any pressures expected here. The parameter $\rho_{Rd} = 999.96\text{kg/m}^3$ is the reference density of water at zero pressure, B and n are constants with values of 3.31×10^8 and 7, respectively. The post-shock density ρ^* from Equation a) is then substituted into Equation b) in which the subscript u indicates the value of a variable pre-shock. Equation b) arises from considering discontinuity conditions across the shock wave [41]. This then gives u^*, the post-shock particle velocity, which is substitued into Equation c) to finally give the shock velocity U_s. We take values of $a_k = 1480m/s$ and $A_k = 1.815$, respectively which are determined from shock Hugoniot data of water [72]. We assume that the rheology of the fluid has no effect on these values.

Non-dimensionalisation

The same non-dimensionalisation employed in Chapters 3 and 4 is used, i.e.

$$r^* = \frac{r}{R_m}, \quad z^* = \frac{z}{R_m} \tag{5.7}$$

$$t^* = \frac{U}{R_m} t = \frac{t}{R_m}\left(\frac{P_{ref}}{\rho}\right)^{1/2} \tag{5.8}$$

$$\phi^* = \frac{\phi}{U R_m} = \frac{\phi}{R_m}\left(\frac{\rho}{P_{ref}}\right)^{1/2}. \tag{5.9}$$

This results in the equations presented in Table 5.1. These are, of course, identical to the equations presented in Chapter 3 for the freely oscillating bubble with the exception of the new term p^*_∞ which represents the influence of the pressure pulse and is time/spatially dependent, rather than constant.

Table 5.1: Non-dimensionalised equations.

Newtonian Fluid
$$\frac{\mathrm{D}\mathbf{x}^*}{\mathrm{D}t^*} = \nabla\phi^*$$ $$\frac{\mathrm{D}\phi^*}{\mathrm{D}t^*} = p^*_\infty + \frac{1}{2} \mid \nabla\phi^* \mid^2 - \frac{2}{Re}\frac{\partial^2\phi^*}{\partial n^{*2}} + \frac{C}{We} - \varepsilon\left(\frac{\bar{R}_0}{R}\right)^{3\kappa}$$
Oldroyd-B Fluid
$$\frac{\mathrm{D}\mathbf{x}^*}{\mathrm{D}t^*} = \nabla\phi^*,$$ $$\frac{\mathrm{D}\phi^*}{\mathrm{D}t^*} = p^*_\infty + \frac{1}{2} \mid \nabla\phi^* \mid^2 - \frac{2E}{Re}\frac{\partial^2\phi^*}{\partial n^{*2}} - \tau^{p^*}_{nn} + \frac{C}{We} - \varepsilon\left(\frac{\bar{R}_0}{R}\right)^{3\kappa}$$ $$\frac{\mathrm{D}\tau^{p^*}_{nn}}{\mathrm{D}t} = \frac{1}{De}\left[- \tau^{p^*}_{nn} - 2\left(De\tau^{p^*}_{nn} + \frac{(1-E)}{Re}\right)\frac{\partial^2\phi^*}{\partial n^{*2}}\right]$$

The pulse is determined completely by the non-dimensionalised shock parameters

$$P^*_s = P_s/P_{ref}, \quad W^*_s = W_s/R_m, \quad U^*_s = U_s\sqrt{(\rho/P_{ref})}, \tag{5.10}$$

which are the non-dimensionalised shock strength, width and speed, respectively.

5.3.1 Results

Infinite Fluid

It will be shown that the point in the bubble oscillation cycle at which the pressure pulse impacts the bubble greatly affects the ensuing dynamics. For Figures 5.4 - 5.6

the following labels are defined

- Case i): $V = V_0$,
- Case ii): $V = V_{\max}/3$ (growing),
- Case iii): $V = 2V_{\max}/3$ (growing),
- Case iv): $V = V_{\max}$,
- Case v): $V = V_{max} - (V_{\max} - V_{min,2})/3$ (collapsing),
- Case vi): $V = V_{max} - 2(V_{\max} - V_{min,2})/3$ (collapsing),

where $V_{min,2}$ is the second local volume minimum. These six cases form a discrete approximation of one oscillation cycle of the bubble and allows us to compare fluids with different rheology (in which bubbles will oscillate differently). Fig. 5.2 displays these points on the oscillation of a free bubble in an infinite, inviscid fluid for clarification.

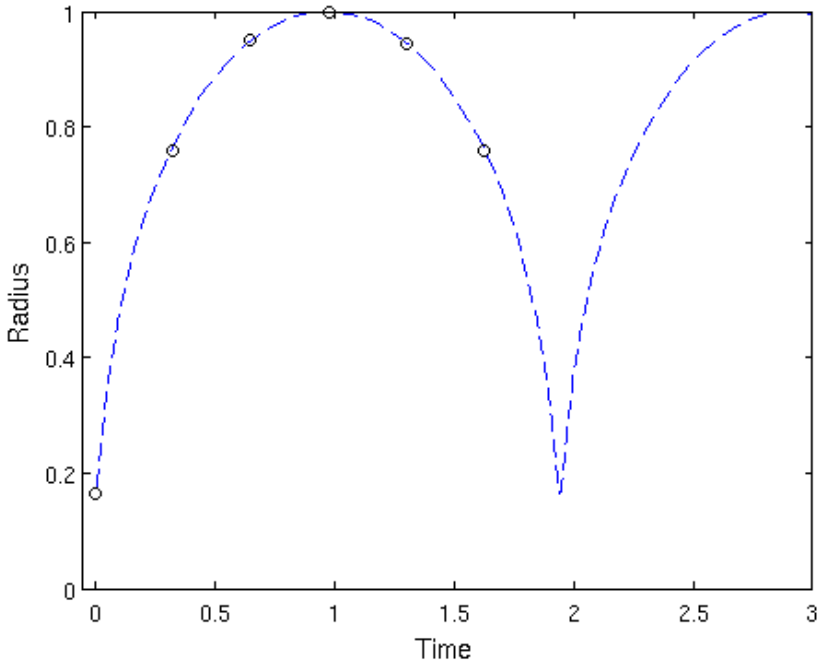

Figure 5.2: Cases i) - vi) for a bubble oscillating in an infinite, inviscid fluid. The cases i) - vi) are represented by the circles and run from left to right.

For Figs. 5.4 - 5.6 the shock strength is $P_s^* = 90$, corresponding to $P_s = 9$MPa. This is at the lower end of the range of values normally used in ESWL [59]. Using Equations

(5.4) - (5.6) this results in a velocity of $U_s = 1490.59$m/s and a non-dimensional width of $W_s^* = 2$ is chosen.

Firstly, considering the inviscid case (Figs. 5.4a and 5.5a) it is clear that, for these shock parameters, the state of the bubble when the pulse hits has a profound effect on the bubble dynamics. For cases i), ii), iii) (during the growth phase of the bubble) the pressure pulse causes a small spike in the jet velocity which corresponds to the bubble shrinking. A jet does not form in any of these cases, however, and the bubble stays roughly spherical as it continues to oscillate. Fig. 5.7 shows the jet velocity and volume for case b) as well as the volume for the freely oscillating bubble for comparison. The arrival of the pulse initially impedes the expansion of the bubble compared to the freely oscillating case. In the long term this results in more unstable oscillations until the bubble collapses to a very small radius and the simulation stops. For cases iv), v) and vi) where the bubble is collapsing, the pressure pulse accelerates this collapse causing surface velocities of up to 188. This value is non-dimensionalised and corresponds to an actual velocity of 1880m/s. Note that since the fluid is assumed the be incompressible and inviscid this velocity is probably higher than that which would occur in reality.

The bubble surface just before jet impact for case v) is shown in Fig.5.3; the bubble has translated in the direction of the pulse more so than for the case of collapse near a rigid wall and jet velocities are significantly higher. The bubble is also much more flattened due to this larger translational movement. Unfortunately, due to these extreme velocities and the thin shape of the bubble the simulation is unable to continue to the toroidal phase. It is thought though that maximum velocities and pressures are generated during the initial collapse.

For the case $Re = De = 1$, it can be seen from Figs. 5.4b, 5.5b and 5.6 that the rheology of the fluid significantly reduces surface velocities in an analogous manner to the case of a bubble near a rigid wall. In fact, for the relative weak and narrow pulse studied here, jet impact does not occur for any cases a) - f). The impact of the pulse is seen to generate a spike in velocities in cases d) - f) but the viscoelastic effects are sufficiently strong to overcome this and over time the bubble falls back into oscillations similar to that of the freely oscillating bubble.

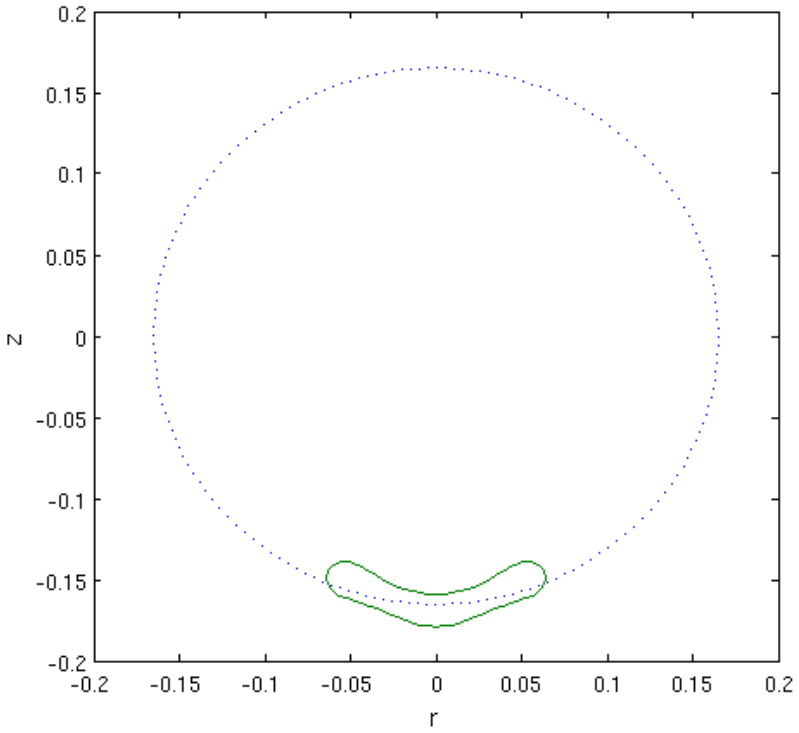

Figure 5.3: Initial and final bubble surfaces for inviscid case v).

Analogously to the case of a bubble near a rigid wall, viscoelasticity is seen to prevent jets forming for the pressure pulse case with $P_s = 9$MPa. This is due to the viscous and elastic forces competing with inertial forces to determine the dynamics. The effects of rheology of the fluid can, in fact, be overcome though by increasing the pulse strength or width as shown in Fig. 5.8 for the case $P_s^* = 90$ and $W_s^* = 1490$. In this cas the bubble spends significantly more time in the high pressure region of the pulse. Note that if the pulse is assumed to have a duration of 1μs [34] then an increase in width W_s^* corresponds to a decrease in initial bubble size R_0. The above case $W_s^* = 2$ corresponds to $R_0 = 0.745$mm and $W_s^* = 1490$ to $R_0 = 1\mu$m.

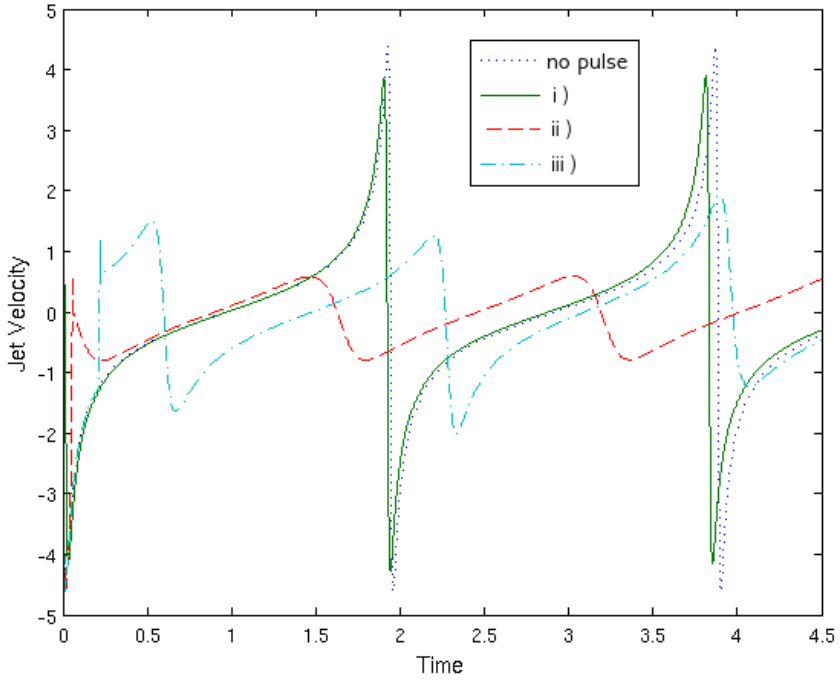

(a) Jet velocities for cases i), ii) and iii) compared with no pulse (dotted line). The fluid parameters are $De = 0$, $Re = \infty$ (Inviscid) and the pulse parameters are $P_s^* = 90$ and $W_s^* = 2$.

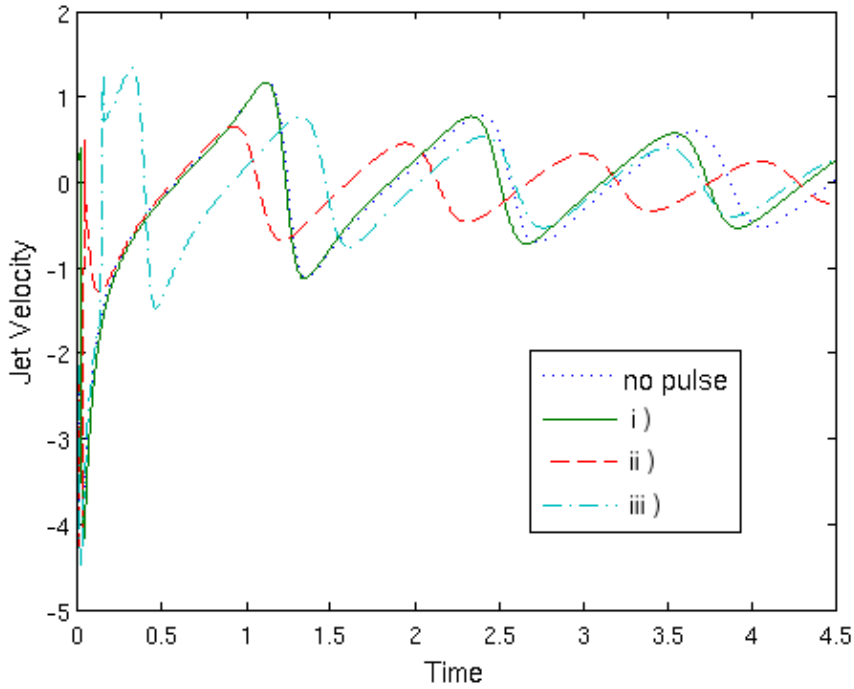

(b) Jet velocities for cases i), ii) and iii) compared with no pulse (dotted line). The fluid parameters are $De = 1$, $Re = 1$ and the pulse parameters are $P_s^* = 90$ and $W_s^* = 2$.

Figure 5.4: Effect of oscillation stage on jet velocities.

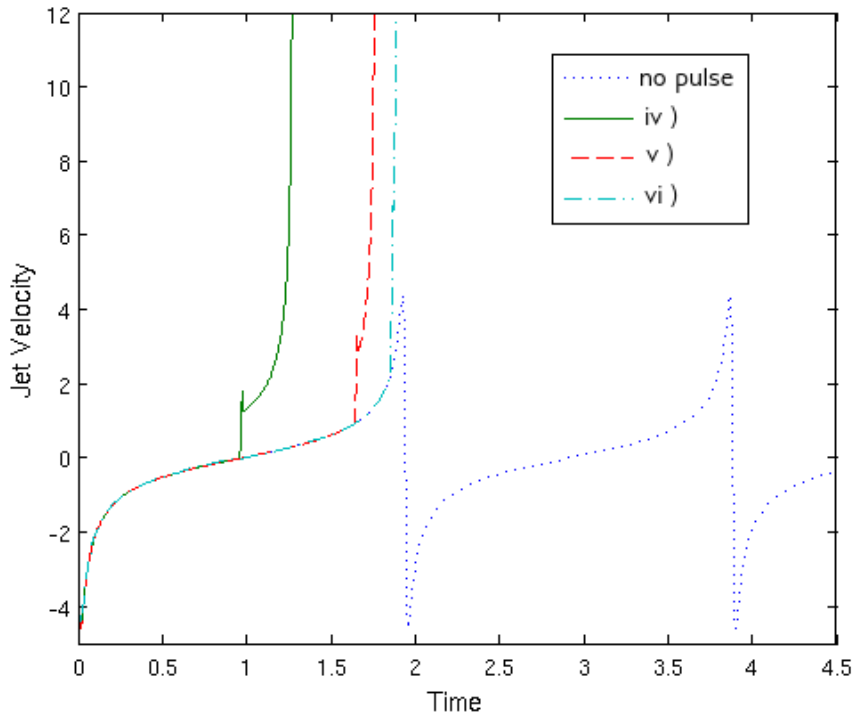

(a) Jet velocities for cases iv), v) and vi) compared with no pulse (dotted line). The fluid parameters are $De = 0$, $Re = \infty$ (Inviscid) and the pulse parameters are $P_s^* = 90$ and $W_s^* = 2$.

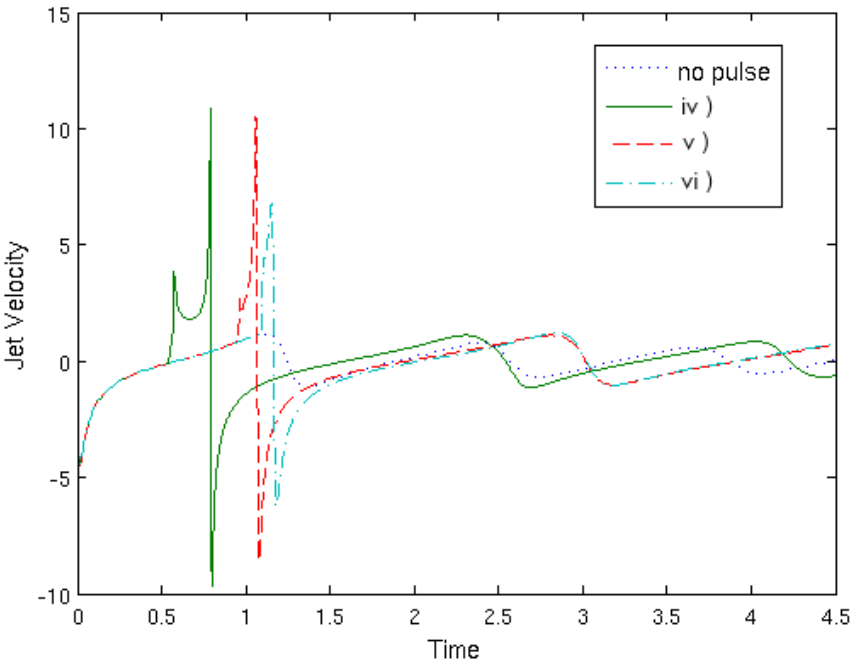

(b) Jet velocities for cases iv), v) and vi) compared with no pulse (dotted line). The fluid parameters are $De = 1$, $Re = 1$ and the pulse parameters are $P_s^* = 90$ and $W_s^* = 2$.

Figure 5.5: Effect of oscillation stage on jet velocities.

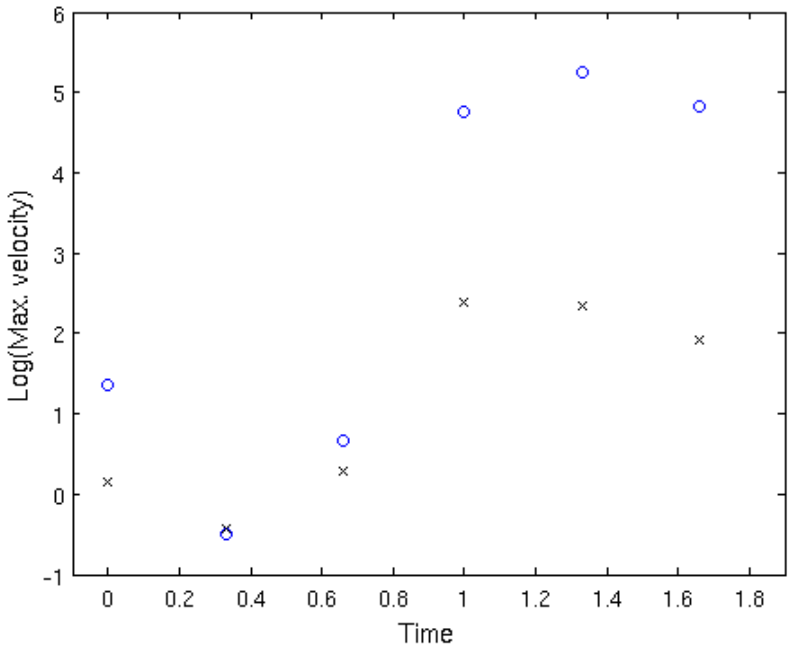

Figure 5.6: The maximum jet velocities for the results of Figures 5.4, 5.5 are plotted. The x-axis represents the relative stage of oscillation where one is the first maximum and two the second minimum. The circles represent the inviscid case and the crosses represent $Re = De = 1$.

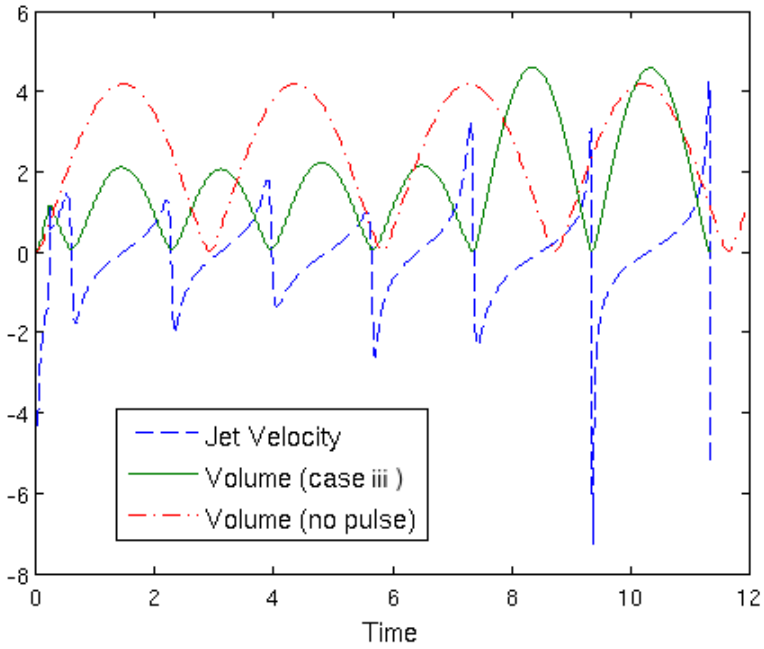

Figure 5.7: Jet velocity and volume for inviscid case ii).

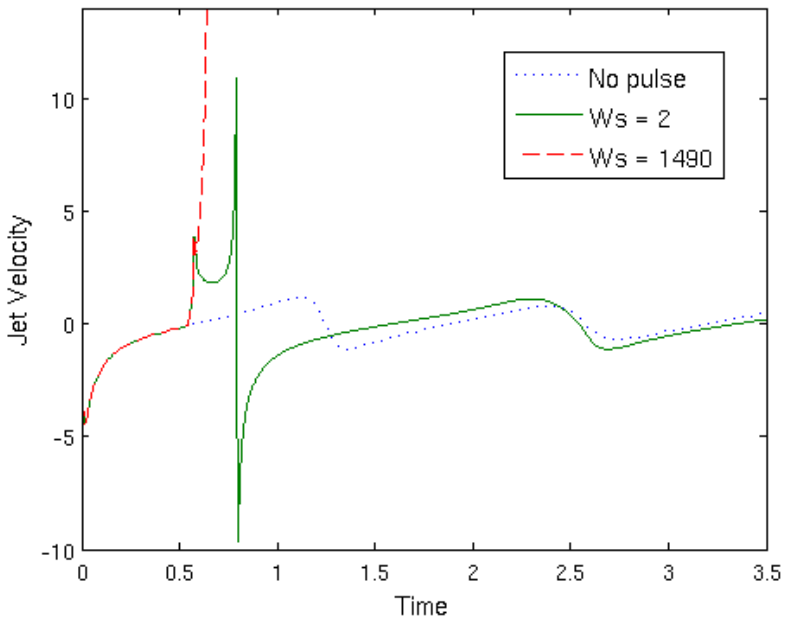

Figure 5.8: Effect of pulse width on dynamics for $Re = De = 1$ and case iv).

Although modelling the pressure pulse as a step function is an acceptable initial approximation, it does not really represent the form of shock waves in biomedical applications such as ESWL or sonoporation. Furthermore, in ESWL the cavitation is initiated by the ultrasound field and so more realistic initial conditions would be beneficial. A more complex model of the pulse is now presented to more accurately model bubble dynamics in these applications.

5.4 Shock Wave Lithotripsy Pulse

In shock wave lithotripsy (SWL) a series of ultrasonic pulses are administered in order to disintegrate renal calculi. This is achieved through the direct impact of the pulse on the wall (and resulting stress) as well as the formation of cavitation bubbles which can significantly intensify this damage. Understanding the interaction between the pulse and cavitation bubbles is thus of great importance in determining and controlling the potential damage which is caused.

5.4.1 Description of Pulse

For a typical lithotripter the pressure waveform at the focal point (of each pulse) is a sharp positive pressure compressive wave followed by a longer duration negative pressure tensile wave [119]. Typical time scales for the compressive and tensile waves are 1μs and 6μs, respectively [59]. In SWL, cavitation is initiated by the ultrasound. Gas-filled microbubbles often exist in fluids and can in fact be almost impossible to remove completely. The negative pressures created by the ultrasound field can cause these microbubbles to grow to macroscopic bubbles and then collapse violently.

In our model, at the point in the fluid at which the pressure falls below -2MPa a small bubble is assumed to nucleate. In Fig. 5.9 the pressure at the nucleation point is shown in time for parameters $P_{max} = 9$MPa and $P_{min} = -2.2$MPa. The negative pressure between $t = 0$ and $t = 0.5\mu$s is the tail end of the pulse which initiates the cavitation. The pressure then returns to atmospheric pressure (101kPa) until the next pulse arrives. The time between the pulses D, is taken to be twice the length of each pulse here although this value will be varied later to investigate its effect on the bubble dynamics.

Similar to the step-pressure case, the influence of the pressure pulses are implemented through the pressure term $p_\infty(t)$ in the Bernoulli equation. Rather than entering the explicit equation into the dynamic boundary conditions, however, the whole waveform is translated with a velocity U_s. This allows the reflection of the pulse on the rigid boundary to be modelled, a feature which has been neglected in many previous studies. The 'reflection' is modelled by introducing a new waveform which is a mirror of the original and which is initiated as the original waveform reaches the rigid wall.

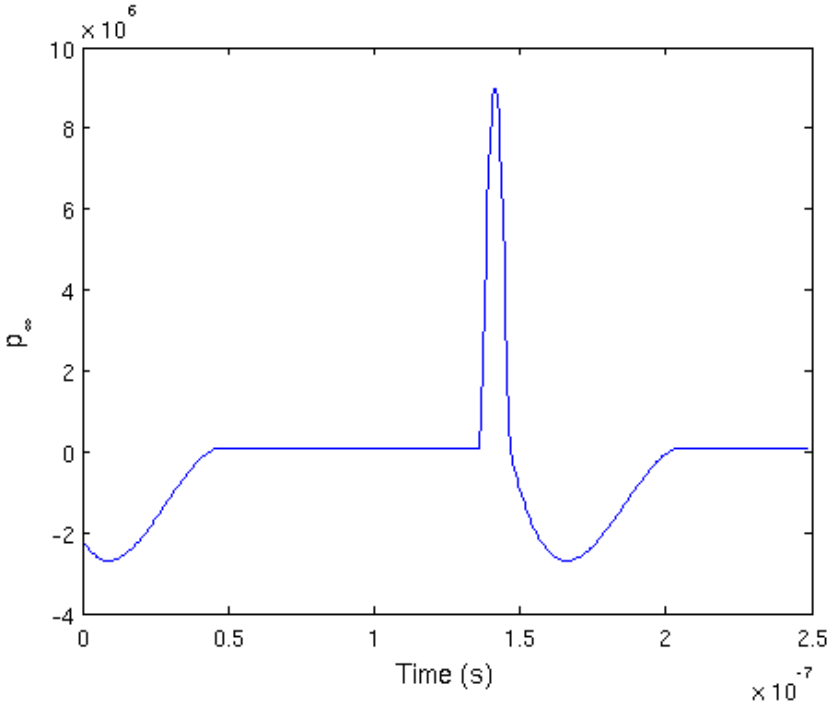

Figure 5.9: Pressure at a fixed point in space for a typical SWL waveform. The pulses are separated by a distance $D = 2 \times W_s^*$.

The pressure waveform parameters are the width W_s, the speed U_s and the amplitudes P_{max}, P_{min}. The same non-dimensionalisation as in the single-step pulse described above is chosen; this leads to the non-dimensional quantities

$$P_{max}^* = P_{max}/P_{ref}, \quad P_{min}^* = P_{min}/P_{ref}, \quad W_s^* = W_s/R_m, \quad U_s^* = U_s\sqrt{(\rho/P_{ref})}. \quad (5.11)$$

If the pulse is assumed to last approximately 7μs and using a velocity $U_s = 1490$m/s (as in the step-pressure case) gives a width of $W_s = 0.0105$m. A change in W_s^* then amounts to a change in R_m (maximum radius). In Table 5.2 the non-dimensional width W_s^* is given for a range of bubble sizes under these assumptions.

Table 5.2: Pulse widths

R_m	1μm	10μm	100μm	1mm
W_s^*	10430	1043	104.3	10.43

A typical lithotripsy shock is characterised by a compressive wave of strength $9-114$MPa and a tensile wave of $2.8-9.9$MPa (negative pressure) [34]. Note that modelling the rigid wall as completely flat and infinite in the radial direction (as in Chapters 3 and 4) assumes that the bubbles are significantly smaller than the kidney stone, which is usually the case in ESWL. If the stone is of comparable size to the bubble, however, the curvature of the stone would need to be taken into account and the wall modelled as a curved boundary as in the paper by Tomita et al. [100], for example. We will focus on the dynamics of a bubble near a flat, rigid wall to approximately model ESWL. To begin with though, some results are presented for an infinite, inviscid fluid.

5.4.2 Infinite, Inviscid Fluid

In Figs. 5.10-5.13 the bubble centroid position, equivalent radius R_{eq} and jet velocities are shown for a bubble subject to an ESWL field. Two pulses are modelled as in Fig. 5.9, the first of which initiates the growth of the bubble. The amplitudes $P_{max} = 9$MPa and $P_{min} = -2.2$MPa are chosen. The shock waves are separated by a distance D which is expressed as a multiple of the pulse width W_s.

Figs. 5.10, 5.11 show dynamics for a pulse width of $W_s^* = 10.43$ and a range of D. Case 1 (solid line) shows a single pulse and Cases 2 (dashed line) and 3 (dot-dash line) correspond to $D = 2$ and $D = 4$, respectively. In all three cases the bubble grows to an equivalent bubble radius close to 10μm, which is the non-dimensionalised radius that a pre-existing bubble would reach in the absence of the SWL field. The shock waves cause the bubble to translate in the direction of wave propagation, however, and the jet velocities that occur as the bubble collapses are significantly higher than those achieved in collapse due to the presence of a rigid wall. These high velocities arise due to the extra kinetic energy imparted to the bubble from the shock waves.

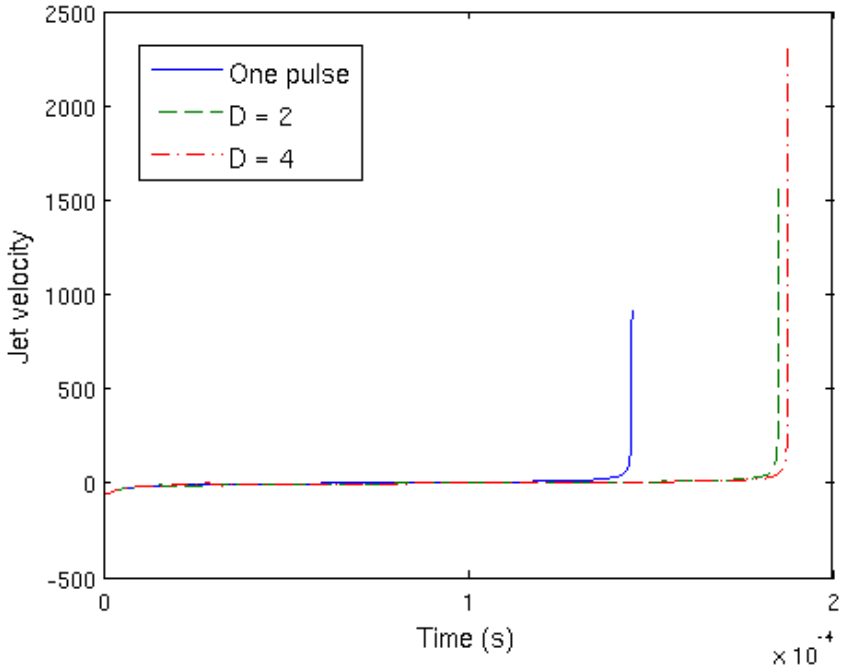

Figure 5.10: Jet velocities for $W_s^* = 10.43$, $P_{max} = 9$MPa, $P_{min} = -2.2$MPa. The parameter D is the distance between pulses (given as a multiple of W_s^*).

In Figs. 5.12, 5.13 a wider pulse is considered, with $W_s^* = 104.3$. The wider pulse causes the bubble to grow much larger and translate further than in the previous case since the bubble is exposed to the negative tensile wave for much longer. The jet velocities achieved, however, are very similar to the case $W_s^* = 10.43$.

Note that the very high velocities of ~ 2000m/s observed here are higher than those typically observed in experiments (see, for example, [60]). This is likely due to the assumption of incompressibility in the model as well as the neglection of viscous effects in these results.

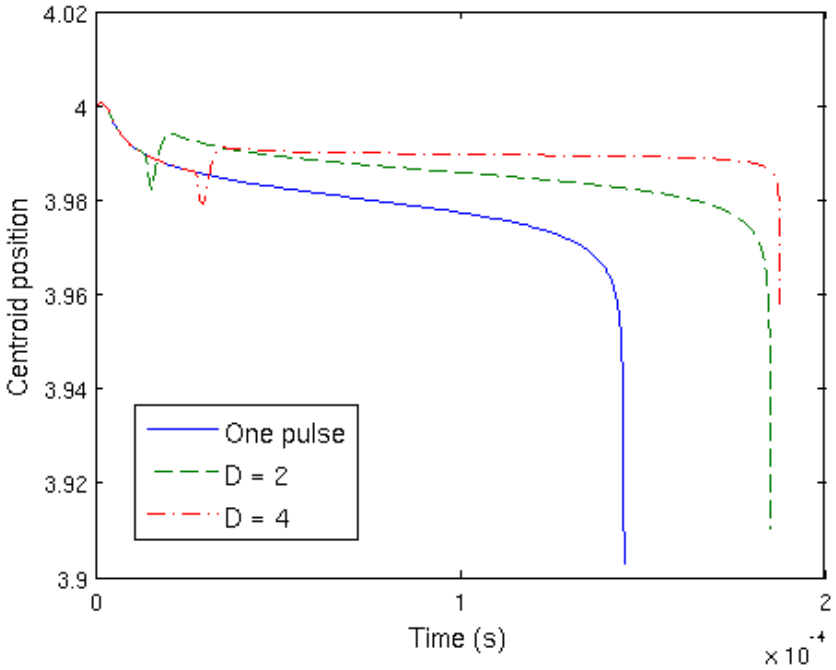

(a) Centroid position vs time for $W_s^* = 10.43$, $P_{max} = 9$MPa and $P_{min} = -2.2$MPa. The parameter D is the distance between pulses (given as a multiple of W_s^*).

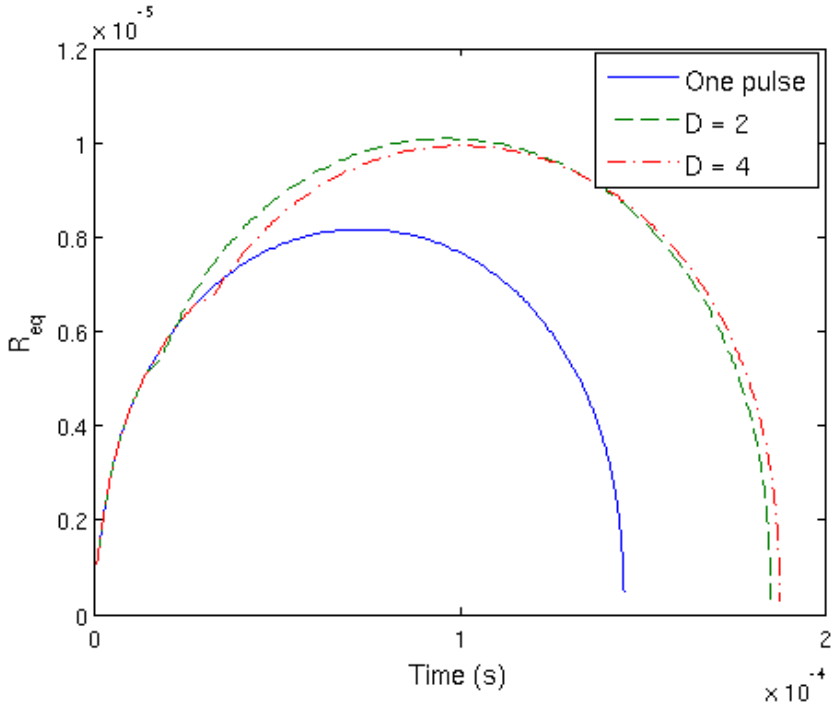

(b) Equivalent radius (m) vs time for $W_s^* = 10.43$, $P_{max} = 9$MPa and $P_{min} = -2.2$MPa. The parameter D is the distance between pulses (given as a multiple of W_s^*).

Figure 5.11: Effect of frequency on dynamics for $W_s^* = 10.43$, $P_{max} = 9$MPa and $P_{min} = -2.2$MPa.

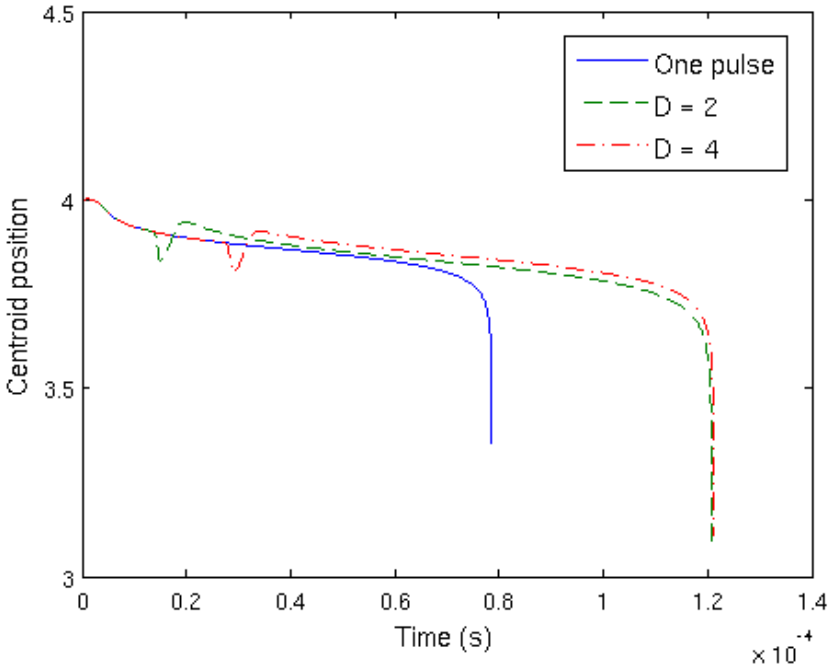

(a) Centroid position vs time for $W_s^* = 104.3$, $P_{max} = 9$MPa and $P_{min} = -2.2$MPa. The parameter D is the distance between pulses (given as a multiple of W_s^*).

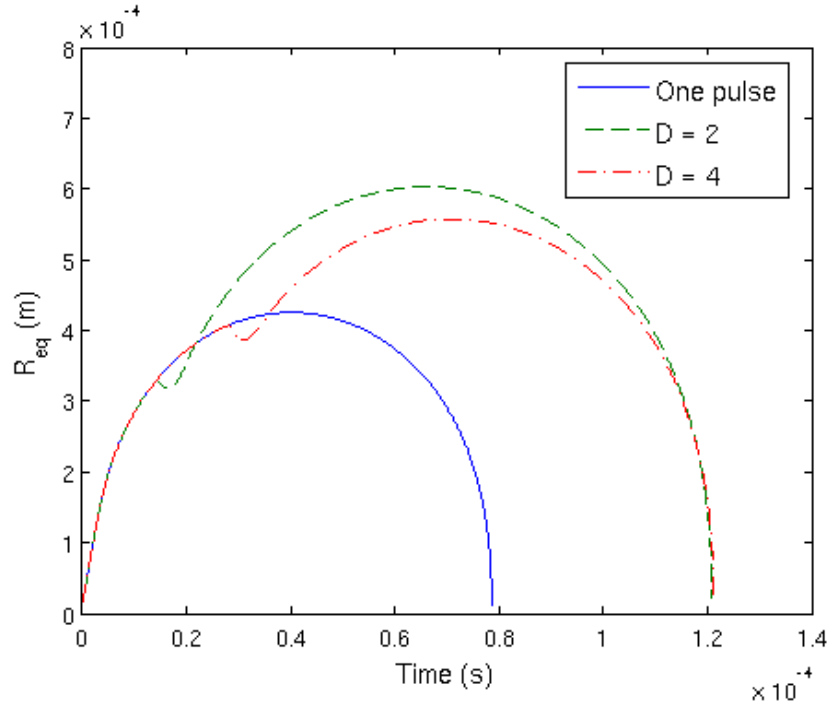

(b) Equivalent radius (m) vs time for $W_s^* = 104.3$, $P_{max} = 9$MPa and $P_{min} = -2.2$MPa. The parameter D is the distance between pulses (given as a multiple of W_s^*).

Figure 5.12: Effect of frequency on dynamics for $W_s^* = 104.3$, $P_{max} = 9$MPa and $P_{min} = -2.2$MPa.

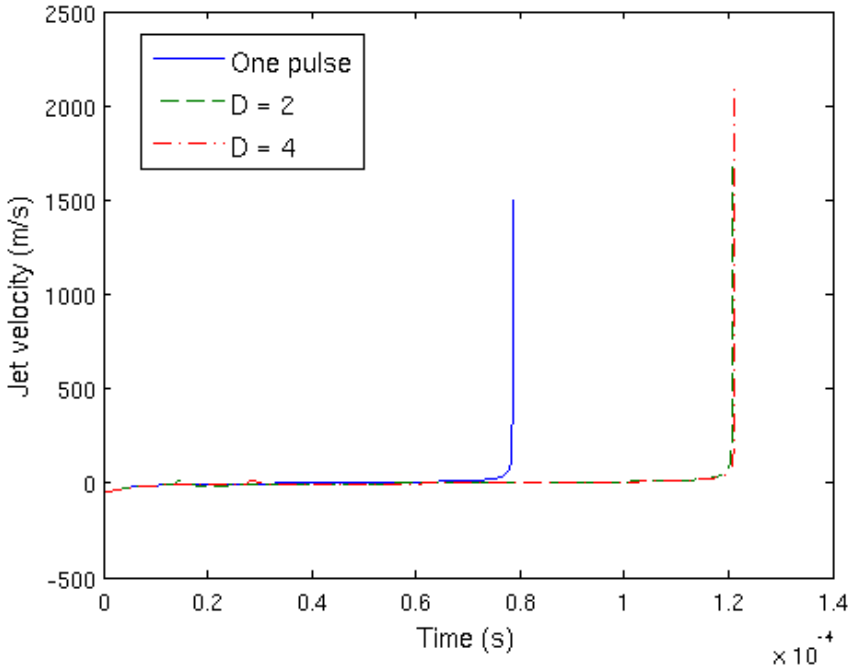

Figure 5.13: Effect of frequency on dynamics for $W_s^* = 104.3$, $P_{max} = 9$MPa and $P_{min} = -2.2$MPa.

For $W_s^* = 10.43$, $P_{max} = 9$MPa, $P_{min} = -2.2$MPa and $D = 4$ the bubble surfaces are shown in Fig. 5.14. Since the pulse is relatively thin it causes very little translational movement and, although high velocities occur, the bubble remains roughly spherical for much of the collapse phase. It is only when the bubble is very small that a liquid jet occurs. Due to the small size of the bubble and the very high velocities, the bubble is very unstable when jet impact occurs and the simulation is not able to continue.

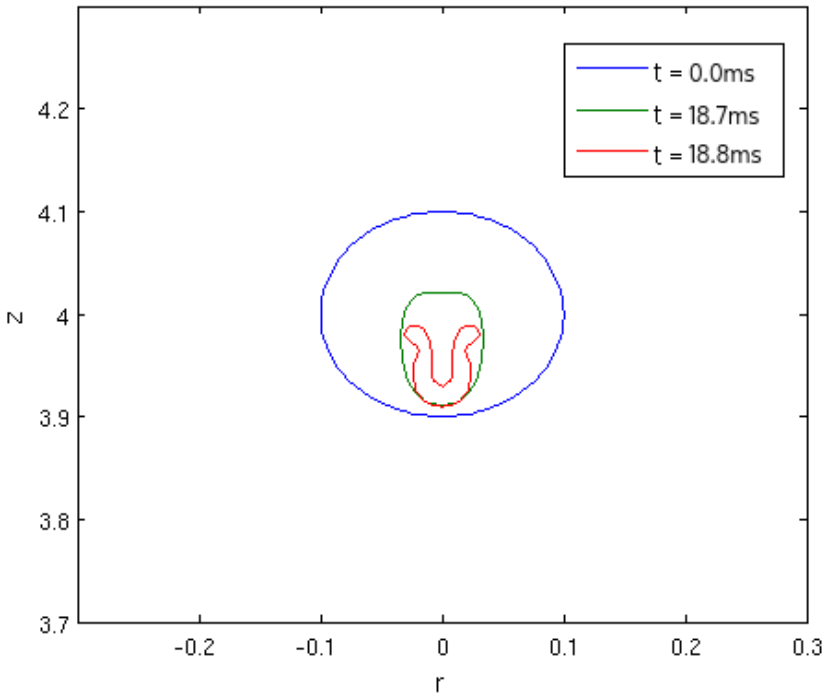

Figure 5.14: Bubble surfaces for $W_s^* = 10.43$, $P_{max} = 9$MPa, $P_{min} = -2.2$MPa, $D = 4$ and an inviscid fluid.

5.4.3 Bubble Near a Rigid Wall

Since we are aiming to model a cavitation bubble in ESWL, a rigid wall is included as an approximation to a kidney stone. As seen in Chapters 3 and 4, the presence of a rigid wall can cause a bubble to collapse asymmetrically. Furthermore, the shock wave applied here will be reflected off the wall and interact with the bubble a second time. In reality, once the shock wave impacts the stone it will split into a reflected wave and a transmitted wave. The nature of these waves will depend on the change of acoustic impedance between the fluid and the stone. For simplicity, however, we assume here that the entire wave is reflected off the stone.

In Figs. 5.15 - 5.19, a pulse with parameters $P_{max} = 9$MPa, $P_{min} = -2.2$MPa and $D = 4$ nucleates a cavitation bubble in an Oldroyd-B fluid at an initial stand-off distance $h = 4$ from a rigid boundary.

For a non-dimensional pulse width $W_s^* = 10.43$ the bubble size and centroid position are shown in Fig. 5.15 for $De = 1$ and $Re = 1, 10, 25$. Similarly to the freely oscillating

bubble considered in Chapters 3 and 4, an increase in viscosity leads to damped oscillations and less translational movement towards the wall. Although the shock consists of pressures roughly ten times the reference pressure (which one would expect to dominate the dynamics), the pulse width in this case is relatively thin and thus the interaction between the shock wave and the bubble takes place over a very short time scale. The pulse, then, initiates the growth of the bubble but the long-term dynamics are greatly influenced by the fluid rheology. For the same parameters the jet velocities and pressure at the midpoint of the rigid wall are shown in Fig. 5.16. The initial large pressures at (i) are due to the direct impact of the shock wave on the wall. It is this impact which is understood to cause the initial damage to the stone [86]. The large spikes in pressure (ii) and (iii) are a consequence of the intense bubble collapse. This intense collapse also results in very high liquid jet velocities as seen in Fig. 5.16a. The pressures due to the liquid jet and compression of bubble contents are almost as large as those due to the direct impact of the shock wave. This agrees with experimental observations that cavitation contributes to stone damage, working synergistically with the applied shock waves.

In general, an increase in Re leads to larger oscillations and more intense collapses although the bubble does not become toroidal in any of the cases shown here.

For the same pulse parameters as those used in Figs. 5.15 and 5.16 the effect of changing De is shown in Figs. 5.17 and 5.18 for a fixed value of $Re = 25$. The bubble size and position are initially almost indistinguishable from each other for each value of De considered. A liquid jet forms in all cases as the bubble undergoes its initial collapse. For $De = 1$, however, the fluid viscosity just stops the bubble transitioning to a toroidal geometry whereas for $De = 5, 10$ jet impact does occur. When jet impact occurs in these cases the extremely high velocities mean the simulation is unable to continue past jet impact. The model is not able to deal with these high velocities but it is argued that the extreme collapse undergone here will probably lead to the fragmentation of the bubble into a number of smaller cavities. This situation, though, is not modelled here.

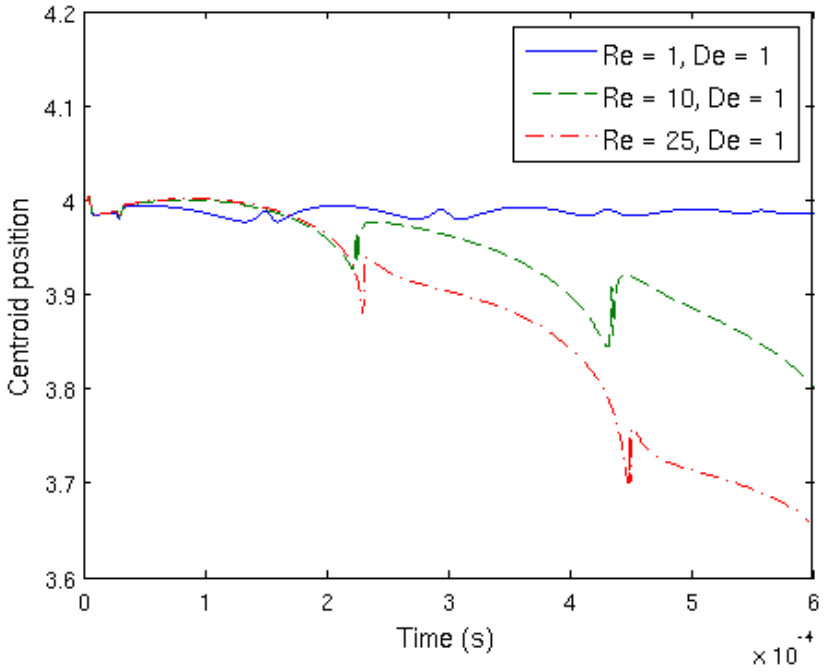

(a) Centroid position vs time for $W_s^* = 10.43$, $P_{max} = 9$MPa, $P_{min} = -2.2$MPa and $D = 4$.

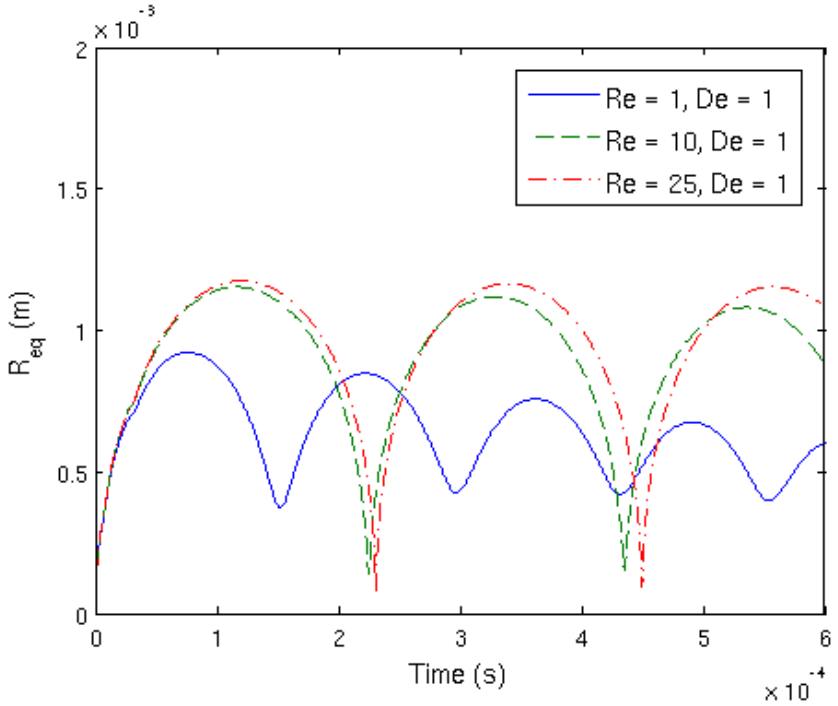

(b) Equivalent radius vs time for $W_s^* = 10.43$, $P_{max} = 9$MPa, $P_{min} = -2.2$MPa and $D = 4$.

Figure 5.15: Effect of changing fluid viscosity on bubble size and position.

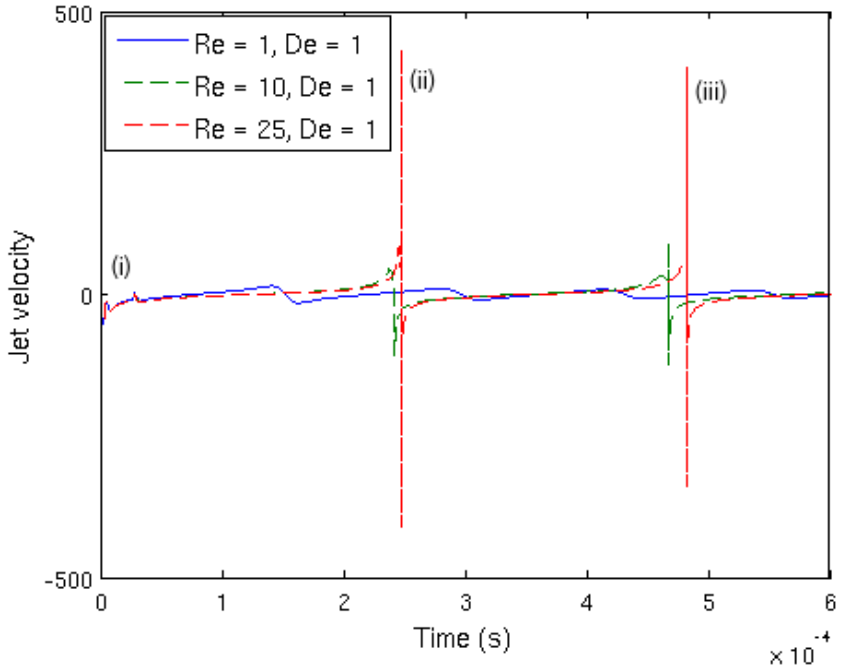

(a) Jet velocity vs time for $W_s^* = 10.43$, $P_{max} = 9$MPa, $P_{min} = -2.2$MPa and $D = 4$.

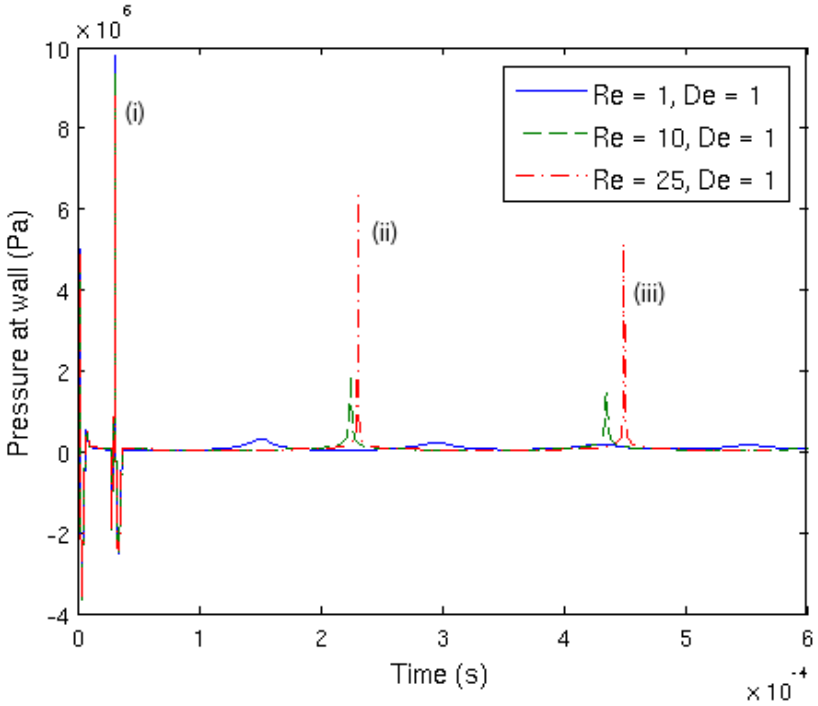

(b) Pressure at the wall vs time for $W_s^* = 10.43$, $P_{max} = 9$MPa, $P_{min} = -2.2$MPa and $D = 4$.

Figure 5.16: Effect of changing fluid viscosity on jet velocity and pressure at the mid-point of the rigid wall.

It is clear that, despite the high pressures due to the shock wave, the fluid viscosity and fluid elasticity are both important in determing the bubble dynamics for the given pulse parameters. For the same parameters but with a wider pulse: $W_s^* = 104.3$, the jet velocities are shown for $De = 1$ and $Re = 1, 10, 25$ in Fig. 5.19. In this case the compressive wave is reflected off the wall as the bubble is nucleated and since the pulse is wider the bubble experiences the high positive pressures for a much longer time. This causes the bubble to collapse almost immediately for all three cases and inertial effects dominate, with fluid viscosity having little effect. Jet velocities of approximately 200m/s are obtained which are high enough to damage hard engineering materials such as metals.

Fig. 5.20 shows jet velocities when the width is kept at $W_s^* = 10.43$ but the strength of the pulse is increased to $P_{max} = 90$MPa and $P_{min} = -8.8$MPa and the fluid parameters are $De = 1$, $Re = 1, 10, 25$. The very strong compressive wave (reflected off the wall) causes the bubble to collapse before the tensile wave can cause the bubble to grow to a significant size. Little difference is observed from altering the Reynolds number with a powerful liquid jet forming in all cases, in a similar manner to the wider pulse in Fig. 5.19.

A cavitation bubble generated and forced by a SWL pulse has been shown to collapse more violently than a free bubble near a rigid wall; this is due to the very high pressures generated by the pulse. This agrees with the experimental findings of the many studies which have investigated shock-induced collapse of bubbles. Furthermore, very large pressures are observed at the wall when the bubble is near minimum volume. This pressure is an indicator of the potential damage to the stone and thus confirms the idea that cavitation can aid stone disintegration.

At the lower end of the range of typical pulse strengths ($P_{max} = 9$MPa, $P_{min} = -2.2$MPa), the tail end of the initial pulse causes large growth of the cavity up to fifty times its original size followed by a rapid collapse. In this case, the viscoelastic effects of the fluid are found to be important to the dynamics. In particular, effects similar to those in Chapter 3 are found with viscosity lowering jet velocities and more translational movement of the bubble centroid with increasing elasticity. For very strong pulses, or very wide pulses, the collapse can occur before the bubble expands very much. In this case the rheological effects are secondary and inertia dominates.

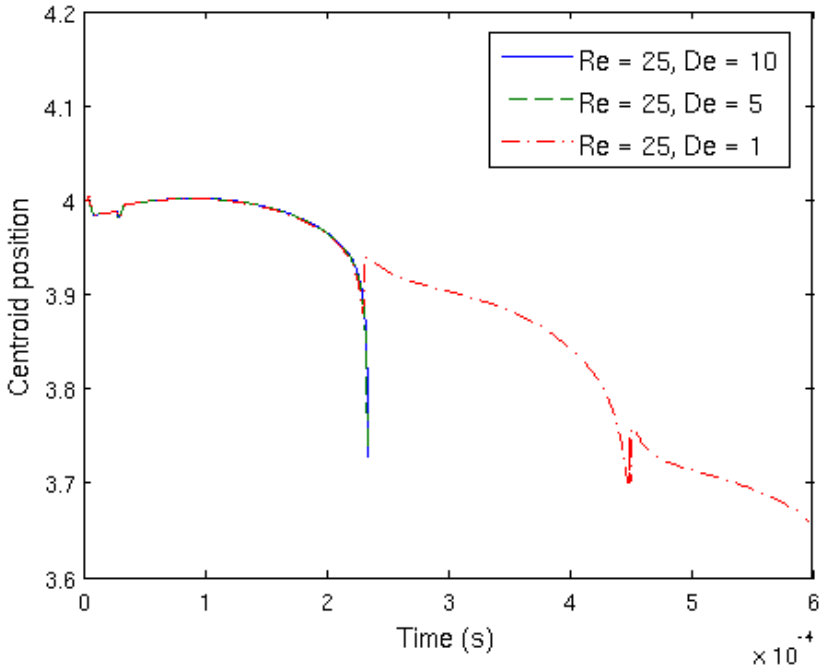

(a) Centroid position vs time for $W_s^* = 10.43$, $P_{max} = 9$MPa, $P_{min} = -2.2$MPa and $D = 4$.

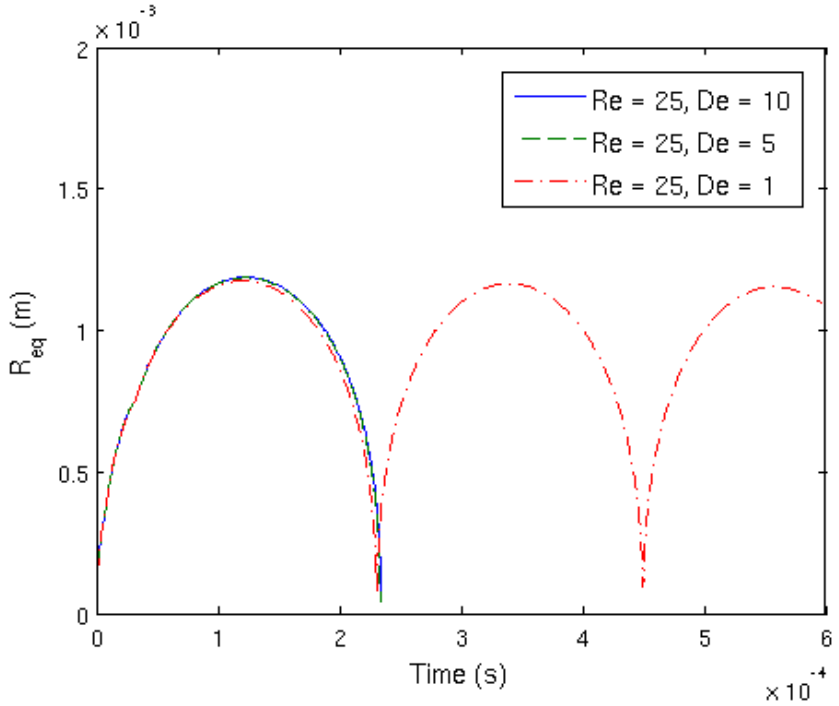

(b) Equivalent radius vs time for $W_s^* = 10.43$, $P_{max} = 9$MPa, $P_{min} = -2.2$MPa and $D = 4$.

Figure 5.17: Effect of changing fluid elasticity on bubble size and position.

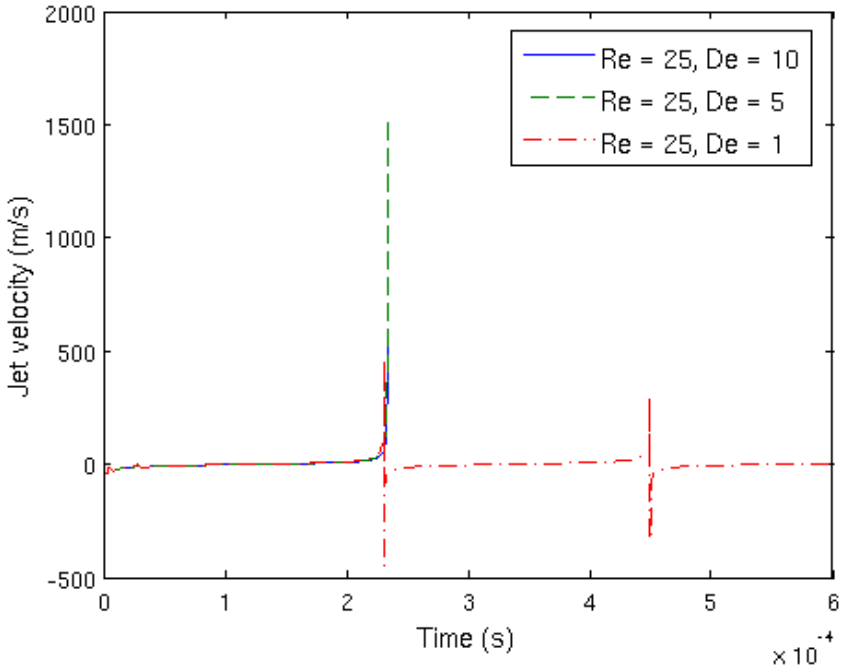

(a) Jet velocity vs time for $W_s^* = 10.43$, $P_{max} = 9$MPa, $P_{min} = -2.2$MPa and $D = 4$.

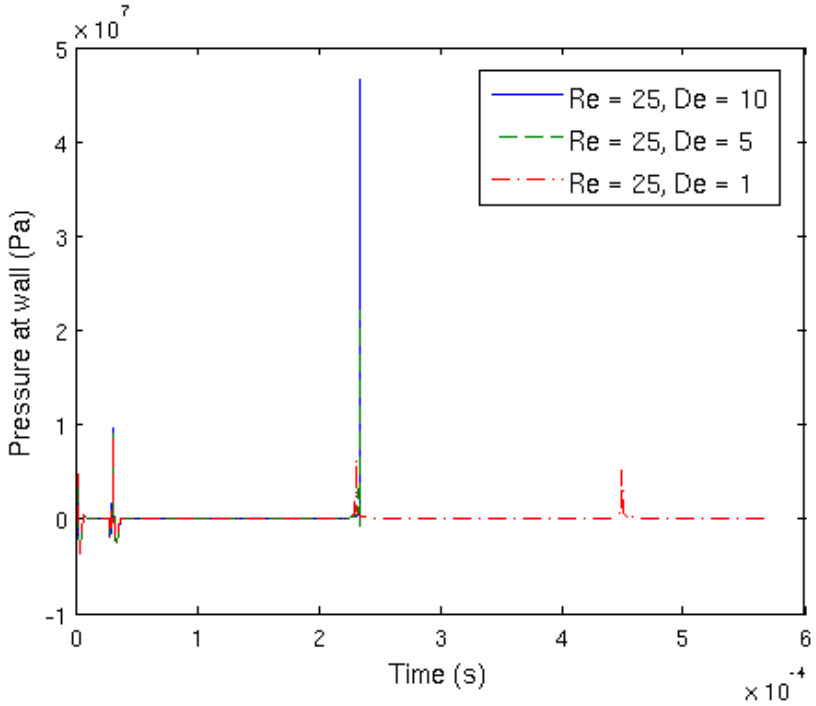

(b) Pressure at the wall vs time for $W_s^* = 10.43$, $P_{max} = 9$MPa, $P_{min} = -2.2$MPa and $D = 4$.

Figure 5.18: Effect of changing fluid elasticity on jet velocity and pressures at the midpoint of the rigid wall.

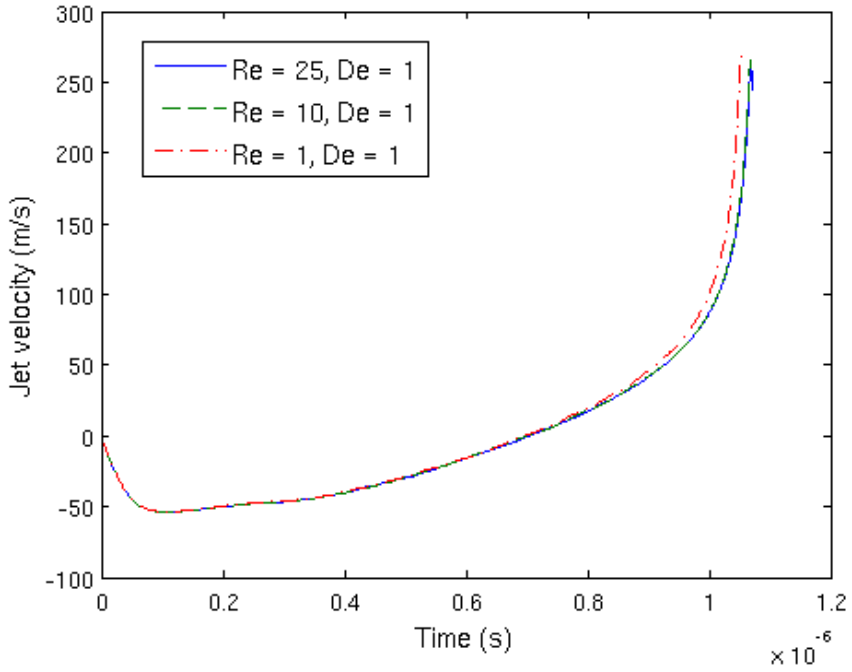

Figure 5.19: Jet velocities for $W_s^* = 104.3$, $D = 10$, $P_{max} = 9$MPa, $P_{min} = -2.2$MPa and $h = 4$.

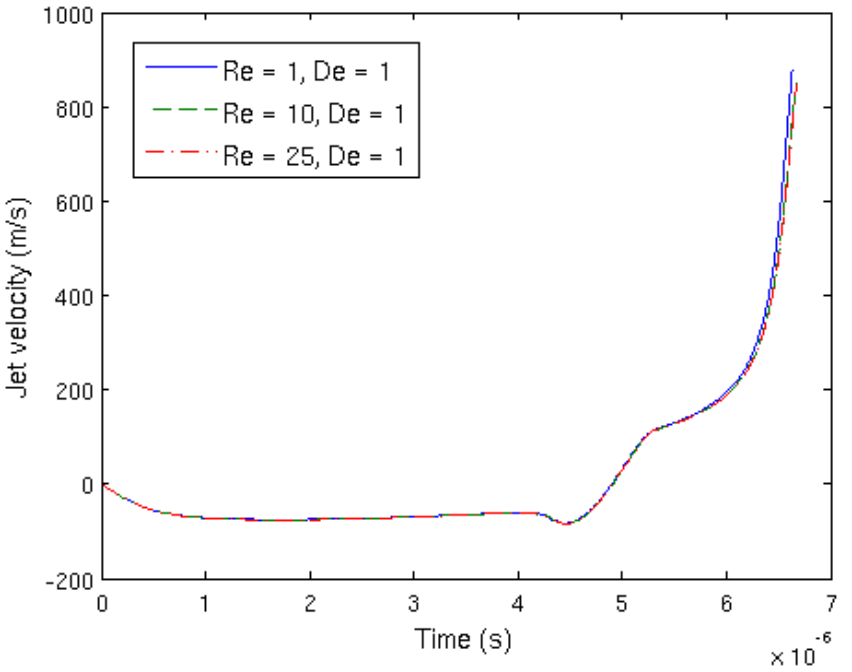

Figure 5.20: Jet velocities for $W_s^* = 10.43$, $D = 1$, $P_{max} = 90$MPa, $P_{min} = -8.8$MPa and $h = 4$.

5.5 Conclusions

In this chapter, the dynamics of cavitation bubbles and encapsulated microbubbles forced by a pressure pulse are studied. To begin with, a step function of high positive pressure form is considered. This model was originally used by Klaseboer et al. [59] for an infinite, inviscid fluid. A more intense collapse and higher jet velocities was observed compared to collapse of a bubble due to a rigid wall. Using an Oldroyd-B model for the fluid, it was observed that viscoelasticity can significantly reduce velocities and prevent jet impact, depending on the strength and width of the pressure pulse. Another impact factor is the stage of oscillation of the bubble when the pulse impacts. This model can be seen as approximating the conditions in ESWL but the form of the pulse, as well as the initial conditions of the bubble, are quite unrealistic.

To more accurately model conditions in ESWL a more complex description of the pulse was implemented which initiates a cavitation bubble when the pressure falls below a certain value. Since the pulse consists of negative as well as positive regions of pressure, bubble growth is seen as well as collapse. Due to this, the dynamics are found to be even more dependent on the fluid rheology in a similar manner to the freely oscillating bubble considered in Chapters 3 and 4. Compared to the freely oscillating bubble, however, much higher velocities were observed due to the extra energy imparted to the bubble from the pulse and since the bubble collapse in a higher pressure field.

Chapter 6

Modelling an Encapsulated Bubble Forced by an Ultrasound Field

6.1 Introduction

Encapsulated microbubbles (EMBs) are gas-filled bubbles encapsulated by either an albumin or lipid shell. Due to their nonlinear response to an ultrasound field, they are commonly used as nucleates for cavitation. By facilitating cavitation, EMBs can greatly improve the efficacy of biomedical procedures such as ultrasound contrast imaging and sonoporation.

By modifying the spherical model for an EMB described in Chapter 2, the nonspherical oscillations of an EMB can be approximately modelled using the boundary element method developed in Chapters 3 and 4. This is useful since the microbubbles are unlikely to remain spherical, particularly when forced by an ultrasound field. This new model also allows an EMB near a boundary to be considered, which is a situation particularly important for sonoporation.

6.2 Nonspherical Encapsulated Microbubbles

For a nonspherical encapsulated bubble, a generalisation of the method for spherical bubbles presented in Chapter 2 is considered. A similar approach has been used by Wang et al. [107] for Hoff's model of spherical EMBs [52]. Using the model in Chapter

2, for a spherical EMB the pressure on the fluid side of the bubble wall p_B is written as

$$p_B = \left(p_{g0} + \frac{2\chi}{R_0}\right)\left(\frac{R_0}{R}\right)^{3\kappa} - \frac{2\sigma}{R} - \tau_{rr} + \tau_{rr}^{(sh)} - \frac{2\chi}{R}\left(\frac{R_0}{R}\right)^2, \tag{6.1}$$

where χ and η_{sh} are the shell elasticity and viscosity, respectively, σ is the static surface tension, p_{g0} is the internal pressure of the EMB and τ_{rr}, $\tau_{rr}^{(sh)}$ are the stresses of the fluid and shell, respectively. This pressure is constant over the bubble surface for a spherical bubble at a particular instant in time. To modify Eqn. (6.1) for a nonspherical bubble we replace the radius R with the local radius of curvature $R_c(i)$ at each node. This can be calculated as $R_c(i) = 1/C(i)$ where $C(i)$ is the curvature at node i

$$C(i) = -\left(\frac{dr}{ds}(i)\frac{d^2z}{ds^2}(i) - \frac{dz}{ds}(i)\frac{d^2r}{ds^2}(i)\right)\left(\left(\frac{dr}{ds}(i)\right)^2 + \left(\frac{dr}{ds}(i)\right)^2\right)^{-3/2}. \tag{6.2}$$

The pressure at each node is then

$$p_B = \left(p_{g0} + \frac{2\chi}{R_0}\right)\left(\frac{R_0}{R_c}\right)^{3\kappa} - \frac{2\sigma}{R_c} - \tau_{rr} + \tau_{rr}^{(sh)} - \frac{2\chi}{R_c}\left(\frac{R_0}{R_c}\right)^2 \tag{6.3}$$

For a spherical bubble, and under the thin shell approximation, the viscous contribution of the shell is (for a Newtonian shell)

$$2\int_{R_1}^{R_1+\varepsilon}\left(\frac{\tau_{rr}^{(sh)} - \tau_{\theta\theta}^{(sh)}}{r}\right)dr = -12\eta_{(sh)}\varepsilon\frac{\dot{R}}{R(R-\varepsilon)}, \tag{6.4}$$

where higher order terms have been dropped (since the shell is assumed to be thin). In the same manner as the elastic term, the radius R is replaced by R_c for the nonspherical bubble and the velocity becomes $\partial\phi/\partial n$. The Bernoulli equation used to update ϕ at each node for a non-spherical EMB in an Oldroyd-B fluid is then

$$\begin{aligned}\rho\frac{\mathrm{D}\phi(\mathbf{x}_i)}{\mathrm{D}t} = p_\infty(\mathbf{x}_i) - \left(p_0 + \frac{2\chi}{R_0}\right)\left(\frac{V_0}{V}\right)^{\kappa} + \frac{\rho}{2}|\nabla\phi(\mathbf{x}_i)|^2 - 2\eta_s\frac{\partial^2\phi(\mathbf{x}_i)}{\partial n^2} \\ + \frac{2\chi}{R_c(i)}\left(\frac{R_0}{R_c(i)}\right)^2 - 12\eta_{(sh)}\varepsilon\frac{\frac{\partial\phi}{\partial n}}{R_c(i)(R_c(i)-\varepsilon)} - \tau_{nn}^p(\mathbf{x}_i) + \frac{\sigma}{R_c(i)}.\end{aligned} \tag{6.5}$$

6.3 Boundary Element Method

The boundary element method developed in Chapters 3 and 4 is used to model a non-spherical EMB in an Oldroyd-B fluid. The influence of the shell is modelled using a modified Bernoulli equation (6.5) and any forcing is applied through the pressure term $p_\infty(\mathbf{x}_i)$, as in Chapter 5.

Initially, the bubble is spherical and it is assumed the shell contents are concentrated evenly around the bubble surface. If the bubble is assumed to remain spherical, as in Chapter 2, the concentration at each node will change over time due to the changing size of the bubble but the concentration at a particular time is constant over the bubble surface.

For the non-spherical case, different parts of the bubble surface have different local curvatures and thus the concentration of the substrate will not be constant over the surface. This will give rise to a tangential force characterised by a surface tension gradient from points with lower surface tension to points with higher surface tension. This tangential gradient term is analogous to the term $(2\chi/R_c)(R_0/R_c)^2$, which comes from a gradient in the normal direction (due to changing bubble radius). The tangential force is not included, however, since it is not clear how this would be implemented. Furthermore, it is argued that while the bubble is roughly spherical this force will be small whereas any significant deviation from this will involve high velocities which will dominate the dynamics. Unless stated otherwise, the shell parameters $\varepsilon = 1\text{nm}$, $\chi = 0.5\text{N/m}$, $\sigma = 0.051\text{N/m}$ and $\eta_{sh} = 1\text{Pa·s}$ are used, as in Chapter 2.

6.4 Comparison to Spherical Model

To validate the model, an initially spherical EMB in an infinite fluid is considered. Fig. 6.1 shows a comparison of the BEM model to the spherical ODE model presented in Chapter 2 for both an inviscid and Oldroyd-B fluid. In these results it is assumed the EMB has a high initial internal pressure to facilitate comparisons with a cavitation bubble and to show the influence of the extra shell parameters. In reality, the EMB will be at some equilibrium radius and it will be assumed later in the chapter that the internal pressure is equal to atmospheric pressure.

Good agreement is found in both cases, validating the new model. The differences for

the Oldroyd-B case are due to the BEM model neglecting viscoelastic effects in the bulk of the fluid. Note that this affects the behaviour for the first couple of oscillations but the long term behaviour (equilibrium radius) is identical.

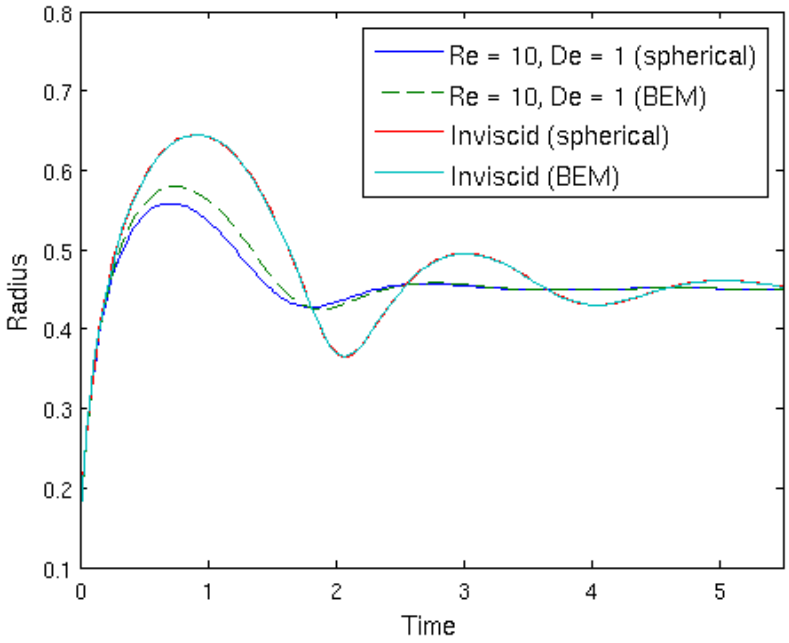

Figure 6.1: Comparisons between the BEM model and the explicit solution of the modified Rayleigh-Plesset equation (spherical model).

The differences in behaviour of a clean bubble and an EMB situated in an inviscid fluid at an initial stand-off distance $h = 2$ from a rigid boundary can be seen in Fig. 6.2. As can be seen in Fig. 6.2a (plotted until jet impact) the cavitation bubble grows to a large size and then collapses asymmetrically, developing a strong liquid jet. The EMB's growth is significantly dampened in comparison with much lower jet velocities. Similar to a cavitation bubble in a highly viscous fluid, the bubble is stable despite the presence of the rigid wall. This concurs with the stability that is required for EMBs to be useful as contrast agents and cavitation nuclei.

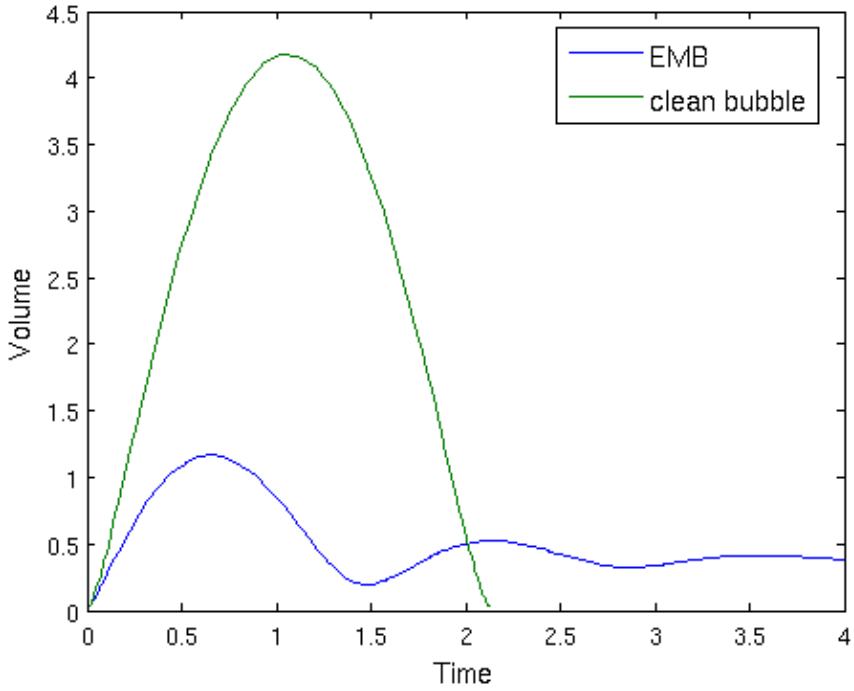

(a) Volume vs. time for a cavitation bubble and an EMB.

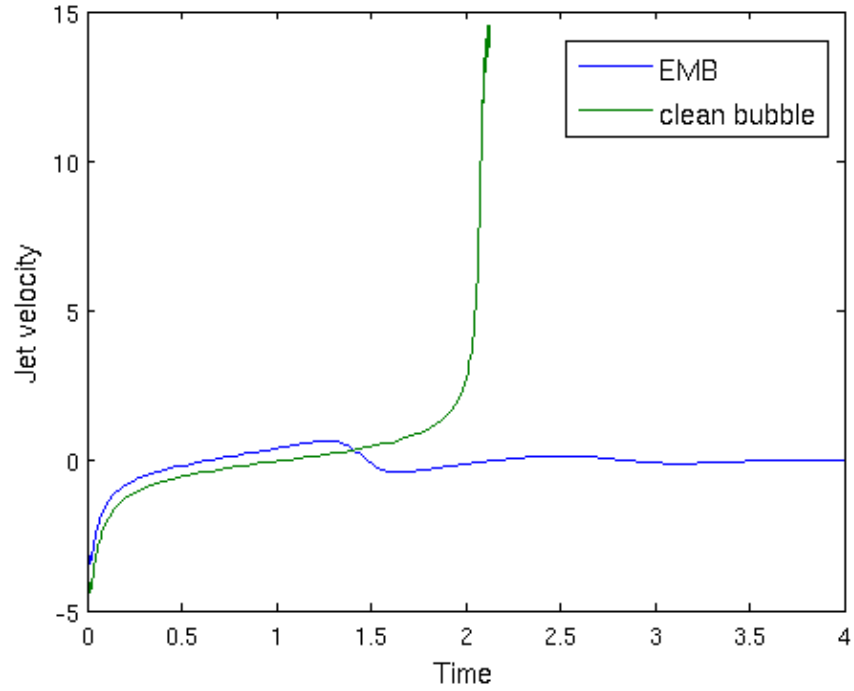

(b) Jet velocity vs. time for a cavitation bubble and an EMB.

Figure 6.2: Effect of an encapsulating shell on dynamics for a bubble situated at $h = 2$ from a rigid boundary.

6.4.1 Gaussian Acoustic Pulse

To simulate the interaction between ultrasound and an encapsulated bubble, a Gaussian acoustic pulse is used. The focal area of the pulse is assumed to be much larger than the bubble and the applied pressure field is thus approximated as being infinite in width (in radial direction). This pulse is incorporated into the model through the term $p_\infty(\mathbf{x})$ in a similar manner to the single step and SWL pulses described in Chapter 5. The explicit form for the Gaussian pulse is

$$p_\infty(t) = p_0 + p_A \sin[2\pi f(t - t_p)]\exp[-\pi^2 h^2 f^2 (t - t_p)^2]. \tag{6.6}$$

Here p_A is the maximum amplitude of the pulse, f is the frequency and h determines the width of the pulse. Figure 6.3 shows the pulse as a function of time at a fixed point in space for parameters $f = 2$MHz and $p_A = 200$kPa.

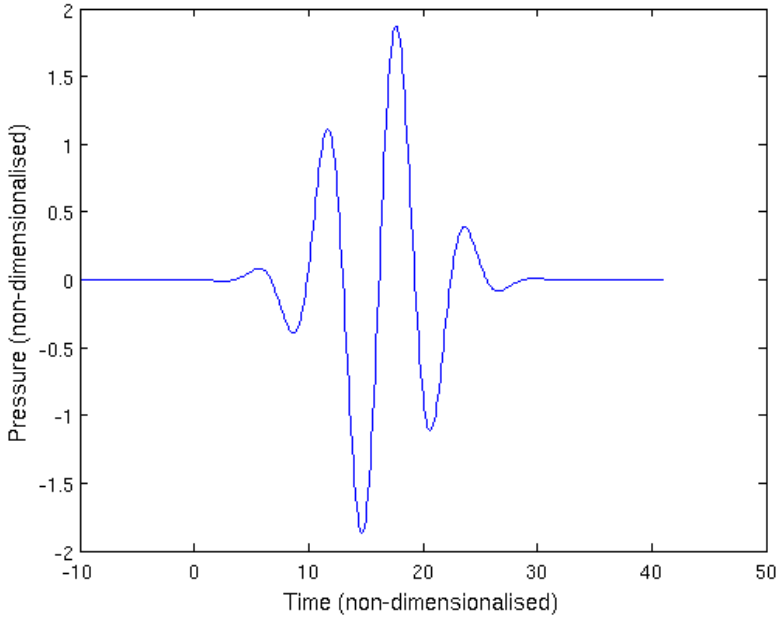

Figure 6.3: Typical Gaussian pulse as a function of time.

Note that for the spherically symmetric bubble in Chapter 2, the pulse is assumed to act on the whole bubble simultaneously. In reality, however, the pulse is moving with some velocity U_s downwards which will cause the bubble to collapse asymmetrically, since one side begins collapsing earlier. Also, if the bubble is situated near a rigid wall the pulse will reflect off the wall and interact with the bubble a second time. As in the

previous sections it is assumed that the pulse is completely reflected off the wall with no energy lost and no wave transmitted through the wall.

Since the pulse has a frequency f it is natural to use the following non-dimensionalisation

$$t = \frac{1}{\omega}t^*, \quad r = R_0 r^*, \quad z = R_0 z^*, \quad \tau_{nn} = p_c \tau^*_{nn} = \rho\omega^2 R_0^2 \tau^*_{nn}, \tag{6.7}$$

where $\omega = 2\pi f$. Note that the initial bubble radius, R_0, is used instead of the maximum radius. The reason for this is that the EMB is assumed to be at some equilibrium radius before the pulse hits, due to the stability of the shell. This also results in a non-dimensional ratio of pressures of $\varepsilon = p_0/p_c + We$, rather than the strong initial internal pressure that the cavitation bubble possesses. Rather than expressing the pressure term p^*_∞ as a function of time, it is expressed as a function of z and the centre of the pulse z_c is moved downwards with time. The pulse at node $\mathbf{x}_i = (r(i), z(i))$ is then

$$p^*_\infty(\mathbf{x}_i) = \frac{p_0}{p_c} + \frac{p_A}{p_c}\sin[z(i) - z_c(t)] \exp\left[-\frac{h^2}{4}(z(i) - z_c)^2 \right]. \tag{6.8}$$

where the midpoint of the pulse, z_c, is redefined each time step to move the pulse. The values $h = 1/3$ and $z_c(0) = 15$ are chosen as in Chapter 2.

In Figs. 6.4 - 6.6 the BEM code is compared to the spherical solution for an encapsulated microbubble forced by a Gaussian pulse with parameters: $p_A = 200$kPa, $f = 1$MHz, $Re = 6.3$, $De = 0$ and $R_0 = 1\mu$m and no wall present. The pressure of the pulse for the BEM code is measured at node 1 and the 'radius' is $R_{eq} = (3V/4\pi)^{1/3}$.

The models predict similar behaviour initially. However, the pressures begin to deviate as the BEM bubble translates downwards due to the imparted energy from the pulse. This translation does not exist within the spherical model. Also, as seen in Fig. 6.6, the EMB is shown to flatten considerably as it moves downwards (light blue line) and as it shrinks the surface becomes very distorted until the simulation terminates due to two nodes becoming too close (yellow line). The more complete BEM model thus indicates that an encapsulated microbubble can be significantly deformed, and potentially disintegrate, even at these relatively low pressure amplitudes. This agrees with experimental observations that contrast microbubbles can be destroyed during routine examinations [3].

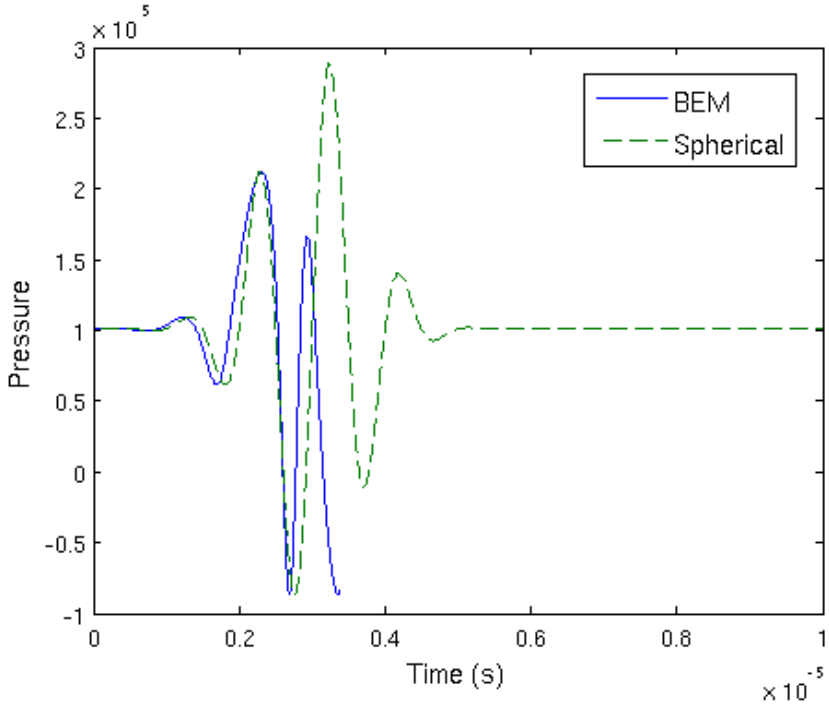

Figure 6.4: Pressure at node 1 of an EMB forced by a Gaussian pulse with $p_A = 200$kPa, $f = 1$MHz, $Re = 6.3$, $De = 0$ and $R_0 = 1\mu$m.

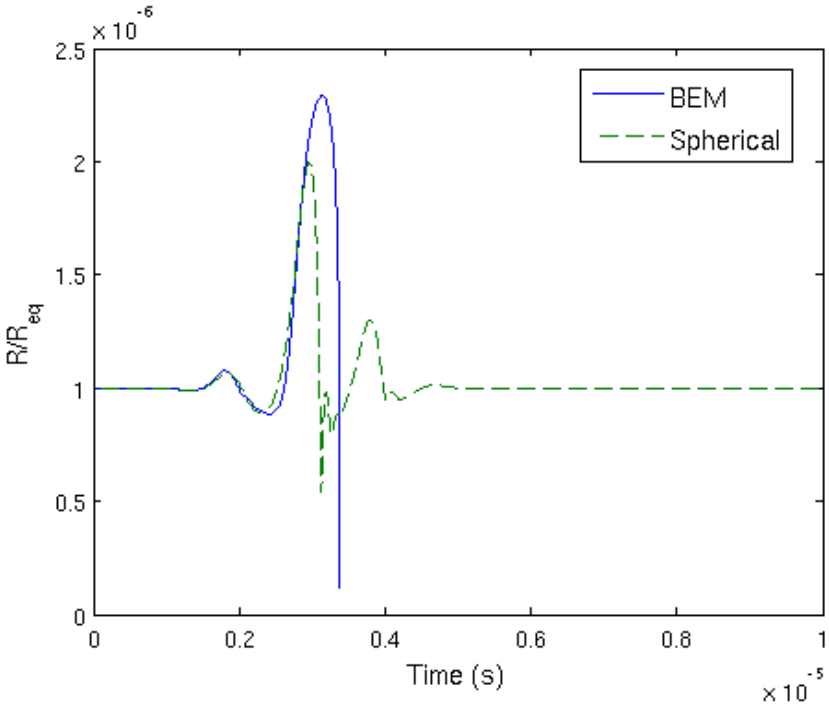

Figure 6.5: Equivalent bubble radius of an EMB forced by a Gaussian pulse with $p_A = 200$kPa, $f = 1$MHz, $Re = 6.3$ and $R_0 = 1\mu$m.

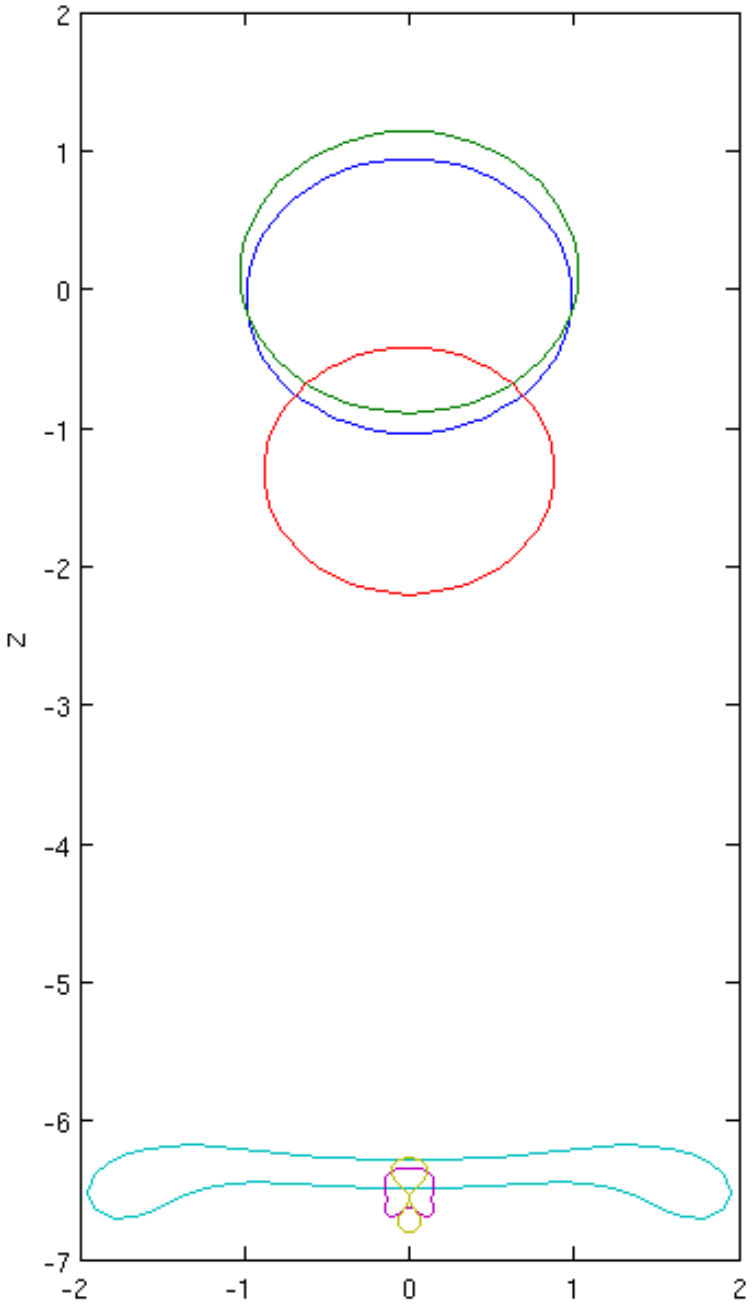

Figure 6.6: Bubble surfaces for $p_A = 200$kPa, $f = 1$MHz, $Re = 6.3$ and $R_0 = 1\mu$m. The times are $t = 0.000$s (dark blue), $t = 0.1503 \times 10^{-5}$s (green), $t = 0.2104 \times 10^{-5}$s (red), $t = 0.3016 \times 10^{-5}$s (light blue), $t = 0.3321 \times 10^{-5}$s (pink) and $t = 0.3376 \times 10^{-5}$s (yellow).

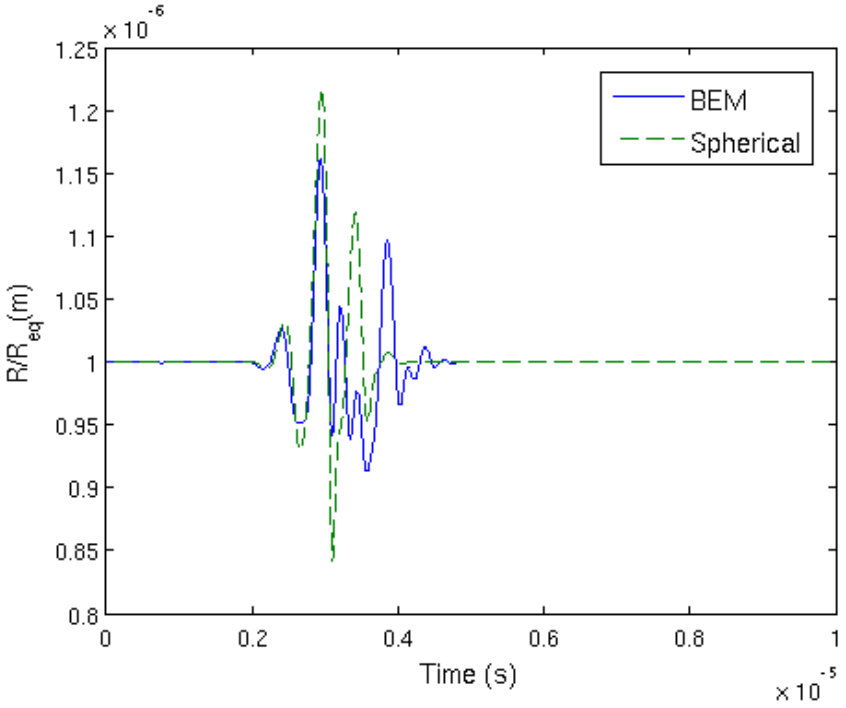

Figure 6.7: Equivalent bubble radius of an EMB forced by a Gaussian pulse with $p_A = 100$kPa, $f = 2$MHz, $Re = 6.3$ and $R_0 = 1\mu$m.

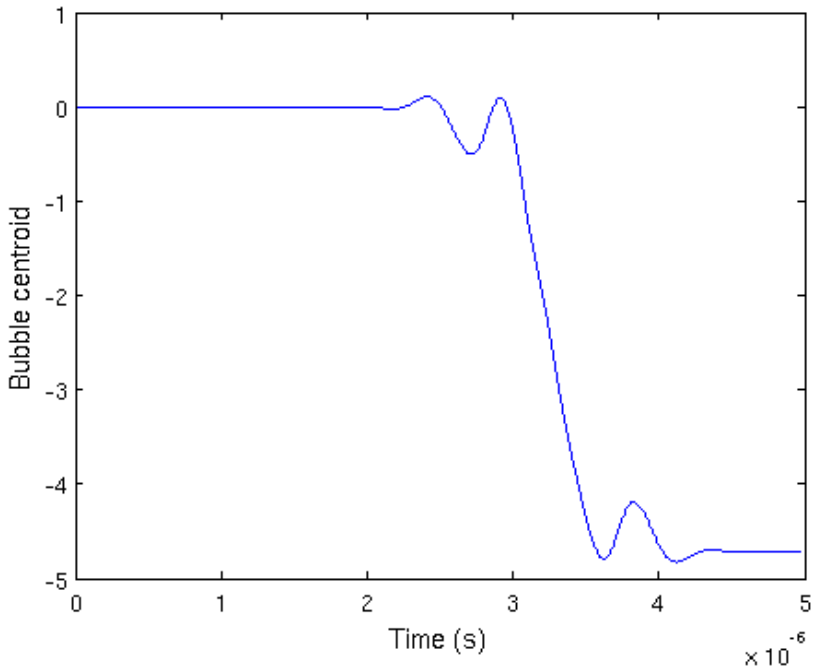

Figure 6.8: Centroid position for an EMB forced by a Gaussian pulse with $p_A = 100$kPa, $f = 2$MHz, $Re = 6.3$ and $R_0 = 1\mu$m.

Figs. 6.7, 6.8 show the bubble radius and centroid, respectively for $p_A = 100$kPa, $f = 2$MHz, $Re = 6.3$ and $R_0 = 1\mu$m. Similar to the previous case, the models agree initially with similar dynamics up to roughly 3μs. At this point the translation of the bubble in the direction of the pulse and the bubble becoming non-spherical in the BEM simulations leads to discrepancies. Note, though, that the deviation in radius from $R_0 = 1$ is of the same order for both simulations; both predict nonlinear, stable oscillations before a return to the initial radius for these parameters. The spherical model described in Chapter 2 is clearly too simplified to describe realistic dynamics of EMB's. The predictions are qualitatively similar to those obtained using the axisymmetric BEM model for some parameters but the translational movement of the bubble and non-spherical oscillations can lead to significantly different results to the spherical model.

6.4.2 Effect of viscoelasticity for an EMB near a rigid boundary

We now consider an EMB forced by a Gaussian pulse, near a rigid boundary. It is assumed the pulse is entirely reflected when it reaches the rigid boundary and thus no wave is transmitted through the material on the other side. This reflected pulse will interact with the bubble a second time and alter the dynamics. For low pulse amplitudes, $P_A = 50 - 200$kPa, the model is an approximation of an EMB used in ultrasound contrast imaging and it is expected the microbubble will experience stable, nonlinear oscillations in most cases. In sonoporation, higher amplitudes of $P_A \approx 2$MPa are used and explosive growth and collapse occurs for certain frequencies.

Contrast Imaging (Low Amplitude Shock Waves)

In Fig. 6.9, the equivalent radius and maximum pressure at the bubble wall are shown for parameters $P_A = 1$kPa, $f = 2$MHz, $R_0 = 1\mu$m, $Re = 6.27$, $De = 1$ and a range of initial stand-off distances $h = 1.5, 4, 10$. For all cases shown, the bubble exhibits stable oscillations similar to the spherical bubble in Chapter 2. Due to the stabilising shell, the solid boundary has little effect on the encapsulated bubble. Larger amplitude oscillations in equivalent radius occur for the case $h = 1.5$, although this could just be due to the reflected pulse being more in phase with the original pulse, rather than the proximity to the wall intensifying the oscillations. In general, the initial distance from

the wall h has little effect on the dynamics. This is expected, since the highly viscous shell negates the effect of the wall and the acoustic forcing dominates the dynamics.

For the same pulse parameters as Fig. 6.9 and $Re = 6.27$, the effect of changing De is shown in Fig. 6.10. Similar to the spherical model in Chapter 2, the fluid elasticity has little effect on the bubble oscillations since the effect of the highly viscous shell dominates. The position of the bubble, however, is more affected for larger De (see Fig. 6.12) which is not included in the spherical model. Changing the Reynolds number, on the other hand, has a more pronounced effect, as seen in Fig. 6.11. A higher Reynolds number (corresponding to lower viscosity) results in a more pronounced response to the acoustic forcing and consequently, higher pressures at the bubble surface. Note that these high pressures correspond to the minimums of bubble volume where the internal gas is highly compressed (dashed vertical lines).

Compared to the bubble in an infinite fluid (see, for example, Fig. 6.6) the bubble centroid does not move much in the direction of the shock wave propagation. Even though the pulse 'pushes' the bubble towards the wall, the reflected pulse is pushing it away from the wall. For an EMB the Bjerknes force towards the wall is negligible and the centroid position can actually move away from the wall during the oscillations, as seen in Fig. 6.12.

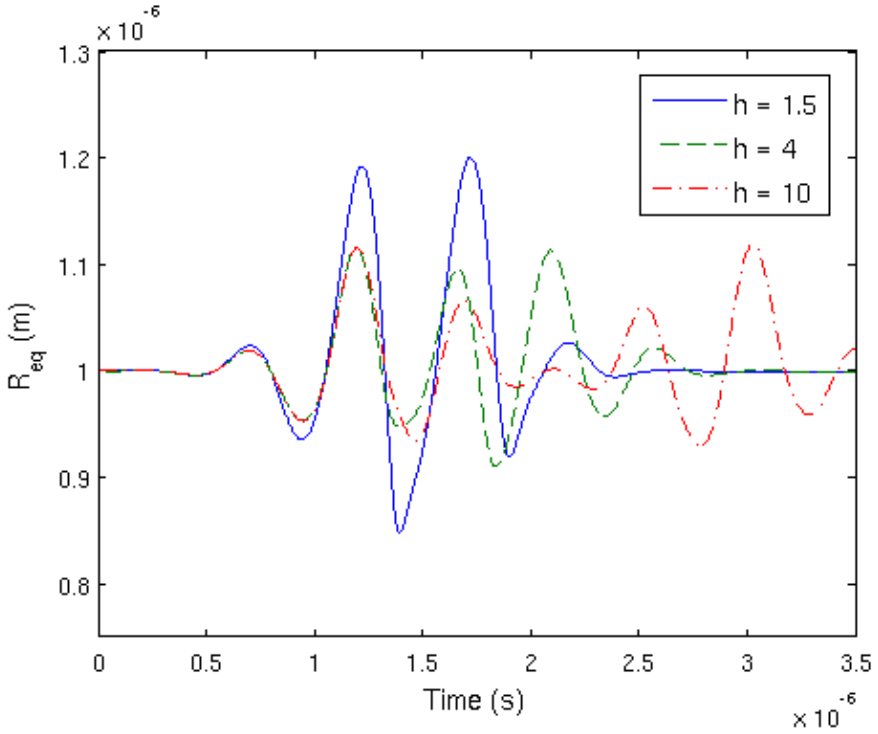

(a) Equivalent radius for an EMB of initial size $R_0 = 1\mu$m with $P_A = 1$kPa, $f = 2$MHz, $Re = 6.27$, $De = 1$ and varying h.

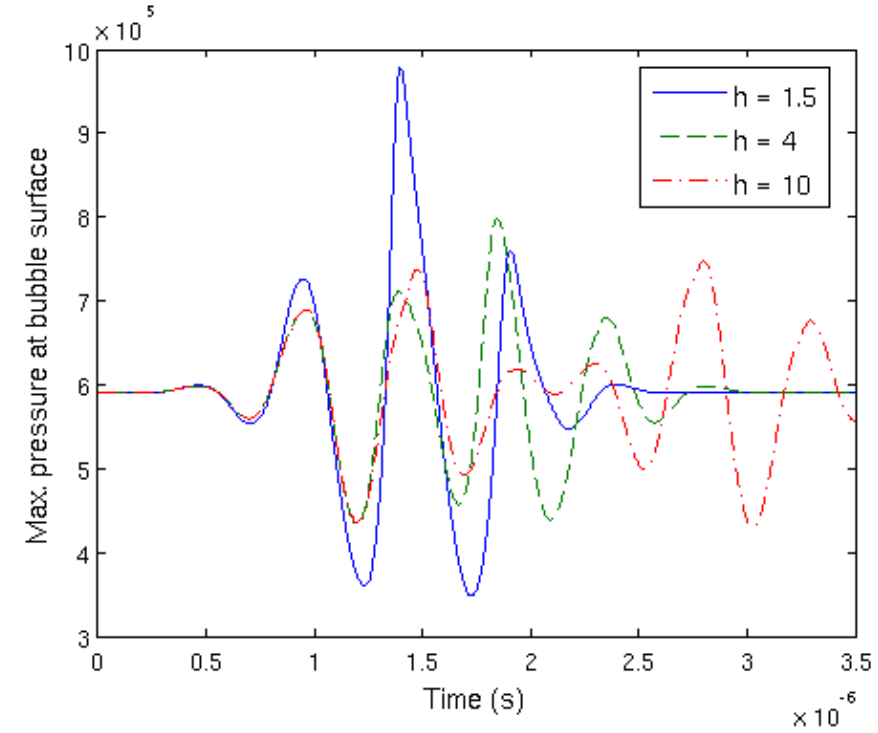

(b) Maximum pressure at the bubble wall for an EMB of initial size $R_0 = 1\mu$m with $P_A = 1$kPa, $f = 2$MHz, $Re = 6.27$, $De = 1$ and varying h.

Figure 6.9: Effect of initial stand-off distance with $R_0 = 1\mu$m, $P_A = 1$kPa, $f = 2$MHz, $Re = 6.27$ and $De = 1$.

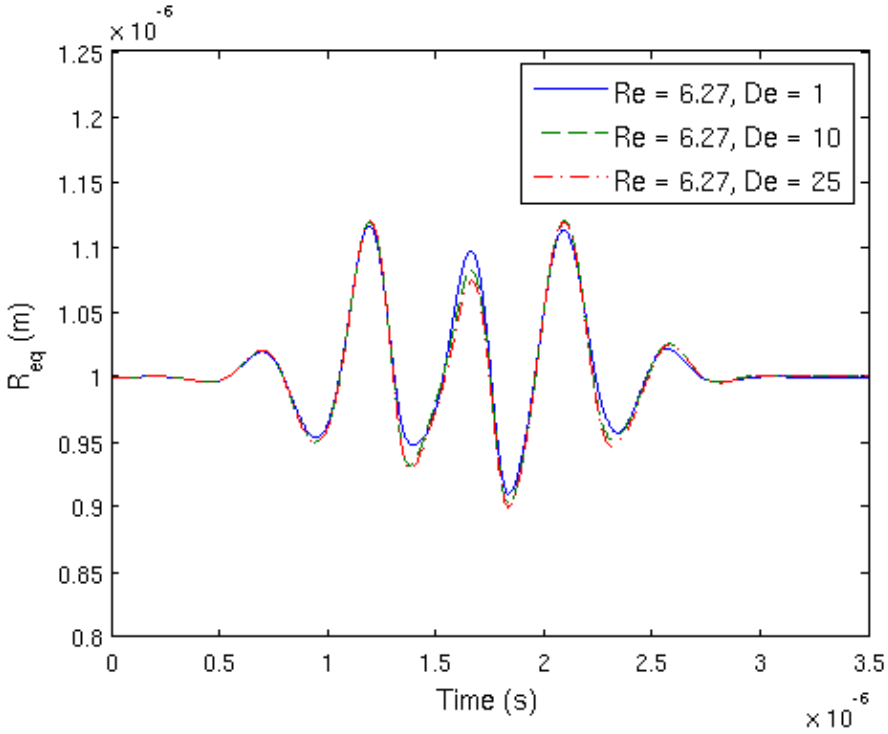

(a) Equivalent radius for an EMB of initial size $R_0 = 1\mu$m with $P_A = 1$kPa, $f = 2$MHz, $h = 4$, $Re = 6.27$, and varying De.

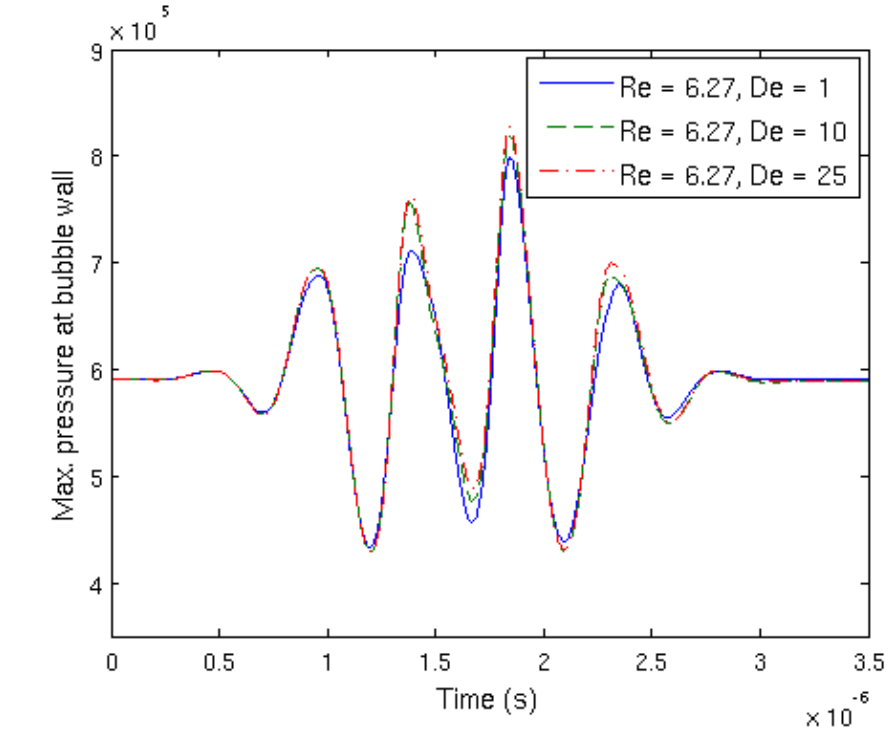

(b) Maximum pressure at the bubble wall for an EMB of initial size $R_0 = 1\mu$m with $P_A = 1$kPa, $f = 2$MHz, $h = 4$, $Re = 6.27$, and varying De.

Figure 6.10: Effect of fluid elasticity with $R_0 = 1\mu$m, $P_A = 1$kPa, $f = 2$MHz, $Re = 6.27$ and $h = 4$.

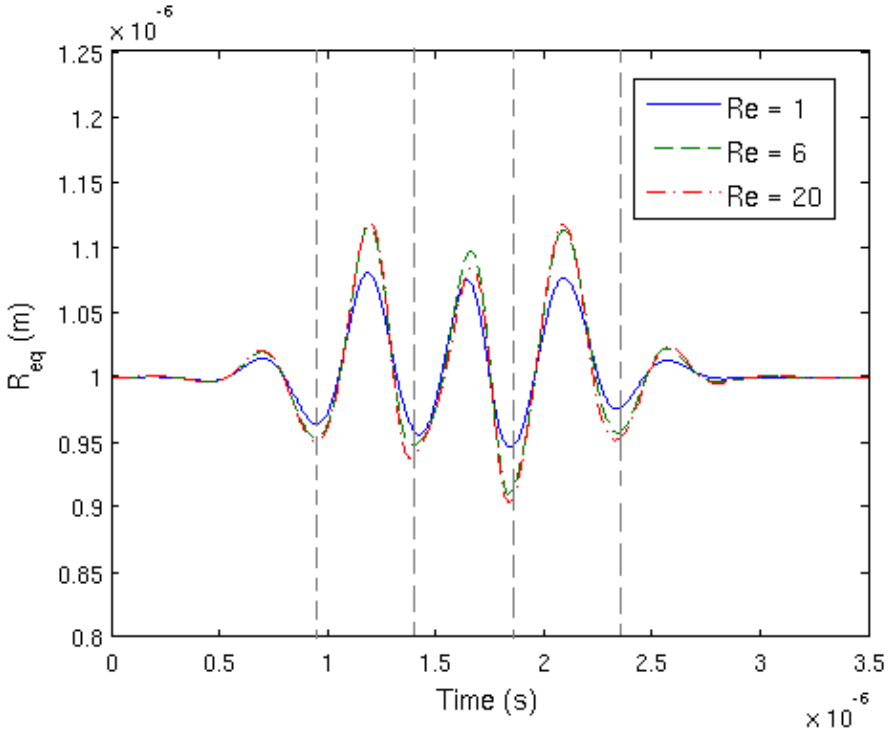

(a) Equivalent radius for an EMB of initial size $R_0 = 1\mu$m with $P_A = 1$kPa, $f = 2$MHz, $h = 4$, $De = 1$, and varying Re.

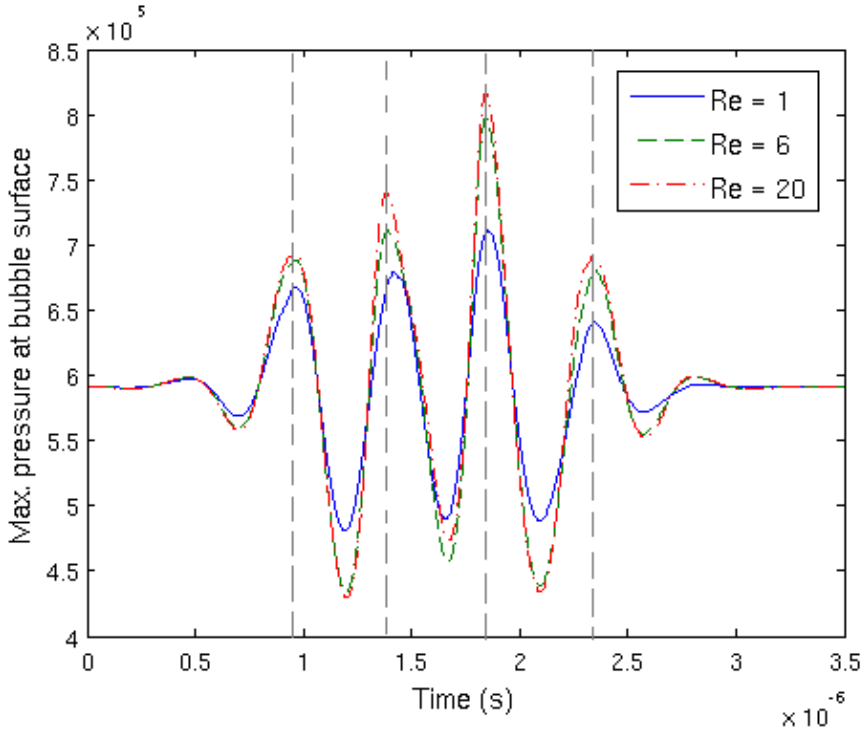

(b) Maximum pressure at the bubble wall for an EMB of initial size $R_0 = 1\mu$m with $P_A = 1$kPa, $f = 2$MHz, $h = 4$, $De = 1$, and varying Re.

Figure 6.11: Effect of fluid viscosity with $R_0 = 1\mu$m, $P_A = 1$kPa, $f = 2$MHz, $De = 1$ and $h = 4$.

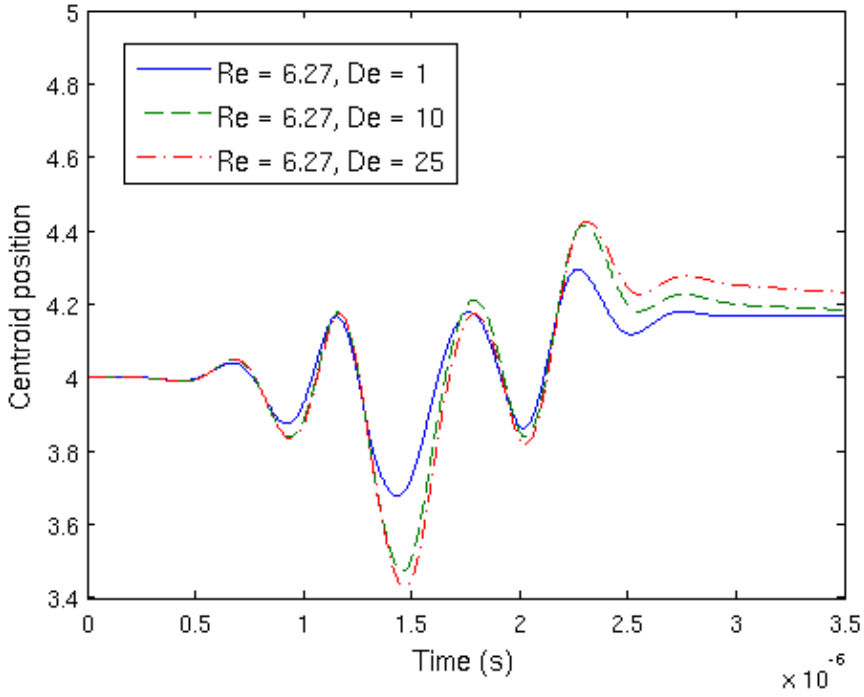

Figure 6.12: Centroid position for an EMB of initial size $R_0 = 1\mu$m with $P_A = 1$kPa, $f = 2$MHz, $h = 4$, $Re = 6.27$, and varying De.

Sonoporation (High Amplitude Shock Waves)

In sonoporation, high intensity ultrasound is used to increase the permeability of cells and allow the uptake of large molecules such as DNA. Cavitation has been shown to enhance the efficacy of this procedure, possibly due to liquid jets from collapsing cavities directly impacting the surface of the cell wall. Encapsulated microbubbles containing DNA or some other large molecule can be excited by ultrasound util disintegrate and release their contents. When disintegrating near a cell, the contents can potentially be injected into the cell directly as the bubble collapses or due to cavitation bubbles collapsing once the EMB has released its contents.

The effect of initial stand-off distance is shown in Fig. 6.13 for parameters $P_A = 2$MPa, $f = 2$MHz, $R_0 = 4\mu$m, $Re = 6.27$ and $De = 1$. For the case $h = 15$, the bubble is pushed towards the boundary before the reflected pulse reaches the bubble. Once the initial pulse has passed by the bubble, the reflected pulse then causes the bubble to move away from the boundary. Similar behaviour is seen for $h = 3$ and $h = 1.4$, with less translation as h decreases. For both $h = 3$ and $h = 1.4$ a very large spike in

pressure is seen at $t \approx 1.4\mu$s. This is due to the bubble becoming very distorted while it is at minimum volume.

In Fig. 6.14, the effect of fluid viscosity is shown for $De = 5$, $R_0 = 1\mu$m, $h = 10$ and a pulse with $P_A = 3$MPa and $f = 1$MHz. The fluid viscosity has little effect on the bubble position; for all the cases the bubble is driven towards the wall by the powerful pulse. In all cases, large growth is seen for the EMB to over twice the initial radius R_0 and, for $Re = 1$ and $Re = 6$, there is a subsequent violent collapse.

For $Re = 1$, the bubble surfaces are plotted in Fig. 6.15. The bubble flattens as it is pushed against the wall which resists the motion. The elasticity of the shell and fluid then cause the sides to rebound until the two sides touch (black line). At this point it is expected that the bubble will split into multiple bubbles or release its contents into the fluid. In contrast, for the case $Re = 15$ a liquid jet forms as the bubble moves towards the wall, as seen in Fig. 6.16 until jet impact occurs. The toroidal bubble then continues to move towards the wall until the expansion of the bubble leads to reconnection. Note that for the freely oscillating bubble in Chapter 4, the viscoelasticity of the fluid caused the toroidal bubble to rebound and move away from the wall. This does not happen here as the bubble is still being driven by the pulse towards the wall. Once reconnection occurs, explosive growth is seen until the bubble hits the wall which is shown in Fig. 6.18. Once the bubble becomes too close to the wall, numerical instabilities occur due to a very thin layer of fluid between the bubble and the wall.

The effect of changing the frequency is shown in Fig. 6.19 for parameters $P_A = 3$MPa, $Re = 6$, $De = 5$, $R_0 = 1\mu$m and $h = 10$. It seems as if he growth of the bubble increases as frequency is increased. However, the lower frequencies actually produce a larger initial growth and more intense collapse. The simulations for $f = 1$MHz and $f = 2$MHz are terminated at $t \approx 0.25\mu$s and $t \approx 0.52\mu$s, respectively, due to extremely large distortions in the bubble surface. For all cases, however, large pressure are produced as the bubble collapses and becomes appreciably deformed. If the EMB is situated close to a boundary it is hypothesised that these pressures of the order 10^8Pa could cause considerable damage. The case $f = 1$MHz produces a faster jet with the bubble transitioning to a toroidal form, unlike the other cases. The bubble surfaces for $f = 2$MHz are shown in Fig. 6.20 and are very similar to the case $f = 3$MHz with the simulation ending when the two sides of the bubble become too close together. Once again, it is expected at this point that the bubble will release its contents into the fluid or split into a number of smaller bubbles which in turn will eventually disintegrate.

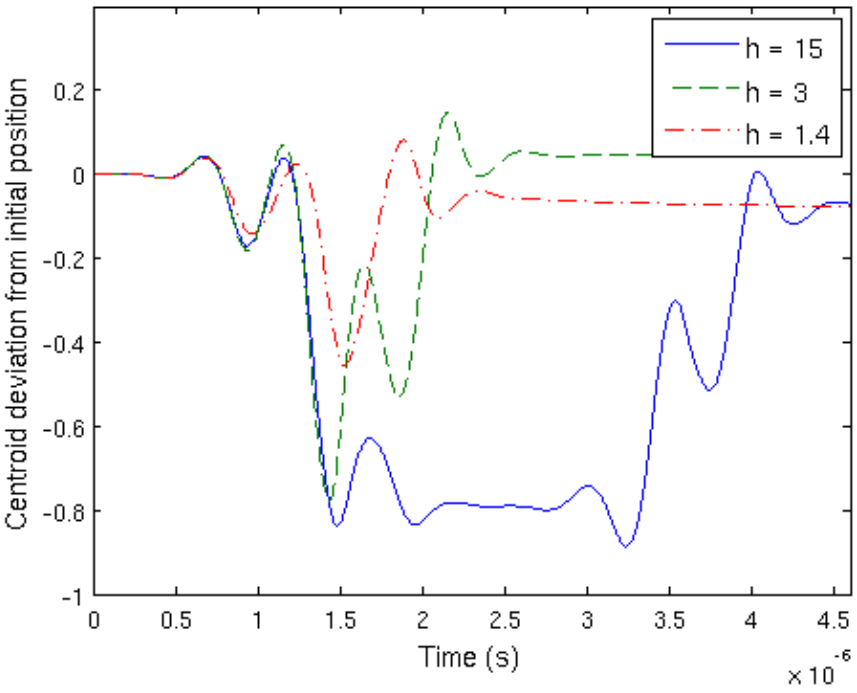

(a) Translational movement from initial position in the z-direction.

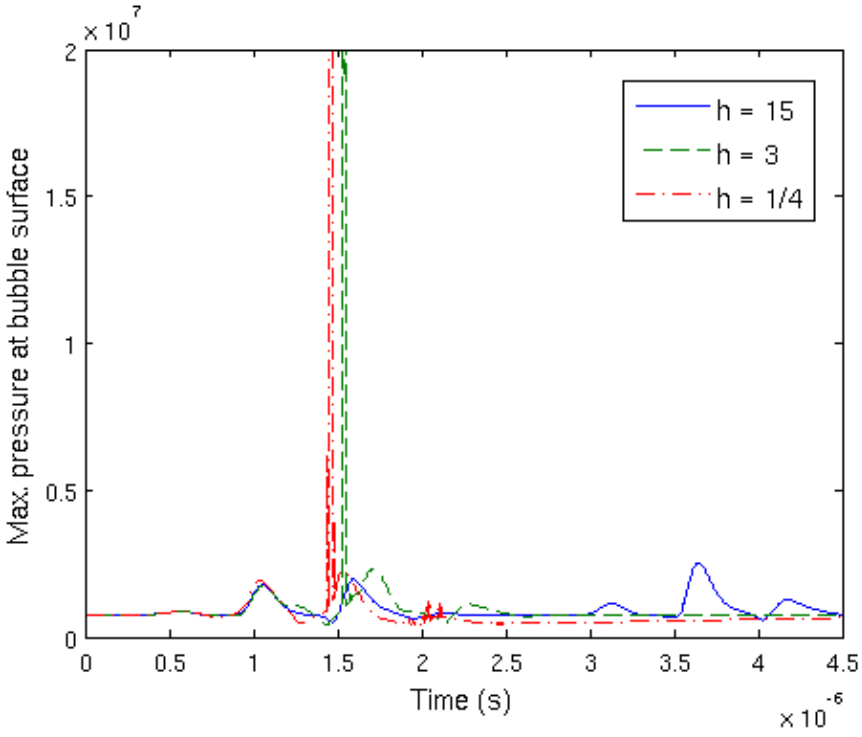

(b) Maximum pressure at the bubble surface.

Figure 6.13: Effect of initial stand-off distance for $P_A = 2$MPa, $f = 2$MHz, $R_0 = 4\mu$m, $Re = 6.27$ and $De = 1$.

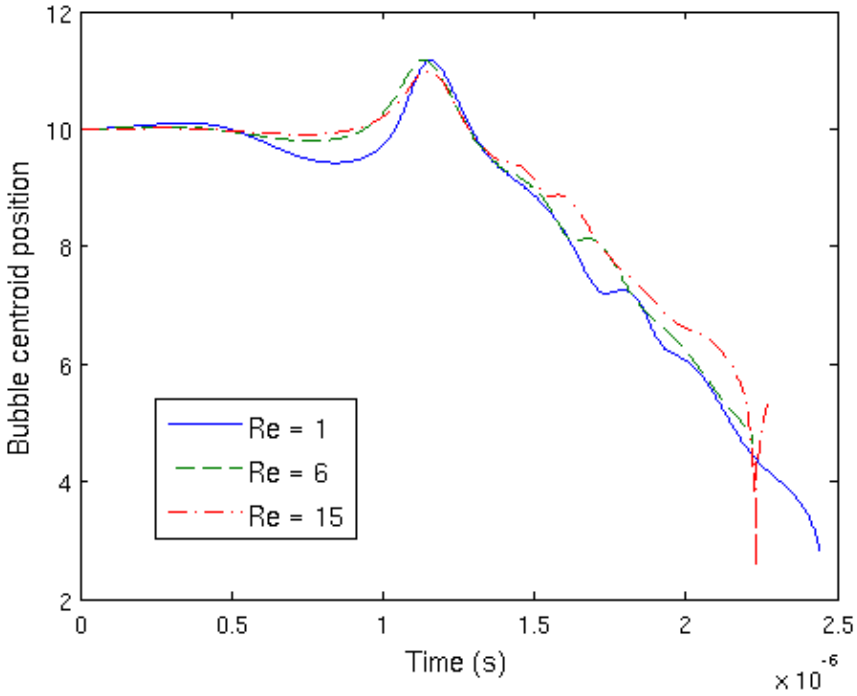

(a) Bubble centroid position for parameters: $P_A = 3$MPa, $f = 1$MHz, $De = 5$, $R_0 = 1\mu$m, $h = 10$ and $Re = 1, 6, 15$.

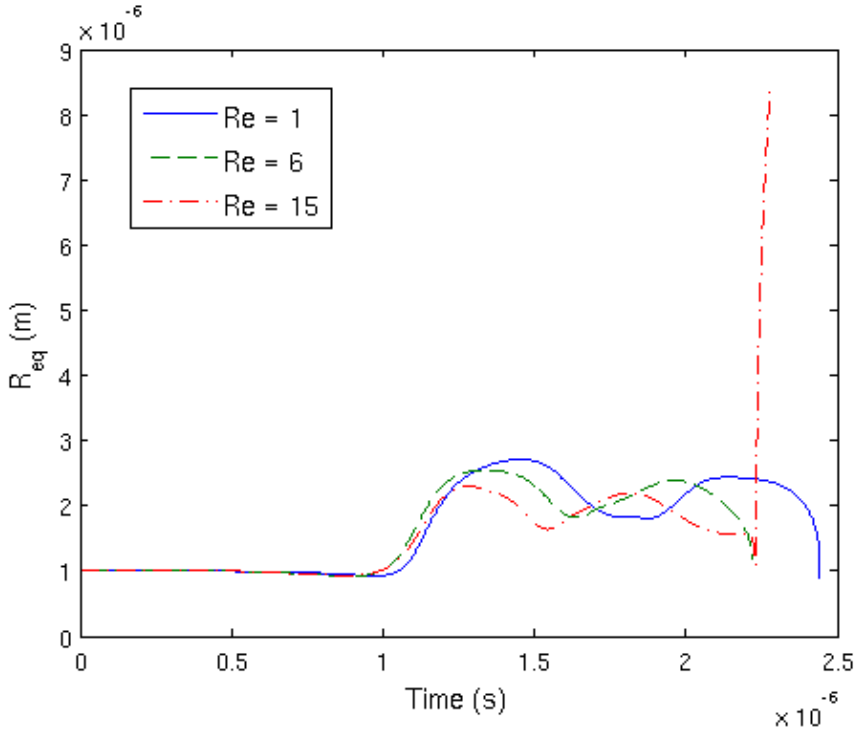

(b) Equivalent bubble radius for parameters: $P_A = 3$MPa, $f = 1$MHz, $De = 5$, $R_0 = 1\mu$m, $h = 10$ and $Re = 1, 6, 15$.

Figure 6.14

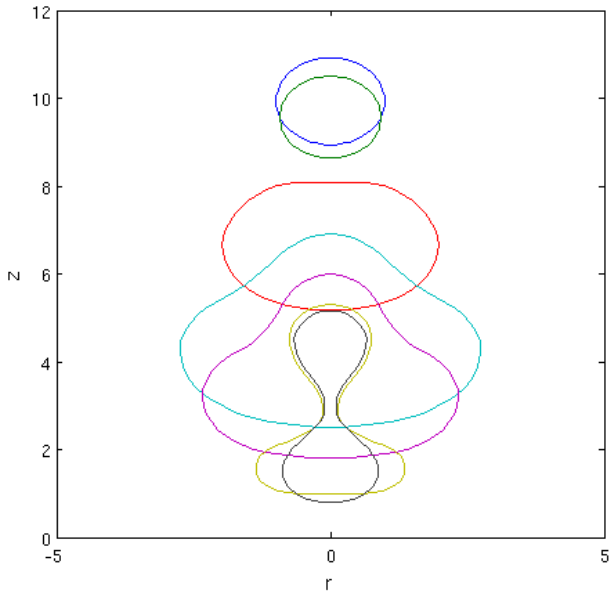

Figure 6.15: Bubble surfaces for parameters: $P_A = 3$MPa, $f = 1$MHz, $Re = 1$, $De = 5$, $R_0 = 1\mu$m, $h = 10$. The times are $t = 0.000$s (dark blue), $t = 0.857$ (green), $t = 1.741$ (red), $t = 2.182$ (light blue), $t = 2.383$ (purple), $t = 2.411$ (yellow) and $t = 2.428$ (black).

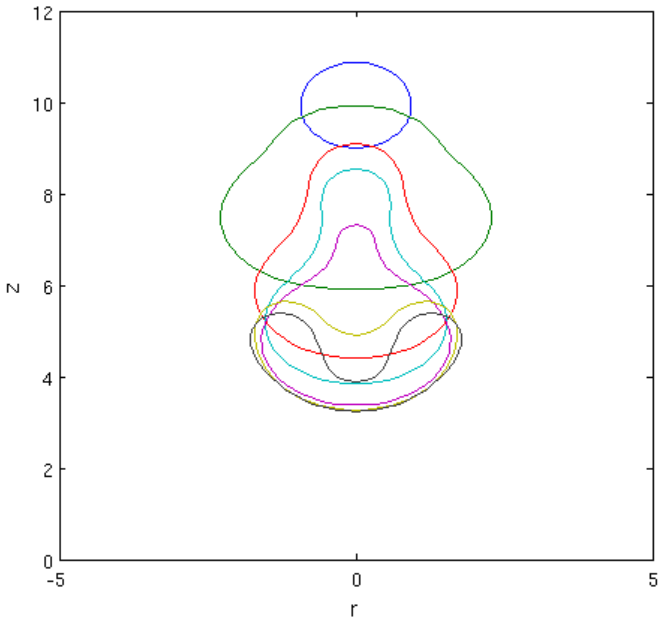

Figure 6.16: Initial singly-connected phase for parameters: $P_A = 3$MPa, $f = 1$MHz, $Re = 15$, $De = 5$, $R_0 = 1\mu$m, $h = 10$. The initial bubble surface (dark blue line) is at $t = 0$ and the final bubble surface (black line) occurs at $t \approx 2.224\mu$s.

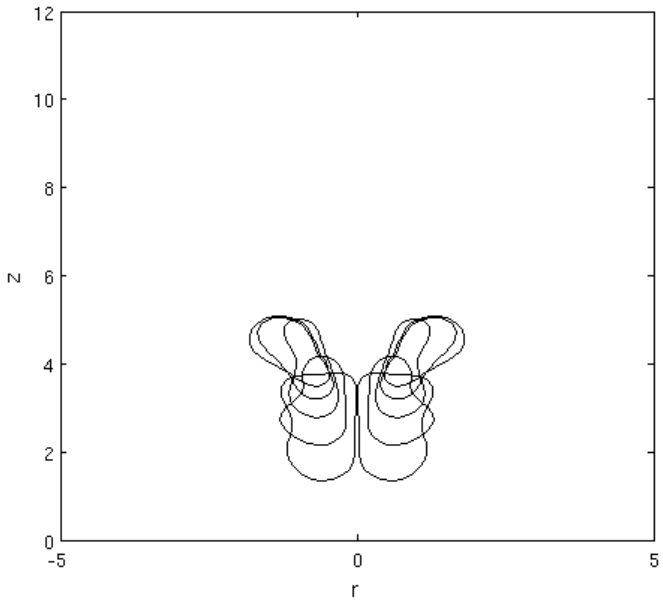

Figure 6.17: First toroidal phase for parameters: $P_A = 3\text{MPa}$, $f = 1\text{MHz}$, $Re = 15$, $De = 5$, $R_0 = 1\mu\text{m}$, $h = 10$. The first and last bubble surfaces are at $t \approx 2.224\mu\text{s}$ and $t \approx 2.231\mu\text{s}$, respectively (top to bottom).

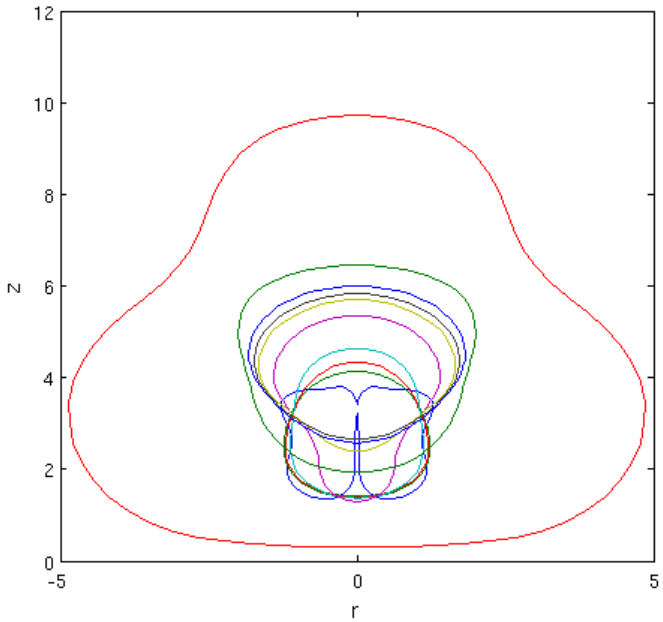

Figure 6.18: Second singly connected phase for parameters: $P_A = 3\text{MPa}$, $f = 1\text{MHz}$, $Re = 15$, $De = 5$, $R_0 = 1\mu\text{m}$, $h = 10$. The first and last bubble surfaces are at $t \approx 2.231\mu\text{s}$ and $t \approx 2.278\mu\text{s}$, respectively.

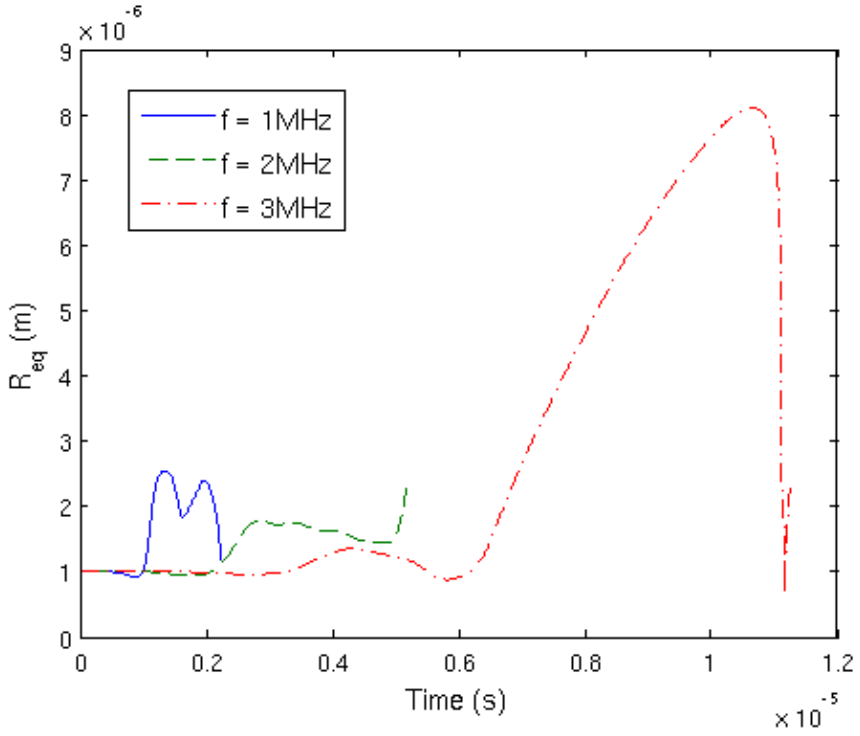

(a) Equivalent radius vs. time.

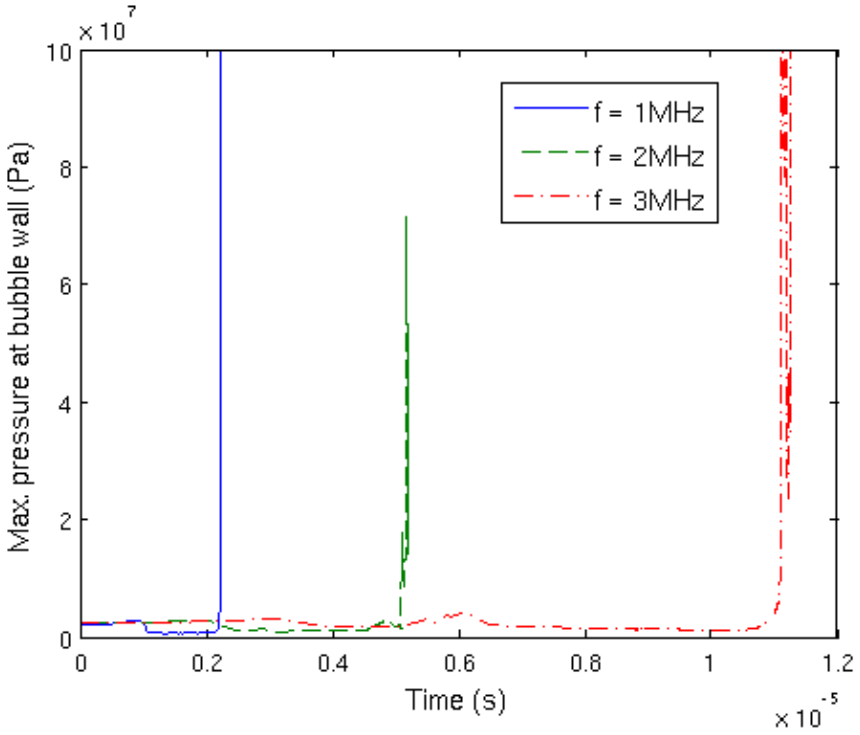

(b) Maximum pressure at the bubble wall vs. time.

Figure 6.19: Effect of changing frequency for parameters $P_A = 3$MPa, $Re = 6$, $De = 5$, $R_0 = 1\mu$m and $h = 10$.

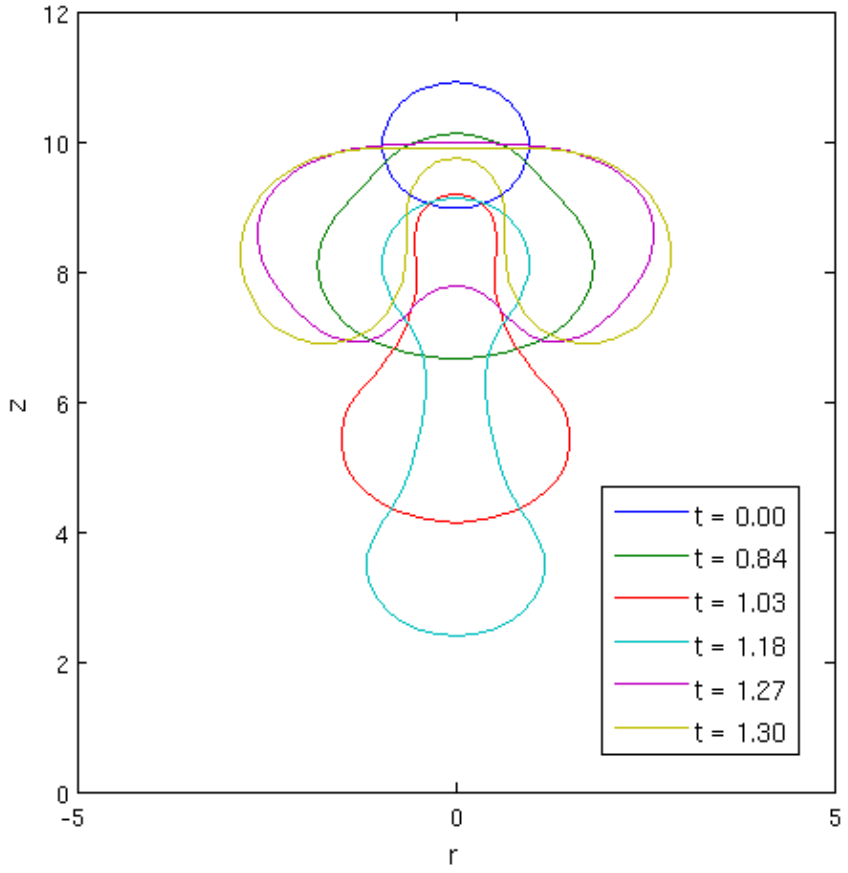

Figure 6.20: Bubble surfaces for parameters: $P_A = 3$MPa, $f = 2$MHz, $Re = 1$, $De = 5$, $R_0 = 1\mu$m, $h = 10$. The times are given in microseconds.

The effects of changing the width of the shell on the bubble position and size are shown in Figs. 6.21 and 6.22, respectively for $P_A = 2$MPa, $f = 1$MHz, $Re = 6$, $De = 1$, $R_0 = 1\mu$m, $h = 8$ and $\varepsilon = 1, 5, 10$nm (shell width). The thicker the shell is, the more it resists the motion induced by the ultrasonic forcing. Due to the powerful pulse, however, a liquid jet forms in all cases and the bubbles become unstable. The different widths in this case thus produce results that are different only in degree, rather than in type.

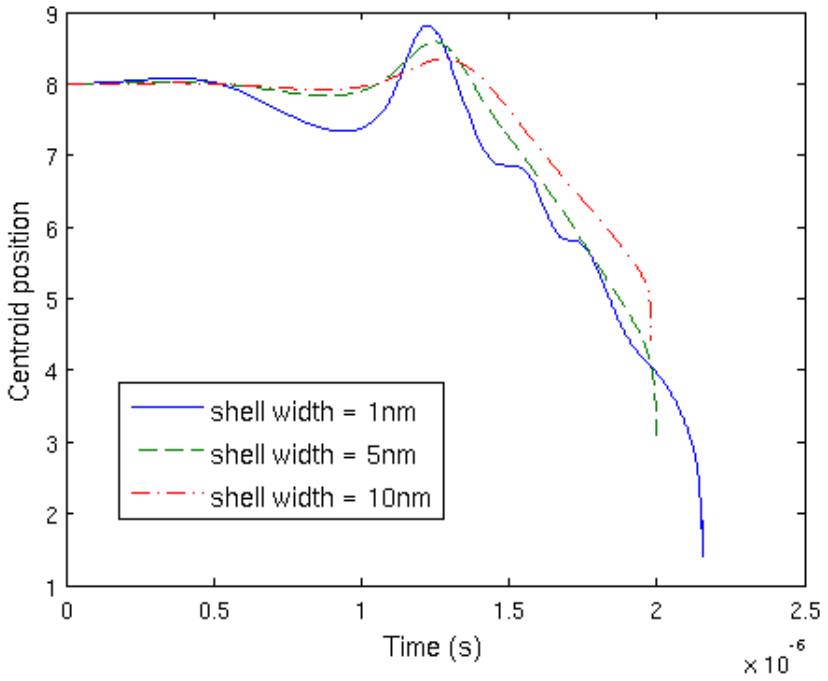

Figure 6.21: Effect of changing the shell width on centroid position for $P_A = 2$MPa, $f = 1$MHz, $Re = 6$, $De = 1$, $R_0 = 1\mu$m and $h = 8$.

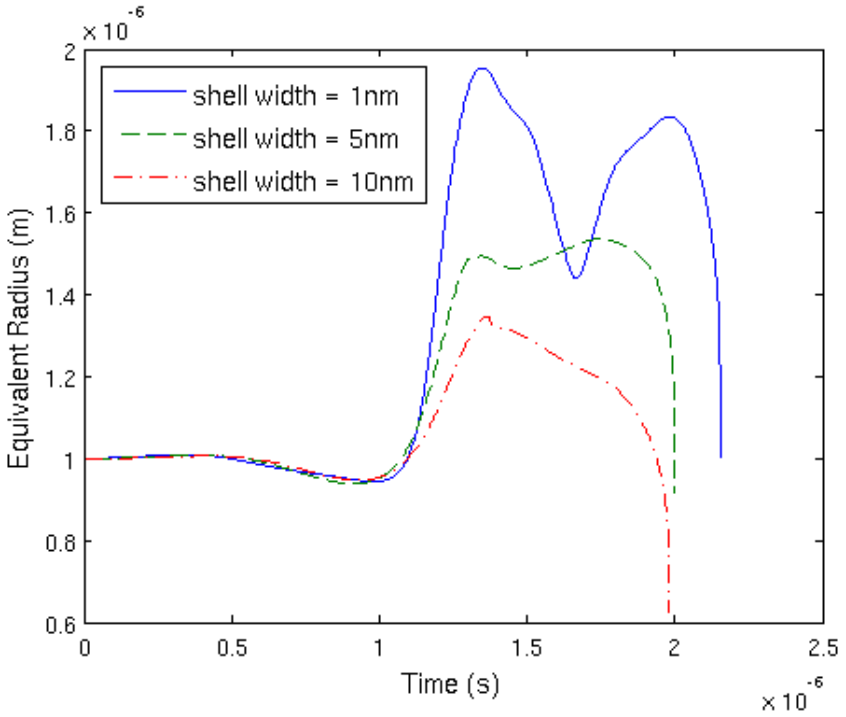

Figure 6.22: Effect of changing the shell width on bubble size for $P_A = 2$MPa, $f = 1$MHz, $Re = 6$, $De = 1$, $R_0 = 1\mu$m and $h = 8$.

6.5 Conclusions

In this chapter, a model for a non-spherical encapsulated microbubble (EMB) is developed using the boundary element method. Considering an EMB forced by a Gaussian pulse gives an initial approximation of applications such as contrast imaging and sonoporation. Compared to a clean cavitation bubble, the EMB is found to be much more stable due to its shell. This agrees with the spherical models of Chapter 2 and experimental observations of commercially used encapsulated bubbles.

For pressure amplitudes in the range common to ultrasound contrast imaging, stable nonlinear oscillations are seen for an EMB near a wall, with the bubble translating in the direction of the wave propagation. This agrees with the spherical model as well as experimental observations [35]. In some cases, however, when the bubble is in a large expanse of fluid it can actually disintegrate at low pressure amplitudes. This occurs due to the translational movement of the bubble and the asymmetric collapse resulting in a highly distorted bubble surface. Due to the highly viscous shell, the fluid rheology is found to have less effect on an EMB, compared to a cavitation bubble of similar size. In particular, the fluid elasticity seems to have very little effect on the dynamics.

For higher pressure amplitudes of roughly 2MPa, the dynamics are more unstable with the bubble either transitioning to a toroidal form or becoming highly deformed. Much larger growth is also seen with a maximum radius nearly ten times larger than the initial radius found in some cases. For these larger pressure amplitudes, the fluid rheology actually seems to be more influential. It is thought that this is due to the bubble surface being more unstable with higher velocities encountered. These high velocities lead to large stresses and thus a wider range of dynamics.

Chapter 7

Conclusions

In this thesis the dynamics of cavitation bubbles and encapsulated microbubbles in a viscoelastic fluid have been investigated numerically, both in an infinite fluid and near a solid boundary.

7.1 Spherical, Incompressible Bubble Dynamics

In Chapter 2, an initial study of bubble dynamics is undertaken under the assumption that the bubble remains spherical for all time. Results for the oscillations of a gas-filled cavitation bubble in both a Linear Jeffreys and Oldroyd-B fluid are presented. Both models predict similar behaviour with damped oscillations of the bubble radius relative to an inviscid fluid and larger, slower oscillations as fluid elasticity is increased. The primary difference between the models is a more intense collapse and higher pressures observed for the linear model. This discrepancy is due to the lack of accuracy of a linear model for large deformations. The Oldroyd-B model is chosen to represent fluid rheology throughout the thesis since it is able to model common features of viscoelastic fluids but is simply enough to implement in the numerical methods used.

An encapsulated microbubble (EMB) is also modelled in a similar manner by modifying the Rayleigh-Plesset model with terms representing the viscosity and elasticity of the shell. Typically, the shell is highly viscous and has a stablising effect on the dynamics similar to an increase in the fluid viscosity. The dynamics of an EMB forced by an acoustic field are explored and it is found that the fluid rheology has less effect on the dynamics than in the case of a clean cavitation bubble. For the forced EMB, the critical

parameters are the strength and frequency of the acoustic forcing.

7.2 Cavitation Bubble Dynamics Near a Rigid Wall

The boundary element method (BEM) is chosen to model non-spherical bubbles. A new, non-singular formulation of the BEM with a quintic spline discretisation is presented with an improved accuracy and stability over the standard formulation.

7.2.1 Singly-Connected Bubble

For an initially spherical bubble, the non-singular formulation of the BEM is compared to the standard formulation. Originally, the quintic spline discretisation is compared to results using a cubic spline discretisation by Lind and Phillips [67] for the standard BEM. It is found that the quintic spline discretisation is more accurate and stable. This increase, however, is marginal and involves an increase in computational time. On the other hand, the non-singular formulation is significantly more stable than the original formulation and accumalates less numerical errors over time. This shows that the numerical errors of the original BEM are caused by two nodes becoming too close together. When this happens, the influence of the nearby node on the kernel of integration causes near-singular behaviour and numerical errors. In the non-singular formulation, the singular integrals are removed at the onset meaning that errors do not arise from nodes being too close together.

Using the non-singular BEM, the dynamics of a gas-filled cavitation bubble in an Oldroyd-B fluid is studied, near a rigid wall. It was found that, in general, viscoelasticity inhibits the formation of a liquid jet. In particular, an increase in fluid viscosity results in smaller velocities and less deformation of the bubble. The ratio of the Reynolds to Deborah number is important since the dynamics are governed by a competition between viscous, elastic and inertial effects. Due to this, liquid jets can also form for a bubble in a viscoelastic fluid. If this occurs, the centre of the bubble was found to be thinner with distinctive 'lobes' forming either side. Including surface tension effects also results in more unstable oscillations as parts of the bubble oscillate out of phase; leading to highly deformed bubble surfaces.

7.2.2 Toroidal Bubble

In Chapter 4, the non-singular formulation of the boundary element method developed in Chapter 3 is extended to model the transition to a toroidal geometry. The vortex ring method is used in which a vortex ring is seeded inside the bubble. This vortex ring accounts for the new circulation in the fluid as well as the discontinuity in the velocity potential.

For an inviscid fluid, the bubble moves towards the wall with a powerful liquid jet forming and causing high pressures at the rigid wall. These velocities and pressures are found to increase as the cavitation bubble nucleates closer to the wall.

It was found in Chapter 3 that, although viscosity tends to inhibit jet formation (and thus transition to a toroidal geometry), it can happen if the fluid elasticity is strong enough to overcome the viscous effects. When a liquid jet does form for a bubble in an Oldroyd-B fluid, the bubble centre is much flatter than the inviscid case near jet impact. This, along with the fluid elasticity, results in the bubble rebounding and moving away from the boundary for a short amount of time after the transition to toroidal form. Furthermore, the bubble is also seen to form a liquid jet *away* from the rigid wall after reconnecting to a singly-connected form, for certain parameters. This behaviour results in lower velocities and pressures produced compared to the inviscid case. This indicates that the damage done to a nearby surface could be reduced by the rheology of the surrounding fluid but that high pressures and stresses can still occur for a bubble in a viscoelastic fluid.

This work has been submitted to the Journal of Non-Newtonian Fluid Mechanics [105].

7.3 Interaction Between a SWL Pulse and a Cavitation Bubble

In Chapter 5, the BEM developed in Chapters 3 and 4 is used to model a cavitation bubble forced by a pressure pulse. Initially, a simple step function for the pressure is considered as a simple initial approximation to the conditions found in shock wave lithotripsy (SWL). This was first implemented by Klaseboer et al. [59] for an inviscid fluid and is extended to consider a bubble in an Oldroyd-B fluid. Using pulse strengths typical to SWL it was found that the fluid rheology does affect the dynamics, despite

the very high pressures involved. Similar behaviour to the freely oscillating bubble considered in Chapters 3 and 4 was found, with fluid viscosity lowering velocities and preventing transition to a toroidal form. In comparison to the freely oscillating bubble, however, much higher velocities were obtained in general. A key feature highlighted was the stage of oscillationg of the bubble at the time at which the pulse impacts. If the bubble is growing the inertia of the bubble causes the pulse to have less effect than if the bubble is at maximum volume or collapsing. This model is not very accurate, however, since the pressure pulse only consists of a region of positive pressure which causes the bubble to collapse immediately. In reality, the shock contains a negative (tensile) region as well which can cause bubble growth. Furthermore, it is this negative pressure which actually initiates the cavitation.

To more accurately simulate the conditions in SWL, a more accurate description of the pressure field is then developed. Since it is known that the applied ultrasound field initiates the cavitation, we model a small bubble being created when the pressure at a particular point (due to the pulse) falls below a certain value. In reality, the ultrasound field causes a microscopic cavity in the fluid to grow and form a cavitation bubble. The precise details of the location of such cavities, as well as the pressures required to cause cavitation, are not considered for simplicity. Depending on the strength of the pulse, the bubble can grow significantly larger than in the freely oscillating bubble case before collapsing with very high velocities. With this more accurate model, the fluid rheology is found to be even more important since it can affect the growth phase of the bubble as well as the collapse. For high enough pressure amplitudes, however, the dynamics are found to be governed by inertia with viscoelastic effects negligible.

7.4 Dynamics of an Encapsulated Bubble Forced by Ultrasound

In Chapter 2, a model for a spherical encapsulated microbubble (EMB) was developed by modifying the Rayleigh-Plesset equation to account for the viscosity and elasticity of the shell. Using a similar argument, the boundary element method is modified to approximately model an EMB forced by a Gaussian pulse and near a rigid wall.

Similar to the spherical model, fairly stable oscillations were observed for low pressure amplitudes. Significant translation of the bubble in the direction of wave propagation

was observed, however, which is not accounted for in the spherical model. Furthermore, allowing the bubble to become non-spherical shows that the acoustic forcing can cause the bubble to become highly distorted, leading to potential disintegration of the bubble even at the fairly low amplitudes used in ultrasound contrast imaging.

For high pressure amplitudes (in the range typical for sonoporation), explosive growth and collapse was observed for certain parameters with the bubble either becoming toroidal or splitting into two bubbles. The dynamics predicted by this model fit well with the behaviour seen in experiments. The fluid viscosity is found to be very important, despite the high pressure amplitudes involved. The bubble becomes very deformed with large velocities occuring. These, in turn, lead to high stresses and thus a larger influence of the fluid rheology.

This work has been submitted to the Journal of Non-Newtonian Fluid Mechanics [104].

7.5 Further Work

Throughout this thesis, the fluid surrounding the bubble has been assumed to be incompressible. This is a useful approximation since the velocity potential then satisfies the Laplace equation and can be solved using a boundary integral. This is only accurate, though, when the wall velocity is significantly less than the fluid Mach number. It has been shown that during the final stages of collapse and jet formation the bubble wall can reach high enough velocities to make this approximation no longer strictly valid. The bubble also loses energy through the generation of shock waves near minimum volume [106], which is not accounted for by the incompressible modelling.

7.5.1 Modelling Weak Compressibility of the Fluid

Spherical Bubbles

In Chapter 2, the dynamics of a spherical bubble in an incompressible fluid were shown to be governed by the Rayleigh-Plesset equation (2.15). For a weakly compressible fluid, a family of equations exist which are all accurate to the same order in the fluid Mach number.

Using an extension of the Kirkwood-Bethe approximation [46], the following family of

equations can be derived for a spherical bubble in a weakly compressible, viscoelastic fluid

$$R\ddot{R}\left(1-\frac{\alpha+1}{c_\infty}\dot{R}\right)+\frac{3}{2}\dot{R}^2\left(1-\frac{3\alpha+1}{3c_\infty}\dot{R}\right)=\frac{(p_i-\frac{2\sigma}{R}-p_\infty)}{\rho_\infty}\left(1+\frac{1-\alpha}{c_\infty}\dot{R}\right)$$
$$\frac{R}{c_\infty}\frac{(\dot{p}_i+\frac{2\sigma}{R^2}-\dot{p}_\infty)}{\rho_\infty}-\frac{2}{\rho_\infty}\left(1+\frac{1-\alpha}{c_\infty}\dot{R}\right)\int_R^\infty\frac{\tau_{rr}-\tau_{\theta\theta}}{r}dr-\frac{2}{\rho_\infty}\frac{R}{c_\infty}\frac{\mathrm{d}}{\mathrm{d}t}\int_R^\infty\frac{\tau_{rr}-\tau_{\theta\theta}}{r}dr, \tag{7.1}$$

where c_∞ is the speed of sound in the fluid and α is some parameter which must be of order 1 to retain the accuracy of the equation.

Fig. 7.1 shows the oscillation of a bubble in a weakly compressible fluid (using Equation (7.1) with $\alpha = 0$ and Mach number $= 0.0214$) compared to the incompressible model.

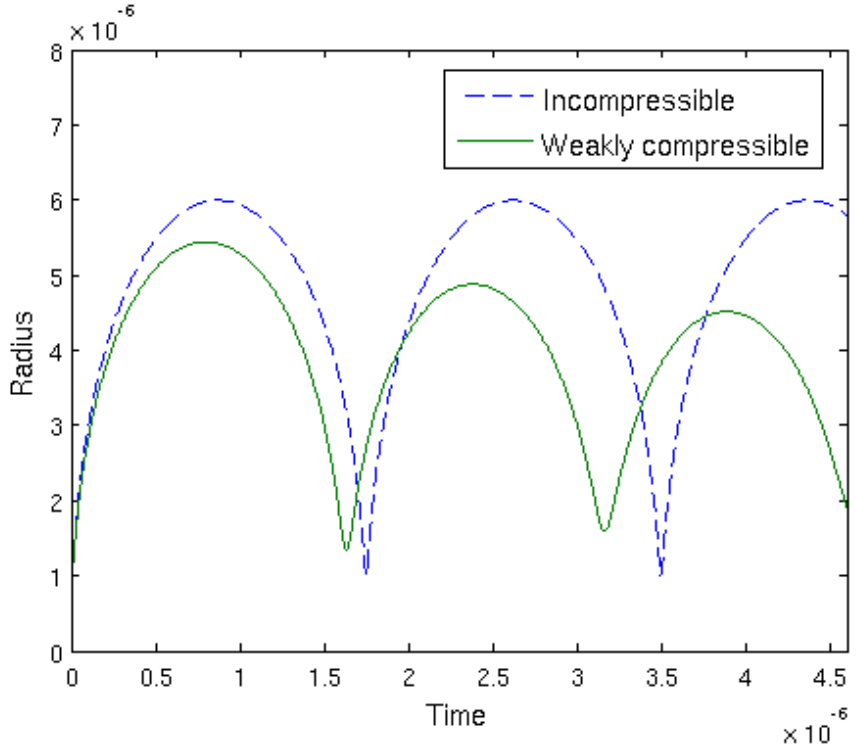

Figure 7.1: Oscillations of a spherical bubble in an incompressible fluid and a weakly compressible fluid. For the compressible fluid the Mach number is taken to be 0.0214.

BEM Modelling

In two papers [108, 109] Wang and Blake incorporated weak compressibility of the fluid into the model through the method of matched asymptotic expansions. The method is

extended here to a viscoelastic fluid.

For a compressible fluid the equations of motion are

$$\frac{\mathrm{D}\rho}{\mathrm{D}t} + \rho(\nabla \cdot \mathbf{u}) = 0, \tag{7.2}$$

$$\rho\frac{\mathrm{D}\mathbf{u}}{\mathrm{D}t} = -\lambda_v \nabla^2 \mathbf{u} - [\nabla \cdot \boldsymbol{\pi}] + \rho\mathbf{g}, \tag{7.3}$$

where λ_v is the second coefficient of viscosity (bulk viscosity) [24].

Writing the velocity in terms of a potential φ gives the equation of mass conservation

$$\nabla^2\varphi + \frac{1}{\rho}\frac{\mathrm{D}\rho}{\mathrm{D}t} = 0, \tag{7.4}$$

which can also be written as

$$\nabla^2\varphi + \frac{1}{c^2}\left(\frac{\partial\hat{p}}{\partial t} + \nabla\varphi \cdot \nabla\hat{p}\right) = O(\varepsilon^4), \tag{7.5}$$

where c is the speed of sound in the fluid and $\hat{p} = (p - p_\infty)/\rho_\infty$. Similarly, the Bernoulli equation becomes

$$\frac{\partial\varphi}{\partial t} + \frac{1}{2}|\nabla\varphi|^2 + \hat{p} = O(\varepsilon^2), \tag{7.6}$$

where gravity and buoyancy effects have been neglected. As in Chapters 3-6 the fluid rheology is introduced through the boundary condition with bulk viscosity neglected. The variables are non-dimensionalised as in Chapters 3-6 to give

$$\nabla_*^2\varphi_* + \frac{\varepsilon^2}{c_*^2}\left(\frac{\partial\hat{p}_*}{\partial t} + \nabla_*\varphi_* \cdot \nabla_*\hat{p}_*\right) = 0(\varepsilon^4), \tag{7.7}$$

$$\frac{\partial\varphi_*}{\partial t_*} + \frac{1}{2}|\nabla_*\varphi_*|^2 + \hat{p}_* = O(\varepsilon^2), \tag{7.8}$$

with $c_*^2 = c/c_\infty$ and c_∞ is the speed of sound in the fluid.

Matched asymptotic expansions

The fluid domain is divided into an inner region in which $(r, z) = 0(R_m)$ and an outer region where $(r, z) = 0(c_\infty T)$ where $T = R_m/U$. The length scale of the outer region is much larger than that of the inner region whereas the time scales are the same. The second order derivative of the velocity potential is thus two orders smaller than the second order derivative in space and Eqn. (7.7) reduces to Laplace's equation to second order. The inner domain is thus approximately incompressible with compressible effects appearing in the far field.

For the far field the outer variable $\bar{r}$ is defined as $\bar{\mathbf{r}} = r/(c_\infty T) = \varepsilon \mathbf{r}_*$. In terms of this variable the outer expansions of φ and $\hat{p}$ are

$$\varphi_*(\mathbf{r}, t_*) = \phi(\tilde{\mathbf{r}}, t_*) = \phi_0(\tilde{\mathbf{r}}, t_*) + \varepsilon\phi_1(\tilde{\mathbf{r}}, t_*) + \ldots, \tag{7.9}$$

$$\hat{p}_*(\mathbf{r}, t_*) = P(\tilde{\mathbf{r}}, t_*) = P_0(\tilde{\mathbf{r}}, t_*) + \varepsilon P_1(\tilde{\mathbf{r}}, t_*) + \ldots. \tag{7.10}$$

Substituting these into Equations (7.7,7.8) gives

$$\tilde{\nabla}^2\phi_0 + \varepsilon\tilde{\nabla}^2\phi_1 + \frac{1}{c^2}\left(\frac{\partial P_0}{\partial t} + \varepsilon\frac{\partial P_1}{\partial t} + (\varepsilon\tilde{\nabla}\phi_0 + \varepsilon^2\tilde{\nabla}\phi_1)(\varepsilon\tilde{\nabla}P_0 + \varepsilon^2\tilde{\nabla}P_1)\right) = O(\varepsilon^2), \tag{7.11}$$

$$\frac{\partial^2\phi_0}{\partial t^2} + \varepsilon\frac{\partial^2\phi_1}{\partial t^2} + \frac{1}{2}\frac{\partial}{\partial t}|\varepsilon\tilde{\nabla}\phi_0 + \varepsilon\tilde{\nabla}\phi_1|^2 + \frac{\partial P_0}{\partial t} + \varepsilon\frac{\partial P_1}{\partial t} = O(\varepsilon^2). \tag{7.12}$$

where $\tilde{\nabla}$ is defined in terms of the outer variable $\bar{\mathbf{r}}$. Considering terms of order 1 and ε the first two orders of the outer solution satisfy the wave equation

$$\tilde{\nabla}^2\phi_i - \frac{\partial^2\phi_i}{\partial t^2} = 0, \quad \text{for } i = 0, 1. \tag{7.13}$$

The far field is not affected by the existence of the bubble to first order so

$$\phi_0 = 0, \tag{7.14}$$

whereas the second-order outer solution is given by the well known d'Alembert solution of the wave equation

$$\phi_1 = \frac{F_1(t - \tilde{\mathbf{r}}) + G_1(t + \tilde{\mathbf{r}})}{\tilde{\mathbf{r}}} = \frac{F_1(t - \tilde{\mathbf{r}})}{\tilde{\mathbf{r}}}, \tag{7.15}$$

for some function F_1 which is found by matching the inner and outer solutions. The

function G_1 vanishes since, according to the Sommerfeld radiation condition, no energy may be radiation from infinity into the field and thus ϕ_1 cannot contain incoming waves.

The inner expansions in terms of $\mathbf{r}$ are

$$\varphi_*(\mathbf{r}_*, t_*) = \varphi_0(\mathbf{r}_*, t_*) + \varepsilon\varphi_1(\mathbf{r}_*, t_*) + \ldots, \tag{7.16}$$

$$\hat{p}_*(\mathbf{r}_*, t_*) = p_0(\mathbf{r}_*, t_*) + \varepsilon p_1(\mathbf{r}_*, t_*) + \ldots. \tag{7.17}$$

Substitution into Equations (7.7,7.8) shows that the first two orders of the inner solutions satisfy Laplace's equation

$$\nabla^2\varphi_i = 0, \quad \text{for } i = 0, 1. \tag{7.18}$$

Using Green's third identity these solution can be written in terms of an integral over the boundary of the fluid domain. For $i = 0, 1$

$$\varphi_i(\mathbf{r}_*, t_*) = f_i(t_*) + \frac{1}{4\pi}\int_S \left(\frac{\partial\varphi_i(\mathbf{q}, t_*)}{\partial n} G(\mathbf{r}_*, \mathbf{q}) - \varphi_i(\mathbf{q}, t_*)\frac{\partial G(\mathbf{r}_*, \mathbf{q})}{\partial n}\right) dS(\mathbf{q}), \tag{7.19}$$

where $f_i(t_*)$ are arbitrary functions to be determined through matching with the outer expansion. The Greens function when a rigid wall is present is (as in Chapter 3)

$$G(\mathbf{r}_*, \mathbf{q}) = \frac{1}{|\mathbf{r}_* - \mathbf{q}|} + \frac{1}{|\mathbf{r}'_* - \mathbf{q}|}, \tag{7.20}$$

where $\mathbf{r}^{'}$ is the image point of $\mathbf{r}$. Defining $\tilde{r} = |\tilde{\mathbf{r}}|$ the following estimations are now made

$$\begin{aligned} G(\mathbf{r}_*, \mathbf{q}) = \frac{1}{|\mathbf{r}_* - \mathbf{q}|} + \frac{1}{|\mathbf{r}_* - \mathbf{q}^{'}|} &= \frac{1}{|\tilde{\mathbf{r}}/\varepsilon - \mathbf{q}|} + \frac{1}{|\tilde{\mathbf{r}}/\varepsilon - \mathbf{q}'|} \\ &= 2\frac{\varepsilon}{\tilde{r}} + \varepsilon^2\frac{(\tilde{\mathbf{r}}\cdot\mathbf{q} + \tilde{\mathbf{r}}\cdot\mathbf{q}')}{\tilde{r}^3} + O(\varepsilon^3), \end{aligned} \tag{7.21}$$

$$\begin{aligned} \nabla G(\mathbf{r}_*, \mathbf{q}) = \frac{\mathbf{r}_* - \mathbf{q}}{|\mathbf{r}_* - \mathbf{q}|^3} + \frac{\mathbf{r}_* - \mathbf{q}'}{|\mathbf{r}_* - \mathbf{q}'|^3} &= \frac{\varepsilon^2\tilde{\mathbf{r}} - \varepsilon^3\mathbf{q}}{|\tilde{\mathbf{r}} - \varepsilon\mathbf{q}|^3} + \frac{\varepsilon^2\tilde{\mathbf{r}} - \varepsilon^3\mathbf{q}'}{|\tilde{\mathbf{r}} - \varepsilon\mathbf{q}'|^3} \\ &= 2\varepsilon^2\frac{\tilde{\mathbf{r}}}{\tilde{r}^3} + O(\varepsilon^3) \end{aligned} \tag{7.22}$$

Substituting these into Equation (7.19) gvies the outer limit of the inner expansion

$$(\varphi)^o = f_0(t_*) + \frac{1}{2\pi}\frac{m_0(t_*)}{r_*} + \varepsilon f_1(t_*) + O(\varepsilon^2), \tag{7.23}$$

with

$$m_0(t) = \int_S \frac{\partial \varphi_0(\mathbf{q}, t_*)}{\partial n} dS(\mathbf{q}). \tag{7.24}$$

The inner limit of the outer expansion is obtained by taking a Taylor series expansion of the first two-order terms

$$(\phi_1)^i = \frac{F_1(t_* - \varepsilon r_*)}{\varepsilon r_*} = \frac{F_1(t_*)}{\varepsilon r_*} - \dot{F}_1(t_*) + O(\varepsilon), \tag{7.25}$$

which yields

$$(\phi)^i = (\phi_0)^i + \varepsilon(\phi_1)^i = \frac{F_1(t_*)}{r_*} - \varepsilon \dot{F}_1(t_*) + O(\varepsilon). \tag{7.26}$$

Using Van Dyke's matching principle to match the inner and outer expansions determines the functions

$$f_0(t) = 0, \quad f_1(t_*) = -\frac{\dot{m}_0(t_*)}{2\pi}, \quad F_1(t_*) = \frac{m_0(t_*)}{2\pi}. \tag{7.27}$$

Governing equations

Dropping the asterisks the combined first two order inner solutions $\varphi(r,t) = \varphi_0(r,t) + \varepsilon\varphi_1(r,t)$ are thus governed by the following equations

$$\nabla^2 \varphi = O(\varepsilon^2), \tag{7.28}$$

$$\frac{\mathrm{d}r}{\mathrm{d}t} = \nabla\varphi + O(\varepsilon^2) \text{ on } S, \tag{7.29}$$

$$\frac{\partial \varphi}{\partial t} + \frac{1}{2}|\nabla\varphi|^2 + p_B = O(\varepsilon^2) \text{ on } S, \tag{7.30}$$

$$\varphi|_{r\to\infty} = (\varphi)^o = -\varepsilon \frac{\dot{m}_0(t)}{2\pi} + O(\varepsilon^2), \tag{7.31}$$

with initial condition

$$\varphi_n|_{t=0} = -R_t|_{t=0}. \text{ on } r = R_0. \tag{7.32}$$

The integral equation (7.19) cannot be used to solve for the velocities $\nabla\varphi$ due to the non-zero value of φ at infinity (which depends on $\partial\varphi/\partial n$). To solve this problem the

following decomposition is made

$$\varphi = \Phi - \varepsilon \frac{\dot{m}_0(t)}{2\pi}. \tag{7.33}$$

The variable Φ is then governed by the following equations

$$\nabla^2 \Phi = O(\varepsilon^2), \tag{7.34}$$

$$\frac{\mathrm{d}r}{\mathrm{d}t} = \nabla\Phi + O(\varepsilon^2) \text{ on } S, \tag{7.35}$$

$$\frac{\mathrm{d}\Phi}{\mathrm{d}t} = \frac{1}{2}|\nabla\Phi|^2 - p_B + \varepsilon \frac{\ddot{m}_0(t)}{2\pi} + O(\varepsilon^2) \text{ on } S, \tag{7.36}$$

$$\Phi|_{r\to\infty} = O(\varepsilon^2), \tag{7.37}$$

with initial condition

$$\Phi_n|_{t=0} = -R_t|_{t=0}. \text{ on } r = R_0. \tag{7.38}$$

The term m_0 can be found in terms of the new potential Φ as

$$m_0(t) = \int_S \frac{\partial \varphi_0}{\partial n} = \int_S \frac{\partial \varphi}{\partial n} dS + O(\varepsilon) = \int_S \frac{\partial \Phi}{\partial n} dS + O(\varepsilon). \tag{7.39}$$

Note that the term involving $\ddot{m}_0$ in Equation (7.36) is a combination effect of the bubble and its image to the rigid boundary. For a free surface or infintie fluid the term becomes

$$\varepsilon \frac{\ddot{m}_0(t)}{4\pi}. \tag{7.40}$$

In fact, due to stability issues, the second derivative $\ddot{m}_0$ is not calculated. Instead, we can move it to the left hand side of Equation (7.36) to give

$$\nabla^2 \Phi = O(\varepsilon^2), \tag{7.41}$$

$$\frac{\mathrm{d}r}{\mathrm{d}t} = \nabla\Phi + O(\varepsilon^2) \text{ on } S, \tag{7.42}$$

$$\frac{\mathrm{d}}{\mathrm{d}t}\left[\Phi - \frac{\varepsilon}{2\pi}\dot{m}_0\right] = \frac{1}{2}|\nabla\Phi|^2 - p_B + O(\varepsilon^2) \text{ on } S, \tag{7.43}$$

$$\Phi|_{r\to\infty} = O(\varepsilon^2). \tag{7.44}$$

The variable $\varphi = \Phi - \frac{\varepsilon}{2\pi}\dot{m}_0$ can then be updated in time. To find Φ at the new time step, we then require a method for calculating $\dot{m}_0$.

7.5.2 Calculation of $\dot{m}_0$

The calculation of $\dot{m}_0$ must be done carefully, since the system is numerically unstable. Once φ is updated, the system of equations to solve at time step $k+1$ is

$$\Phi_{k+1}(\mathbf{p}_i) = \varphi_{k+1}(\mathbf{p}_i) + \frac{\varepsilon}{4\pi}\dot{m}_0(k+1), \tag{7.45}$$

$$m_0(k+1) = \int_S \frac{\partial \Phi_{k+1}(\mathbf{p}_i)}{\partial n} dS, \tag{7.46}$$

$$c(\mathbf{p}_i)\Phi_{k+1}(\mathbf{p}_i) + \int_S \Phi_{k+1}(\mathbf{p}_i)\frac{\partial G}{\partial n}(\mathbf{p}_i, \mathbf{q})dS = \int_S G(\mathbf{p}_i, \mathbf{q})\frac{\partial \Phi_{k+1}(\mathbf{p}_i)}{\partial n} dS \tag{7.47}$$

With an initial guess for $m_0(k+1)$, this system can be solved iteratively with the derivative approximated using a least-squares method for stability

$$\dot{m}_0(k+1) \approx \frac{\sum_{i=1}^{N}(t_i - T)(m_0(i) - M)}{\sum_{i=1}^{N}(t_i - T)^2}, \tag{7.48}$$

where t_i are the times and

$$T = \sum_{i=1}^{N} \frac{t_i}{N}, \quad M = \sum_{i=1}^{N} \frac{m_0(i)}{N}. \tag{7.49}$$

7.5.3 Compressible Viscoelastic Models

In the results that will be presented here, the Oldroyd-B model used in previous Chapters will be chosen to model the fluid rheology

$$\boldsymbol{\tau} + \lambda_1 \overset{\nabla}{\boldsymbol{\tau}} = \eta\left(\mathbf{D} + \lambda_2 \overset{\nabla}{\mathbf{D}}\right). \tag{7.50}$$

The derivation of this equation, however, assumes an incompressible fluid. Belblidia et al. [7] developed a compressible Oldroyd-B model given by

$$\boldsymbol{\tau}^s = 2\eta_s \mathbf{D} + \eta_s\left(\frac{\kappa}{\eta_s} - \frac{2}{3}\right)(\nabla \cdot \mathbf{u})\mathbf{I}, \tag{7.51}$$

$$\lambda \overset{\nabla}{\boldsymbol{\tau}^p} + \boldsymbol{\tau}^p = 2\eta_p \mathbf{D}, \tag{7.52}$$

where κ is bulk viscosity and η_s, η_p are the dynamic solvent viscosity and dynamic polymeric viscosity, respectively. This model is not completely general as κ and any

isotropic parts of $\boldsymbol{\tau}^p$ are ignored. Furthermore, generalising a viscoelastic model to a compressible fluid is not as easy as simply including an extra term in the constitutive equation [20]. The question of whether to use the static or augmented pressure must be addressed and mass conservation is now a dynamic equation coupled to the momentum equation. In our BEM model, we are ignoring bulk viscosity, with the stress applied through a boundary condition at the bubble surface. In the near region by the bubble surface the fluid is roughly incompressible and thus it is acceptable to use the incompressible Oldroyd-B equation (7.41).

7.5.4 Other Extensions

The modelling of the fluid rheology throughout most of this thesis was restricted to an Oldroyd-B equation, for simplicity. An interesting extension would be the inclusion of, and comparison between, more complex viscoelastic models. This would allow a more thorough investigation of the effects of fluid rheology on a bubble in specific fluids or applications.

For a cavitation bubble near a rigid wall, the Bjerkness effect causes the bubble to migrate towards the wall. In some cases it was found that the bubble becomes very close to the wall and at this point numerical instabilities can occur due to a very thin fluid layer between the bubble and wall. This numerical difficulty could be overcome by 'attaching' the bubble to the boundary when it becomes too close. This would imply the bubble moving towards the wall pushes the fluid outward until it impacts the wall. A method for achieving this has recently been implemented by Ni et al. [79].

In terms of modelling shock wave lithotripsy, the model could be improved by more accurately modelling the stone surface; either by accounting for the curvature of the stone or more accurately describing the interaction between the ultrasound with the stone surface. For applications such as sonoporation, of paramount importance is a better description of the cell wall; in particular, accounting for some elasticity of the wall. The reaction of the wall to the bubble and fluid motion can drastically affect the dynamics, in some cases even changing the direction of liquid jets.

In all applications, a single bubble has been considered with the influence of nearby bubbles ignored. Often cavitation bubbles will exist in a bubble cloud and thus it would be desirable to extend the model to multiple bubbles.

Appendix A

Oldroyd-B Fluid

For a spherically symmetric bubble in an incompressible Oldroyd-B fluid the integral term in the Rayleigh-Plesset equation (2.53) is given by

$$S_p(t) = 2\int_R^\infty \frac{\tau_{rr}^p(r,t) - \tau_{\theta\theta}^p(r,t)}{r} dr. \tag{A.1}$$

The components of the polymeric stress satisfy

$$\tau_{rr} + \lambda_1\left(\frac{\partial \tau_{rr}}{\partial t} + \frac{R^2\dot{R}}{r^2}\frac{\partial \tau_{rr}}{\partial r} + \frac{4R^2\dot{R}}{r^3}\tau_{rr}\right) = 4\eta_0\frac{R^2\dot{R}}{r^3}, \tag{A.2}$$

$$\tau_{\theta\theta} + \lambda_1\left(\frac{\partial \tau_{\theta\theta}}{\partial t} + \frac{R^2\dot{R}}{r^2}\frac{\partial \tau_{rr}}{\partial r} - \frac{2R^2\dot{R}}{r^3}\tau_{\theta\theta}\right) = -2\eta_0\frac{R^2\dot{R}}{r^3}. \tag{A.3}$$

Using a transformation to Lagrangian coordinates $h = \frac{1}{3}[r^3 - R^3(t)]$ these equations become linear, first-order ordinary differential equations

$$\frac{\mathrm{d}x}{\mathrm{d}t} + \left(\frac{1}{\lambda_1} + 4A\right)x = 4\frac{\eta_0}{\lambda_1}A, \tag{A.4}$$

$$\frac{\mathrm{d}y}{\mathrm{d}t} + \left(\frac{1}{\lambda_1} + 4A\right)y = -2\frac{\eta_0}{\lambda_1}A, \tag{A.5}$$

where the variables have been relabelled $\tau_{rr} = x$, $\tau_{\theta\theta} = y$ and

$$A = \frac{R^2\dot{R}}{r^3} = \frac{R^2(t)\dot{R}(t)}{3h + R^3(t)}. \tag{A.6}$$

Equations (A.4,A.5) are of the form $z' + P(t)z = Q(t)$ which has the general solution

$$z = \mathrm{e}^{-\int_{s_0}^{t} P(s)ds} \int_{\xi_0}^{t} Q(\xi)\mathrm{e}^{-\int_{s_0}^{\xi} P(s)ds} d\xi + C\mathrm{e}^{-\int_{s_0}^{t} P(s)ds} \tag{A.7}$$

For $x = \tau_{rr}$ and $y = \tau_{\theta\theta}$, Equations (A.8) and (A.9) hold, respectively

$$\int P_{(x)}(s)ds = \int \left(\frac{1}{\lambda_1} + \frac{4R^2(s)\dot{R}(s)}{3h + R^3(s)}\right)ds = \frac{s}{\lambda_1} + \frac{4}{3}\ln[3h + R^3(s)], \tag{A.8}$$

$$\int P_{(y)}(s)ds = \int \left(\frac{1}{\lambda_1} - \frac{2R^2(s)\dot{R}(s)}{3h + R^3(s)}\right)ds = \frac{s}{\lambda_1} - \frac{2}{3}\ln[3h + R^3(s)]. \tag{A.9}$$

Substituting these into the general solution (A.7) gives expressions for the stresses in terms of an integral

$$\tau_{rr} = x = \frac{4\eta_0}{\lambda_1}\int_0^t \mathrm{e}^{(\xi-t)/\lambda_1}\left[\frac{[3h + R^3(\xi)]^{1/3}}{[3h + R^3(t)]^{4/3}}\right]R^2(\xi)\dot{R}(\xi)d\xi, \tag{A.10}$$

$$\tau_{\theta\theta} = y = -\frac{2\eta_0}{\lambda_1}\int_0^t \mathrm{e}^{(\xi-t)/\lambda_1}\left[\frac{[3h + R^3(t)]^{2/3}}{[3h + R^3(\xi)]^{5/3}}\right]R^2(\xi)\dot{R}(\xi)d\xi. \tag{A.11}$$

Inserting these solutions into the integral $S_p(t)$ and changing the order of the integration

$$S_p(t) = \frac{2\eta_0}{\lambda_1}\int_0^t \mathrm{e}^{(\xi-t)/\lambda_1}R^2(\xi)\dot{R}(\xi)\left(\int_0^\infty \frac{B(\xi,h,t)}{3h + R^3(\xi)}dh\right)d\xi, \tag{A.12}$$

where the function B is

$$B(\xi,h,t) = 4\frac{[3h + R^3(\xi)]^{1/3}}{[3h + R^3(t)]^{4/3}} + 2\frac{[3h + R^3(t)]^{2/3}}{[3h + R^3(\xi)]^{5/3}}. \tag{A.13}$$

Labelling the expression in brackets in Equation (A.12) as I then

$$T = 4I_1 + 2I_2 = 4\int_0^\infty \frac{[3h + R^3(\xi)]^{1/3}}{[3h + R^3(t)]^{7/3}}dh + 2\int_0^\infty \frac{[3h + R^3(t)]^{-1/3}}{[3h + R^3(\xi)]^{5/3}}dh. \tag{A.14}$$

It can be seen that the integrals I_1 and I_2 are of the form

$$I(a,b) = \int_0^{h^*} \frac{dh}{[3h + R^3(t)]^{a/3}[3h + R^3(\xi)]^{b/3}} \tag{A.15}$$

which, for $(a+b)/3 = 2$ and $h^* \to \infty$ has the solution [94]

$$I(a,b) = \frac{1}{(3-a)[R^3(\xi) - R^3(t)]}\left[1 - \left(\frac{R^3(t)}{R^3(\xi)}\right)^{1-a/3}\right] \tag{A.16}$$

Putting this all together the integral term $S_p(t)$ is finally found to be

$$S_p(t) = \frac{2\eta_0}{\lambda_1 R^4(t)} \int_0^t \mathrm{e}^{(\xi-t)/\lambda_1}\left(R^3(t) + R^3(\xi)\right)\dot{R}(\xi)d\xi. \tag{A.17}$$

Appendix B

Derivation of Periodic Splines

For the toroidal bubble described in Chapter 4 the bubble surface is closed and nodes 1 and $N+1$ coincide. When constructing the system of equations which are solved for the quintic spline coefficients, different boundary conditions are then required to the natural and clamped conditions discussed in Chapter 3. For $i = 1, \ldots, N-2$

$$2h_{i+1}\bar{b}_{i+2} + 4\bigg(h_{i+1} + h_i\bigg)\bar{b}_{i+1} + 2h_i\bar{b}_i = \frac{1}{h_{i+1}}\bar{d}_{i+2} - \bigg(\frac{1}{h_{i+1}} + \frac{1}{h_i}\bigg)\bar{d}_{i+1} + \frac{1}{h_i}\bar{d}_i. \quad \text{(B.1)}$$

$$\frac{-7h_{i+1}^3}{15}\bar{b}_{i+2} - \frac{8}{15}\bigg(h_{i+1}^3 + h_i^3\bigg)\bar{b}_{i+1} - \frac{7h_i^3}{15}\bar{b}_i + \frac{h_{i+1}}{3}\bar{d}_{i+2} + \frac{2}{3}\bigg(h_{i+1} + h_i\bigg)\bar{d}_{i+1} + \frac{h_i}{3}\bar{d}_i$$

$$= \frac{1}{h_{i+1}}\bigg(\bar{f}_{i+2} - \bar{f}_{i+1}\bigg) - \frac{1}{h_i}\bigg(\bar{f}_{i+1} - \bar{f}_i\bigg). \quad \text{(B.2)}$$

Since the surface is now closed, near node $1/N+1$ the boundary conditions are given

by

$$2h_1b_2 + 4(h_1 + h_N)b_1 + 2h_Nb_N = \frac{1}{h_1}d_2 - (\frac{1}{h_1} + \frac{1}{h_N})d_1 + \frac{1}{h_N}d_N, \tag{B.3}$$

$$2h_Nb_1 + 4(h_N + h_{N-1})b_N + 2h_{N-1}b_{N-1} = \frac{1}{h_N}d_1 - (\frac{1}{h_N} + \frac{1}{h_{N-1}})d_N + \frac{1}{h_{N-1}}d_{N-1}, \tag{B.4}$$

$$\frac{-7h_1^3}{15}\bar{b}_2 - \frac{8}{15}\Big(h_1^3 + h_N^3\Big)\bar{b}_1 - \frac{7h_N^3}{15}\bar{b}_N + \frac{h_1}{3}\bar{d}_2 + \frac{2}{3}\Big(h_1 + h_N\Big)\bar{d}_1 + \frac{h_N}{3}\bar{d}_N = \frac{1}{h_1}\Big(\bar{f}_2 - \bar{f}_1\Big) - \frac{1}{h_N}\Big(\bar{f}_1 - \bar{f}_N\Big), \tag{B.5}$$

$$\frac{-7h_1^3}{15}\bar{b}_2 - \frac{8}{15}\Big(h_1^3 + h_N^3\Big)\bar{b}_1 - \frac{7h_N^3}{15}\bar{b}_N + \frac{h_1}{3}\bar{d}_2 + \frac{2}{3}\Big(h_1 + h_N\Big)\bar{d}_1 + \frac{h_N}{3}\bar{d}_N = \frac{1}{h_1}\Big(\bar{f}_2 - \bar{f}_1\Big) - \frac{1}{h_N}\Big(\bar{f}_1 - \bar{f}_N\Big). \tag{B.6}$$

Appendix C

Choice of Function for Nonsingular BEM

The conditions the function f_i (for $i = 1, \ldots, N+1$) in (3.28) must satisfy are

$$\nabla^2 f_i(r, z) = 0, \text{ in } \Omega, \tag{C.1}$$

$$f_i(r_i, z_i) = 0, \tag{C.2}$$

$$\frac{\partial f_i}{\partial n}(r_i, z_i) = 1, \tag{C.3}$$

$$\frac{\partial f_i}{\partial z}(r, 0) = 0. \tag{C.4}$$

To satisfy Laplace's equation (C.1) we try the form

$$f_i(r, z) = A + \frac{B}{|\mathbf{x} - \mathbf{x}_D|} + \frac{C}{|\mathbf{x} - \mathbf{x}_D^{'}|}, \tag{C.5}$$

where A, B, C are constants, $\mathbf{x} = (r\cos\theta, r\sin\theta, z)$ and $\mathbf{x}_D = (0, 0, z_D)$, $\mathbf{x}_D^{'} = (0, 0, z_D^{'})$ are some points not in the domain. Eqn. (C.2) implies

$$A = -\frac{B}{|\mathbf{x}_i - \mathbf{x}_D|} - \frac{C}{|\mathbf{x}_i - \mathbf{x}_D^{'}|}. \tag{C.6}$$

Differentiating f_i then gives

$$\frac{\partial f_i}{\partial n} = -B\frac{\sigma}{\rho^3} - C\frac{\sigma^{'}}{\rho^{'3}} \tag{C.7}$$

with

$$\rho \equiv \sqrt{r^2+(z-z_d)^2},\ \ \rho^{'} \equiv \sqrt{r^2+(z+z_d)^2}\ \ \sigma \equiv rn_r+(z-z_d)n_z,\ \ \sigma^{'} \equiv rn_r+(z+z_d)n_z, \tag{C.8}$$

Evaluating this at $(r,z)=(r_i,z_i)$ Eqn. (C.3) gives

$$-B\frac{\sigma_i}{\rho_i^3} - C\frac{\sigma_i^{'}}{\rho_i^{'3}} = 1. \tag{C.9}$$

The final condition (C.4) leads to following relation

$$\frac{Bz_D}{(r^2+z_D^2)^{3/2}} + \frac{Cz_D^{'}}{(r^2+z_D^{'2})^{3/2}} = 0, \tag{C.10}$$

which has a solution

$$z_D^{'} = -z_D, \quad B = C. \tag{C.11}$$

Finally, solving Eqns (C.6),(C.9) and (C.11) for A, B and C and substituting them into (C.5) yields the expression for f_i

$$f_i(\mathbf{p}) = \frac{-\rho_i^3\bar{\rho}_i^3}{\bar{\rho}_i^3\sigma_i+\rho_i^3\bar{\sigma}_i}\left[\left(\frac{1}{\rho}-\frac{1}{\rho_i}\right)+\left(\frac{1}{\bar{\rho}}-\frac{1}{\bar{\rho}_i}\right)\right]. \tag{C.12}$$

Bibliography

[1] J. S. Allen and R. A. Roy. Dynamics of gas bubbles in viscoelastic fluids. I. Linear viscoelasticity. *J. Acoust. Soc. Am.*, 107:3167–3178, 2000.

[2] J. S. Allen and R. A. Roy. Dynamics of gas bubbles in viscoelastic fluids. II. Nonlinear viscoelasticity. *J. Acoust. Soc. Am.*, 108:1640–1650, 2000.

[3] M. Averkiou, J. Powers, D. Skyba, M. Bruce, and S. Jensen. Ultrasound contrast imaging research. *Ultrasound Quarterly*, 19(1):27–37, 2003.

[4] S. Bao, B. D. Thrall, and D. L. Miller. Transfection of a reporter plasmid into cultured cells by sonoporation in vitro. *Ultrasound Med. Biol.*, 23(6):953–959, 1997.

[5] G. K. Batchelor. *An Introduction to Fluid Dynamics*. Cambridge University Press, London, 1967.

[6] D. W. Beard and K. Walters. Elastico-viscous boundary-layer flows. *Proc. Camb. Phil. Soc.*, 60:667, 1964.

[7] F. Belblidia, I. J. Keshtiban, and M. F. Webster. Stabilised computations for viscoelastic flows under compressible implementations. *J. Non-Newton. Fluid*, 134(1):56–76, 2006.

[8] T. B. Benjamin and A. T. Ellis. The collapse of cavitation bubbles and the pressures thereby produced against solid boundaries. *Phil. Trans. R. Soc. Lond*, 1966.

[9] J. P. Best. The formation of toroidal bubbles upon the collapse of transient cavities. *J. Fluid Mec. A.*, 251:79–107, 1993.

[10] J. P. Best. The rebound of toroidal bubbles. In *Bubble Dynamics and Interface Phenomena*, pages 405–412. Springer, 1994.

[11] J. P. Best and A. Kucera. A numerical investigation of non-spherical rebounding bubbles. *J. Fluid Mech*, 245:137–154, 1992.

[12] R. B. Bird. Useful non-Newtonian models. *Annu. Rev. Fluid Mech.*, 8:13–34, 1976.

[13] R. B. Bird, R. C. Armstrong, and O. Hassager. *Dynamics of Polymeric Liquids. Volume 1: Fluid Mechanics*. John Wiley and Sons, New York, 1987.

[14] J. R. Blake. The Kelvin impulse: Application to cavitation bubble dynamics. *J. Austral. Math. Soc.*, 30:127–146, 1988.

[15] J. R. Blake and P. Cerone. A note on the impulse due to a vapour bubble near a boundary. *J. Austral. Math. Soc.*, 23:383–393, 1982.

[16] J. R. Blake and D. C. Gibson. Growth and collapse of a vapour cavity near a free surface. *J. Fluid Mech.*, 111:123–140, 1981.

[17] J. R. Blake, M. C. Hooton, P. B. Robinson, and R. P. Tong. Collapsing cavities, toroidal bubbles and jet impact. *Philosophical Transactions of the Royal Society of London. Series A: Mathematical, Physical and Engineering Sciences*, 355(1724):537–550, 1997.

[18] J. R. Blake, B. B. Taib, and G. Doherty. Transient cavities near boundaries. Part 1. Rigid boundary. *J. Fluid Mech.*, 170:479–497, 1986.

[19] J. R. Blake, B. B. Taib, and G. Doherty. Transient cavities near boundaries. Part 2. Free surface. *J. Fluid Mech.*, 181:197–212, 1987.

[20] P. C. Bollada and T. N. Phillips. On the mathematical modelling of a compressible viscoelastic fluid. *Archive for Rational Mechanics and Analysis*, 205(1):1–26, 2012.

[21] J. M. Boulton-Stone. The effect of surfactant on bursting gas bubbles. *J. Fluid Mech.*, 302:231–257, 1995.

[22] J. M. Boulton-Stone and J. R. Blake. Gas bubbles bursting at a free surface. *J. Fluid Mech.*, 254:437–466, 1993.

[23] C. E. Brennen. *Cavitation and Bubble Dynamics*. Oxford University Press, Oxford, 1995.

[24] E. A. Brujan. A first-order model for bubble dynamics in a compressible viscoelastic liquid. *J. Non-Newtonian. Fluid Mech.*, 84(1):83–103, 1999.

[25] E. A. Brujan. The equation of bubble dynamics in a compressible linear viscoelastic liquid. *J. Fluid Dyn. Res.*, 29:287–294, 2001.

[26] E. A. Brujan. Cardiovascular cavitation. *Med. Eng. Phys.*, 31:742–751, 2009.

[27] E. A. Brujan. *Cavitation in Non-Newtonian Fluids With Biomedical and Bioengineering Applications*. Springer, Berlin, 2011.

[28] M. L. Calvisi, O. Lindau, J. R. Blake, and A. J. Szeri. Shape stability and violent collapse of microbubbles in acoustic traveling waves. *Phys. Fluids (1994-present)*, 19(4):47–101, 2007.

[29] G. Chahine and A. Bovis. Pressure field generated by nonspherical bubble collapse. *J. Fluids Eng.*, 105:356–362, 1983.

[30] C. Chaussy, G. Tailly, B. Forssmann, C. Bohris, A. Lutz, M. Tailly-Cusse, and T. Tailly. Extracorporeal shock wave lithotripsy in a nutshell, 2014.

[31] Y. L. Chen and J. Israelachvili. New mechanism of cavitation damage. *Science*, 252:1157–1160, 1991.

[32] I. Chilibon, M. Wever, J-P. Lafaut, and L. Baert. Cavitation role in extracorporeal shock wave lithotripsy. *J. Optoelectron Adv. M.*, 8(1):235–237, 2006.

[33] C. C. Church. The effects of an elastic solid surface layer on the radial pulsations of gas bubbles. *J. Acoust. Soc. Am.*, 97(3):1510–1521, 1995.

[34] A. J. Coleman, J. E. Saunders, L. A. Crum, and M. Dyson. Acoustic cavitation generated by an extracorporeal shockwave lithotripter. *Ultrasound Med. Biol.*, 13(2):69–76, 1987.

[35] D. Cosgrove. Ultrasound contrast agents: An overview. *European Journal of Radiology*, 60:324–330, 2006.

[36] Z. Ding and S. M. Gracewski. The behaviour of a gas cavity impacted by a weak or strong shock wave. *J. Fluid Mech.*, 309:183–209, 1996.

[37] A. A. Doinikov, J. F. Haac, and P. A. Dayton. Modeling of nonlinear viscous stress in encapsulating shells of lipid-coated contrast agent microbubbles. *Ultrasonics*, 49(2):269–275, 2009.

[38] D. G. Dommermuth and D. K. P. Yue. Numerical simulations of nonlinear axisymmetric flows with a free surface. *J. Fluid Mech.*, 178:195–219, 1987.

[39] A. T. Ellis. Techniques for pressure pulse measurement and high-speed photography in ultrasonic cavitation. Technical report, DTIC Document, 1955.

[40] D. J. Flannigan and K. S. Suslick. Plasma formation and temperature measurement during single-bubble cavitation. *Nature*, 434:52–55, 2005.

[41] J. Flores and M. Holt. Glimm's method applied to underwater explosions. *J. Comput. Phys.*, 44(2):377–387, 1981.

[42] H. S. Fogler and J. D. Goddard. Collapse of spherical cavities in viscoelastic fluids. *Phys. Fluids*, 13:1135–1141, 1970.

[43] H. S. Fogler and J. D. Goddard. Oscillations of a gas bubble in viscoelastic liquids subject to acoustic and impulsive pressure variations. *J Appl. Phys.*, 42(1):259–263, 1971.

[44] D. F. Gaitan, L. A. Crum, C. C. Church, and R. A. Roy. Sonoluminescence and bubble dynamics for a single, stable, cavitation bubble. *J. Acoust. Soc. Am.*, 91:3188–3183, 1992.

[45] H. Giesekus. A simple constitutive equation for polymer fluisd based on the concept of deformation-dependent tensorial mobility. *J. Non-Newtonian Fluid*, 11:69–109, 1982.

[46] F. R. Gilmore. The collapse and growth of a spherical bubble in a viscous compressible liquid. *California Institute of Technology Hydrodynamics Laboratory, Report*, (26-4), 1952.

[47] R. E. Glazman. Effects of adsorbed films on gas bubble radial oscillations. *The Journal of the Acoustical Society of America*, 74(3):980–986, 1983.

[48] A. A. Gubaidullin, O. Sh. Beregova, and S. A. Bekishev. Shock waves in non-newtonian bubbly liquids. *Int. J. Morphol.*, 27:635–655, 2001.

[49] L. Guerri, G. Lucca, and A. Prosperetti. A numerical method for the dynamics of non-spherical cavitation bubbles. In *Proc. 2nd Int. Colloq. on drops and bubbles*, page 175, 1981.

[50] J-F. Haas and B. Sturtevant. Interaction of weak shock waves with cylindrical and spherical gas inhomogeneities. *J. Fluid Mech.*, 181:41–76, 1987.

[51] C. Hastings. *Approximations for Digital Computers*. Princeton University Press, Princeton, N.J., 1995.

[52] L. Hoff. *Acoustic characterization of contrast agents for medical ultrasound imaging*. Springer Science & Business Media, 2001.

[53] A. R. Jamaluddin. *Free-Lagrange simulations of shock-bubble interaction in ESWL*. PhD thesis, University of Southampton, 2004.

[54] H. Jeffreys. *The Earth*. Cambridge University Press, Cambridge, 1929.

[55] J. Jimenez-Fernandez and A. Crespo. Bubble oscillation and inertial cavitation in viscoelastic fluids. *Ultrasonics*, 43:643–651, 2005.

[56] D. D. Joseph and T. Y. Liao. Potential flows of viscous and viscoelastic fluids. *J. Fluid Mech.*, 256:1–23, 1994.

[57] E. KLaseboer and B. C. Khoo. An oscillating bubble near an elastic material. *J. Appl. Phys.*, 96:5808–5818, 2004.

[58] E. Klaseboer, Q. Sun, and D. Chan. Non-singular boundary integral methods for fluid mechanics applications. *J. Fluid Mech.*, 696:468–478, 2012.

[59] E. Klaseboer, C. Turangan, S. W. Fong, T. G. Liu, K. C. Hung, and B. C. Khoo. Simulations of pressure pulse-bubble interaction using boundary element method. *Comput. Methods Appl. Mech. Engrg.*, 195:4287–4302, 2006.

[60] T. Kodama and K. Takayama. Dynamic behaviour of bubbles during extracorporeal shock-wave lithotripsy. *Ultrasound Med. Biol.*, 24(5):723–738, 1998.

[61] M. Kornfeld and L. Suvorov. On the destructive action of cavitation. *J. Appl. Phys.*, 15(6):495–506, 1944.

[62] W. Lauterborn. Cavitation bubble dynamics - new tools for an intricate problem. *Appl. Sci. Res.*, 38:165–178, 1982.

[63] W. Lauterborn and H. Bolle. Experimental investigations of cavitation-bubble collapse in the neighbourhood of a solid boundary. *J. Fluid Mech.*, 72:391–399, 1975.

[64] M. Lee and E. Klaseboer. On the boundary integral method for the rebounding bubble. *J. Fluid Mech*, 570:407–429, 2007.

[65] S. P. Levitskiy and Z. P. Shulman. *Bubbles in polymeric liquids: dynamics and heat-mass transfer*. Lancaster: technomic, Lancaster, 1995.

[66] S. J. Lind. *A Numerical Study of the Effect of Viscoelasticity on Cavitation and Bubble Dynamics*. PhD thesis, Cardiff University, 2010.

[67] S. J. Lind and T. N. Phillips. Spherical bubble collapse in viscoelastic fluids. *J. Non-Newtonian Fluid Mech*, 165, 2010.

[68] S. J. Lind and T. N. Phillips. The influence of viscoelasticity on the collapse of cavitation bubbles near a rigid boundary. *Theor comp fluid dyn*, 26(1-4):245–277, 2012.

[69] T. S. Lundgren and N. N. Mansour. Oscillations of drops in zero gravity with weak viscous effects. *J. Fluid Mech.*, 194:479–510, 1988.

[70] T. S. Lundgren and N. N. Mansour. Vortex ring bubbles. *J Fluid Mech.*, 224(5):177–196, 1991.

[71] S. W. J. Brown M. S. Barrow and P. R. Williams. Extensional flow of liquid jets formed by bubble collapse in oils under cavitation-generated pressure waves. *Exp. Fluids*, 36:463–472, 2004.

[72] S. P. Marsh. *LASL shock Hugoniot data*, volume 5. Univ of California Press, 1980.

[73] D. L. Miller, S. V. Pislaru, and J. F. Greenleaf. Sonoporation: Mechanical DNA delivery by ultrasonic cavitation. *Somat cell molec gen*, 27:115–134, 2002.

[74] L. M. Milne-Thomson. *Theoretical Hydrodynamics*. St Martin's Press Inc., New York, 1960.

[75] M. Minnaert. Xvi. on musical air-bubbles and the sounds of running water. *The London, Edinburgh, and Dublin Philosophical Magazine and Journal of Science*, 16(104):235–248, 1933.

[76] T. M. Mitchell, C. L. Kling, R. Cheesewright, and F. G. Hammitt. Numerical and photographic studies of axisymmetric bubble collapse, 1983.

[77] K. E. Morgan, J. S. Allen, P. A. Dayton, J. E. Chomas, A. L. Klibanov, and K. E. Ferrara. Experimental and theoretical evaluation of microbubble behaviour: effect of transmitted phase and bubble size. *IEEE transactions on ultrasonics, ferroelectrics and frequency control*, 47(6):1494–1509, 2000.

[78] C. Naude. *On the mechanism of cavitation damage by non-hemispherical cavities collapsing in contact with a solid boundary.* PhD thesis, California Institute of Technology, 1960.

[79] B. Y. Ni, A. M. Zhang, and G. X. Wu. Numerical and experimental study of bubble impact on a solid wall. *J. Fluid Eng*, 137(3):1–16, 2015.

[80] J. G. Oldroyd. On the formulation of rheological equations of state. *Proc. Roy. Soc.*, pages 523–541, 1950.

[81] J. G. Oldroyd. Non-Newtonian effects in steady motion of some idealized elastico-viscous liquids. *Proc. Roy. Soc.*, pages 278–297, 1958.

[82] U. Parlitz, R. Mettin, S. Luther, I. Akhatov, M. Voss, and W. Lauterborn. Spatio–temporal dynamics of acoustic cavitation bubble clouds. *Philosophical Transactions of the Royal Society of London. Series A: Mathematical, Physical and Engineering Sciences*, 357(1751):313–334, 1999.

[83] N. Phan-Thien and R. I. Tanner. A new constitutive equation derived from network theory. *J. Non-Newtonian Fluid*, 2:69–109, 1977.

[84] A. C. Pipkin. *Lectures on Viscoelasticity Theory.* Springer, New York, 1972.

[85] M. Plesset and R. Chapman. Collapse of an initially spherical vapour cavity in the neighbourhood of a solid boundary. *J. Fluid Mech.*, 47:283–290, 1971.

[86] J. J. Rassweiler, T. Knoll, K. Köhrmann, J. A. McAteer, J.E. Lingeman, R. O. Cleveland, M. R. Bailey, and C. Chaussy. Shock wave technology and application: An update. *Eur. Urol.*, 59(5):784–796, 2011.

[87] M. Rattray. *Perturbation effects in cavitation bubble dynamics.* PhD thesis, California Institute of Technology, 1951.

[88] Lord Rayleigh. On the pressure developed in a liquid during the collapse of a spherical cavity. *Phil. Mag.*, 34:94–98, 1917.

[89] A. M. Robertson. Lecture notes on non-newtonian fluids. Part I: Inelastic fluids. University Lecture, 2005.

[90] B. M. Rush and A. Nadim. The shape oscillations of a two-dimensional drop including viscous effects. *Eng. Anal. Bound. Elem.*, 24:43–51, 2000.

[91] R. P. Sear. Nucleation: theory and applications to protein solutions and colloidal suspensions. *J. Phys-Condens. Mat.*, 19(3):33–61, 2007.

[92] Z. P. Shulman and S. P. Levitskii. Closure of a cavity in polymer liquid. *J. Eng. Phys*, 53:893–897, 1987.

[93] D. Y. Song and T. Q. Jiang. Study on the constitutive equations with fractional derivative for the viscoelastic fluids - modified Jeffreys model and its application. *Rheol. Acta.*, 37:512–517, 1998.

[94] J. R. Street. The rheology of phase growth in elastic liquids. *J Rheol.*, 12(1):103–131, 1968.

[95] J. R. Street, A. L. Fricke, and L. Philip Reiss. Dynamics of phase growth in viscous, non-newtonian liquids. *Ind. Eng. Chem. Fundam.*, 10.

[96] Q. Sun, E. Klaseboer, B. C. Khoo, and D. Y. C. Chan. A robust and non-singular formulation of the boundary integral method for the potential problem. *Eng. Anal. Bound. Elem.*, 43:117–123, 2014.

[97] B. B. Taib. *Boundary integral method applied to cavitation bubble dynamics*. PhD thesis, University of Wollongong, 1985.

[98] I. Tanasawa and W. J. Yang. Dynamic behaviour of a gas bubble in viscoelastic liquids. *J. Appl. Phys.*, 41:4526–4531, 1970.

[99] R. Y. Ting. Viscoelastic effect of polymers on single bubble dynamics. *AIChE J.*, 21:810–813, 1975.

[100] Y. Tomita, P. B. Robinson, R. P. Tong, and J. R. Blake. Growth and collapse of cavitation bubbles near a curved rigid boundary. *Journal of Fluid Mechanics*, 466:259–283, 2002.

[101] C. K. Turangun, G. P. Ong, E. Klaseboer, and B. C. Khoo. Experimental and numerical study of transient bubble-elastic membrane interaction. *J. Appl. Phys.*, 100, 2006.

[102] H. von Bibra, J. Voigt, M. Fröman, D. Bone, B. Wranne, and A. Juhlin-Dannfeldt. Interaction of microbubbles with ultrasound. *Echocardiography*, 16(s1):733–741, 1999.

[103] J. K. Walters and J. F. Davidson. The initial motion of a gas bubble formed in an inviscid liquid. *J. Fluid Mech.*, 17(03):321–336, 1963.

[104] M. J. Walters and T. N. Phillips. Modelling encapsulated bubbles near a boundary using a non-singular boundary element method. *J. Non-Newtonian Fluid Mech. (in preparation)*, 2015.

[105] M. J. Walters and T. N. Phillips. A non-singular boundary element method for modelling bubble dynamics in viscoelastic fluids. *J. Non-Newtonian Fluid Mech. (in preparation)*, 2015.

[106] Q. Wang. Multi-oscillations of a bubble in a compressible liquid near a rigid boundary. *J. Fluid Mech.*, 745:509–536, 2014.

[107] Q. Wang, K. Manmi, and M. L. Calvisi. Numerical modeling of the 3D dynamics of ultrasound contrast agent microbubbles using the boundary integral method. *Physics of Fluids (1994-present)*, 27(2):022104, 2015.

[108] Q. X. Wang and J. R. Blake. Non-spherical bubble dynamics in a compressible liquid. Part 1. Travelling acoustic wave. *J Fluid Mech.*, 659:191–224, 2010.

[109] Q. X. Wang and J. R. Blake. Non-spherical bubble dynamics in a compressible liquid. Part 2. Acoustic standing wave. *J Fluid Mech.*, 679:559–581, 2011.

[110] Q. X. Wang, K. S. Yeo, B. C. Khoo, and K. Y. Lam. Vortex ring modelling of toroidal bubbles. *Theor Comp Fluid Dyn*, 19:303–317, 2005.

[111] P. N. T. Wells. Ultrasound imaging. *Phys. Med. Biol.*, 51:R83–R89, 2006.

[112] P. R. Williams, P. M. Williams, and S. W. J. Brown. A study of liquid jets formed by bubble collapse under shock waves in elastic and Newtonian liquids. *J. Non-Newtonian Fluid Mech.*, 76:307–325, 1998.

[113] J. Wu, J. Pepe, and W. Dewitt. Nonlinear behaviours of contrast agents relevant to diagnostic and therapeutic applications. *Ultrasound Med. Biol.*, 29(4):555–562, 2003.

[114] W-J. Yang and H-C. Yeh. Theoretical study of bubble dynamics in purely viscous fluids. *AIChE Journal*, 12(5):927–931, 1966.

[115] H. C Yeh and W. J. Yang. The dynamics of gas bubbles moving in liquids with pressure gradients. *J. Appl. Phys.*, 39:3156–3165, 1968.

[116] Z. Zapryanov and S. Tabakova. *Dynamics of Bubbles, Drops and Rigid Particles.* Kluwer Academic Publishers, Dordrecht, Netherlands, 1999.

[117] Y. L. Zhang, K. S. Yeo, B. C. Wang, and C. Wang. 3D jet impact and toroidal bubbles. *J Comput. Phys.*, 166:336–360, 2001.

[118] Z. Zhang and H. Zhang. Surface tension effects on the behaviour of a cavity growing, collapsing and rebounding near a rigid wall. *Phys rev*, 70, 2004.

[119] S. Zhu, F. H. Cocks, G. M. Preminger, and P. Zhong. The role of stress waves and cavitation in stone comminution in shock wave lithotripsy. *Ultrasound Med. Biol.*, 28(5):661–671, 2002.